

Trinity College Dublin
Coláiste na Tríonóide, Baile Átha Cliath
The University of Dublin

Controllable Growth of Few-Layered MoS_2 Films and Their Memristive Behaviours

A Dissertation by
Lulin Wang

Under the supervision of
Prof. Hongzhou Zhang

For the Degree of
Doctor of Philosophy

School of Physics
Trinity College Dublin

2025
Dublin, Ireland

To my dearest Dad, Mom, Haizhong and Canchen, with love.

Declaration

I declare that this thesis has not been submitted as an exercise for a degree at this or any other university and it is entirely my own work. I have made no use of sources, materials or assistance other than those which have been openly and fully acknowledged in the text.

I agree to deposit this thesis in the University's open access institutional repository or allow the Library to do so on my behalf, subject to Irish Copyright Legislation and Trinity College Library conditions of use and acknowledgement.

I consent to the examiner retaining a copy of the thesis beyond the examining period, should they so wish (EU GDPR May 2018).

Signed: Lulin Wang Date: 06/06/2025

Abstract

Two-dimensional (2D) transition metal dichalcogenides (TMDs) have emerged as promising candidates for future electronic materials, enabling data-centred energy-effective applications. 2D MoS_2 is the archetypical member of TMDs, offering exceptional electrical, optoelectronic, and mechanical properties. Despite extensive research efforts, there are still significant hurdles to realise their application potential. Achieving controllable and scalable thesis of 2D MoS_2 remains a critical challenge. While alkali halide assisted chemical vapour deposition (CVD) enables wafer-scale growth of polycrystalline 2D MoS_2 on SiO_2 substrate, the residual alkali atoms are detrimental to device performance, and the uncontrolled grain structures lead to high device variability and poor reliability.

This thesis introduces a novel contamination-free growth promoter, photoresist S1813, which enables the clean and controlled synthesis of 2D MoS_2 with desirable grain structures. At a sulfur temperature of 250 °C, the promoter-enhanced region shows over threefold coverage, a sixfold increase in the monolayer ratio, and a 60-fold enhancement in the proportion of large flakes ($\geq$ 10 µm) compared to pristine regions. Systematical investigation under varing sulfur temperature reveal a transition from homogeneous to heterogeneous nucleation and a strong correlation between sulfur temperature and sulfur vacancy density.

Using photoresist patternability, a scalable and highly controllable polymer-assisted CVD method is developed for the selective growth of MoS_2. By strategically incorporating polymer mesas patterned via laser direct writing (LDW) and optical lithography (OL), we demonstrate precise spatial control over nucleation and film morphology. Systematic analyses across the substrate revealed a clear correlation among MoO_x particle density, mesa thickness, and surrounding film dimensions, highlighting the critical influence of reactant concentrations, particularly MoO_x and sulfur, on MoS_2 growth outcomes. These findings elucidate the diffusion-controlled growth mechanisms responsible for patterned MoS_2 formation. Importantly, this method was successfully scaled to achieve milimeter-scale patterned growth, demonstrating significant potential for industrial adoption. By carefully controlling the initial polymer thickness and

pattern geometry, we consistently produce monolayer MoS_2 films with lateral dimensions exceeding 5 mm.

To demonstrate the versatility of the growth method, we have fabricated planar memristors based on the 2D MoS_2 films. A forming process enables bipolar switching in the $Au/MoS_2/Au$ memristor, where a low operating voltage (< 1 V) drives defect migration and modulates the Schottky barrier at the film-metal interface. The tuning of the Schottky barrier regulates the resistance states of the channel as well as the dynamics of the switching.

The growth strategy is intrinsically simple, scalable, controllable, and compatible with current semiconductor technology. The research can be extended to other TMDs and enable a wide range of 2D electronic devices. Specifically, the controllability and versatility of the method enable us to explore (1) selective stable unipolar non-degenerated p-type doping in 2D MoS_2 films, (2) patterned 2D TMD functional blocks with desirable grain structures, and (3) the potential of the 2D memristors as an artificial synapse in neuromorphic applications.

Keywords Two-dimensional layered materials, molybdenum disulfide, chemical vapour deposition, controllable growth, memristor.

Publications

Journal Articles

1. **L.L. Wang**, K. Kannan, Y. Sun, N. B. Mullani, H.Z. Zhang. Patterned growth of MoS_2 and its controllability. *in preparation*.

2. **L.L. Wang**, K. Kannan, Y. Sun, N. B. Mullani, H.Z. Zhang. Contact modulated resistive switching in MoS_2-MoO_2 based planar memristors. *in preparation*

3. **L.L. Wang**, Y. Sun, K. Kannan, L. Gannon, X.Y. Guo, A. Rafferty, K. Gaff, N. B. Mullani, H.Z. Weng, Y.B. Zhou, V. Nicolosi, C. McGuinness, P. Gleeson, H.Z. Zhang. Enhanced chemical vapour deposition of monolayer MoS_2 films via a clean promoter. *Advanced Materials Interfaces* (in revision). ArXiv preprint arXiv:2502.04505 (2025).

4. H.Z. Weng, H.L. Tu, V. Kumar, **L.L. Wang**, et. al. Thermally controlled dual-mode Si_3N_4 microresonators for generation of octave-spanning Kerr solitons. *Physical Review Applied*, 23.3 (2025), 034029.

5. S. Aldana, **L.L. Wang**, I. A. Spiridon, H.Z. Zhang. Understanding Substrate Effects on 2D MoS_2 Growth: A Kinetic Monte Carlo Approach. *Advanced Materials Interfaces*, 11.32 (2024): 2400209.

Talks & Conferences

1. **L.L. Wang**, Enhanced chemical vapor deposition of monolayer MoS_2 films via a clean promoter. (poster) *Ireland Spring Conference (IOP Ireland), Galway, Ireland, Feb. 2025.*

2. **L.L. Wang**, Enhanced chemical vapor deposition of monolayer MoS_2 films via a clean growth promoter. (poster) *It's Her. Women in STEM Summit. Dublin, Ireland, March 2024.*

3. **L.L. Wang**, Enabling applications of monolayer MoS_2 films: controllable growth and synaptic devices. (Invited seminar) *Components Research, Intel*

Oregon, online, Feb. 2024.

4. **L.L. Wang**, Enhanced chemical vapor deposition of monolayer MoS_2 films via a clean growth promoter. (contributed talk) *Microscopy Society of Ireland Symposium, Limerick, Ireland, Jan. 2024.*

5. **L.L. Wang**, Enhance chemical vapor deposition of large scale monolayered MoS_2 films via a clean growth promoter. (poster) *SFI summit, Cork/online, Ireland, Nov. 2023.*

6. **L.L. Wang**, Substrate roughness dominated CVD growth of morphology controllable MoS_2. (poster) *2D TMDs, Cambridge, UK, June 2023.*

7. **L.L. Wang**, A novel polymer-assisted CVD method for controllable and scalable 2D MoS_2 deposition. (contributed talk) *14^{th} Spanish Conference on Electron Devices, Valencia, Spain, June 2023.*

8. **L.L. Wang**, Contact modulated resistive switching in a planar oxygen-doped MoS_2 memristor. (abstract) *It's Her. Women in STEMM Summit, Dublin/online, Ireland, March 2023.*

9. **L.L. Wang**, Contact modulated resistive switching in a planar oxygen-doped MoS_2 memristor. (poster) *SFI summit, Ireland, Nov. 2022.*

Acknowledgements

Undertaking a PhD has been a challenging yet profoundly rewarding journey, and I am deeply grateful to the many people who have supported me along the way.

First and foremost, I would like to express my sincere gratitude to my supervisor, Prof. Hongzhou Zhang, for his steadfast guidance and patience throughout my PhD. His insightful advice, constructive feedback, and dedication have been invaluable in shaping both my research and my growth as a researcher. His ability to inspire critical thinking has been instrumental in my development.

Second, I would like extend my sincere appreciation to my Intel mentor, Dr. Peter Gleeson, whose expertise and insights have greatly enhanced my hands-on experimental skills and advancing this project. His unwavering support and encouragement—through insightful discussions, valuable suggestions, and technical guidance—have been pivotal in navigating my research and inspiring me to persevere and complete this journey.

Special thanks to my fellow group members, past and present. Samuel, Navaj, Yue, Kaushik and Xilong, Yangbo and Jakub and others. The collaborative and stimulating research environment, enriched by their generosity in sharing knowledge and ideas, has been invaluable. Whether through scientific discussions or casual meal conversations, their support has been deeply appreciated.

Over the years, I have been fortunate to collaborate with a diverse group of researchers from across different teams, each contributing in their own way—whether through experimental guidance, thought-provoking discussions, or much-needed moments of levity. While it would be impossible to name everyone, I am particularly grateful to Dr. Ke Li, Prof. Cormac Mc Guinness, Dr. Lee Gannon, Dr. Xuyun Guo, Dr. Aran Rafferty, Dr. Mugahid Ali, Dr. Jing Li, Dr. Shixin Liu, Dr. Jing Qian, Dr. Meiying Liang, Dr. Xiaoqiong Du, Dr. Ruiyuan Tian, Dr. Gaozhong Wang, Dr. Xia Zhang, Dr. Yunhong Shi, Dr. Luming Yang, Dr. Nishtha Shelly, Dr. Arvind Venkatraman, Cansu Ihan, and many others who

made this journey richer.

Access to state-of-the-art facilities and resources has been crucial in advancing this work, in particular, I would like to express my gratitude to the dedicated staffs and technicians at CRANN, SNIAM, and AML for their invaluable support with equipment and data collection. Special thanks go to Dr. Riley Gatensby, Dr. Chris Murray, Dr. Jingjing Wang, Dr. David Caffrey, Enda O'Reilly, Kenneth Concannon, James McLoughlin, Karl Gaff, Patrick Murphy, Christopher Smith, Dr. Victor Usov, Alan O'Meara, Dermot Daly, Clive Downing, Dr. Megan Canavan, etc.

I would like to extend my deepest gratitude to my dear friends, Yutong's family, Lily and Jackey's family, and Jack's family, for their enduring care, support, and encouragement throughout my journey. Whether it was the hot meal delivered to my doorstep on a windy and rainy winter evening or the joyful weekends we spent together. These gestures shone like warm sunlight into my heart, giving me the strength to keep moving forward. I could not have weathered those stressful periods without them.

Above all, I own my deepest gratitude to my family—my husband Haizhong and my son Canchen for their unconditional love, encouragement, and unshakable belief in me. To my parents and parents-in-law, thank you for your boundless support and patience. I am especially grateful to them for overcoming all obstacles to care for my son, which allowed me to dedicate more time to my research and thesis. Whether through uplifting words or quiet presence, their support has been the foundation that sustained me through this journey.

Contents

Abstract v

Publications vii

Acknowledgements ix

List of Figures xiii

List of Tables xviii

Nomenclature xix

1 Introduction 1

2 Two-dimensional MoS_2 5

2.1 MoS_2 structure and properties . . . 5

2.1.1 Structure of MoS_2 . . . 5

2.1.2 Electronic properties of 2H MoS_2 . . . 7

2.2 Synthesis of two-dimensional (2D) MoS_2 . . . 15

2.2.1 Overview of 2D MoS_2 synthesis . . . 15

2.2.2 Scalable MoS_2 growth via chemical vapour deposition (CVD) method . . . 18

2.2.3 Spatially controlled growth of 2D MoS_2 . . . 21

2.3 MoS_2 memristor . . . 23

2.3.1 Memristor fundamentals . . . 24

2.3.2 2D memristors . . . 27

2.3.3 Switching mechanisms in 2D MoS_2 . . . 29

3 Fabrication and characterization techniques 39

3.1 Material preparation . . . 39

3.1.1 Chemical vapour deposition (CVD) . . . 39

3.1.2 2D MoS_2 transfer . . . 43

3.2 Device fabrication . . . 44
3.2.1 Lithography . . . 45
3.2.2 Dry Etching . . . 46
3.2.3 E-beam evaporation . . . 49
3.3 Characterisation techniques . . . 51
3.3.1 Microscopy . . . 52
3.3.2 Spectroscopy . . . 62
3.3.3 Thermal analysis . . . 72
3.3.4 Electrical measurement . . . 73

4 Polymer-enhanced deposition of 2D MoS_2 77
4.1 Introduction . . . 77
4.2 Substrate preparation and typical CVD process . . . 78
4.3 Promoter effects on the MoS_2 growth . . . 80
4.3.1 Enhanced growth on the promoter region . . . 80
4.3.2 Morphology of the 2D MoS_2 flakes . . . 82
4.3.3 Characterisation of the particles in pristine region . . . 85
4.3.4 Cleanliness of the promoter-enhanced growth . . . 86
4.4 Effects of the sulphur-source temperature . . . 88
4.4.1 Morphological changes in MoS_2 . . . 89
4.4.2 Quality variation in MoS_2 . . . 93
4.4.3 Sulphur vacancies in MoS_2 . . . 95
4.5 The mechanism of growth promotion . . . 98
4.6 Conclusions . . . 101

5 Patterned growth of MoS_2 103
5.1 Substrate preparation and CVD process . . . 103
5.2 Patterned MoS_2 films using laser direct writing (LDW) mesas . . . 106
5.2.1 General morphology . . . 106
5.2.2 Optical properties of patterned MoS_2 . . . 111
5.3 Morphology evolution of patterned MoS_2 . . . 113
5.3.1 Growth variation in a single CVD run . . . 113
5.3.2 Reduction of MoO_x in the growth environment . . . 115
5.4 Growth mechanism of MoS_2 patterns . . . 117
5.4.1 Morphological variations with distance from the MoO_3 source . . . 118
5.4.2 Growth mechanism of patterned MoS_2 . . . 120
5.4.3 Evidence supporting the growth mechanism . . . 122
5.5 Optimisation of the patterned growth . . . 126

5.6 Conclusion . . . 128

6 Resistive switching in MoS_2 based planar memristors **131**
6.1 Device fabrication . . . 131
6.2 Electroforming and quasi-static response . . . 133
6.3 Dynamic response and conduction mechanism . . . 137
6.4 Switching mechanism . . . 141
6.5 Neuromorphic Applications . . . 147
6.6 Conclusions . . . 150

7 Conclusions and Outlook **151**
7.1 Conclusions . . . 151
7.2 Outlook . . . 152

References **153**

A Appendices **181**
A.1 Optical contrast analyze of MoS_2 . . . 181
A.2 Grain boundary visibility . . . 183
A.3 Survey spectra of X-ray photoelectron spectroscopy (XPS) . . . 185
A.4 Thermal stability of photoresist S1813 . . . 187
A.5 XRD main peaks of Mo_xS_y and Mo_xO_y . . . 189
A.6 Overview of patterned growth samples . . . 191
A.7 Diffusion process of sulphur and molybdenum . . . 195
A.8 Transfer length method (TLM) measurement . . . 197
A.9 *I-V* fittings . . . 199

List of Figures

2.1 Schematics of the crystal structure of 2H-MoS_2. 6
2.2 Band structure of MoS_2. 8
2.3 Electrical transport in MoS_2. 10
2.4 Energy band diagram of metal-semiconductor (n-type) contact. . . 11
2.5 Charge-injection in two-dimensional (2D) MoS_2. 13
2.6 The disadvantage of NaCl-assisted growth of MoS_2. 20
2.7 Selective growth of MoS_2 by different methods. 23
2.8 The first memristor. 24
2.9 Typical I-V characteristic of a memristor device. 25
2.10 Schematic illustration of biological synapses. 28
2.11 Typical defect types in 2D materials. 29
2.12 Representative switching mechanisms of 2D memristors. 30
2.13 I–V characteristics of MoS_2 memristors with grain boundary (GB). . 31
2.14 MoS_2 memtransistors by localized Helium ion beam irradiation. . . 32
2.15 In situ Scanning Transmission Electron Microscopy (STEM) observation of the conduction channel in $MoS_{2-x}O_x$ memristor. 33
2.16 Resistive and capacitive switching characteristics of MoOx/MoS_2 heterostructures. 35
2.17 Characteristics of polycrystalline MoS_2 memtransistor. 35
2.18 Variable switching characteristics of few-layer MoS_2 memristors. . 36

3.1 Basic chemical vapour deposition (CVD) process and boundary layer. 40
3.2 Film growth rate and ternary phase diagram of Mo-S-O. 42
3.3 CVD furnace system for MoS_2 deposition. 43
3.4 Global transfer process of MoS_2. 44
3.5 Optical lithography process. 45
3.6 The typical inductively coupled plasma (ICP) system. 48
3.7 The process of MoS_2 isolation. 49
3.8 The schematic of electron beam evaporation system. 50
3.9 The metallisation process of isolated MoS_2 to fabricate metal contact. 51

3.10 Schematic of optical reflection and transmission for a nano material. 52
3.11 Optical contrast values for MoS_2 on 285 nm SiO_2/Si substrate. . . . 54
3.12 The basic principle of atomic force microscopy (AFM). 55
3.13 The main components of an Scanning Electron Microscopy (SEM) instrument and the interaction volume. 58
3.14 Simplified Transmission Electron Microscopy (TEM) system highlighting the major components. 60
3.15 Atomistic configuration of MoS_2. 62
3.16 The fundamental principle of Energy-dispersive X-ray Spectroscopy (EDX) process and typical EDX spectrum of MoS_2. 63
3.17 TEM specimen beam interactions. 65
3.18 The diagram of X-ray photoelectron spectroscopy (XPS) process and typical XPS spectra of MoS_2. 66
3.19 Raman scattering process and the origin of Raman effect. 67
3.20 Typical Raman active modes of MoS_2. 69
3.21 The photoluminescence spectroscopy (PL) process and typical PL spectrum of monolayer MoS_2. 70
3.22 Diagram of Bragg's Law and X-ray diffraction (XRD) spectra of MoS_2. 72
3.23 Flow chart of two-probe electrical characterisation. 73

4.1 Substrate preparation for polymer-enhanced growth. 79
4.2 A typical promoter-enhanced MoS_2 growth. 81
4.3 Flake recognition using Python. 82
4.4 Thickness analysis of MoS_2 in the promoter region with the sulphur source of 250 °C. 83
4.5 Characterisation of the flakes on the promoter region. 84
4.6 Pristine region of the sample with sulphur temperature of 250 °C. . 86
4.7 Cleanliness of the promoter-enhanced growth. 88
4.8 Morphology and flake size distribution of samples at varied sulphur temperature. 90
4.9 Quantified statistical analysis compare the samples after CVD at varied sulphur temperature. 91
4.10 MoS_2 quality at varied sulphur temperature. 94
4.11 Sulphur vacancy analysis by Raman spectroscopy and XPS. 96
4.12 Sulphur vacancy observation in the MoS_2 at sulphur temperature of 200 °C. 98
4.13 Thermal behaviour of S and MoO_3. 99
4.14 Chemical composition analysis of the polymer promoter. 100

4.15 A schematic illustration of the promoter effects at varied temperatures. . . . 101

5.1 Optical images of laser direct writing (LDW) photoresist (PR) patterns on SiO_2/Si. . . . 104
5.2 Mesa positioning in the patterned growth. . . . 105
5.3 Typical morphology of the CVD products synthesized using the LDW patterned mesa array. . . . 106
5.4 AFM characterisation of samples grown from LDW mesas. . . . 108
5.5 Chemical analysis and microstructure of the patterned MoS_2. . . . 110
5.6 Optical properties of the patterned MoS_2. . . . 112
5.7 Growth variation in a single CVD run with $z = 10$ mm. . . . 114
5.8 Patterned growth in a reduced MoO_x environment. . . . 116
5.9 Critical morphological features of patterned growth. . . . 118
5.10 Growth mechanism of patterned MoS_2. . . . 121
5.11 Initiation of 2D film growth. . . . 123
5.12 Growth kinetics of 2D Films: geometry and grain structure. . . . 125
5.13 Optimisation of patterned growth. . . . 126

6.1 MoS_2 based planar memristor device. . . . 132
6.2 Electroforming of the memristor device. . . . 133
6.3 Device quasi-static properties. . . . 135
6.4 Device cycling performance. . . . 136
6.5 Device fatigue. . . . 137
6.6 The effect of pulse width on memristor resistance. . . . 138
6.7 Conduction mechanisms. . . . 140
6.8 Schottky barrier height and dopant concentration. . . . 141
6.9 The flow chart of the measurement steps for 3-channel measurement. 142
6.10 Resistance of three channels at different operation states of Ch_M. . . . 144
6.11 EDX of MoS_2/MoO_2 at an electron beam energy of 10 keV. . . . 145
6.12 Simulation and experimental EDX of MoS_2/MoO_2 at an electron beam energy of 30 keV. . . . 146
6.13 Observation of biosynaptic behaviour. . . . 147
6.14 artificial neural networks (ANN) pattern recognition of Modified National Institute of Standards and Technology (MNIST) and Fashion-MNIST. . . . 149

A.1 MoS_2 grain boundary visibility in SEM images at varying modes: (a) InLens mode and (b) secondary electron (SE)2 mode. . . . 184
A.2 MoS_2 grain boundary visibility in SEM images. . . . 184

A.3 XPS survey spectra of MoS_2 grown at suphur temperature of 250 °C. 185
A.4 Thermal stability of photoresist S1813. 187
A.5 MoS_2 patterned growth after CVD under a sulphur-deficient condition at z = 10 mm. 191
A.6 MoS_2 patterned growth after CVD under a sulphur-moderate condition at z = 12 mm. 192
A.7 MoS_2 patterned growth after CVD under a sulphur-rich condition at z = 15 mm. 193
A.8 TLM measurements in the initial state of the devices. 197
A.9 Five conduction mechanism fittings for RESET with varied pulse width. 199
A.10 Five conduction mechanism fittings for SET with varied pulse width. 200

List of Tables

2.1 MoS_2 memristor devices with different switching mechanisms. . . 37

3.1 The etching recipe for monolayer MoS_2 isolation. 49

5.1 Topological features of the CVD products using LDW mesas 109
5.2 MoS_2 Raman peaks detected from the laser direct writing (LDW) pattern. 113
5.3 Detailed chemical vapour deposition (CVD) parameters of the patterned growth. 128

A.1 X-ray diffraction (XRD) main peaks of Mo_xS_y. 189
A.2 XRD main peaks of Mo_xO_y. 190

Nomenclature

2D two-dimensional

vdW van der Waals

PTAS Perylene-3,4,9,10-tetracarboxylic acid tetrapotassium salt

PTCDA 3,4,9,10-perylene-tetracarboxylicacid-dianhydride

TMD transition metal dichalcogenide

hBN hexagonal boron nitride

BP black phosphorus

MXene transition metal carbide and nitride

PDMS polydimethylsiloxane

PMMA polymethyl methacrylate

IPA isopropyl alcohol

DI deionized

PR photoresist

PAC photoactive compound

PGMEA propylene glycol monomethyl ether acetate

ATM anhydrous ammonium tetrathiomolybdate

L-PEI linearpoly (ethylenimine)

PR photoresist

GB grain boundary

SV sulphur vacancy

UV ultraviolet

OL optical lithography

LDW laser direct writing

ICP inductively coupled plasma

RF radio frequency

e-beam electron beam

RIE reactive ion etching

ME mechanical exfoliation

CVD chemical vapour deposition

MOCVD metal–organic chemical vapour deposition

PVD physical vapour deposition

ALD atomic layer deposition

PLD pulsed laser deposition

TAC thermally assisted conversion

LPE liquid phase exfoliation

MBE molecular beam epitaxy

VLSI very-large-scale integration

DFT density function theory

RMS root mean square

NA numerical aperture

TGA thermo-gravimetric analysis

DTG differential thermo-gravimetric

OC optical contrast

SE secondary electron

BSE backscattered electron

SEM Scanning Electron Microscopy

TEM Transmission Electron Microscopy

BF bright-field

HRTEM high-resolution Transmission Electron Microscopy

SAED selected area electron diffraction

ADF annular dark-field

HAADF high-angle annular dark-field

CBED convergent beam electron diffraction

AFM atomic force microscopy

EFM electrostatic force microscopy

STEM Scanning Transmission Electron Microscopy

ACSTEM aberration-corrected scanning transmission electron microscopy

LOD limit of detection

EDX Energy-dispersive X-ray Spectroscopy

EELS electron energy loss spectroscopy

XPS X-ray photoelectron spectroscopy

PL photoluminescence spectroscopy

Xa A exciton

SAED selected-area diffraction

CBED convergent beam electron diffraction

XRD X-ray diffraction

LA longitudinal acoustic

ESCA Electron Spectroscopy for Chemical Analysis

CMOS complementary metal-oxide semiconductor

FET field-effect transistor

GND ground

TLM transfer length method

SBH Schottky barrier height

SBW Schottky barrier width

$E_{v,max}$ valence band maximum

$E_{c,min}$ conduction band minimum

CC compliance current

ITRS International Technology Roadmap for Semiconductors

FLP Fermi-level pinning

FN Fowler-Nordheim

PF Poole-Frankel

SCLC space charge limited conduction

HRS high resistance state

LRS low resistance state

LTP long-term potentiation

LTD long-term depression

URS unipolar resistive switching

BRS bipolar resistive switching

CRS complementary resistive switching

ANN artificial neural networks

ECM electrochemical metallization mechanism

VCM valence change mechanism

MNIST Modified National Institute of Standards and Technology

sccm standard cubic centimeters per minute

rpm revolutions per minute

N/m Newtons/meter

FWHM full width at half maximum

CAD computer aided design

T_s sulphur temperature

CRANN Centre for Research on Adaptive Nanostructures and Nanodevices

AML Advanced Microscopy Laboratory

1 | Introduction

"Nothing in life is to be feared, it is only to be understood. Now is the time to understand more, so that we may fear less."

- Marie Curie

Since the 1960s, the number of transistors in electronic circuits has doubled every two years, which is known as Moore's law. As the size of traditional semiconductor devices has been extremely reduced, the short-channel effect significantly impacts the device. At this time, improving the ability of the gate voltage control is essential to maintain the device performance.

To maintain the ability of the gate voltage to control the channel, the channel material must be thin. As far as the current semiconductor process is concerned, after the semiconductor is thinned, its surface roughness is very large, and the surface dangling bonds increase, resulting in surface scattering that is much larger than that of natural crystal planes. Surface scattering of semiconductors will seriously inhibit device performance and render its operation. Therefore, new semiconductor materials are necessary to extend Moore's law beyond its physical limits.

In the past decades, two-dimensional (2D) materials with atomic-level dimensions have been widely studied. Since mechanically exfoliated graphene was first reported by Geim etc. (University of Manchester) in 2004 [172], van der Waals (vdW) materials with layered structures have gained significant attention. Transition metal dichalcogenide (TMD), a representative class of 2D materials, exhibits remarkable electronic, optical, and mechanical properties due to their unique atomic structure. TMDs share a generalized formula MX_2 where M represents transition metal from group IV (Ti, Zr, Hf, etc.), group V (V, Nb, Ta, etc.), and group VI (Mo, W, etc.) while X is a chalcogen (e.g. S, Se, Te) [236]. It is also worth noting that compared with MTe_2 and MSe_2, the sulphide has larger valence

band maximum ($E_{v,max}$) value and the conduction band minimum ($E_{c,min}$) value. As the bottom of the conduction band increased more than the valence band, the sulphide has a larger band gap than other TMD members, which attracts us to the study of MoS_2.

MoS_2 offers several key advantages as a memristor material compared to other semiconductor material, for example, oxides, perovskites and organic materials. First, the atomic thickness of MoS_2 allows device scaling. This is beneficial for high-density integration and ultra-low power operation, which are critical for next-generation neuromorphic and memory devices. Second, it is compatible with complementary metal-oxide semiconductor (CMOS) processes, which facilitates their practical applications.

The aim of this thesis is to investigate the synthesis, characterization, and application of 2D MoS_2 in electronic devices. This involves developing methods for the controllable and scalable growth of high-quality MoS_2 films, fabricating and optimizing devices based on MoS_2 and understanding the fundamental mechanisms that govern their performance. The specific objectives are:

To develop reliable and scalable synthesis methods for high-quality MoS_2 films. To characterize the structural, electronic, and optical properties of the synthesized MoS_2. To fabricate and optimize MoS_2-based field-effect transistors (FETs) and memristors.

In this thesis, the study will focus on the central research question:

"How to improve the achieve large-scale controllable growth of MoS_2 and its application in electronic devices?"

To address the research question, this thesis will focus on two main topics: controllable large-scale MoS_2 growth and enabling MoS_2 synaptic devices. The chapter outline is provided below:

Chapter 2 - Two-dimensional MoS_2 : First discuss the atomic and electronic structure of MoS_2, then review on the controllable synthesis methods of MoS_2, and then review on the MoS_2 electronic devices and their key figure of merits.

Chapter 3 - Fabrication and characterization techniques : Clarify the methodologies to be employed in this thesis. This will include fundamental physical knowledge, detailed parameters and instrument information for material preparation, device fabrication, and characterization.

Chapter 4 - Polymer-enhanced deposition of 2D MoS_2: Explore an innovative nano promoter for clean and controllable growth of MoS_2 using chemical vapour de-

position (CVD) method. Investigate the reactant concentration effect on the film quality, and study the heterogeneous growth mechanism.

Chapter 5 - Patterned growth of MoS_2: Based on the nano promoter research, we further developed the patternable growth for CVD MoS_2. The film quality was studied. S/Mo ratio and pattern design will be considered to enlarge the growth of MoS_2.

Chapter 6 - Resistive switching in MoS_2 based planar memristors : Memristor devices were fabricated based on the patterned growth MoS_2. Examines the switching behaviour in MoS_2 memristors and understands the Schottky barrier modulation switching phenomenon.

Chapter 7 - Conclusions and outlook: We will summarize the accomplishments of this thesis and discuss potential future work that could be significant for the advancement of 2D applications.

2 | Two-dimensional MoS_2

"Science knows no country, because knowledge belongs to humanity, and is the torch which illuminates the world."

- Louis Pasteur

In this chapter, I will delve into the foundational knowledge and background of MoS_2. This chapter begins with an in-depth examination of the atomic structure of MoS_2. It continues with the background of electrical properties of MoS_2, including electronic bandgap structure and electrical transport. The optical properties of MoS_2 will then be briefly discussed. Subsequently, a review will focus on the diverse synthesis techniques employed to produce 2D MoS_2, particularly the large-scale and controllable growth methods. Finally, the last section of this chapter will provide a background of 2D memristor devices.

2.1 MoS_2 structure and properties

2.1.1 Structure of MoS_2

MoS_2 displays rich polymorphism with different polytypes [119], for example, 1T, 2H, 3R and 2T. The first digit (1, 2, 3) indicates the number of layers in a unit cell, while 'T', 'H' and 'R' denote trigonal, hexagonal and rhombohedral structures, respectively. The 2H structure is the dominant phase observed in nature due to the stability of the ABA layer stacking [119]. The 1T and 3R types are unstable and easily transform to 2H upon heating [50]. In this thesis, I focus on 2H MoS_2, and unless explicitly stated otherwise, all mentions of MoS_2 refer to the 2H phase.

In 2H-MoS_2, as illustrated in **Fig. 2.1**, the Mo and S atoms form a covalently bonded S-Mo-S sandwich structure [103]. Each unit cell contains two Mo atoms and four S atoms, arranged in two such layers. A single S–Mo–S layer is referred to as a monolayer. In multi-layer MoS_2, additional layers are stacked vertically

with an interlayer spacing of approximately 0.65 nm. These layers are bonded by weak van der Waals (vdW) force without chemical bonding. As a result, it is easy to cleave the crystal surface layers from its bulk along the in-plane direction by disrupting weak vdW bonds. This characteristic enables the production of monolayer or few-layer MoS_2 by exfoliation.

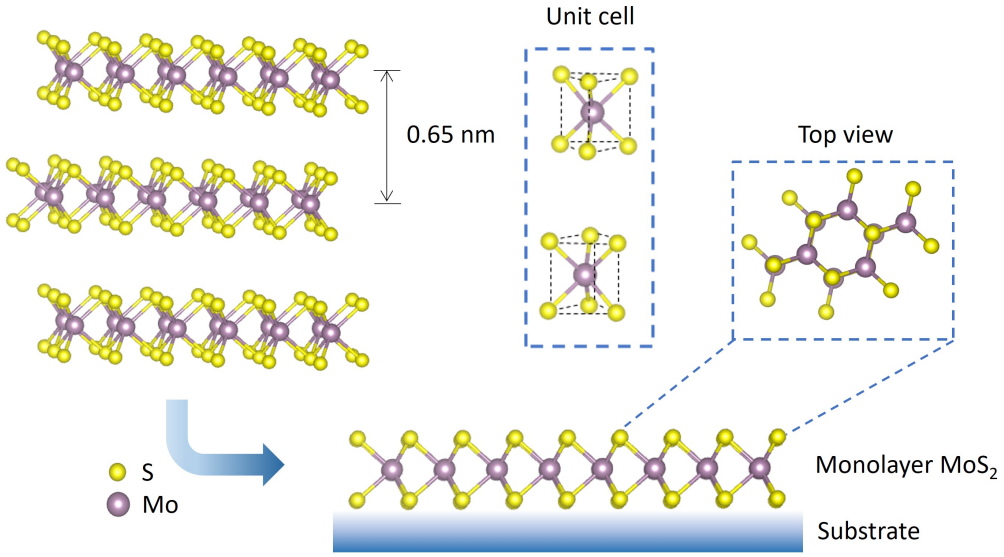


Figure 2.1: **Schematics of the crystal structure of 2H-MoS_2.** Yellow and purple spheres represent S and Mo atoms, respectively.

2H-MoS_2 belongs to the hexagonal crystal system, with a space group of P63/mmc (No. 194 in the International Tables for Crystallography) [182]. The top-down view image in **Fig. 2.1** reveals a hexagonal arrangement of molybdenum and sulfur atoms, with molybdenum in trigonal prismatic coordination. Each molybdenum atom is surrounded by six sulphur atoms. The top three sulfur atoms and bottom three sulfur atoms are overlapping, thus only three bonds are shown in the image. A single unit cell of 2H phases consists of two layers of MoS_2 with each layer containing a single Mo atom and two S atoms. In the unit cell of 2H-MoS_2, the Mo atoms occupy the Wyckoff position 2c (1/3, 2/3, 1/4), while the S atoms occupy the Wyckoff position 4f (1/3, 2/3, z_s), with z_s approximately equal to 0.63 [182]. The unit cell is defined by three lattice parameters: a, b and c. The in-plane lattice parameters a and b are directly related to the Mo-S bond length, which is $\sim$ 0.316 nm. The out-of-plane lattice parameter c reflects the interlayer spacing of the unit cell, which is typically $\sim$ 1.23 nm [6]. The precise lattice parameters can vary slightly depending on factors such as temperature and strain.

2.1.2 Electronic properties of 2H MoS_2

Thickness dependent electronic band structure

Few-layered 2H-MoS_2 is found to be semiconducting [50], and possesses a fascinating electronic structure with properties that depend on layer thickness. As the thickness decreases from bulk to monolayer, changes in interlayer coupling and quantum confinement lead to a change in hybridization between S p and Mo d orbitals, converting it from an indirect-gap semiconductor to a direct-gap semiconductor [142, 161, 216]. **Figure 2.2** illustrates the calculated band structures of bulk, few-layer and monolayer MoS_2 by density function theory (DFT) [216]. For bulk material, the $E_{c,min}$ and $E_{v,max}$ occur at different values of momentum, where the $E_{v,max}$ is at the Γ point and the $E_{c,min}$ is located between the Γ and K points in the Brillouin zone. The valence band at the Γ point of the Brillouin zone is diffused with broadening electronic states, which is due to the Mo d and S p orbitals of antibonding character [142, 216, 236]. Therefore, the band energy at the Γ-point is strongly affected by the interlayer coupling. On the contrary, the conduction band at the K-point of the Brillouin zone is mainly dominated by the localized d-type orbitals on the Mo atoms, which are insensitive to the interlayer coupling. Therefore, as the layer numbers decrease, the valance band at the Γ-point shifts significantly while the conduction band at the K-point remain unchanged. This finally results in the transition from indirect band-gap ($\sim$ 1.3 eV) to direct band-gap ($\sim$ 1.9 eV) when the MoS_2 layer thickness decreases from bulk to monolayer [16, 81, 161].

Compared to the silicon bandgap of 1.1 eV, the large bandgap of monolayer MoS_2 offers several advantages for electronic applications. The wide bandgap of MoS_2 not only allows for high on/off current ratios but also reduces leakage currents, making it particularly suitable for energy-efficient electronics. Additionally, the direct bandgap in monolayer MoS_2 enables efficient optical transitions, opening possibilities for integrating electronic and optoelectronic functionalities in the same device. The photoluminescence spectroscopy (PL) is an effective method for determining the optical bandgap of MoS_2, with the PL intensity being inversely proportional to the layer thickness. In monolayer MoS_2, the direct bandgap significantly enhances PL intensity by up to a factor of 10^4, with even higher quantum yield for suspended monolayers [161, 216]. The fundamentals of PL spectroscopy and the PL spectrum of MoS_2 will be discussed in section 3.3.2.

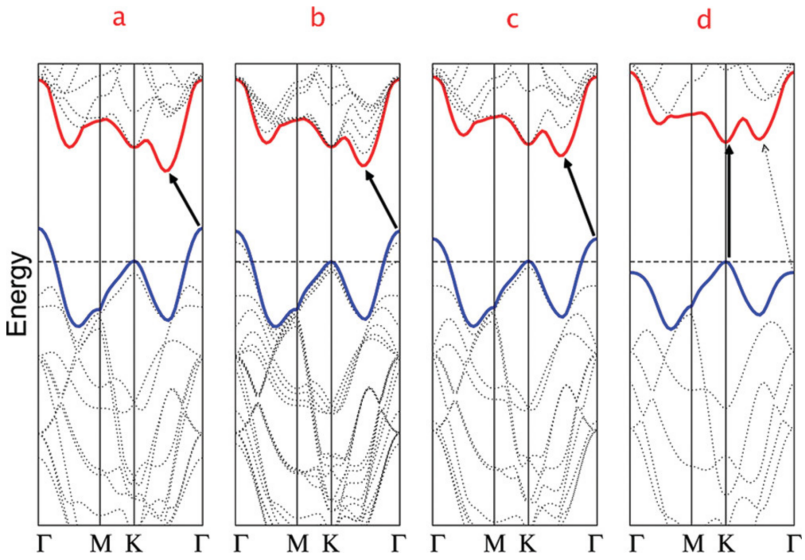


Figure 2.2: **Band structure of MoS_2 predicted by DFT calculation.** (a) Band structure of bulk, quadrilayer, bilayer and monolayer MoS_2 predicted by DFT calculation. The arrows indicate the bandgap transition from the valence band maximum to the conduction band minimum. Adapted from [216].

Electrical transport

In traditional semiconductors, the carrier mobility is typically inversely related to the effective mass of the charge carriers [220]. Achieving high mobility generally requires a low effective mass, but this often comes at the cost of a small bandgap, which leads to a high off-state leakage current. In contrast, studies have shown that in two-dimensional (2D) semiconductors, the mobility does not exhibit a strong correlation with the effective mass [157]. Among 2D materials, MoS_2 is particularly attractive due to its combination of a large bandgap and theoretically high carrier mobility [27, 107, 187]. The intrinsic phonon-limited mobility of MoS_2 is theoretically calculated to be $\sim$410 $cm^2V^{-1}s^{-1}$at room temperature [270].

However, the experimental carrier mobility in MoS_2 devices typically ranges from a few to tens of $cm^2V^{-1}s^{-1}$[25, 43, 270], which is significantly lower than the theoretical value. This discrepancy reflects extrinsic factors that limit the mobility, such as charge impurities, structural defects and traps [27, 185, 236, 270]. Generally, the overall carrier mobility, μ_{TOTAL}, can be obtained by Mattheisen's Rule [4]:

$$\frac{1}{\mu_{TOTAL}} = \frac{1}{\mu_C} + \frac{1}{\mu_A} + \frac{1}{\mu_{PO}} + \frac{1}{\mu_{SR}} \tag{1}$$

where the μ_C, μ_A, μ_{PO} and μ_{SR} are the effective carrier mobility limited by Coulombic, acoustic phonon, optical phonon and surface roughness scattering

mechanisms, respectively. The contributions of different scattering mechanisms are temperature dependent. **Figure 2.3** (a) shows the relationship between the mobility, μ, and the temperature, T, for a back-gated monolayer MoS_2 field-effect transistor (FET). In the low temperature regime, Coulombic scattering dominates which typically arises from charged impurities. In this regime, mobility increases with temperature [236]. These impurities can be introduced randomly during fabrication or through adsorption from the environment. Due to its atomic thickness, 2D MoS_2 is particularly sensitive to such impurities. In a device, the use of a high-k gate oxide, such as hafnium oxide, is found to improve the monolayer MoS_2 mobility (e.g. 217 $cm^2V^{-1}s^{-1}$in ref [186]) by suppressing the Coulomb scattering [44, 186]. When the temperature is above 200 K, the mobility is limited by phonon scattering, resulting in a reduction in mobility as the temperature increases.

In a theoretical defect-free 2D MoS_2, phonon scattering is the dominant scattering mechanism at room temperature. Experimentally, tremendous efforts have been made to improve the room temperature mobility of MoS_2, however, it remains lower than the theoretical value, suggesting the existence of additional scattering mechanisms such as structural defects and traps. In mechanical exfoliation (ME) and chemical vapour deposition (CVD) MoS_2, sulfur vacancies are the most common intrinsic defect [88, 193]. The MoS_2 can retain its structure despite the presence of vacancies [285], but these vacancies can trap carriers and contribute to scattering, thereby limiting mobility [270]. Gali [65] reported that the mobility drops by two orders of magnitude when the sulphur vacancy concentration is increased from 0.1 to 3%.

The charges can transport through electron hopping through sulfur vacancies, which exhibits variable-range hopping at low temperatures and nearest-neighbour hopping at relatively high temperatures [72, 184, 287]. Cho [32] found that the mobility decreases after passivating sulfur vacancies with alkanethiol molecules when the carrier density is in the range from 2.4×10^{12} cm^{-2} to 7.1×10^{12} cm^{-2}, which can be attributed to the reduction in hopping sites [184]. D. S. Fox et al. demonstrated that the transition of semiconducting-insulating-metallic behaviour by tuning the vacancy density in mechanical exfoliated MoS_2 using He^+ irradiation. **Figure 2.3** (b) illustrates the relationship between MoS_2 resistivity and He^+ dose [62].

Contact interface

Metal-semiconductor contact When a metal contacts a semiconductor, a potential energy barrier forms at the interface, arising from the difference in the

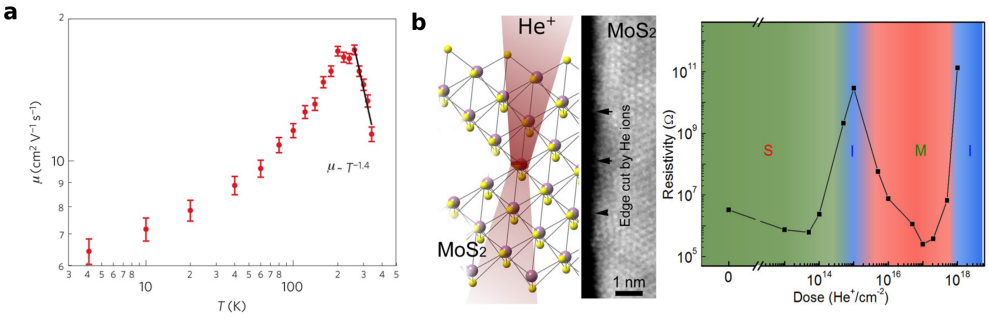


Figure 2.3: **Electrical transport in MoS_2.** (a) Temperature dependent mobility in back-gated monolayer MoS_2 [185]. (b) Observation of semiconductin-insulating-metallic transition in MoS_2 using He^+ beam [62].

thermionic work functions between the metal and the semiconductor and this impedes efficient carrier injection. The energy barrier is also affected by the surface states [84]. **Figure 2.4** provides an idealized energy band diagram for a metal and an n-type semiconductor after contact. On the metal side, the work function $W_m = q\phi_m$ is the energy required for an electron to move from the Fermi level (E_F) to the vacuum level. On the semiconductor side, the electron affinity $q\chi$ is the energy required for an electron to escape from the $E_{c,min}$ to the vacuum. $W_s = q\phi_s$ is defined as the work function of the semiconductor, which is the energy difference between the vacuum level and the E_F of the semiconductor. $E_{c,min}$ and $E_{v,max}$ are the lowest energy level of the conduction band and the highest energy level of the valence band, respectively. The E_F represents the highest occupied energy level at 0 K, which is close to the $E_{c,min}$ the n-type semiconductor. E_{Fi} refers to the intrinsic Fermi level which is located halfway between $E_{c,min}$ and $E_{v,max}$.

If the metal and semiconductor contact with $W_m < W_s$ (**Fig. 2.4** (a)), electrons will move to achieve thermal equilibrium and the Fermi level will equalise across the junction. As electrons move from the high energy state metal into the low energy state semiconductor, the energy band of the semiconductor bends near the interface to reach the same E_F as the metal. In this scenario, an Ohmic contact is formed, characterized by a linear I-V characteristic.

However, if $W_n > W_s$, a so-called Schottky contact will form, as shown in **Fig. 2.4** (b). To reach thermal equilibrium and keep the E_F constant, electrons move from the semiconductor to the metal, leaving positive charges in the semiconductor. This creates an energy barrier that electrons must overcome to move from the metal into the semiconductor, known as the Schottky barrier. The Schottky barrier height (SBH), ϕ_B, can be expressed as:

$$\phi_B = \phi_m - \chi \tag{2}$$

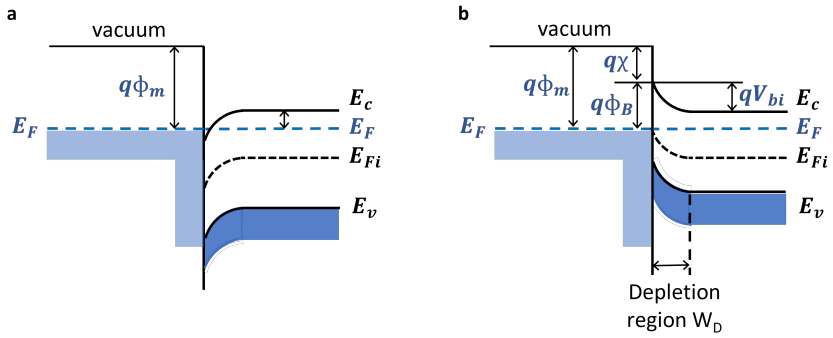


Figure 2.4: **Energy band diagram of metal-semiconductor (n-type) contact.** Energy band diagram for a metal and n-type semiconductor illustrating (a) Ohmic contact ($W_m < W_s$), and (b) Schottky contact ($W_m > W_s$).

In the semiconductor near the interface, a depletion region due to reduced electrons forms a built-in potential V_{bi}. The Schottky barrier width depends on the semiconductor dopant concentration.

The SBH can be modulated by doping. To do this, a thin layer (< 10 nm) of dopants is introduced close to the semiconductor surface [201]. In this case of thin layer doping, if the $N_d a$ is larger than 10^{11} cm^{-2}, the Schottky barrier change is given by:

$$\Delta\phi_B \approx \frac{q}{\varepsilon_s}\sqrt{\frac{N_d a}{4\pi}} \tag{3}$$

where q is the elementary charge, ε_s is the permittivity, N_d is the dopant concentration with a unit of cm^{-3}, a is the depletion width in cm. In 2D MoS_2, the sulphur vacancies can move between electrodes and modify the electrode metal and MoS_2 interface, acting as an n-type dopant. However, the dopant layer thickness is very thin compared with the contact lateral dimension, so $N_d a$ can be simplified as sheet dopant concentration N_{2D} with a unit of cm^{-2}. Rearranging eq. (3), the N_{2D} is expressed as:

$$N_{2D} \approx \frac{4\pi\Delta\phi_B^2\varepsilon_s^2}{q^2} \tag{4}$$

The abrupt approximation assumes that the transition between semiconductor and metal is sudden. With this simplification, if $x < W_D$, the charge density $\rho \approx qN_d$. Conversely, if $x > W_D$, $\rho \approx 0$. The depletion width W_D is a function of bias voltage which can be written as:

$$W_D = \sqrt{\frac{2\varepsilon_s}{qN_d}\left(V_{\text{bi}} - V - \frac{kT}{q}\right)} \tag{5}$$

where V_{bi} is the built-in potential, V is the applied bias voltage, ε_s is the permit-

tivity of the semiconductor, k is the Boltzmann constant (1.381×10^{-23} JK^{-1})), T is the temperature and $q = 1.602 \times 10^{-19}$ C is the electronic charge. The depletion layer capacitance C_D per unit area are calculated from the following equation:

$$C_D = \frac{\varepsilon_s}{W_D} \tag{6}$$

Considering eq. (5) and eq. (6), the depletion capacitance is proportional to the square root of dopant concentration $C_D \propto \sqrt{N_D}$, while the depletion width is inversely proportional to the square root of dopant concentration $W_D \propto \frac{1}{\sqrt{N_D}}$.

Charge injection at 2D MoS_2 contact In MoS_2 electronic devices, such as memristor, understanding the carrier transport mechanism is critical to improving the device performance. As shown in **Fig. 2.5** (bottom), at low doping levels, thermionic emission dominates carrier transport in the pristine MoS_2. As doping concentration increases and reaches the flat band condition, **Fig. 2.5** (centre), thermionic emission remains the dominant mechanism. However, with further increases in doping concentration, **Fig. 2.5** (top), the thermionic field emission and field emission also contribute, with field emission facilitating carrier tunnelling [2]. The thermionic emission and field emission are the two main mechanisms for charge injection at the Schottky barrier, with thermionic emission being the dominant one in most cases for MoS_2 with low doping concentration.

Thermionic emission is a process in which charge carriers overcome an energy barrier, such as a Schottky barrier, at elevated temperatures. This phenomenon is described by the Richardson equation, which gives the relationship between the current density (J), temperature (T) and the SBH:

$$J = A^* T^2 \exp\left(-\frac{q\phi_B}{kT}\right)\left(\exp\left(\frac{qV}{kT}\right) - 1\right) \tag{7}$$

where A^* is the Richardson constant (1.2×10^6 $Am^{-2}K^{-2}$), V is the applied voltage.

In MoS_2 devices, defects such as sulphur vacancies (SVs) and grain boundarys (GBs) can introduce localized states within the bandgap [11, 215], influence charge trapping and de-trapping behaviour, and modulate the SBH and Schottky barrier width (SBW), thereby affecting the efficiency of thermionic emission. The reduction in SBH is attributed to the localized states introduced by SVs, which lower the energy barrier for electron transport. Consequently, defective MoS_2 with SVs exhibits a notable increase in thermionic emission current [164]. P. Bampoulis et al. demonstrated that metal-like defects can drastically reduce the SBH

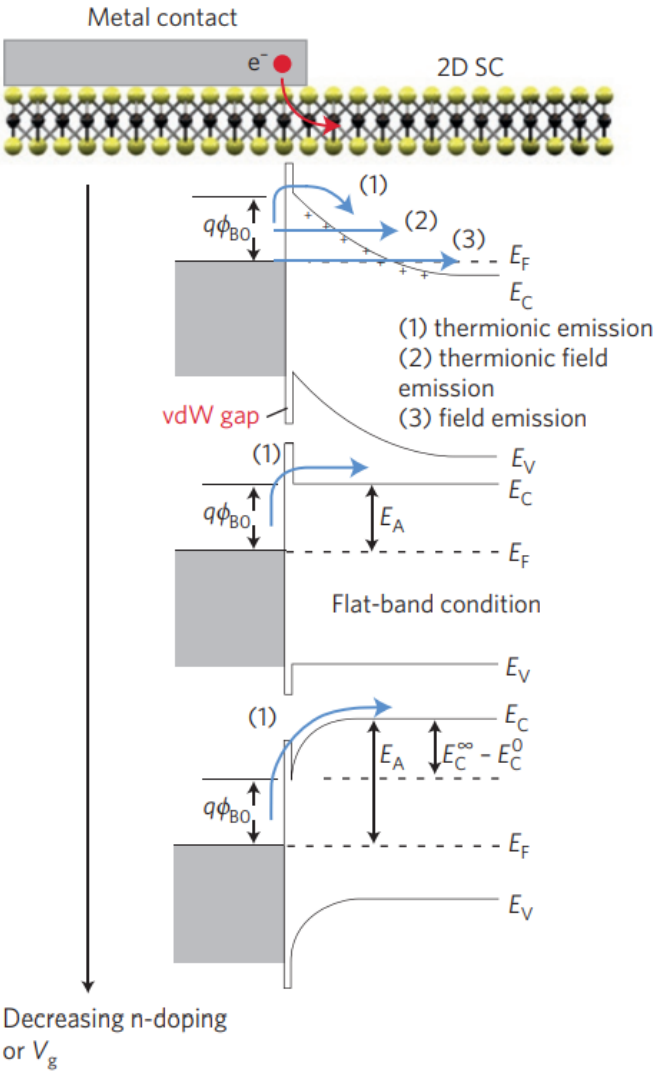


Figure 2.5: **Charge-injection in 2D MoS_2.** Comparing the charge-injection mechanisms in 2D MoS_2 at various doping concentration [2].

compared to pristine regions [10]. Similarly, Feng et al. found that SVs reduce the SBH, while Mo vacancies completely eliminate the Schottky barrier due to their strong interactions with the underlying substrate [57]. Yang et al. discovered that the monolayer MoS_2 at the Au/MoS_2 contact acts as an electron acceptor at relatively low concentrations of SVs, but transitions to an electron donor at higher concentrations [262]. Moreover, V. K. Sangwan et al. proposed that defects in MoS_2 act as dopants and their local migration under an applied bias is facilitated by GBs. The defect density varies with the applied bias, and the defect migration modulates the thermionic emission [197].

Despite considerable progress in understanding charge injection at defective MoS_2 contacts, several challenges remain, including the precise control of defect density and distribution. Variations in defect density can result in fluctuating

barrier heights and an inhomogeneous contact interface, ultimately causing non-uniform charge transport. Therefore, further efforts should focus on defect control of the material.

Contact resistance in 2D MoS_2 device The electrical contact plays a crucial role in charge injection and collection in all electronic devices, and this becomes even more critical in 2D systems. The extremely high surface area-to-volume ratio of 2D materials makes their electronic structure highly susceptible to perturbations at metal-2D interfaces. As channel length decreases, the contribution of contact resistance, R_c, increases significantly and can even dominate the total resistance. For pristine 2D MoS_2, the lack of dangling bonds causes the weak bonding with metal electrodes, leading to a vdW gap and high R_c [2]. In an ideal, ballistic transport regime, the minimum possible R_c is given by $R_c \sim h/(2e^2M)$, where h is Planck's constant, e is the electron charge and M is the number of electron modes whose wavelength fit the narrow conductor [104]. In 2D system, $M \sim k_F W$, where W is the width of the channel and k_F is the Fermi wavevector. Thus, the quantum limit of 2D R_c is given by:

$$R_c^{min} = \frac{h}{2e^2 k_F} = \frac{0.026}{\sqrt{n_{2D}}} \tag{8}$$

where n_{2D} is 2D charge carrier density [2], which is strongly depends on the charge carrier density. For 2D materials, carrier density of $n_{2D} \sim 10^{13}$ cm^{-2} yields a theoretical minimum contact resistace, R_c^{min}, as low as 30 $\Omega \cdot \mu$m [104]. It is significantly lower than the maximum source/drain resistance limits for high-performance Si complementary metal-oxide semiconductor (CMOS) technology (80 $\Omega \cdot \mu$m for multiple-gate technology) following the International Technology Roadmap for Semiconductors (ITRS) projections for 2026 [187]. This makes 2D materials highly promising for the next generation semiconductor technology.

However, the experimental R_c value is usually orders of magnitude higher than the theoretical limit value which severely confines the practical 2D electrical properties [2, 29]. The unexpectedly high contact resistance for 2D devices can be attributed to several reasons. First, the inherent Schottky barrier at the metal-2D interface lowers the charge injection efficiency. Two typical methods to minimize the impacts of the Schottky barrier are decreasing the SBH, so the carriers can go across the barrier with low energy and narrowing the SBW so the carriers can go through the barrier by the tunnelling effect [187]. For conventional semiconductors, selecting a metal with an appropriate work function is an effective method to lower the SBH or achieve Ohmic contact. However, in 2D systems, Fermi-

level pinning (FLP) near the conduction band can be induced by surface states (Bardeen model), metal-induced gap states (Heine model) or defect-induced gap states [42, 52, 143], making the SBH insensitive to changes in the metal work function.

Interestingly, it has been recognised that the Schottky barrier at the MoS_2 and metal interface is highly dependent on the defects, for instance, the current through a defective contact junction with even low density (0.3% coverage) can be several orders of magnitude higher than that through a defect-free junction [164]. Similar studies have demonstrated that R_c can be reduced by tuning the Fermi energy through introducing Mo or S vacancies [57, 153]. Futhermore, increasing electron doping density via doping can significantly reduce the R_c by narrowing the SBW [263]. Such Schottky barrier tunning behaviour induced by defects has been identified as one of the key mechanisms in MoS_2 memristive switching devices [197].

As discussed above, the doping density is important to the carrier injection at the contact interface. The precise control of doping density, such as SV in MoS_2, plays a crucial role in modulating the carrier transport. Therefore, controlling the growth conditions to minimize unwanted impurities while managing defect concentrations is essential for fine-tuning the transport properties and switching mechanisms of MoS_2 memristors. In addition, improving the uniformity of the MoS_2 film is necessary to achieve low device variability. This underscores the critical need for clean and controlled growth methods to produce high-quality 2D MoS_2 and an effective way to control the SV density for tuning the device performance.

2.2 Synthesis of 2D MoS_2

In this section, I will first briefly review the synthesis method for MoS_2 and discuss the necessity of CVD as the primary method used in this thesis. Then, I will discuss the controllable growth of MoS_2 and highlight the spatially controlled growth particularly the crucial requirements for electrical and optoelectronic applications, which drives our research on large-scale and uniform growth of 2D MoS_2.

2.2.1 Overview of 2D MoS_2 synthesis

To ensure compatibility with semiconductor industry applications, it is important to improve the yield and achieve high-quality wafer-scale MoS_2. As discussed in

the previous section, the controllability and uniformity of MoS_2 films are crucial to their electrical performance. Films with poor uniformity and limited control lead to significant device variability and reduced reliability. Therefore, the controlled synthesis of MoS_2 with uniform thickness and quality is essential for ensuring consistent electrical properties across devices, minimizing variability and enhancing reliability.

Various methods have been developed to prepare monolayer and few-layered MoS_2, which can broadly be categorized into two approaches: top-down and bottom-up. When evaluating these methods regarding memristor applications, key factors such as scalability, defect control and uniformity must be carefully considered.

Top-down methods usually refer to exfoliation methods, including ME, liquid phase exfoliation (LPE) and chemical intercalation. The key to the exfoliation of 2D crystals is to break the weak vdW bonds between adjacent layers. The ME method overcomes the vdW force by applying a macro scale mechanical force, which gained prominence in 2004 due to the successful isolation of a single layer of graphene by A. Geim and K. Novoselov at the University of Manchester [173]. This groundbreaking discovery was rewarded with the Nobel Prize in Physics in 2010. Due to its simplicity, ME has been expanded to be utilized for exfoliation of high-quality 2D MoS_2 with few defects [23, 92, 136]. The disadvantages of the ME method include a low yield of monolayer MoS_2 and the film is prone to damage and cracking, resulting in poor control over film size [66] (typically <10 μm). However, introducing defects [235] or incorporating an oxide layer [13, 96] has enabled memristive switching behaviour in exfoliated MoS_2. The ease of ME in producing high-quality MoS_2 films presents substantial benefits for advancing fundamental research.

The LPE is a scalable method to obtain monolayer or few-layer 2D materials, and was first demonstrated by J. N. Coleman's group in 2008 for graphene [85]. External energy, such as ultrasonic [37] or high-shear mix [180], is required to break the vdW bonds between layers in a suitable solvent. By optimizing the LPE process, nanosheets can be obtained with high yield, for example, 5.3 g/h in Ref [180]. Another advantage of LPE is that the resulting dispersions can be easily converted to inks, which facilitates the applications in printed electronics [17, 224]. The MoS_2 nanosheets obtained by LPE have a broad distribution of lateral size (40-400 nm) and thickness (1-10 atomic layers) [8]. Due to the small size of each nanosheet, the formed MoS_2 film composed of stacked nanosheets typically has large junction resistance and significant porosity. Additionally, the randomly

stacked nanosheets [194] create multiple paths at the nanosheet-junction for current flow [64]. This makes it challenging to ensure consistent current paths during each cycle of the memristor device, leading to difficulties in minimizing cycle-to-cycle variability. Liquid phase exfoliated MoS_2 [194] and MoS_2-PVP [155] have been reported to exhibit memristive behaviour due to charge traping, however, there is a lack of evaluation on the variability of these devices.

The chemical intercalation method is another solvent based approach to obtain MoS_2 flakes [48]. In this process, MoS_2 is first immersed in a solution and soaked for a period, allowing ions (e.g. Li^+) or molecules to intercalate between the layers. After treatment, the MoS_2 is placed in a solvent environment. The intercalated ions or molecules weaken the vdW forces, making the MoS_2 layers easy to separate under external energy, such as gas production (e.g. hydrogen) or ultrasonic treatment. The obtained MoS_2 nanosheets can reach μm-scale sizes [254]. Similar to other exfoliation methods, controlling the thickness and size of the nanosheets remains a challenge. Although these nanosheets are larger than those produced by traditional LPE method, they still tend to form a large film by stacking with the random nanosheet-junction inevitably increasing device variability. Therefore, the variability of chemical intercalation based MoS_2 memristor [13, 221] requires further investigation.

Bottom-up approaches involve building up MoS_2 films from atoms or molecules in a solution environment [39, 77] or on a substrate [58, 113, 129]. Solution-based synthesis is relatively simple and cost-effective, and it can be scaled up for large-scale production. However, controlling the uniformity and quality of the synthesized MoS_2 is challenging [39, 49, 77]. Depending on the growth mechanism, the substrate-based method is typically classified as molecular beam epitaxy (MBE) [47, 166], physical vapour deposition (PVD) [58] or CVD [113, 129]. MBE enables epitaxial growth of highly crystalline materials and has been widely used for traditional semiconductor thin films. However, its application in 2D materials has been reported to produce small grain sizes, typically ranging from tens to hundreds of nanometers [47, 166].

PVD method utilizes high energy to vaporize the pristine material, which then transfers and solidifies on the substrate in a high vacuum environment. The physical deposition process ensures stoichiometric transfer of the pristine MoS_2. Pulsed laser deposition (PLD) and sputtering are commonly employed techniques that used for 2D MoS_2. PLD uses laser pulses to ablate a target and condense films onto the substrate. This method has been reported to enable wafer-scale synthesis [160, 205]. Instead of a laser pulse, sputtering uses high

energy ions (e.g. Ar ions) to ablate the target [79]. Sputtering has been combined with CVD method to synthesis MoS_2. This approach, known as thermally assisted conversion (TAC), can facilitate large-area [68, 131, 223, 271] and selective-area [249, 265] growth of MoS_2. However, the PVD process produces polycrystalline films with small grains (tens of nm [79, 112]) and limited control over grain distribution. This lack of control over film uniformity increases the device variability and reduces the reliability. In addition, the PVD system usually requires an ultra-high vacuum, which is costly and complex to maintain.

The CVD method generally involves the decomposition, evaporation and reaction of various chemical species in the gas phase, followed by the deposition of the synthesized material onto the target substrate. The details of the film growth mechanism will be discussed in the methodology chapter section 3.1.1. CVD can be further categorized into sub-techniques, including metal–organic chemical vapour deposition (MOCVD) [41, 126, 159] and atomic layer deposition (ALD) [230]. As it does not require vacuum or high voltage power, CVD was practised commercially prior to PVD [174]. Scalable growth of MoS_2 is essential for device application, and CVD provides a solution to synthesize large-scale monolayer MoS_2, which has been widely used in memristor application. Research has shown that SV originating from the GBs in MoS_2 is crucial for the memristive switching behaviour, with no switching observed in the absence of GB [196, 197]. Filament conduction [70, 97] and phase change [28, 280] resistive switching have also been reported related to SV density and lattice structure. Therefore, controlling the SV, GB and lattice structure are necessary for tuning its electrical properties. Moreover, CVD offers the potential for p-type doping, which is crucial in CMOS technology. Considering the scalability and controllability, the CVD method will be the primary focus in this thesis for the synthesis of MoS_2 for next-generation electronic devices. The state-of-the-art techniques for MoS_2 in terms of scalability and controllability will be reviewed in the following sections.

2.2.2 Scalable MoS_2 growth via CVD method

The scalability of MoS_2 synthesis is necessary for realizing its potential in semiconductor applications. In this section, I will review the state-of-the-art techniques for the scalable growth of MoS_2, with examples that reveal specific achievements and remaining challenges, particularly in the context of memristor applications.

In recent years, the epitaxial growth of MoS_2 on sapphire substrates has gained attention as a promising approach to achieve wafer-scale MoS_2 films.

While 300 mm wafer-scale deposition of polycrystalline MoS_2 via CVD has been demonstrated [252, 257, 267], these polycrystalline films typically exhibit high GB density, with a corresponding increase in charge carrier scattering, compromising electrical performance and increasing device variability. To address this, efforts have focused on epitaxial growth of single crystalline MoS_2 on sapphire substrates using specially designed setups [237, 266] or miscut substrates [141], aiming to reduce GB formation. The largest single-crystalline MoS_2 achieved to date spans up to 8 inches [266]. While 4|4P-type GBs, which typically appear at 60° tilted grains, are still present, this symmetric periodic boundary without SV is considered stable and has less effect on the conductivity [109, 266, 285]. However, there are some reports of such 1D GBs exhibiting metallic behaviour [285, 291].

For the semiconductor device applications, a significant disadvantage of using a sapphire substrate is that it requires an additional transfer step to relocate the as-synthesised MoS_2 onto the SiO_2/Si substrate for further device fabrication. The transfer process may inevitably introduce contamination and strain which can alter the film quality. Recently, the 2D Czochralski method [106] achieved uniform single-crystal MoS_2 with centimetre-scale domains on a molten glass substrate. While the etching-free transfer process is cleaner than the conventional wet transfer, it may still introduce strain, and the substrate introduced contamination (e.g. Na^+) remains unverified. Synthesizing MoS_2 directly on the SiO_2/Si substrate provides a solution to these transfer and substrate related issues. However, due to the absence of epitaxial templating of MoS_2 on amorphous SiO_2 surface, it is challenging to control the nucleation and synthesis of single-crystal MoS_2 on a large scale.

Numerous efforts have been undertaken to achieve the growth of MoS_2 on SiO_2 substrates. Due to the absence of epitaxy on the isotropic amorphous SiO_2 surface, MoS_2 is usually randomly distributed in a triangular or polygonal geometry [207, 250, 282]. The growth of monolayer MoS_2 on a SiO_2 substrate can be optimized by carefully refining the CVD conditions, such as the choice of precursor chemicals, gas flow rates, and temperatures [276]. However, misoriented MoS_2 domains tend to grow and merge, resulting in disordered GBs [54, 170].

To facilitate the 2D growth of MoS_2 on amorphous SiO_2, seeding promoters are introduced to the substrate prior to the CVD process. For example, alkali metal cations (e.g. NaOH [113], NaCl [82, 211], KI [111]) have been reported to reduce the reaction temperature and weaken the interlayer adhesion, thereby enhancing the lateral growth of transition metal dichalcogenide (TMD) films. By

using Na_2SO_4 as a synergetic additive, centimetre scale continuous MoS_2 with a single domain as large as 632 μm has been achieved on SiO_2/Si substrate [135]. In addition, IIa metal chlorides (e.g. $CaCl_2$, $SrCl_2$) have been demonstrated to significantly increase the size of 2D MoS_2 on SiO_2/Si substrate by enhancing the adsorption of the acidic precursor through increased substrate basicity [140]. However, residual metal ions introduced by the promoters can lead to uncontrollable growth and are detrimental to electric properties. K. Zhang et. al [278] (**Fig. 2.6**) found that, compared to alkali-free synthesis under the same growth conditions, the use of NaCl can lead to variation in growth rates, loss of epitaxy, and a high density of nanoscale MoS_2 particles. Additionally, the field effect mobility was degraded by more than 30%, the on/off ratio dropped by two orders of magnitude from 10^6-10^7 to 10^4-10^5, and there was a threefold increase in threshold voltage variation. These results indicate dramatically increased device variability and degraded transistor performance, which suggests that residual sodium significantly impacts the interface between the substrate and the MoS_2 film.

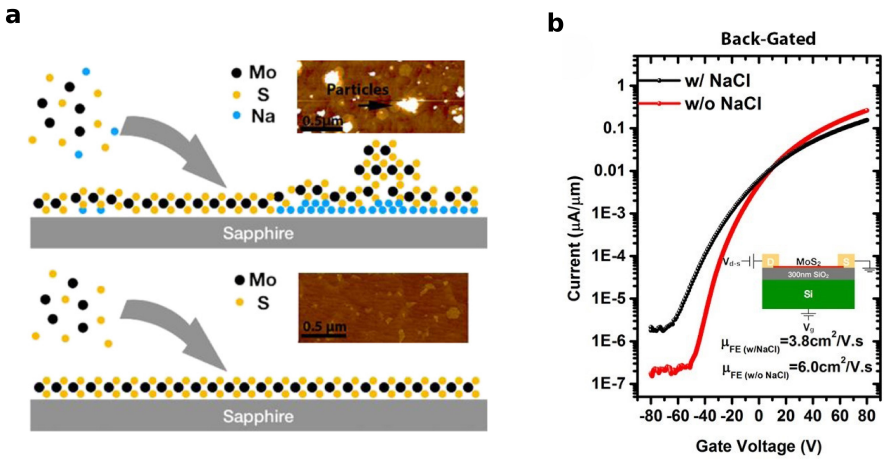


Figure 2.6: **The disadvantage of NaCl-assisted growth of MoS_2.** (a) NaCl induced growth heterogeneities compares with the w/o NaCl growth. (b) Transfer curves of monolayer MoS_2 FETs. The on/off ratio is reduced by two orders of magnitude with NaCl as well as a two times degradation in subthreshold swing. Adapted from [278].

Alternatively, organic promoters such as Perylene-3,4,9,10-tetracarboxylic acid tetrapotassium salt (PTAS) or 3,4,9,10-perylene-tetracarboxylicacid-dianhydride (PTCDA) can also facilitate the synthesis of monolayer MoS_2 up to millimetre-size, owing to the enhanced surface adhesion of MoS_2 and induced heterogeneous nucleation sites [128, 129, 151]. Polymer complex thin film comprising anhydrous ammonium tetrathiomolybdate (ATM) and linearpoly (ethylenimine) (L-PEI) is observed to effectively improve the growth uniformity and control the thickness of MoS_2 film in the range of 2-30 nm [260]. However, precisely controlling the MoS_2 film thickness down to monolayer is

not demonstrated. It is worth mentioning that non-volatile species, such as potassium in PTAS, can be inadvertently incorporated in the MoS_2 and alter its intrinsic properties. In addition, ATM will decompose and release H_2S when the temperature is in the range of 155 to 280 °C, and this is further exacerbated when the temperature exceeds 450 °C. H_2S is, of course, a toxic and extremely flammable gas [247].

Therefore, a clean promoter that ensures minimal contamination and improved film uniformity is essential for achieving scalable growth of 2D MoS_2 on SiO_2/Si substrate. The impact of the promoter will be further explored in chapter 4.

2.2.3 Spatially controlled growth of 2D MoS_2

I now turn our focus to the critical aspect of spatially controlled growth. As semiconductor technology advances rapidly, the continuous scaling of devices has driven the development of sophisticated fabrication techniques within very-large-scale integration (VLSI). Traditional semiconductor manufacturing relies heavily on planar processing [3, 167], which enables the integration of millions of transistors onto a single chip. However, the continued reduction in component size, especially with 2D materials, poses challenges in achieving accurate nanoscale patterning without compromising material properties.

A common approach to fabricating electronic devices involves using photolithography and etching processes to pattern the MoS_2 film into isolated sections [122, 237, 252]. However, these steps present significant challenges, including the procedural complexity which leads to increased costs and low yield, and the inevitable chemical contamination that degrades device performance. These limitations highlight the need for alternative methods that simplify fabrication while preserving the integrity of the 2D MoS_2 film.

A promising solution is the direct patterned growth of MoS_2 on the target substrate, which eliminates the need for transfer and etching [34, 206]. By minimising potential chemical contamination and physical damage, this approach not only simplifies the fabrication process but also maximises the preservation of the film's intrinsic properties.

Significant efforts have been made to achieve spatially controlled growth of MoS_2. Chen et al. utilised selective O_2 plasma treatment on a SiO_2/Si substrate to enhance the hydrophilicity by increasing oxygen dangling bonds, thereby reducing surface energy and facilitating the nucleation and growth of MoS_2 [24]. It was found that the MoS_2 selectively deposited on the pre-treated areas, forming

triangular and circular geometries with a minimum size of 50 μm. Guo et al. further demonstrated that the combination of O_2 plasma treatment with PTAS as a promoter enables MoS_2 growth in a kirigami pattern with minimum feature size of ~ 3 μm [78]. These lithography and plasma treatment processes are compatible with the current semiconductor fabrication techniques, allowing for scalable growth. However, the induced oxygen on the substrate by plasma can potentially modify the MoS_2, altering its intrinsic properties.

Attempts have also been made to achieve patterned growth through geometric confinement using physical masks. Alumina [178] has been reported as a physical mask to partially expose the substrate, enabling patterned growth of 550 μm features in a 20 mm $\times$ 20 mm area. The spatial extent of MoS_2 growth depends heavily on the dimensions of the mask openings and the distance between the mask and substrate, which is typically limited to patterns of hundreds of micrometres. Using such physical masks requires precise positioning and close contact with the substrate, which is challenging. K. S. Kim et al. [115] further developed patterned SiO_2 mask on Al_2O_3/HfO_2 substrate, as shown in **Fig. 2.7** (a). According to DFT calculations, TMDs require higher bonding energy on Al_2O_3 compared to SiO_2, making nucleation more favourable on Al_2O_3. Monolayer MoS_2 and WSe_2 were successfully grown over a 200 mm $\times$ 200 mm area. Since the mask was prepared using lithography and e-beam evaporation, the minimum pattern size can be reduced to 1 μm. However, the SiO_2 mask created a 25 nm deep trench, and after CVD, a significant gap remained between the surface of the SiO_2 and the MoS_2. This gap significantly impacts electrical contact at the trench edge, making it prone to failure. Additionally, the use of a physical mask adds complexity to the process.

Instead of building a physical mask to confine the growth area, a pre-patterned seeding layer can be applied to control the growth of MoS_2 at the designated locations by prompting the nucleation and growth. The typical seeding layer materials are molybdenum and molybdenum compounds, e.g. Mo [68, 249, 265], MoO_3 [206, 239], MoO_2 [240], $(NH_4)_2MoS_4$ [156, 177], and Na_2MoO_4 [139]. As shown in **Fig. 2.7** (b), the seeding is first deposited onto the substrate at the designed location and then sulfurized into MoS_2. However, the thickness of MoS_2 is constrained by the thickness of the seeding layer, the difficulty of depositing sub-nano meter thick pre-seeding layer making it challenging to achieve monolayer MoS_2. Other metals, e.g. Au [145, 214], Pt [242], Cr [219], have also been utilized for spatially controlled growth of MoS_2 due to metal-induced heterogeneous nucleation. However, as shown in **Fig. 2.7** (c), the Au particles and MoS_2 form the core-shell structure, indicating that the

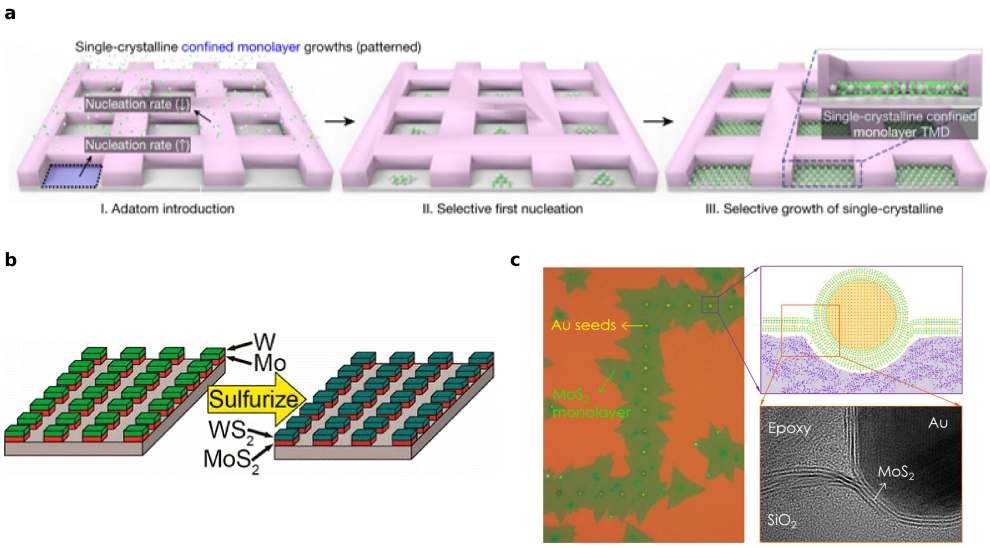


Figure 2.7: **Selective MoS_2 patterning by different methods.** (a) Geometry confinement by physical SiO_2 mask [115]. (b) Patterned growth of MoS_2/WS_2 heterostructure from patterned metallic seed layers [249]. (c) Site-Specific positioning growth of MoS_2 using Au nanoparticles as seeds [145].

film purity has been compromised.

In addition to these methods, alternative approaches such as inkjet printing have been explored for synthesizing MoS_2 films. Inkjet printing [144] stands out for its versatility, cost-effectiveness, and scalability. LPE MoS_2 nanosheets can be used as printable ink, enabling direct deposition onto various substrates including polymers and papers. This approach offers a promising avenue for realizing large-area flexible electronic devices in a single step. However, as mentioned earlier, the thickness and size of MoS_2 nanosheets produced via LPE are difficult to control. Furthermore, the resolution of inject printing is heavily dependent on the printer, ink and substrate, typically ranging from tens to hundreds of micrometres [168, 191], which falls short of the scaling requirement for VLSI applications.

A novel approach, developed in this work with the goal of spatially controlled, contamination-free growth of large scale on SiO_2/Si substrate will be described in chapter 5. This method addresses the limitations of existing techniques by providing improved controllability and scalability, while preserving the integrity of the film's intrinsic properties.

2.3 MoS_2 memristor

This section begins with an introduction to the fundamentals of memristors, then explores their applications in neuromorphic computing, and finally gives a re-

view of the MoS_2 memristor with a particular focus on Schottky barrier modulated memristive switching.

2.3.1 Memristor fundamentals

In circuit theory, two-terminal circuit elements are defined by the relationship between the four fundamental circuit variables: current (i), voltage (v), charge (q), and flux linkage (ϕ). While the resistor ($R = v/i$), inductor ($L = \phi/i$), and capacitor ($C = q/v$) are well-defined elements, the relationship between flux and charge remains less understood until Leon Chua [35] proposed the existence of the fourth fundamental element, memristor, in 1971. A memristor links ϕ and q, and its defining quantity, memristance (M), is mathematically described by:

$$M = \frac{d\phi}{dq} \tag{9}$$

While Chua's theoretical framework formalised the memristor concept, earlier observations laid the groundwork. Notably, in 1962, Hickmott first reported a low-frequency negative resistance in thin anodic oxide films [87]. The memristance depends on the amount of charge that has previously propagated through the device, thus allowing it to remember its past electrical history.

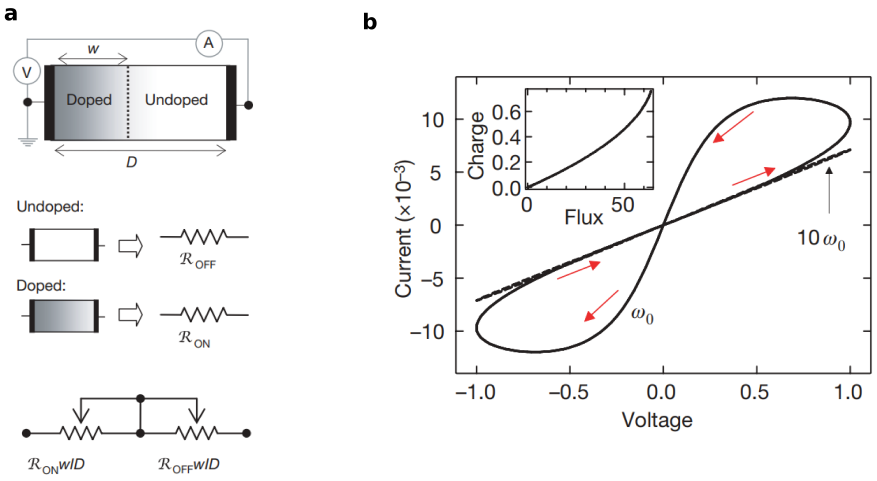


Figure 2.8: **The first memristor.** (a) Diagram with a simplified equivalent circuit and (b) hysteresis I-V curve. Adapted from [217].

After Chua theorized the existence of memristors, in 2008, Stanley Williams and his team in Hewlett-Pckard (HP) Labs announced the first physical realization of a memristor [217]. The first memristor utilized a partially doped titanium dioxide thin film as the active layer and platinum for the electrodes, where **Fig. 2.8** shows its simplified equivalent circuit and the I-V curve. The charge q becomes

significant to the memristance when the device dimensions are reduced to the nano-scale [36]. Therefore, studying the electronic characteristics of memristor devices is crucial for understanding their memristive behaviour.

Basic operation and figure of merits

Figure 2.9 shows the typical I-V characteristic of a memristor device. The hysteresis loop in the I-V characteristic represents the change in resistance. When the device operates in the switchable mode, a positive voltage sweep results in a low current level, corresponding to the high resistance state (HRS), as shown by the red curve. The HRS is also called the OFF state or '0' state. When the applied voltage reaches a threshold, the current level increases abruptly which indicates that the memristor has changed from a HRS to a low resistance state (LRS). This state change is the 'set' process and the threshold voltage that triggers this change is called set voltage, V_{set}. The LRS is also named the ON state or '1' state. During the measurement process, a compliance current is typically set to prevent the device from being damaged by excessive current. If the applied voltage is now reduced, the device remains in the LRS. Once the threshold voltage, V_{reset}, is reached, the device can be reset, which switches back to the HRS, and the current decreases indicating that the device has been 'reset'.

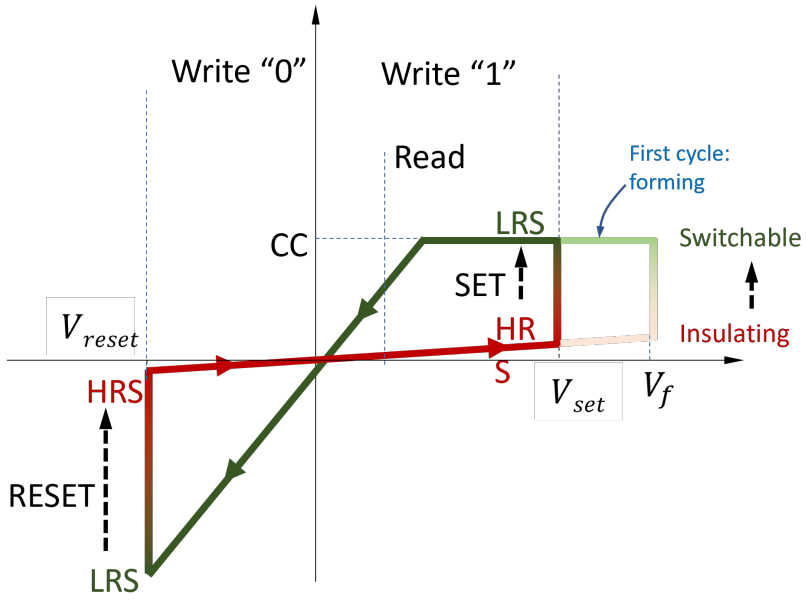


Figure 2.9: **Typical I-V characteristic of a memristor device:** electric forming, set and reset processes.

For some memristors, a high forming voltage (V_f) is required to change the device from insulating mode to switchable mode. This high voltage operation

only occurs in the first cycle, which is called the electric forming process. Depending on the switching mechanism, the forming process is not necessary for all the memristor devices.

The performance of a memristor device can be effectively characterized by several key figures of merit:

- On/off ratio: this is a primary figure of merit and represents the magnitude of resistance change achieved within the device, expressed as R_{on}/R_{off}.
- Endurance: this serves as another critical metric, quantifying the robustness of the memristor by measuring the number of switching cycles it can endure before experiencing fatigue in its on/off ratio. A high endurance value ensures prolonged operational lifespan and reliability in demanding environments.
- Switching time: this describes the device writing speed, delineating the minimum pulse duration required to transit between HRS and LRS effectively. Faster switching times facilitate rapid data processing and manipulation, thereby enhancing overall system performance.
- Data retention: this signifies the duration for which the memristor can retain its state without an applied voltage, underscoring its suitability for non-volatile memory applications. High data retention ensures data integrity and persistence, essential for storing critical information over extended periods.
- Variability: this includes the cell-to-cell variability and cycle-to-cycle variability. The cell-to-cell variability refers to the differences in performance between devices produced through the same fabrication process, highlighting the uniformity and consistency of device performance within a fabrication batch. The cycle-to-cycle variability pertains to the inconsistencies in the operation of an individual device [80, 124]. Reduced variability ensures predictable behaviour and facilitates reliable device operation in practical applications.

Memristors can be catalogued into three typical types depending on the device application. A common type is bipolar resistive switching (BRS), where the set and reset process are performed with different voltage polarities. Bipolar devices show good repeatability and controllability of switching, allowing crossbar arrays without select devices. For unipolar resistive switching (URS) type device, both the write and read operations are conducted with the same voltage polarity. The URS device is limited by switching variability and set/reset instabilities.

In addition, complementary resistive switching (CRS) device has been reported, and can be achieved by connecting two BRS memristors [152]. The CRS device usually exhibits a HRS at low voltage, requiring high operation and read voltages for switching, which can potentially disrupt the logic state.

Applications in neuromorphic computing

Conventional computing systems based on von Neumann architecture, which separates data storage and computation [83, 268], are highly effective at solving structured problems, such as well-defined mathematical tasks. However, for more complex problems and big data processing, neuromorphic computing, inspired by the human brain, becomes essential due to its rapid processing, energy efficiency and self-learning capabilities enabled by integration of data storage and computation [83, 121, 127]. Memristors, which can modulate resistance across multiple states by preserving the history of past electrical inputs, offer the potential to emulate the biological synaptic behaviour observed in neural networks, making them a promising candidate for electronic synaptic devices.

A synapse is the junction that allows a neuron to transmit an electrical or chemical signal to another neuron [248]. As illustrated in **Fig. 2.10**, a typically synapse consists of a presynaptic terminal, neurotransmitter, receptor, and a postsynaptic dendrite [127]. In chemical synapses, electrical signals stimulate ion channels in the presynaptic membrane, triggering the release of neurotransmitters. These neurotransmitters bind to receptors on the postsynaptic dendrite, causing ion channels in the postsynaptic membrane to open. This chemical transmission at the synapse results in either potentiation or depression. Synaptic plasticity refers to the ability of synapses to strengthen or weaken in response to changes in neuronal activity, which is fundamental to various complex brain functions and is a key focus for artificial devices with neural behaviours. Memristors exhibit a range of synapse-like properties that are essential for mimicking neural processes in artificial synaptic devices. In chapter 6, I will discuss the synaptic characteristics, potentiation and depression mechanisms, which are vital for developing advanced neuromorphic systems.

2.3.2 2D memristors

In recent years, due to the unique electronic properties (electrical tunability, low-power switching capability, hetero integration compatibility [93]) and atomically thin nature, 2D materials have emerged as promising candidates for the active layer of next-generation memristor devices with advantages in device scaling and

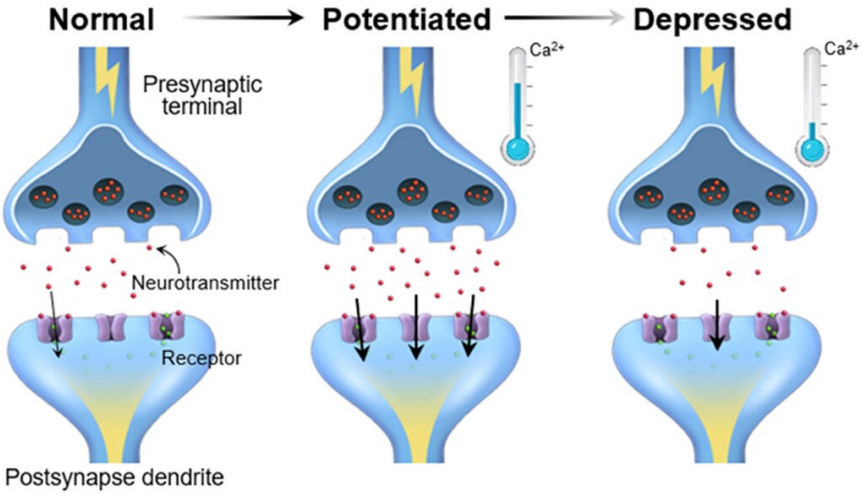


Figure 2.10: **Schematic illustration of biological synapses.** [127]

power consumption. Extensive research has been conducted and demonstrated the switching behaviour in 2D memristors. The active layer material, such as graphene [200], TMDs (MoS_2 [196], WS_2 [259], WSe_2 [95], etc.), hexagonal boron nitride (hBN) [30] and black phosphorus (BP) [241], have been demonstrated in various device structures working under different switching mechanisms.

Memristive devices based on 2D materials are generally categorized into three groups based on their structure: lateral, vertical, and heterojunction configurations [93, 279]. In lateral devices, or planar devices, 2D materials and metal electrodes are horizontally connected, allowing charges to travel along the in-plane direction [196, 197, 288]. Vertical devices, on the other hand, feature in a sandwich structure where the electrodes and 2D material are stacked, with charges flowing through the out-of-plane direction. These vertical memristive device are well-suited for facilitating crossbar array structures [117, 123]. In addition, by vertically stacking two or more layers of different 2D materials, heterojunction-structure devices can be achieved [13, 94, 258]. Among these configurations, planar geometry offers efficient gate modulation and multi-terminal operation, enabling advanced neural functionalities [196].

The conduction mechanism of resistive switching memory varies depending on the electrode-dielectric interface or the dielectric properties. The electrode-limited conduction mechanism includes Schottky emission, Fowler-Nordheim (F-N) tunneling and direct tunnelling. Meanwhile, dielectric-limited mechanism includes Poole-Frenkel (P-F) emission, Ohmic conduction, space-charge-limited conduction (SCLC), ionic conduction, hopping conduction and trap-assisted tunneling (TAT) [149]. Each mechanism exhibits a distinct I-V relationship, which can be used to fit experimental data and provide insights into the device physics.

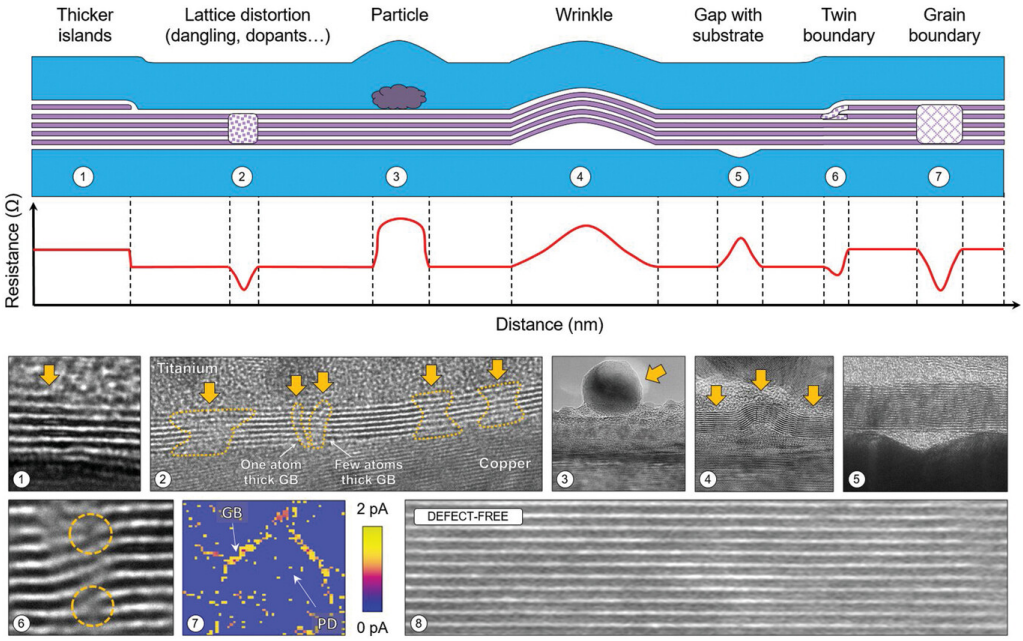


Figure 2.11: **Schematic and corresponding characterization shows the typical defect types in 2D materials.** [208]

For 2D memristors, variability remains a major challenge hindering their widespread adoption in industry [1, 192]. As mentioned in the previous section, the device variability is heavily depending on the quality, uniformity, and homogeneity of the 2D material, with stochastic defects significantly contributing to this variability. **Figure 2.11** illustrates common defects in 2D materials that arise during growth or transfer processes, including thickness variation, lattice distortion, contamination particle, wrinkle, substrate pitch and GB [208]. Each defect impacts resistance in its own way, and the presence of one or a combination of these defects can potentially affect memristive switching behavior in an unpredictable manner.

2.3.3 Switching mechanisms in 2D MoS_2

Numerous studies have demonstrated memristive switching behaviour in 2D MoS_2 memristors, however, the underlying mechanisms vary significantly among these studies. **Figure 2.12** illustrates the representative switching mechanisms of 2D memristors, including filament conduction, phase change, defect migration and charge trapping. Moreover, Schottky barrier-modulated switching based on vacancy migration and charge trapping will be further discussed. The MoS_2 memristor devices with different switching mechanisms are summarized in table 2.1, including their device structure, material preparation method and operating voltage.

Filament conduction

Filament conduction is the major switching mechanism in metal oxide-based memristors [123], which is an electrochemical metallization mechanism (ECM). However, few experiments have demonstrated filament conduction in 2D MoS_2 memristors due to the atomic thickness of MoS_2 [183]. The observed filament conduction in MoS_2 memristors is primarily attributed to Ag ions from the electrodes. Under an electric field, Ag ions penetrate into the SVs and form a conductive filament, which spontaneously collapses when the electric field is removed [46, 59]. Subsequently, single-defect MoS_2 memristors were demonstrated, paving the way for precision defect engineering towards the atomic scale memristors. The resistive switching mechanism is attributed to the Au ion substituting into the SV, leading to a localised conducting density of states and driving the device into a LRS [70, 97].

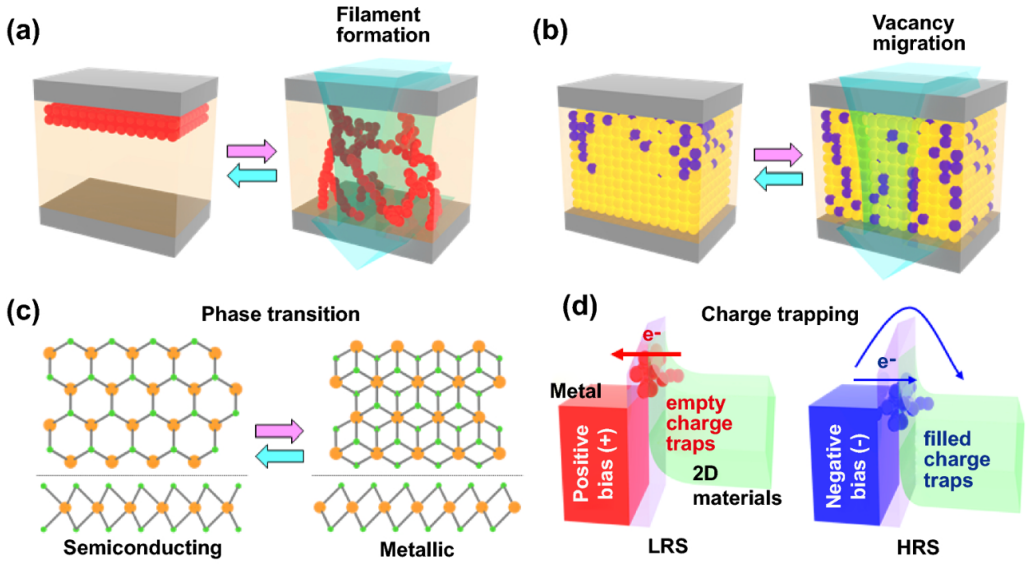


Figure 2.12: **Representative switching mechanisms of 2D memristors:** (a) filament formation, (b) vacancy migration, (c) phase transition, and (d) charge trapping. Adapted from [123].

Phase change

Since the conductivity of MoS_2 depends on its polytypes, the phase change mechanism has been extensively studied. In vertical metal/MoS_2/metal memristors, a phase transition between the 1T metallic MoS_2 and the 2H semiconducting MoS_2 results in a significant change in conductance, leading to resistive switching behaviour [28, 280]. Additionally, the applied electric field induces lattice distortion, which facilitates the delocalization of 1T phase electrons, thereby enhancing the conductivity of 1T MoS_2 and amplifying the resistance change [28].

Defect migration

High quality MoS_2 obtained through ME method does not initially exhibit significant resistive switching behaviour [222, 279]. However, it was reported switching behaviour for defective MoS_2, such as MoS_2 with GBs and SV.

In 2015, M. C. Hersam et al. [196] successfully demonstrated the memristive switching of a MoS_2 memristor, where the MoS_2 was grown by CVD method (**Fig. 2.13**). They discovered that memristive switching behaviour occurred only when GBs were present within the MoS_2 channel, whereas it is absent in the devices without GBs. They proposed that the resistive switching is attributed to the migration of SVs originating from the GB regions, and such migration can be further promoted by applying an electric field parallel to the GB. The GBs geometry effect on the electrical performance was then compared. The devices with GBs connected to only one of the two electrodes exhibited the best performance, which was named 'intersecting-GB memristors'. Furthermore, they first reported the gate tunable electrical performance of MoS_2 memristor, which sparked a wave of research on MoS_2 memtransistors [14, 102, 274].

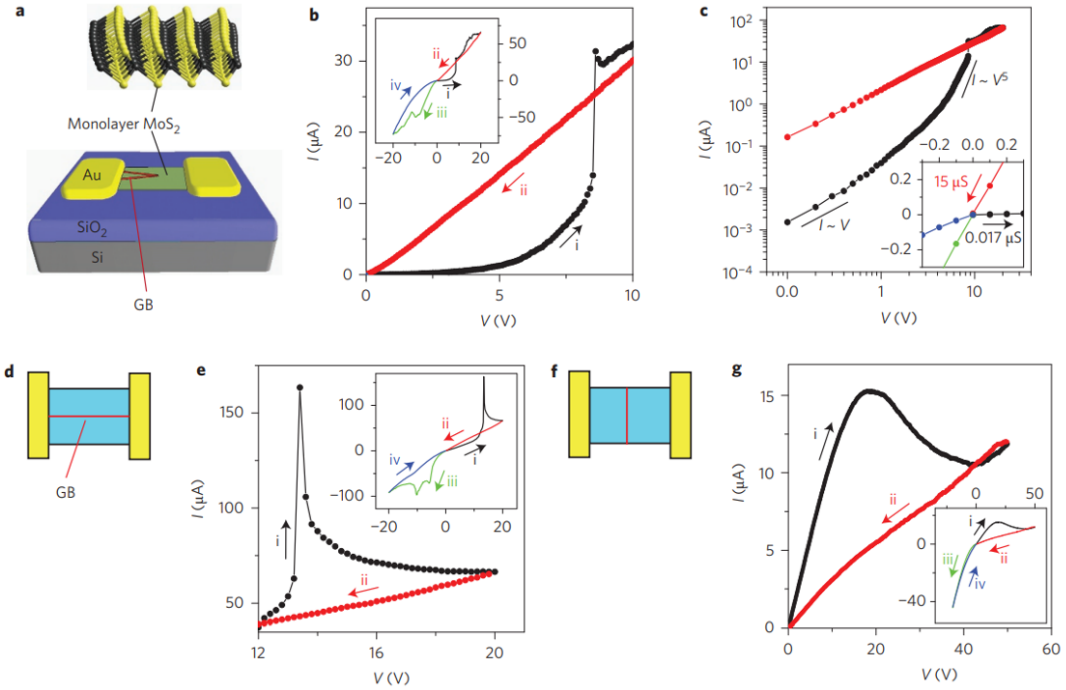


Figure 2.13: **I–V characteristics of MoS_2 memristors with GB.** (a) Schematic of an intersecting-GB MoS_2 memristor. (b) Partial I–V characteristics after electroforming. Inset: Full I-V for one switching cycle. (c) Log-log plot of (b) with an inset zoom-in near zero bias, reveals conductance in the off and on states. (d-g) Schematics and partial I–V characteristics of electroformed bridge-GB memristor and bisecting-GB memristor at V_g = 40 V and V_g = 55 V, respectively. Figures adapted from [196].

Our group has conducted extensive research on MoS_2 memristor devices. In

2018, J. Jadwiszczak demonstrated the MoS_2 lateral memtransistor using a focused helium ion beam [102]. By precisely irradiating specific sites with a helium ion microscope, a defect-rich region is created at the nanoscale, bisecting the MoS_2 lattice. The reversible drift of these defects under an applied electric field modulates the channel resistance, enabling memristive functionality. The device demonstrates stable resistance ratios and set/reset biases over 1180 switching cycles, with long-term potentiation and depression exhibiting sharp habituation. S. Aldana [1] further published the MoS_2 planer memristor devices and demonstrated the defect migration mechanism by building a physical simulator based on the kinetic Monte Carlo algorithm. The effects of initial vacancy distribution, the scaling limits and the factors that regulate device endurance and variability were investigated. For a defect migration-based switching device, the defects migration must be enhanced to reduce the operation voltage.

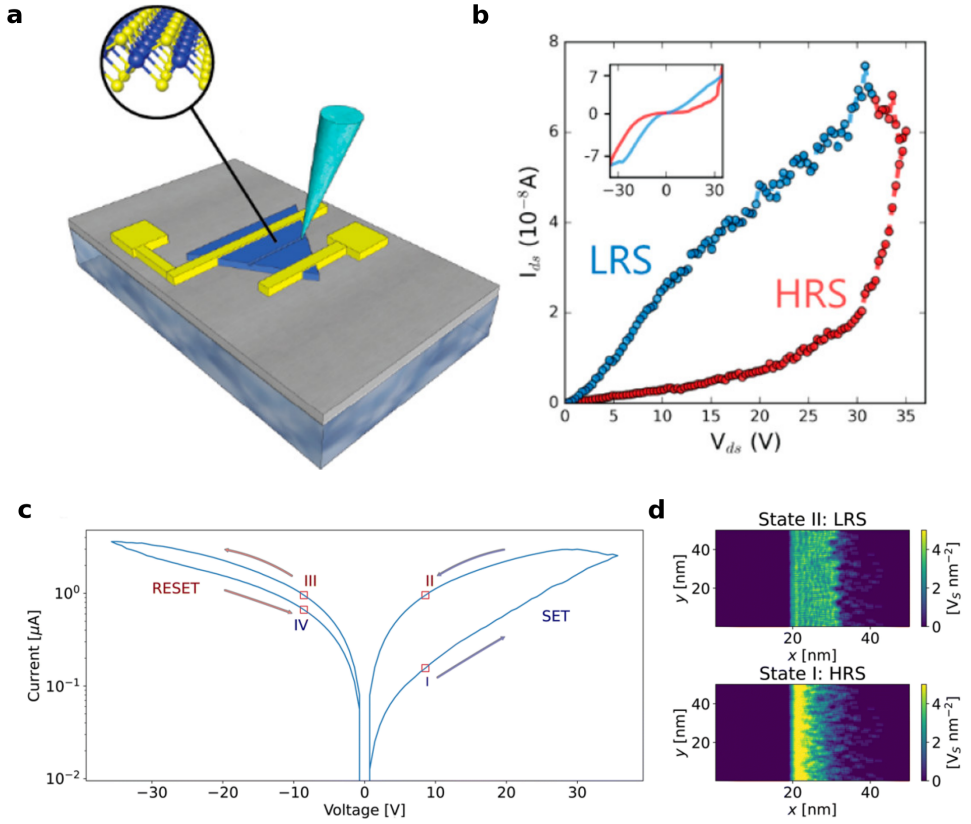


Figure 2.14: **Control the sulphur vacancies and achieve the MoS_2 memtransistors by localized Helium ion beam irradiation.** (a) Illustration of the irradiation strategy. (b) Positive-bias sweep region of an irradiated monolayer memtransistor device at V_g =0 V. Insert shows the full range I-V curve. (a, b) Adapted from [102]. (c) A typical simulated I-V pinched hysteresis loop. Numerals on the loop mark four. (d) Microscopic defect profile of the LRS (top) and HRS (bottom). (c, d) Adapted from [1].

Introducing MoOx is reported to be a useful method to realize the MoS_2 mem-

ristor switching behaviour. Later in 2018, Miao et al. [235] achieved memristive switching by a similar strategy, which obtained $MoS_{2-x}O_x$ by oxidizing exfoliated MoS_2 flakes. The devices exhibited excellent bipolar switching performances with endurance of up to 10^7 cycles and thermal stability of up to 340 °C. The cross-section high-angle annular dark-field (HAADF) images in **Fig. 2.15** present a single $MoS_{2-x}O_x$ memristor in the pristine state, ON state and OFF state, respectively. After electroforming (4.5 V), a dark region in the $MoS_{2-x}O_x$ layer appears in the ON state which corresponds to the conduction channel. This conduction channel remains unchanged when the device is switched to the OFF state. Energy-dispersive X-ray Spectroscopy (EDX) line-scan along the green dashed line of HAADF images are illustrated in **Fig. 2.15** (d-f). The Mo:(S+O) atomic ratio in the pristine state exhibits a uniform distribution, maintaining stoichiometric proportions with an averaged value of approximately 1:2. At the ON state, the ratio in the conduction channel shifts to about 1:1.2, due to a reduction in S atoms (resulting from the generation of SVs) caused by the thermophoresis effect from Joule heating. The conduction channel remains during subsequent OFF states, indicating minimal movement of S atoms. However, the atomic ratio returns to nearly 1:2, which is attributed to the O ions moving toward and filling the SVs driven by the electric field.

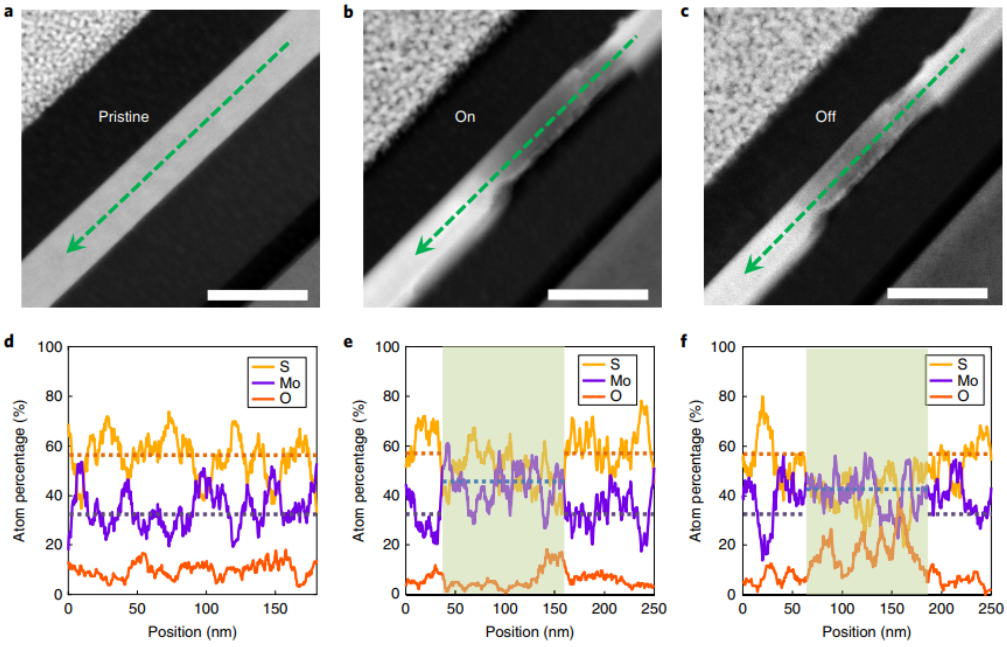


Figure 2.15: **In situ Scanning Transmission Electron Microscopy (STEM) observation of the conduction channel in $MoS_{2-x}O_x$ memristor.** Cross-section HAADF image of $MoS_{2-x}O_x$ memristor in the (a) pristine state, (b) ON state and (c) OFF state, respectively. All scale bars are 50 nm. (d-f) EDX line-scan profiles of the green arrows in (a-c) for different device states. The numbers of Mo, S and O were measured and normalized as atom percentage. Adapted from [235].

Charge trapping

The resistive switching mechanism in MoS_2 devices, attributed to charge trapping and de-trapping, has been widely investigated [13, 96, 155, 194]. The charge trapping and de-trapping of electrons occur at the interface between the electrode and the 2D TMD layers, known as the weight control layer [123].

Additionally, certain memristors operate through a combination of mechanisms. For instance, memristive switching can result from the interplay of charge trapping, defect migration, and Schottky barrier modulation.[13, 96]. Schottky barrier-modulated switching is realized by tuning the SBH at the contact interface, which will be further discussed in the following section.

Schottky barrier modulated memristive switching

The migration of vacancies leads to a change in valence, a process known as valence change mechanism (VCM). When VCM affects the contact interface, it modulates the SBH, resulting in what is referred to as Schottky barrier-modulated memristors. The SBH at the metal-semiconductor junction plays a crucial role in determining the device switching characteristics and overall performance. However, the effectiveness of Schottky modulation is often compromised by FLP, defects and traps at interface, etc. Effectively tuning the SBH is essential to ensure efficient carrier injection, thereby enhancing the device response and reducing power consumption.

The Schottky barrier-dominated memristive switching generally involves two processes: (1) migration of the defects under applied electric field leads to defect concentration change at the contact interface, (2) the changed defect concentration tunes the SBH and thus alters the contact resistance [218]. The defects have different charge polarities depending on the chemical state of the compound. For example, oxygen vacancy [217] in molybdenum oxide and SV [133] in MoS_2 are both positively charged. The first-principle calculation reveals that the SVs in MoS_2 increases the SBH when in contact with Mg, Al and In, while decreases it when in contact with Cu, Ag, Pd, Co, and Ni [284].

Bessonov et al. [13] developed a MoOx/MoS_2 vertical heterostructure memristor and realized the memristor switching for exfoliated MoS_2 in 2015, as shown in **Fig. 2.16**. After thermal annealing, the ultrathin MoOx (< 3 nm) layer was formed in the topmost layers of MoS_2. The devices exhibited a large on/off ratio of around 10^6 and remarkably low programming voltages of 0.1-0.2 V, which is ideal for low-energy consumption and high-performance applications. It is found that the MoS_2 is relatively conductive while the voltage drops mainly on the Ag

electrode and MoOx interface due to the presence of the Schottky barrier. The MoOx serves as oxygen deficiency induced dopants [5], and the electrically activated anionic movement leads to the metal valence change thus the resistance switching behaviour.

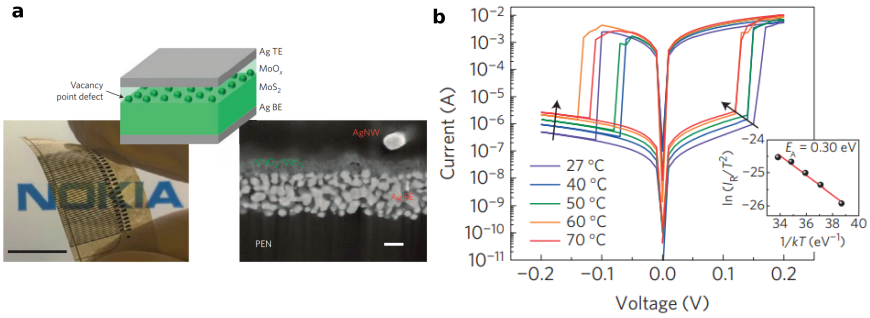


Figure 2.16: **Resistive and capacitive switching characteristics of MoOx/MoS_2 heterostructures.** (a) MoOx/MoS_2 heterostructures structure. The scale bar for the left panel is 10 mm and for the right panel is 100 nm. (b) The MoOx/MoS_2 resistive switch demonstrates a clear temperature dependence of V_{set} and I_{off}, the inset shows the activation energy of the reverse bias current at -0.2 V extracted from temperature-dependent I–V measurements [13].

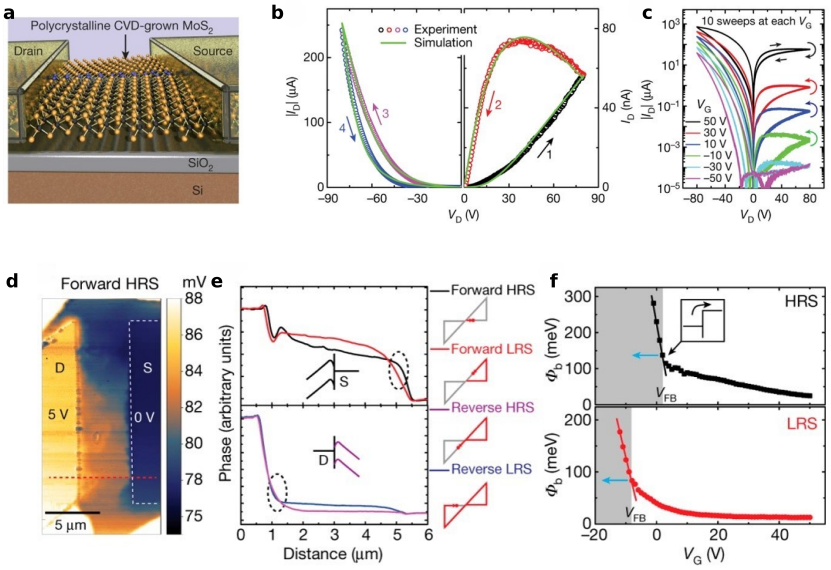


Figure 2.17: **Characteristics of polycrystalline MoS_2 memtransistor.** (a) Schematic of MoS_2 memtransistor. (b) $I_{DS} - V_{DS}$ curve of a MoS_2 memtransistor at V_{GS} = 10 V. The solid green line represents simulated data. (c) $I_{DS} - V_{DS}$ curves for ten consecutive sweeps at each gate bias V_{GS} for the same device. (d) electrostatic force microscopy (EFM) phase image of a MoS_2 memtransistor at V_D = 5 V, V_S=0 V in the forward-biased HRS. (e) Line profiles of EFM phase image along the red dashed line. (f) Dependence of the effective Schottky barrier height (ϕ_b) on V_{GS}. For V_G=V_{FB}, ϕ_b decrease from 125 meV in the HRS to 80 meV in the LRS. All figures are adapted from [197].

In 2018, M. C. Hersam et al. reported the experimental realization of a

multi-terminal memtransistor using polycrystalline monolayer MoS_2 [197] (**Fig. 2.17**).The $I_{DS} - V_{DS}$ curve of the MoS_2 memtransistor (L = 5 μm, W = 100 μm, V_{GS} = 10 V) in **Fig. 2.17** (b) with the switching directions marked by the arrows shows the resistance sequence of HRS - LRS - LRS - HRS. EFM phase image in **Fig. 2.17** (d) shows the MoS_2 memtransistor at V_D = 5 V, V_S=0 V in the forward-biased HRS. **Figure 2.17** (e) plots the line profiles of EFM phase image along the red dashed line. When forward bias is applied, a sharper potential drop (larger field) at the source electrode-MoS_2 interface in the HRS compared to the LRS, suggesting a larger R_c in the HRS. If reverse bias is applied, the I-V characteristic is dominated by the drain electrode-MoS_2 interface. A slightly larger field is observed at HRS than at LRS. The tuning of Schottky barrier results from the defects migration facilitated by GBs. **Figure 2.17** (f) show that when V_G=V_{FB}, ϕ_b is 125 meV in the HRS and decreases to 80 meV in the LRS, which are deviated from the linear dependence on V_{GS} of the thermionic emission model.

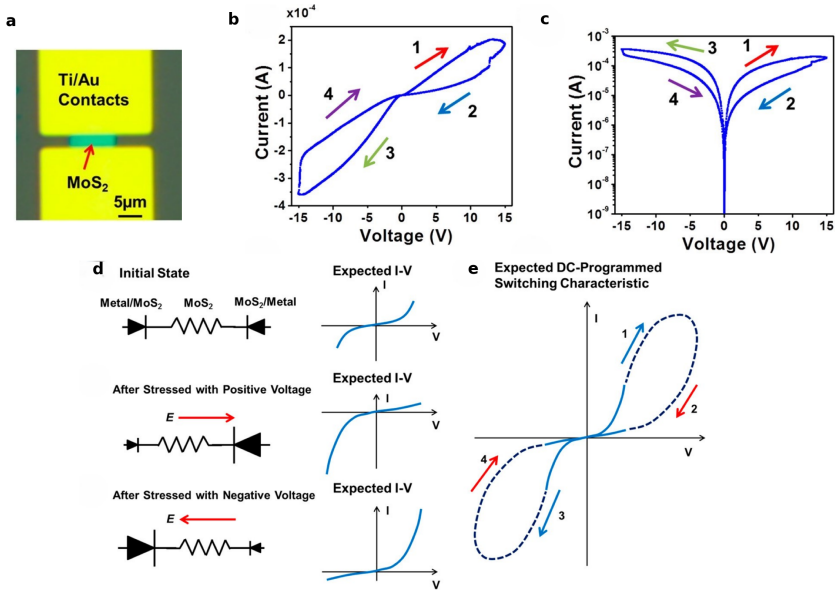


Figure 2.18: **Variable switching characteristics of few-layer MoS_2 memristors.** (a) Structure of a few-layer MoS_2 memristor fabricated by nanoimprint-assisted shear exfoliation. (b, c) Rectification-mediated switching characteristic I-V curve. (d) Device model of the rectification-mediated switching process. (e) Expected switching characteristic I-V curve. All figures are adapted from [133].

Later, D. Li. et al. [133] observed the Schottky barrier dominated switching in the planar MoS_2 devices, as shown in **Fig. 2.18** (a). **Figure 2.18** (b) and (c) depict the I-V curves. The switching behaviour of the MoS_2 memristor is attributed to the modulation of MoS_2 /Ti Schottky barriers. In their model, shown in **Fig. 2.18** (d) and (e), the SV are depleted at the positively biased electrode and accumulated at the negatively biased electrode, leading to the decreased and increased SBH,

respectively.

It is clear that defects in MoS_2, such as SV, oxygen vacancies, and GB, play a critical role in modulating its switching behaviour. Although much research has been done on the Schottky barrier modulated MoS_2 memristor and showing that SV can tune the SBH. However, the relationship between SV density and SBH vary from one to the other. A consistent underlying mechanism still needs to be further explored. In addition, to the best of our knowledge, rarely effort has been on the $MoS_{2-x}O_x$ memristor which is synthesized by CVD method. In chapter 5 and chapter 6, a one-step CVD method is introduced to synthesize patterned $MoS_{2-x}O_x$ for memristor devices. The process allows high-throughput fabrication of $MoS_{2-x}O_x$ memristor devices. The memristive switching mechanism and synapse behaviour are further studied.

Mechanism	Structure	Material preparation	Switching voltage (V)	Refs.
Filament conduction	Ag/MoS_2/Ag	CVD	0.35 - 0.4	[46]
Phase change	Ag/MoS_2/Ag, vertical	lithium intercalation exfoliation	0.1 - 0.2	[28]
	Al/MoS_2/Al, planar	hydro-thermal	1.2	[280]
Defect migration	Au/MoS_2/Au, planar	CVD	10 - 50	[196]
	Au/MoS_2/Au, planar	CVD	35	[102]
Charge trapping	Ag/MoS_2/Ag, vertical	Langmuir – Blodgett method	0.2	[13]
Schottky barrier	Au/MoS_2/Au, planar	CVD	80	[197]
	Au/MoS_2/Au, planar	mechanical printing	15-50	[133].

Table 2.1: **MoS_2 memristor devices with different switching mechanisms.**

3 | Fabrication and characterization techniques

"We cannot solve problems with the same thinking we used to create them."

- Albert Einstein

This chapter delves into the comprehensive methodologies employed for the preparation, fabrication and characterization of MoS_2 materials and devices. The chapter is divided into three sections: material preparation, device fabrication and characterisation techniques, providing a comprehensive description of the processes and methods used throughout this work.

3.1 Material preparation

This section reviews various techniques for preparing two-dimensional (2D) MoS_2 including both mechanical exfoliation and chemical vapour deposition (CVD) methods. Our discussion will focus on the CVD method since it is the main methodology used in this work. The section concludes with a discussion of 2D MoS_2 transfer techniques, which are essential for integrating the material into diverse substrates and devices.

3.1.1 Chemical vapour deposition (CVD)

CVD was first introduced by C. F. Powell in his book in 1966 [181], which is widely used in film formation techniques. CVD is a process in which gaseous or vaporous molecules of volatile compounds react at high temperatures, producing a material that deposits onto the substrate surface. A basic CVD process is sketched in **Fig. 3.1** (a), which involves several steps [174]:

1. Convection and diffusion of gas phase reactants.

2. Gas phase chemical reactions generate non-volatile species and by-products.
3. Transport of initial reactants and resultant products to the substrate surface.
4. Adsorption, diffusion and desorption of adatoms on the substrate surface.
5. Nucleation and film formation.
6. Desorption of volatile by-products from surface reactions.
7. The convective and diffusive dispersal of reaction by-products away from the reaction zone.

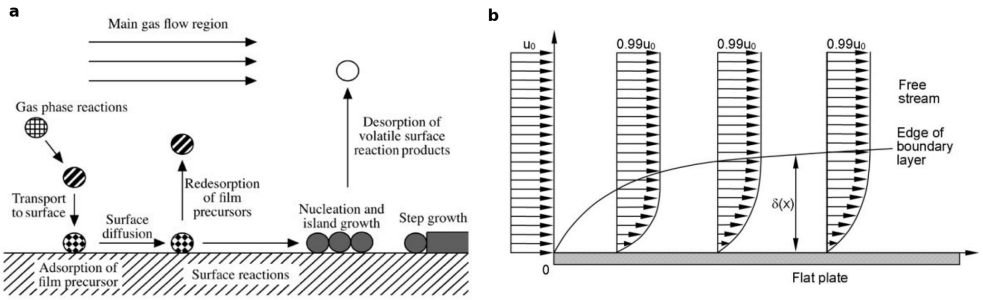


Figure 3.1: **Basic CVD process and boundary layer.** (a) Gas transport and reaction process of CVD film growth [86]. (b) Profile of a boundary layer along a flat surface [264].

The feasibility of the reaction depends on the free energy. The change in free energy, ΔG, determines the reaction direction and extent. If the ΔG is close to zero, a significant amount of both reactants and products coexist. If ΔG is highly negative, the rate of nucleation increases, leading to polycrystalline formation. A slightly negative ΔG is preferred to achieve a low nucleation rate, ensuring controlled growth.

The partial pressure and gas flow are two of the key parameters for the CVD. In a tube furnace, the gas velocity is uniform when it is far from the tube wall and substrate surface. Velocity gradient develops near the tube wall and substrate surface, dropping to zero at these surfaces, which creates a boundary layer (**Fig. 3.1** (b)). The boundary layer thickness is given by $\delta = \frac{5x}{\sqrt{Re}}$, where x is the distance along the flow direction and $Re = v\rho x/\eta$ is the Reynolds number of the flow, v, ρ and η are the flow velocity, density and viscosity of the gas, respectively. Small δ are desirable in enhancing mass-transport rates [174], which can be achieved by increasing gas flow v or decreasing x. Most CVD reactors operate in the laminar flow regime (Re is from tens to several hundreds) to avoid the gas eddies and swirls that may degrade the film uniformity and quality [174].

The surface adhesive energy refers to the interaction energy between the adatoms and the substrate, while the attraction between the adatoms is called the adatom cohesive energy. When the surface adhesive energy is stronger than the adatom cohesive energy, layer growth is favoured. Conversely, if the adatom cohesive energy dominates, island growth becomes dominant [151].

Mass transport and surface reactions are the key kinetics influencing the growth rate and film deposition [264]. At the equilibrium state, the flux of the reactant gaseous from the gas phase to the substrate is equal to that consumed from the substrate. The relationship between the gas phase reactant concentration in the bulk, C_G, and near the substrate surface, C_S, can be given as:

$$C_S = \frac{C_G}{1 + k_S/h_G} \tag{1}$$

where $k_S = K_0 exp(-E_a/kT)$ and $h_G = \frac{D}{\delta}$ are the reaction rate constant and mass transport constant, $D = D_o T^{3/2}/P$ is the diffusion coefficient of the reactant gaseous species. C_G and C_S have the same units, typically mol/^{3}, while both k_S and h_G share the unit of m/s. The relationship between the growth rate and the temperature can be described by the Arrhenius plot, as shown in **Fig. 3.2** (a). At low temperatures, the reaction rate is much lower than the mass transport $k_S << h_G$, therefore, the reactant concentration is constant in the boundary layer $C_S = C_G$. In this surface reaction limited regime, the growth rate increases with the temperature, $r \sim k_s C_G$, the film growth is relatively uniform due to a sufficient supply of the reactant gaseous species. At high temperatures, the mass transport rate is lower than the chemical reaction, $k_S >> h_G$, thus $C_S < C_G$. There is a reactant concentration gradient in the boundary layer, and the reactants are likely to be consumed in the gas phase, resulting in excessive nucleation or by-products. In this mass transport limited regime, the growth rate is less dependent on the temperature. The growth rate can be expressed as $r \sim \frac{DC_G}{\delta} \sim u^{0.5} T^m \frac{P_{partial}}{P}$, which increases with the gaseous partial pressure $P_{partial}$ and inversely proportional to the total pressure P.

CVD enables the synthesis of various 2D materials (e.g. graphene [138], hexagonal boron nitride (hBN) [114], transition metal carbide and nitride (MXene) [176], transition metal dichalcogenide (TMD) [175]). The CVD MoS_2 growth process can be summarized into two strategies: sulfurising a Mo thin film on the substrate directly [272] and converting molybdenum compound (such as MO_3 and $(NH_4)_2MoS_4$) to MoS_2 through gas transport and reaction with a gaseous sulphur source [129, 156]. In the former case, the MoS_2 layer number and quality are strongly dependent on the Mo film, and monolayer

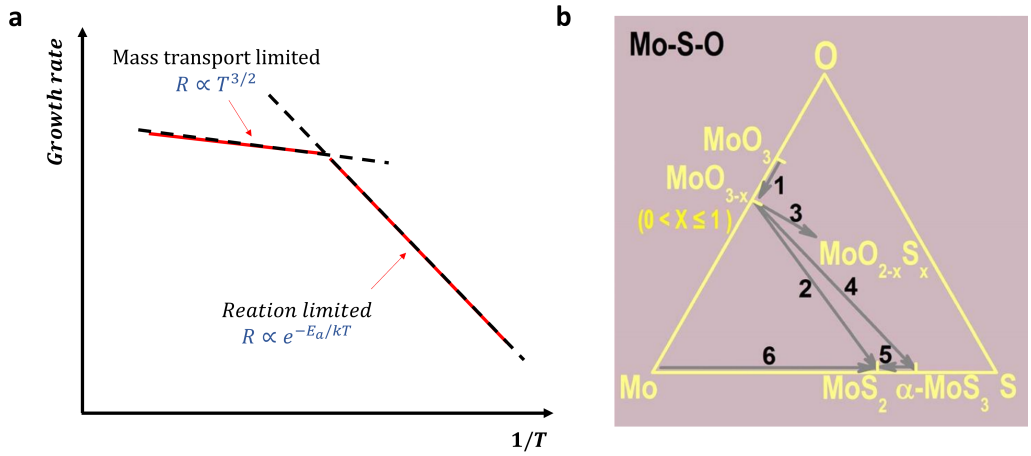


Figure 3.2: **Film growth rate and ternary phase diagram of Mo-S-O.** (a) Relationship between growth rate and temperature. (b) Ternary phase diagram for Mo-S-O, showing the possible reactions to produce MoS_2 [55, 154].

single crystalline growth ($\sim$ 0.65 nm) is challenging. The latter molybdenum compound conversion route is preferred because it can achieve monolayer MoS_2 with high crystallinity. However, the quality and electrical performance of the MoS_2 can vary significantly based on experimental conditions, such as the S/Mo ratio, the temperature, the gas flow rate and the substrate to source distance [203, 251, 264]. MO_3 is a commonly used Mo source. The ternary phase diagram of the Mo-S-O system shown in **Fig. 3.2** (b) provides the equilibrium compositions and possible reactions to produce MoS_2. In a typical CVD reaction, the MoO_3 is first reduced to MoOx and then further sulphurized to MoS_2 [204, 281].

In this thesis, MoS_2 is synthesized on a Si wafer (Graphene Supermarket, $\rho = 0.005\Omega \cdot$ cm) with a SiO_2 cladding layer using the CVD method. The Si substrate is 1.5 $\times$ 1.5 cm^2 and the SiO_2 layer is 285 nm thick unless specified. Prior to MoS_2 deposition, the substrate is ultrasonically cleaned in acetone, isopropyl alcohol (IPA) and deionized (DI) water for 5 min each, followed by drying under N_2 for several seconds. A tube furnace (GSL-1100X, MTI corporation) is utilised for the CVD process as shown in **Fig. 3.3** (a). As illustrated in **Fig. 3.3** (b), the gas inlet is named upstream of the furnace tube and connected to high purity N_2 gas (99.999%), which serves as both a carrier gas and protective gas during the CVD process. MoO_3 (Afla aesar, 99.9%) and sulfur powders (MaTecK, 99%) are used as precursors. In a typical CVD growth, 1 mg of MoO_3 and 120 mg of sulphur powder are placed in separate quartz crucibles. The substrate is positioned in the centre of one crucible with the SiO_2 layer facing the MoO_3 powder. This crucible, containing MoO_3 powder and the substrate, is then placed in the constant temperature reaction zone of the tube furnace. The sulphur powder is located upstream of the reaction zone and heated separately using a heating belt, allow-

ing independent control of the sulphur temperature (T_s).

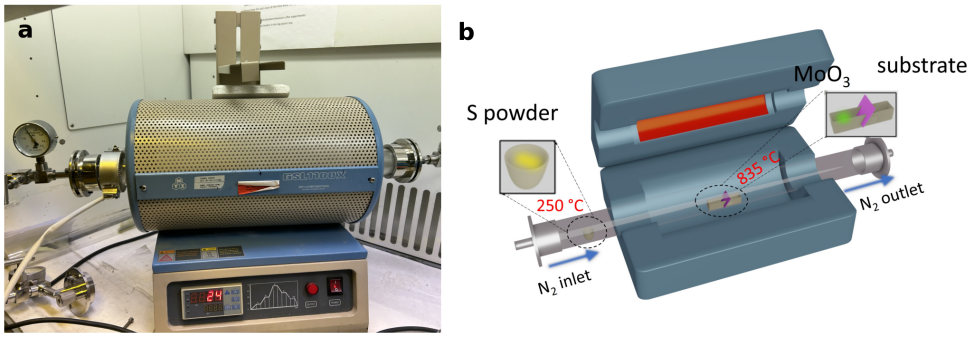


Figure 3.3: **CVD furnace system for MoS_2 deposition.** (a) The furnace with a separate sulphur temperature control for MoS_2 deposition. (b) Diagram of CVD setup showing the gas flow and positions of S source, MoO_3 source and substrate.

The vacuum level of the setup should be checked before heating, as any oxygen leakage from the ambient could lead to deposition failure. A flow rate of N_2 at 500 standard cubic centimeters per minute (sccm) and the temperature of 105 °C are maitained for 1 hour to purge the air from the tube and ensure the elimination of the H_2O molecules. The temperature is then raised to 600 °C at the rate of 14 °C/min, and the N_2 flow is reduced to 30 sccm to control the sulphur vaporisation until the end of the reaction. Subsequently, the temperature is ramped up to 835 °C, where sublimated MoO_3 reacts with sulphur vapour to deposit MoS_2 onto the substrate. The temperature is held constant for 5 minutes to allow for the growth of MoS_2. After this period, the heating is turned off, and the N_2 flow is immediately increased back to 500 sccm. Once the furnace cools down to room temperature, the sample is removed from the tube furnace.

3.1.2 2D MoS_2 transfer

The Transmission Electron Microscopy (TEM) characterisation of as-synthesized MoS_2 requires transferring the sample from the Si substrate onto a TEM grid. The polymer-assisted method was successfully employed for graphene transfer [15]. In this work, we adapt and extend this method for the transfer of MoS_2. Polymethyl methacrylate (PMMA) A3, a widely used positive resist, is utilised as an intermediary in the transfer process. PMMA A3 refers to a 3 wt% solution of PMMA dissolved in anisole solvent. The transfer procedure is as follows:

For global transfer (large area transfer), PMMA A3 is spun onto the 2D sample at 3000 revolutions per minute (rpm) for 40 s and followed by 5-minute hot plate bake at 180 °C, yielding a $\sim$ 200 nm thick film on the surface of our sample. A 1 mm wide strip along the sample edge is manually removed using a sharp

scalpel. The SiO_2 is then etched using a saturated sodium hydroxide (4M NaOH, Sigma-Aldrich) solution in a Teflon beaker. This process takes 1-2 hours at 90°C or overnight at ambient temperature. The etch rate is adjusted to prevent excessive bubbles, as these can damage the PMMA film and degrade the 2D flakes. With the SiO_2 etched off from the edge to the centre, the polymer film will bend due to surface tension. After the SiO_2 layer is totally dissolved, the Si substrate falls down to the bottom of the Teflon beaker while the polymer film with 2D flakes underneath floats on top of the solution.

Filter paper is then used to fish out the polymer film from the sodium hydroxide solution and transfer it to clean DI water. Extensive DI rinsing is carried out to remove the residual aqueous alkali from the film. After washing, the curved film will unfold and float on the surface of the DI water. The clean film is then removed from the DI water using the host substrate and baked for 5 min at 120°C to dry it and enhance the adhesive force between 2D flakes and the target substrate. The PMMA film is then removed by immersing in acetone for 5 min and rinsing with IPA for 5 min. The 2D flakes have now been transferred to the target substrate for further experiments.

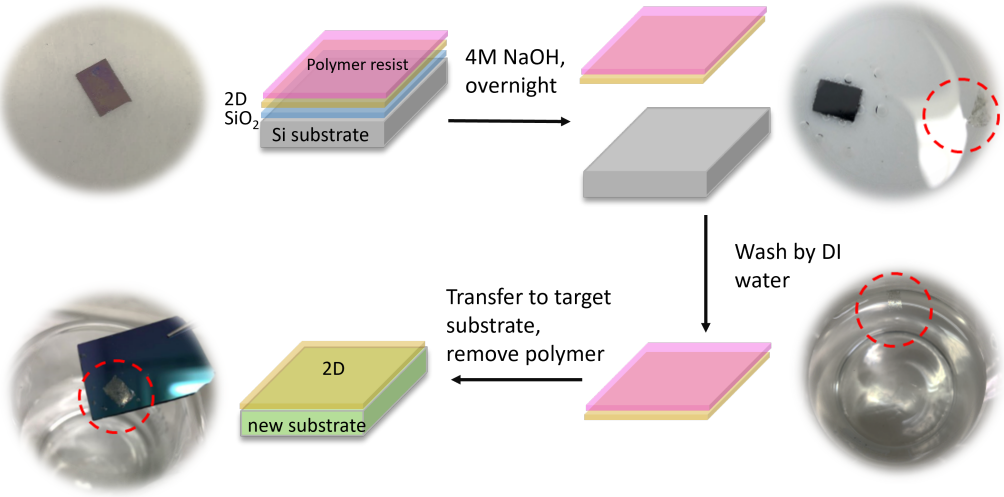


Figure 3.4: **Global transfer process of MoS_2.**

3.2 Device fabrication

This section introduces the techniques used for the fabrication of MoS_2 memristor devices. It begins with the lithography process, a fundamental patterning technique. Next, it covers the dry etching methods necessary for defining device structures. Finally, e-beam evaporation for depositing metal contacts is presented.

3.2.1 Lithography

Photolithography

Photolithography (also named optical lithography (OL) or ultraviolet (UV) lithography) is a widely used method for pattern transfer in semiconductor fabrication. It is crucial to very-large-scale integration (VLSI) and is a mature high throughput manufacturing technology. The process is based on selectively exposing the photoresist, which is a light sensitive polymer. For a positive photoresist, when exposed to light, the chemical structure of the photoresist changes, leading to an increased solubility in the developer solution. This means the exposed areas will be removed during the development process, leaving a pattern that corresponds to the exposed regions. For a negative photoresist, the exposed region has reduced solubility in the developer. Therefore, the exposed areas remain after the development process, and the unexposed areas are removed. Based on different photoresists, there are two routes which can define the same pattern, as illustrated in **Fig. 3.5**. Negative resist will be used when the mask pattern is covered by chromium. In another case, the positive resists should be used when most regions of the mask area are dark, that is light can only pass through several windows where electrodes will be deposited. The resolution of the lithography process is limited by the light diffraction through the mask. The minimum feature size, known as the critical dimension L, is given by the Rayleigh criterion: $L = k\frac{\lambda}{NA}$, where λ is the light wavelength, numerical aperture (NA) is the numerical aperture and k is a process-dependent coefficient with a physical limit of 0.25.

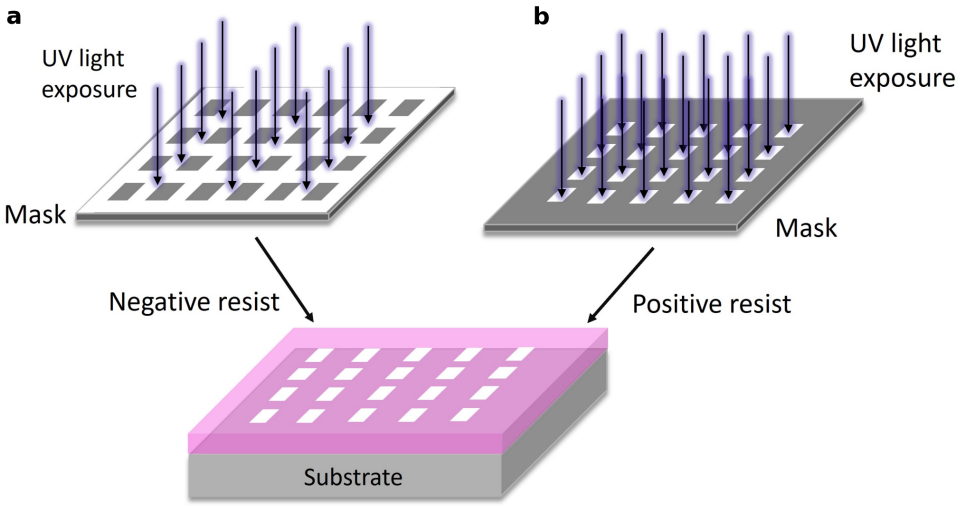


Figure 3.5: **Optical lithography process:** obtaining the same pattern by using (a) negative resist, (b) positive resist.

In this work, photolithography is used for photoresist patterning in both selective growth (chapter 5) and device fabrication (chapter 6). The same procedure is applied for both the purpose of selective growth and device fabrication. Surface cleaning and pre-heating are necessary for defect reduction and photoresist adhesive improvement. The substrates were cleaned by an ultrasonic bath with acetone for 5 minutes and followed by IPA for 5 minutes. Then, the cleaned substrates were dried on a hotplate at 150 °C for 2 minutes to remove volatile contaminants. In this thesis, the word "photoresist" or "resist" represents positive photoresist by default. For a typical lithography process, positive photoresist S1813 (Shipley) is first spun on the dehydrated and cleaned sample for 45 s at 5000 rpm to form a 1.5 μm thick film. The substrate with resist is soft baked at 115 °C for 60 s to partially evaporate the solvents and improve adhesion and uniformity. A mask (with pre-defined device contact areas) will be aligned with the substrate by an OAI mask aligner, and followed by exposure for 6.5 s using a 365 nm UV lamp with a dose of 66 mJ cm^{-2}. The patterns are developed in Microposit MF-319 developer (Shipley) for 45 s, rinsed with DI water, and then hardbake at 90 °C for 90 s.

Laser direct writing (LDW)

LDW lithography is a high-precision lithography device where the UV source is replaced by a laser beam to directly write patterns into the photoresist layer, thereby achieving pattern transfer, with resolution down to 1 µm. The process includes laser beam emission, photoresist exposure, and development. The high energy density laser beam is used to selectively expose the resist, based on a computer aided design (CAD) representation of the mask pattern used in UV lithography. In this way, no physical mask is required.

In this work, LDW lithography is employed for the photoresist (PR) assisted MoS_2 growth, which will be introduced in chapter 5. It provides a high throughput patterning process for sample preparation prior to the CVD process. The experiments were performed using the Heidelberg DWL66 system with a laser wavelength of 375 nm and power of 55.3 mW in Centre for Research on Adaptive Nanostructures and Nanodevices (CRANN) by Dr. Chris Murray.

3.2.2 Dry Etching

Plasma cleaning

Plasma, often termed the fourth state of matter, is a highly ionized gas composed of charged particles, including electrons, ions, and neutral atoms. Distinguished

by its exceptional responsiveness to electric and magnetic fields, plasma processing is critical in semiconductor processes, eg. cleaning, deposition and etching. The generation of plasma typically involves subjecting a neutral gas to a high-energy source, often through the utilization of electrodes within a specialized generator under a low-pressure atmosphere. Through this process, the neutral gas atoms are energetically ionized, liberating electrons and forming a mixture of ions and free electrons within the gas, thus establishing the plasma state. This ionization process may be achieved through various means such as electrical discharge, thermal ionization, microwave or laser excitation, or even through high-energy particle collisions.

Plasma ashing is a technique used in semiconductor manufacturing for removing resist and other organic materials from substrates. It is valued for its ability to uniformly clean surfaces without the need for harsh chemicals. In the photolithography step described earlier, resist residue sometimes arises. For a positive photoresist, ideally, the exposed areas will be totally dissolved by the developer. In reality, a thin layer of resist residue with nanometer scale thickness often remains on the substrate. O_2 plasma is effective for eliminating the thin residual layer of resist in areas post-development process, in a process referred to as a descum. The descum process removes resist residues and organic contaminations, preserving pattern integrity while ensuring a clean interface between the active material and metal electrode.

In this work, a Diener Electronic PICO Barrel Asher is used for substrate cleaning and the resist descum process. The O_2 is used with a power of $\sim$ 120 W (60% of maximum RF power) at a pressure of 0.3 mbar and lasts for 30 s to 10 min upon the sample requirement. Sometimes a cleaning process is required to remove inevitable organic contamination from the TEM specimen. For this purpose, the cleaning process is carried out in the Fischione Instruments 1020 plasma cleaner with a mixture of O_2 and H_2 gas for 30s.

Inductively coupled plasma (ICP)-Reactive ion etching (RIE)

ICP-RIE is a widely used technique that provides high rate, high selectivity and low damage etching. The **Fig. 3.6** (a) illustrates the setup of a typical ICP-RIE system. Source gas is introduced into the chamber from the gas inlet, serving as the plasma medium in the etching process. A radio frequency (RF) power source operating at a typical frequency of 13.56 MHz is connected to the lower electrode. This RIE configuration controls the plasma density (plasma generation) and plasma energy (plasma acceleration), which can obtain an ion density of 10^{10} cm^{-3}.

The applied RF voltage, as shown in **Fig. 3.6** (b), is initially symmetric to 0 V. When a positive RF voltage is applied on the electrode, electrons are attracted to the electrode forming the electron current (I_e). Conversely, ion current (I_{ion}) will formed if a negative RF voltage is applied. Considering the electron is lighter than the ions, electrons are removed faster from the plasma to the electrode than ions, giving a relatively larger current. In the RIE system, the net current (the sum of I_{ion} and the I_e) needs to be zero. In the following periods, to maintain this current balance, the RF voltage develops a so-called "DC bias". The asymmetry RF voltage results in a longer period for I_{ion} and a shorter period for I_e, which gives the integrated current to be zero.

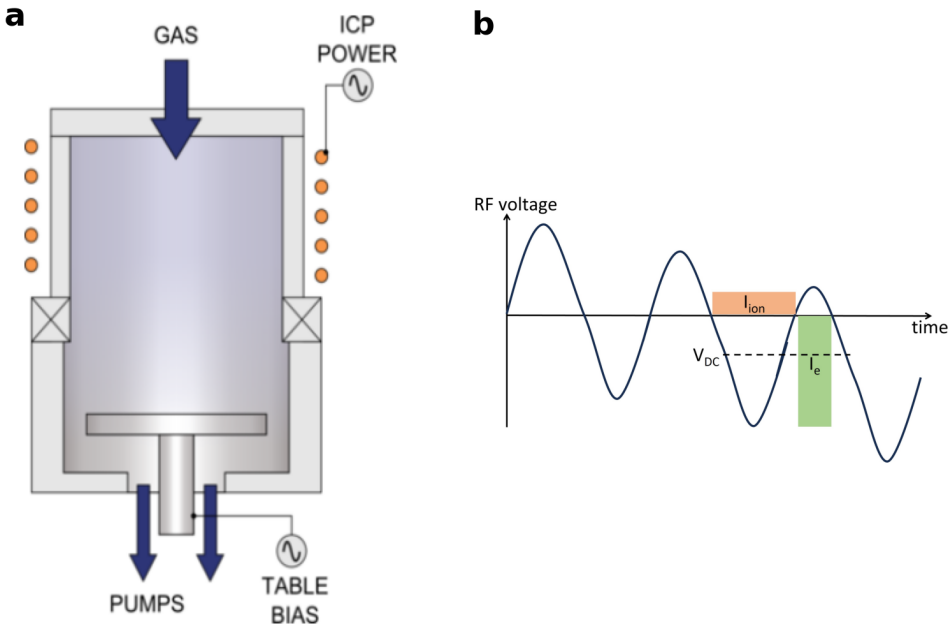


Figure 3.6: **The typical ICP system**. (a) The diagram of a typical ICP system [99]. (b) Origin of the "DC bias".

In the ICP configuration, the plasma density is related to the RF voltage and "DC bias". To decouple the plasma density from the DC bias, a cooled coil is wrapped externally around a Al_2O_3 tube as a second plasma source. This coil is connected to a 3 kW RF generator which is inductively coupled to the plasma, as highlighted by the orange circles in **Fig. 3.6** (a). When RF power is applied, it generates an oscillating electromagnetic field and the magnetic field is coupled inductively to the chamber, where it initiates plasma. Without generating DC bias, it has independent control over the "DC bias" via the electrode, enabling a higher plasma density of 10^{12} cm^{-3}.

To fabricate a large number of devices on a single chip, MoS_2 needs to be iso-

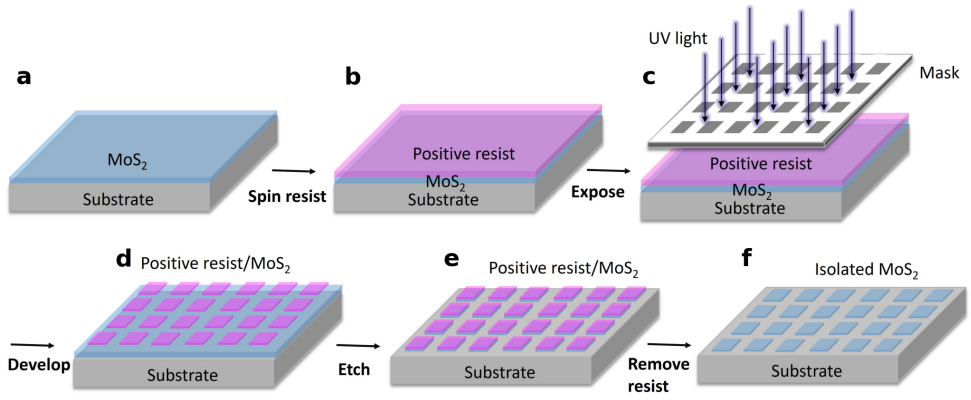


Figure 3.7: **The process of MoS_2 isolation.**

lated into separate islands to avoid electrical stacking between devices. Etching is used to create the required isolation as illustrated in **Fig. 3.7**, the sample is first coated by a layer of photoresist, which is patterned using optical lithography and develop processes to define the etching regions. The exposed areas of MoS_2 are then etched by ICP. Finally, the remaining photoresist is washed away, leaving isolated MoS_2 films on the substrate, which is ready for the devices fabrication. In this work, an Oxford Plasmalab System 100 ICP180 is used for MoS_2 isolation and substrate etching. The tool has a load lock system with a 200 mm lower electrode. For MoS_2 etching, the 1.5 x 1.5 cm^2 substrate is loaded onto a 6-inch carrier wafer, which will be mechanically clamped. Table 3.1 illustrates the etching recipe for monolayer MoS_2. RIE power of 100 W and ICP power of 0 W will be used to etch it with the gas of SF_6 in 20 sccm and Ar in 10 sccm. The monolayer MoS_2 is able to be etched within 30 s. After etching, the sample is immersed in acetone to remove the residual resist, followed by rinsing in IPA and blowing by N_2 gas.

Table 3.1: The etching recipe for monolayer MoS_2 isolation.

RIE power (W)	ICP power (W)	SF_6 (sccm)	O_2 (sccm)	time (s)
100	0	20	10	30

3.2.3 E-beam evaporation

Electron beam (e-beam) evaporation is a physical vapour deposition (PVD) technique for thin film deposition. The schematic of an e-beam evaporation system is depicted in **Fig. 3.8**. In the system, electrons are generated from thermionic emission by heating the filament, which is then accelerated by the accelerator and focused into a beam by a magnetic field generated by coils. The e-beam is

directed towards the source material located in a crucible. When the high-energy e-beam hits the material, it heats the material to the point of evaporation or sublimation. A shutter is positioned above the source to control the deposition. When the shutter is open, the evaporated atoms or molecules travel from the source to the wafer substrate in a vapour phase. The wafer is positioned above and face down to the source, which is typically rotated to ensure uniform deposition across its surface. A quartz crystal microbalance (QCM) deposition monitor is used to measure the deposition rate and the film thickness being deposited. This ensures precise control over the deposition parameters. The entire system operates within a vacuum chamber (typically 10^{-6} Torr), maintained by a vacuum pump. The vacuum environment is crucial to prevent contamination and ensure a sufficient mean-free path for the evaporated atoms, allowing them to reach the wafer substrate without colliding with other molecules.

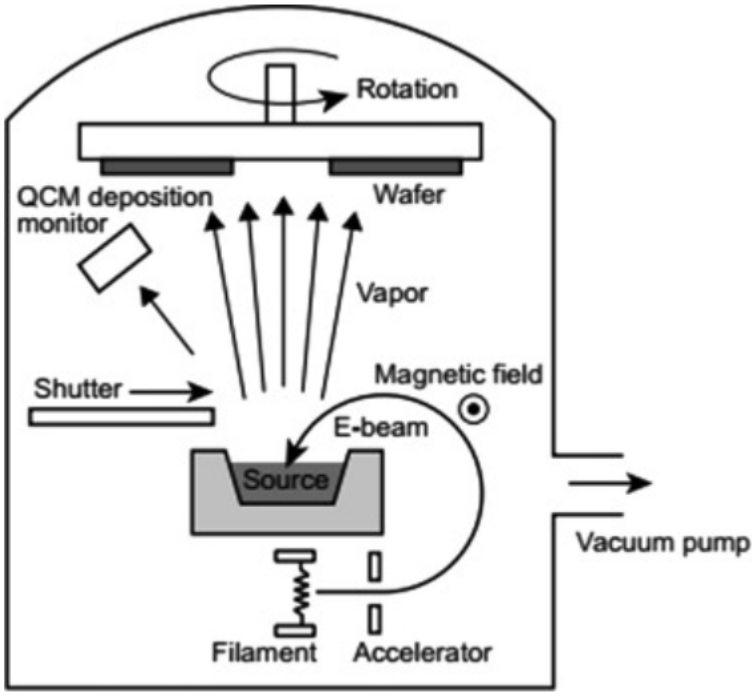


Figure 3.8: **The schematic of electron beam evaporation system.** Adapted from Ref [277].

One of the key advantages of e-beam evaporation is its precise control over the deposition rate and film thickness, achieved by adjusting parameters such as beam intensity, substrate temperature, and deposition time. Additionally, e-beam evaporation enables high deposition rates, excellent film uniformity, and broad compatibility with a wide range of materials, including metals, semiconductors and dielectrics. These characteristics make e-beam evaporation a preferred technique for applications demanding high-quality thin films with precise thickness

control, such as in the metalization of semiconductor devices.

The e-beam evaporation process of this work is carried out in a Temescal FC-2000 system (CRANN). A 6 kW power supply (10 kV, 0.6 A) is employed for the electron beam evaporation process. CT-400 cryopump is engaged to achieve the vacuum of 10^{-6} Torr. The source-to-substrate distance is 27.5 inches. A programmable electron beam sweep controller (Temescal SS64) is applied and allows the user to control the position, amplitude and frequency of the electron beam sweep. The system consists of a 6-pocket electron beam evaporation source containing various materials. In this work, the evaporator will be used to deposit contact metal to the MoS_2 material as shown in **Fig. 3.9**. A film of 1 nm Ti and 35 nm Au will be deposited on the MoS_2 to make metal contact.

After the metallization process, the entire substrate surface is covered by a layer of Ti/Au metal, both the patterned areas and the surrounding substrate. The excess resist along with the excess metal is removed through the lift-off process. During this step, the sample is immersed in acetone or 1165 remover for hours depending on the devices. Ideally, the sacrificial layer (photoresist) is dissolved and lifts away the excessive metal above, leaving behind precisely defined metal contact on the sample. Sometimes, heating is necessary to accelerate this process.

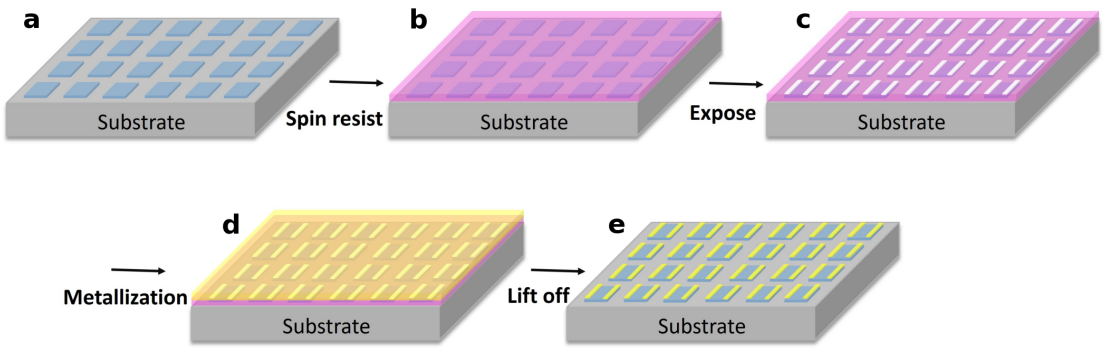


Figure 3.9: **The metallisation process of isolated MoS_2 to fabricate metal contact.**

3.3 Characterisation techniques

This section provides an overview of the characterisation methods used to characterise the material properties and device performance of MoS_2. This includes microscopy techniques for morphological studies, spectroscopy for compositional and structural analysis and thermogravimetric analysis for thermal stability assessments. Additionally, profilometry techniques are discussed for measuring thickness and surface roughness, respectively. Finally, an introduction will be

given to the electrical measurement techniques which are critical for evaluating the performance of MoS_2 based electronic devices.

3.3.1 Microscopy

Optical microscopy

The thickness of 2D layered nanomaterials critically influences their electronic properties, necessitating fast and accurate determination of layer numbers for practical applications. The layer number analysis of 2D material based on optical contrast (OC) is an inexpensive, non-destructive and efficient method. **Fig. 3.10** depicted the optical reflection and transmission in an OC analyze system. The most commonly used 2D semiconductor substrate is a silicon wafer (typically around 500 μm thick) with a dielectric layer (hundreds of nm SiO_2). As the Si wafer thickness is several orders of magnitude larger than the 2D film and SiO_2, it can be considered semi-infinite. When the light from a microscope is incident from the air onto the surface of 2D material, the difference between the intensity of the light that is reflected from the 2D material and that from the bare substrate is called the OC, and is given by:

$$OC = 1 - \frac{I_{2D+Sub}}{I_{Sub}} \tag{2}$$

where I_{2D+Sub} and I_{Sub} are the reflected intensities from the 2D material on the substrate and from the bare substrate, respectively [12, 146].

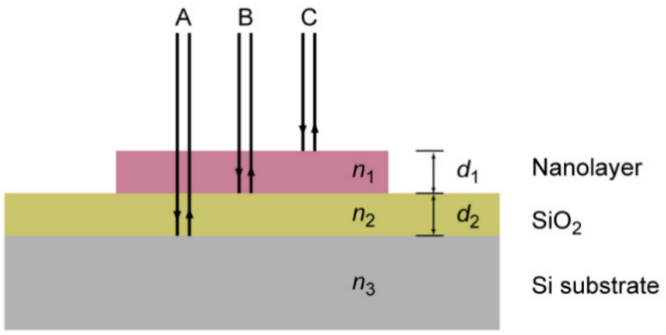


Figure 3.10: **Schematic of optical reflection and transmission for a nano material.** The thickness of the nanolayer is d_1 and refractive index is n_1. The SiO_2 layer characterized by thickness of d_2 and refractive index of n_2 [12].

The reflected light intensity from the surface of the 2D material can be given in eq. (3).

$$I_{2D+Sub} = \left| \frac{r_1 e^{i(\phi_1+\phi_2)} + r_2 e^{-i(\phi_1-\phi_2)} + r_3 e^{-i(\phi_1+\phi_2)} + r_1 r_2 r_3 e^{i(\phi_1-\phi_2)}}{e^{i(\phi_1+\phi_2)} + r_1 r_2 e^{-i(\phi_1-\phi_2)} + r_1 r_3 e^{-i(\phi_1+\phi_2)} + r_2 r_3 e^{i(\phi_1-\phi_2)}} \right|^2 \quad (3)$$

where the relative indices of refraction $r1$, $r2$, $r3$ are:

$$r_1 = \frac{n_0 - n_1}{n_0 + n_1} \quad (4)$$

$$r_2 = \frac{n_1 - n_2}{n_1 + n_2} \quad (5)$$

$$r_3 = \frac{n_2 - n_3}{n_2 + n_3} \quad (6)$$

$n0$, $n1$, $n2$ and $n3$ are the refractive index of the air, nanolayer, SiO_2 and Si, respectively. $\phi = \frac{2dn\pi}{\lambda}$ is the phase shift induced by changes in the optical path. [12]

For the bare substrate, the reflected light intensity can be derived from:

$$I_{Sub} = \left| \frac{r_2' e^{i(\phi_2)} + r_3 e^{-i(\phi_2)}}{e^{i(\phi_2)} + r_2' r_3 e^{-i(\phi_2)}} \right|^2 \quad (7)$$

where $r_2' = \frac{n_0 - n_2}{n_0 + n_2}$ is the relative index of refraction at the interface between air and SiO_2.

From the above equations, it is evident that the OC value is substrate dependent. To identify the optimal conditions for the optical detection of nanolayers, Benameur [12] calculated the OC for MoS_2, WSe_2 and $NbSe_2$ on SiO_2 with varying thicknesses. They found that MoS_2 exhibits the highest contrast on 90 and 270 nm SiO_2. Therefore, a SiO_2 layer with a thickness of 285 nm (close to 270 nm) is selected for this study. **Figure 3.11** exhibits the OC of 1-10 layer MoS_2 on 285 nm SiO_2/Si wafer across the Red, Green and Blue (RGB) channels. This data has been corrected with atomic force microscopy (AFM) measurement by Dr. Yangbo Zhou, a previous postdoctoral researcher in our group. The R-G value is monotonic, making it a reliable variable for OC analysis.

In this work, OC analysis is used to quantify MoS_2 thickness using an Olympus BX51M microscope. The reflected intensities are analyzed by Image J software (version 1.53c, National Institutes of Health, USA). To identify MoS_2 in large areas or multi-flakes, the OC based analysis method is implemented using Python, allowing rapid determination of MoS_2 thickness.

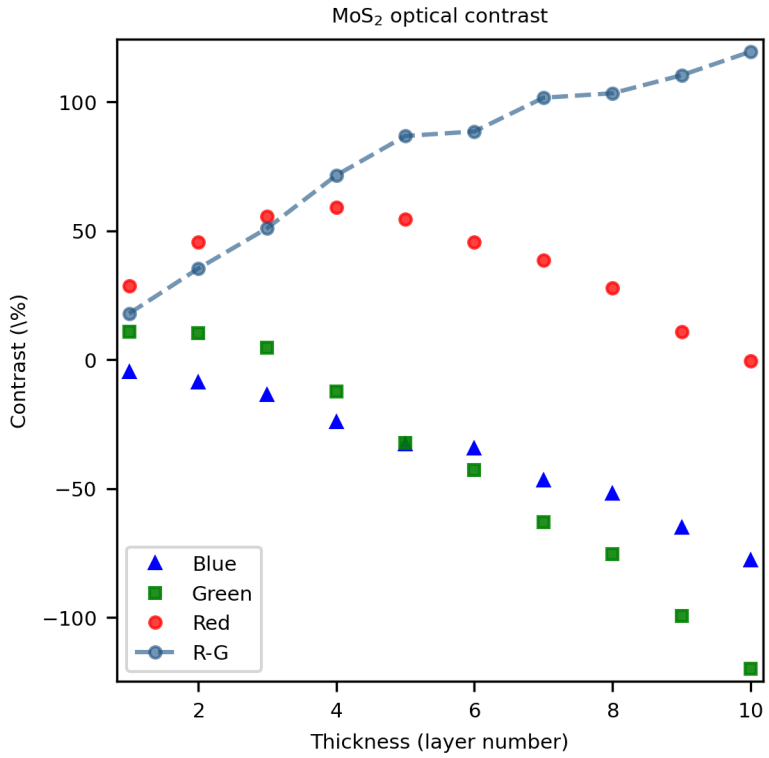


Figure 3.11: **Optical contrast values for MoS_2 on 285 nm SiO_2/Si substrate.** Graph of optical contrast values for the R, G, B channels and R-G as a function of MoS_2 layer number on 285 nm SiO_2/Si substrate.

Atomic force microscopy (AFM)

AFM is a scanning probe microscopy technique developed in the 1980s that allows us to study the surface topography on the nanoscale. The fundamental principle of AFM is based on the interaction forces between a very sharp tip on the end of a cantilever and the sample surface (**Fig. 3.12**(a)). A laser beam is used and focused on the top of the cantilever above the sharp tip, where the reflected laser beam is directed towards a four-quadrant photodetector. When the tip is close to the sample, the atoms at the tip surface interact with the sample surface atoms. The forces between the tip atoms and those surface atoms cause the cantilever to deflect. As the cantilever deflects, the position of the reflected laser beam on the photodetector changes. During a measurement, the tip scans across the sample surface in a raster pattern and the deflection data is collected, allowing the creation of a topographical image of the sample surface.

The interaction force between tip atoms and sample surface atoms is a function of the distance between them as illustrated in **Fig. 3.12** (b). The interaction force, F, follows the well-known Hooke's law:

$$F = -kx \tag{8}$$

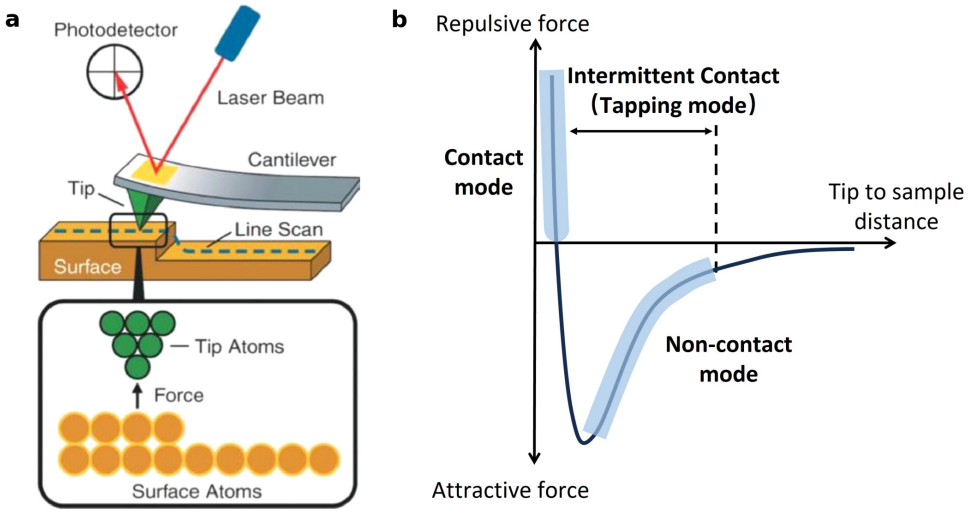


Figure 3.12: **The basic principle of AFM.** (a) Schematic of the basic principle of AFM [108]. (b) The effect of tip-to-sample distance on the force interaction between tip and sample.

where x is the cantilever deflection and k is the spring constant. As the tip approaches close to the sample surface with a separation on the order of a chemical bond (a few angstroms), the repulsive Coulombic force dominates, leading to a deflection of the cantilever. The repulsive force comes from the interaction between the positive nucleus and the overlapping of the electron shells (Pauli principle). In this case, the AFM works under contact mode, where the tip is in contact with the sample surface. While the contact mode allows high-speed scanning, there is a risk of damaging the sample surface. When the tip-to-sample surface separation is increased (several to tens of nm), the Van der Waals force becomes significant. The AFM works in a non-contact mode in this region. In this mode, the tip oscillates at a distance from the surface and thus the risk of sample damage is reduced. When the AFM works in intermittent contact, it is called tapping mode. The tip intermittently contacts the surface and oscillates with sufficient amplitude. The larger amplitude enables higher-resolution atomic topological imaging.

The vertical resolution of AFM is primarily determined by the tip aspect ratio and the system noise level, while the lateral resolution critically depends on the tip features, such as sharpness, shape and material. The key parameters of the AFM probe are as follows:

- Tip sharpness is usually characterized by the radius of curvature at the apex. A sharper tip with a smaller radius of curvature provides higher lateral resolution.

- The aspect ratio of an AFM tip is the ratio of its height to its width. High aspect ratio tips are essential for imaging deep trenches without significant distortion. However, they can be more fragile and prone to bending or breaking. While low aspect ratio tips are more robust, imaging of topography with steep sidewalls is more challenging.
- The tip material affects the tip durability, stiffness, and interaction with the sample. Silicon and silicon nitride tips offer high resolution, while diamond tips are highly durable and suitable for imaging hard surfaces, though they are more expensive. Tips can be coated with various materials for specialized applications (e.g., conductive coatings for electrical measurements). However, it is important to note that the coating increases the tip radius thus may slightly reduce the lateral resolution.
- The cantilever force constant is an important parameter that describes the stiffness of the cantilever in Newtons/meter (N/m). It describes the amount of force required to cause a unit deflection of the cantilever. A low force constant describes a flexible cantilever and an AFM probe with such a cantilever is sensitive to small forces. This is ideal for imaging soft samples. However, it might be susceptible to noise and thermal vibrations, resulting in reduced lateral resolution. Conversely, an AFM probe with a high force constant cantilever has less sensitivity to small force but better control over the tip-to-sample interaction, which is essential for high-resolution imaging of hard surfaces.

In this work, AFM measurements were conducted on the Oxford Asylum system in tapping mode in the CRANN photonics lab, with the assistance of Dr. Jingjing Wang. The AFM probe (Tap150AI-G, BudgetSensors) has a Si tip radius of 10 nm and a height of 17 µm. The AFM cantilever has a force constant of 5 N/m and a resonant frequency of 150 kHz, which has a 30 nm thick aluminium reflective coating layer on the detector side.

Profilometry

Profilometry is a versatile technique used to measure the surface topography of materials, providing information about surface roughness and surface height profile. There are two types of profilometers, stylus and optical-based. The stylus type is used in this work and will be discussed in this section.

In the stylus profilometer system, a probe or so-called "stylus" contacts the sample and is moved along the sample surface. Similar to AFM, the force between the sample and the probe is recorded. The changes of the probe in the Z

direction can then be used to reconstruct the surface topography. The lateral resolution of this technique is dependent on the stylus tip size and shape.

In comparison with AFM, the probe of a stylus profilometer is larger than that of a AFM, and this determines the resolution, which is tens of nm. However, the stylus profilometer has a larger scan region than AFM which is ideal for large and thick samples. In this work, a stylus-type Bruker Dektak profilometer is used to characterize the film thickness when it is higher than 20 nm. The measurement is taken under the stylus force of 1 mg.

Scanning Electron Microscopy (SEM)

As the resolution of a microscope is given by the wavelength of light, the optical microscopes thus give a limit of around 0.2 μm. If the light is replaced by a high energy electron beam with shorter wavelengths, the resolution can be reduced to the nm scale. This led to the development of electron microscopy to achieve higher resolution. The first SEM was developed in 1937 by Manfred von Ardenne and followed by the first commercial SEM instrument by Cambridge Scientific Instrument Company as the "Stereoscan" in 1965. Nowadays, SEM has become a widely used scientific tool providing detailed surface topography and composition analysis.

The wavelength of the electron beam (λ) can be given by the de Broglie wavelength equation:

$$\lambda = \frac{h}{\sqrt{2meV}} \approx \frac{1.227}{\sqrt{V}} \tag{9}$$

where: λ is the wavelength in nm, h is Planck's constant (6.626×10^{-34} Js), m is the electron mass (9.109×10^{-31} kg), e is the elementary charge (1.602×10^{-19} C), V is the accelerating voltage (in V).

In a field emission SEM, as shown in **Fig. 3.13** (a), the electron gun typically consists of a sharp tungsten tip with a radius of curvature on the order of nm is used as the electron source. When high voltage (several kV) is applied between the tip and the anode, the strong electric field (10^7 to 10^8 V/cm) at the tip reduces the potential barrier at the surface, allowing electrons to tunnel through the barrier and escape from the surface and emit a high energy electron beam. The electron beam is accelerated towards the anode by applying an acceleration voltage, which determines the energy of the electrons and the interaction volume in the sample. The accelerated electron beam passes through and is focused by a series of electromagnetic lenses, which are called condenser lenses. The condenser lenses control the beam current and convergence angle, optimizing the

beam for different imaging and analysis modes. In the case of a strong condenser lens, only a small part of the electron beam passes through the aperture reaching the objective lens due to a broader electron beam land on the aperture. The aperture is a thin metal plate with a small hole, which is placed between the condenser lens and the objective lens. Apertures are used to limit the beam diameter and reduce aberrations, ensuring a sharp and well-defined electron beam. The size of the aperture affects the beam current and resolution. A smaller aperture produces finer beams but a lower current. The objective lens further focuses the electron beam and determines the size of the electron probe on the specimen surface. The objective lens is often equipped with a stigmator which corrects the beam astigmatism. The electron beam can be deflected by the scan coils in a raster pattern, enabling the production of a sample topographic image by detecting emitted signals from the sample.

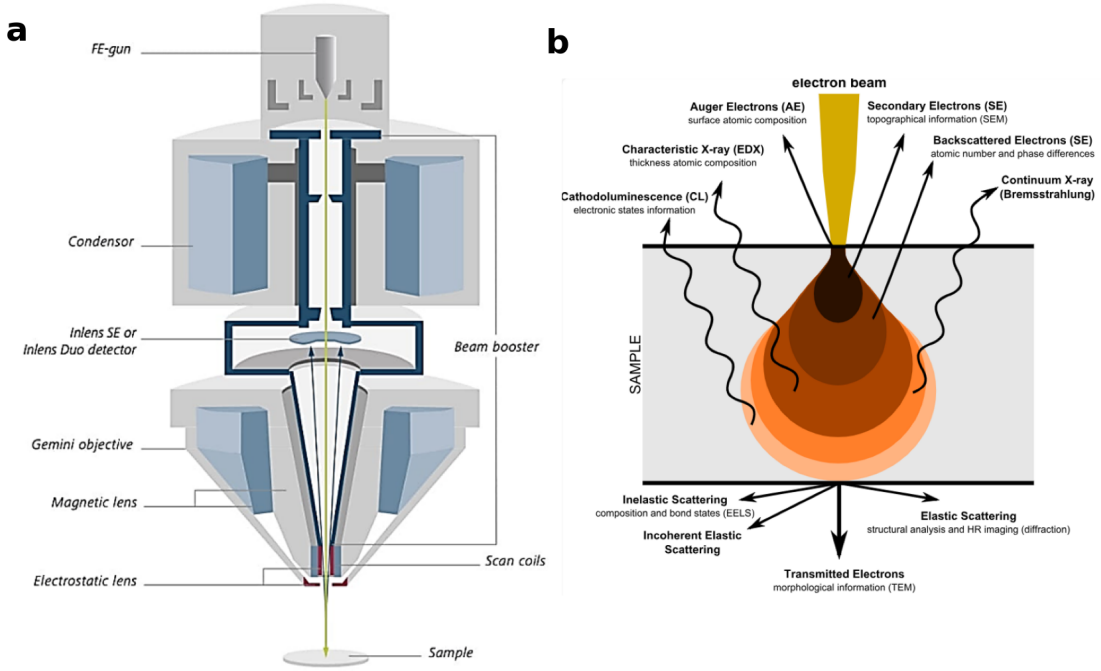


Figure 3.13: **The main components of an SEM instrument and the interaction volume.** (a) The main components of an SEM instrument throughout the column [228]. (b) Interaction volume when an electron beam incident into a sample, also depicting the different types of signals [246].

When the primary electron beam focuses on the sample surface, several interactions occur, leading to the emission of various signals that can be detected and analyzed using various techniques (**Fig. 3.13** (b)). Backscattered electron (BSE) are primary electrons elastically scattered by nuclei. They have higher energy and are ejected from deeper regions within the sample, which gives compositional information. Secondary electron (SE) results from the inelastic interactions between

the primary beam and sample are ejected near the sample surface (a few nm). SE are emitted from the valence electrons with relatively low energy (less than 50 eV), which are surface sensitive and provide high-resolution surface topographical images. Depending on how SE is generated, they can be classified into different types. SE1 electrons are emitted at the point of the primary electron beam [73] incident on the sample surface (1-2 nm), which gives the highest spatial resolution. SE2 electrons are emitted when a BSE leave the sample surface [73]. Due to the energy of BSE, the SE2 leave the sample surface sub-microns away from the position where the primary beam incident. SE2 image provides great overall brightness but reduced resolution. The characteristic X-rays are generated when electron excitation and relaxation happens, which carries elemental composition information and can be used for Energy-dispersive X-ray Spectroscopy (EDX) analysis (see section 3.3.2).

Contrast in SEM images is crucial for interpreting the information conveyed by the specimen signal. A higher contrast is achieved when there is a significant difference in signal intensities between the sample surface and bare substrate. Mathematically, the contrast (C) from the specimen can be expressed by comparing the signal intensity obtained from different points on the specimen: $C = I_1 - I_2$. In SE2 mode, the detector is positioned to the side of the electron column, angled towards the sample to capture the emitted SE2. The image contrast depends on the number of SE2 emitted from the sample. Thus, the edges and features on top of the sample produce more SE2, which corresponds to brighter SE2 images. On the contrary, the bottom of trenches and pits emits fewer SE2 and appears as darker regions in the SE2 images. In a SEM, an InLens detector is inside the objective lens and aligns with the primary electron beam which collects the SE1 signals, as shown in **Fig. 3.13** (a). For the thin layer MoS_2 film, it shows a bright contrast compared with the substrate due to the high escape probability of SE1 from the MoS_2 surface, which is easily detected by the InLens detector. However, it appears darker and less detectable in SE2 mode due to the relatively lower density of SE2 generated from a deeper region of the sample. MoS_2 SE contrast also depends on the film thickness [89] and incident electron beam energy [286]. The electron column optics are optimised to enhance grain boundary visibility (see appendix A.2). We found that an accelerating voltage of 3 - 5 kV is optimum for contrast, and is best suited for imaging the grain structure of few-layer MoS_2.

In our work, SEM images were obtained by using a Zeiss Ultra SEM with a field emission gun in the Advanced Microscopy Laboratory (AML). The SEM images were generally taken under InLens mode with an aperture of 30 µm. The acceleration voltage (0.1 to 30 kV) and working distance were varied according

to the beam sensitivity of the sample and resolution.

Transmission Electron Microscopy (TEM)

When the specimen is thin enough for the electron beam to go through, the transmitted electrons can be collected for TEM analysis. Similar to SEM, a typical TEM system (**Fig. 3.14**) involves the generation of electrons by an electron emission gun. The electrons are then focused by the condenser lenses to form a parallel coherent and high-energy electron beam. The acceleration voltage in a TEM is hundreds of kV, which is much higher than SEM. The high-energy electron beam interacts with the sample, producing transmitted and diffraction signals, which are subsequently collected, amplified, and processed for imaging. TEM provides information on material microstructure with spatial resolutions down to the nm scale. In a bright field image, the contrast is based on mass-thickness and diffraction where heavier or thicker regions appear darker. By precisely controlling the electron optics and aberration correction, an high-resolution Transmission Electron Microscopy (HRTEM) image can be obtained under the phase contrast mode. The contrast in the image is due to differences in the phase of the electron waves scattered by the sample atoms, achieving atomic-scale resolution. This technique is crucial for characterizing the atomic structures, such as grain boundaries, dislocations and phase interfaces.

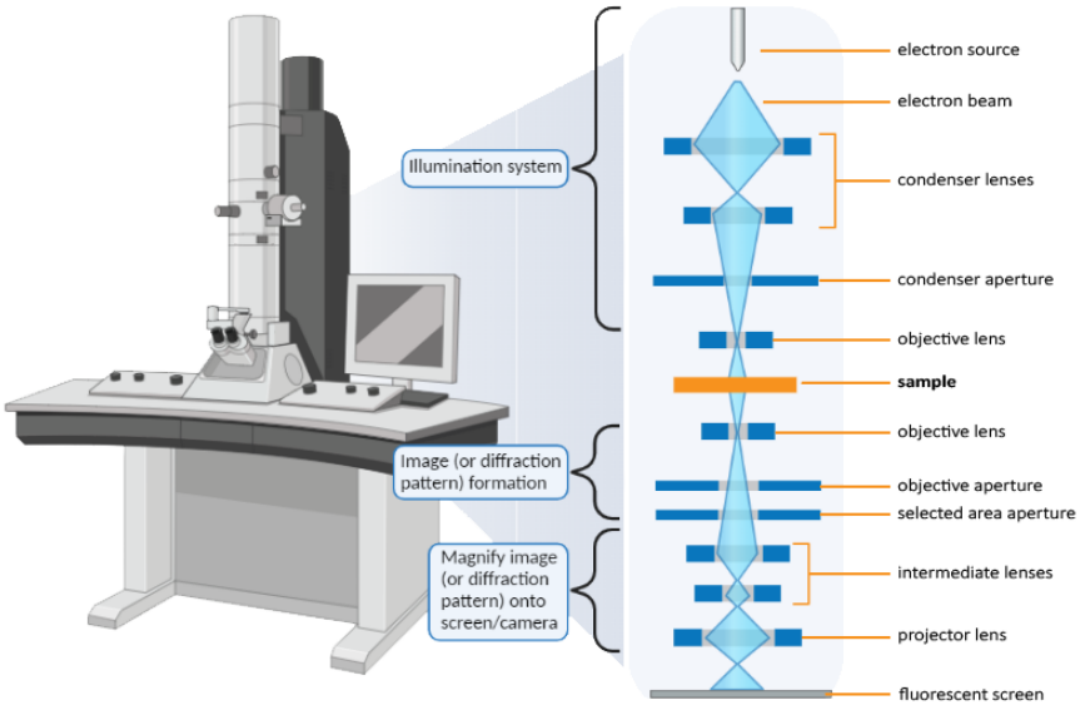


Figure 3.14: **Simplified TEM system highlighting the major components.** [245]

Additionally, by adjusting the lenses within the optical column, the beam can be focused into a probe and scanned across the sample in a raster pattern, which is the Scanning Transmission Electron Microscopy (STEM) mode. Depending on the interaction between electrons and the sample, various signals can be generated and detected by different detectors. An annular dark-field (ADF) detector collects electrons scattered at high angles, providing Z-contrast (based on atomic number variation). The high-angle annular dark-field (HAADF) detector is positioned further out to collect electrons scattered at even higher angles, enhancing Z-contrast and allowing for atomic-resolution imaging. Z-contrast relies on the probability of incident electrons scattering from the atom nuclei, thus it can be interpreted to understand the atomic structure. The bright areas correspond to densely populated scattering centres, which correspond to the higher atomic number. In contrast, the dark region indicates either the absence of atoms, or lighter atoms. This technique greatly facilitates the identification and characterization of the grain boundary (GB), sulphur vacancy (SV) and thickness of 2D materials [229].

When an electron beam is focused in a selected region of the specimen, the electrons interact with the crystal lattice resulting in diffraction. The diffracted electrons form the selected-area diffraction (SAED) pattern. The diffraction pattern consists of a series of bright spots, each corresponding to a specific crystallographic plane, allowing for the identification of the crystalline phase, crystal structure and crystal symmetry. Unlike traditional SAED, which uses a parallel electron beam to produce diffraction patterns, convergent beam electron diffraction (CBED) employs a convergent electron beam that is focused on a small probe size, resulting in a diffraction pattern of a highly localized region (a few nm). The convergent beam illuminates a small area of the sample, producing discs of intensity in the diffraction pattern rather than discrete spots. The larger convergence angle of the beam leads to more detailed diffraction patterns, providing more comprehensive information on the local structure.

Figure 2.1 (a) [229] shows the typical high-resolution ADF-STEM image of MoS_2. From the basal plane view of the atomic structure, it is clearly observed that the molybdenum atoms and sulphur atoms are arranged in a hexagonal pattern. **Figure 2.1** (b) [229] shows the corresponding dark field TEM image of MoS_2, obtained by using an aperture to select a narrow range of the diffracted beam. The dark field TEM image filters the crystallographic orientation [19, 90, 91], highlighting the single crystals. The inserted diffraction pattern exhibits six-fold rotational symmetry around the centre spot, indicating a highly crystallized hexagonal lattice structure [229, 267].

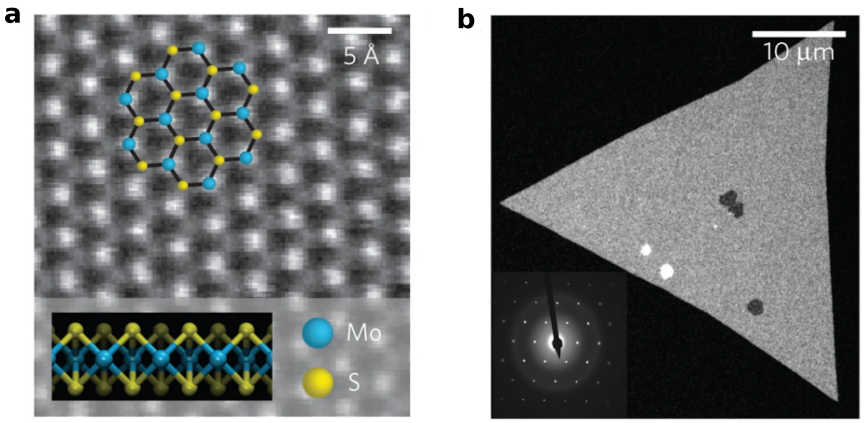


Figure 3.15: **Atomistic configuration of MoS_2.** (a) High-resolution ADF-STEM image and (b) dark field TEM image of MoS_2 with the diffraction pattern inset [229].

As the electron beam penetration is limited, the thickness of TEM samples is usually thinner than 100 nm. The TEM, SAED and CBED measurements were performed with an uncorrected FEI Titan microscope with a Schottky field emission S-FEG source operated at 300 kV. The aberration-corrected scanning transmission electron microscopy (ACSTEM) were performed on a Nion UltraSTEM 200 microscope equipped with a cold field emission gun and a quadrupole-octupole type probe corrector. The results are obtained with the assistance of Dr. Xuyun Guo and Dr. Danielle Douglas-Henry.

3.3.2 Spectroscopy

Energy-dispersive X-ray Spectroscopy (EDX)

EDX is a non-destructive tool to provide qualitative and semi-quantitative elemental analysis with high sensitivity and spatial resolution. It is usually combined with other microscopy techniques such as SEM and TEM to provide comprehensive structural and chemical information. **Fig. 3.16** (a) illustrates the fundamental principles of EDX. When a focused beam of high-energy electrons bombard the sample, they interact with the sample atoms, transferring energy to the inner shell (K-shell, L-shell, M-shell) electrons. The high-energy electrons from the incoming e-beam can knock out inner-shell electrons from their orbits creating vacancies, which is called excitation. To fill these vacancies, electrons from higher energy levels drop down to the lower energy level vacancy which is called relaxation. This process results in the emission of characteristic X-rays. The energy of the emitted X-rays is characteristic of the specific element because the energy difference between the electron shells is unique for each element. When

an electron transit from the L-shell to the K-shell, the released X-ray is called K_α. When an electron transit from the M-shell to the L-shell, the released X-ray is called L_α.

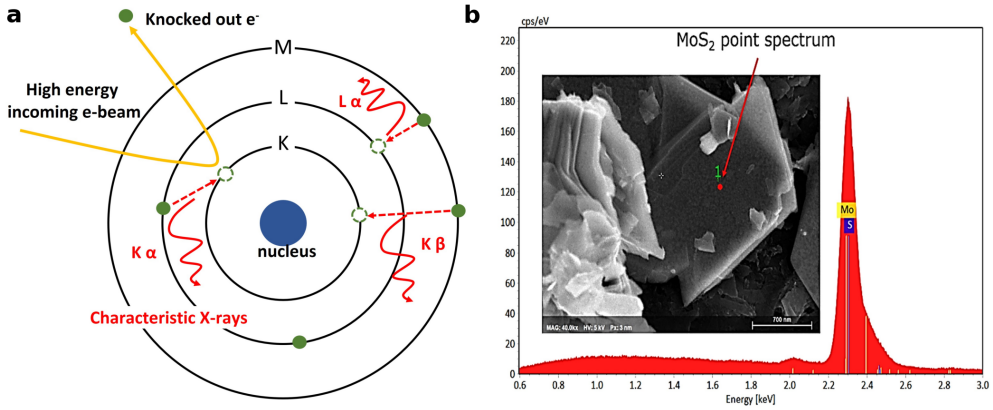


Figure 3.16: **The fundamental principle of EDX process and typical EDX spectrum of MoS_2.** (a) The fundamental principle of EDX process. (b) Typical EDX spectrum of MoS_2 [20].

The characteristic X-rays are detected using an EDX detector (typically composed of a semiconductor material). X-rays ionise the detector material and generate charges (electrons and holes) which are separated by the biased electrode. The generated electrical signals are proportional to the energy of the detected X-rays, which are then processed to create an energy spectrum displaying peaks corresponding to the emitted X-ray energies. By analyzing this spectrum, the element component and their relative concentrations can be identified. **Fig. 3.16** (b) shows the typical EDX spectrum of MoS_2. The spectrum background is mainly contributed by the Bremsstrahlung (from the German word "braking") radiation. It originates from the energy loss of the decelerated incoming electrons due to the Coulomb forces from the nuclei. Bremsstrahlung X-rays have a broad range of energies, resulting in a continuous spectrum background. The intensity follows Kramers' law:

$$I(\lambda)d\lambda = \frac{K}{\lambda^2}\left(\frac{\lambda}{\lambda_{\min}} - 1\right)d\lambda \tag{10}$$

where λ is the wavelength of the emitted photon, $\lambda_{min} = \frac{hc}{eV}$ is the minimum wavelength determined by the maximum energy (equals to the incoming beam energy) and K is a constant that depends on the atomic number of the target material and the energy of the incoming electrons. For MoS_2, the S K_a (2.307 keV) and Mo L_a (2.293 keV) energy are very close results in the overlapping peak in the EDX as shown in **Fig. 3.16** (b), which make it challenging to dissolve the two peaks and impedes the analyze of these element. In this case, a higher energy e-beam is required to observe other peaks (e.g. Mo K_a at 17.441 keV) as a reference

to analyse the overlapping peaks. In addition, EDX simulation can also help to build the model, fit the spectrum and dissolve the overlapping peaks.

In EDX mapping, a single spectrum is collected at each pixel of an SEM or TEM image. By scanning across different pixels, a series of spectra is obtained, creating a comprehensive EDX map of the scanned region. When a filter with a specific energy range is applied, EDX map can visualize the relative concentration of a given element. The spatial resolution of EDX is constrained by the interaction volume, while the accuracy of quantitative analysis can be influenced by the instrument calibration and matrix effects (where the presence of other elements affects the detection and quantification of the target element). Despite these limitations, EDX mapping remains an invaluable tool for understanding the elemental composition and distribution within materials, especially when combined with other imaging techniques for comprehensive material characterization.

In this work, the EDX data was collected using the *Bruker Nano XFlash* 5030 detector integrated with the *Zeiss Ultra* SEM. To complement the experimental results, EDX simulations were performed using *CASINO* software, providing a deeper understanding of the elemental composition and distribution within the sample.

Electron energy loss spectroscopy (EELS)

EELS is a technique commonly used in TEM to analyze materials in complementary to EDX. Different from EDX, EELS is based on the primary electron energy analysis. When high energy incident electron beams are transmitted through a TEM specimen, as shown in **Fig. 3.17** (a) the majority of the electrons undergo elastic scattering without energy change. However, some electrons experience energy loss due to inelastic scattering and are mainly focused within a small angle range from the incident beam direction, which can be easily collected by the detector and used for EELS analysis. The energy loss of primary electrons is characteristic of the elemental composition, chemical bonding, and electronic structure of the elements in the specimen. **Fig. 3.17** (b) illustrates the energy loss of an electron and the generation of EELS signal. E_0 represents the primary electron energy and ΔE denotes the energy loss of the electron after interaction with the electron in the K subshells of the sample.

EELS spectrum typically features distinct regions. The zero energy loss originates from elastically scattered electrons and can be utilized for thickness analysis. The plasmon peaks can provide information about valence and conduction electron density. The low energy region (up to 50 eV) is called the low-loss region

which corresponds to interband transitions and plasmas [202], reflecting the information of the sample optical properties. The core-loss region is when energy is higher than 50 eV and can be up to a few keV, resulting from electrons undergoing energy losses due to the ionization of inner shells to the empty states of the conduction band. The absorption edge position in this region provides information on elemental composition, concentration, and bonding or valence states [51].

The EELS data presented in this thesis was acquired by Dr. Xuyun Guo using the *FEI Titan 80-300* TEM, operated at a beam energy of 300 keV and equipped with a *Gatan* detector.

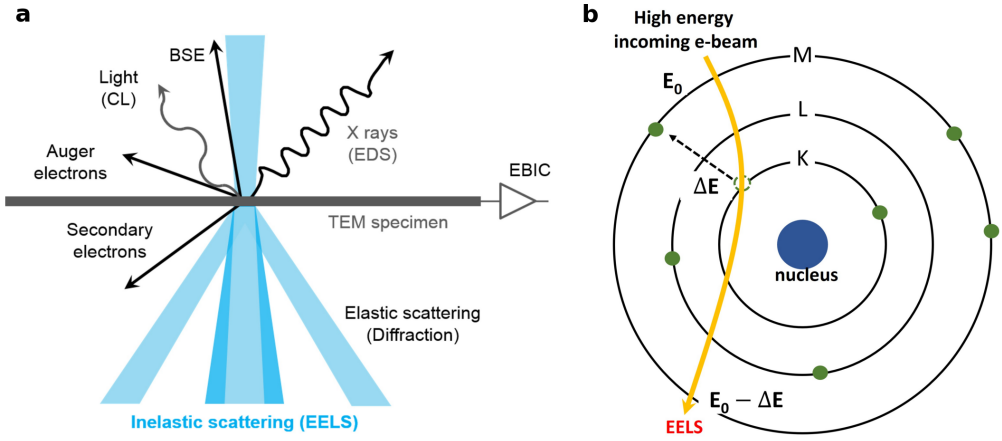


Figure 3.17: **TEM specimen beam interactions and the energy loss of incident electrons.** (a) TEM specimen beam interactions. Adapted from [51]. (b) The energy loss of incident electrons.

X-ray photoelectron spectroscopy (XPS)

XPS, also known as Electron Spectroscopy for Chemical Analysis (ESCA), is a widely utilized technique for analyzing surface composition based on the principles of the photoelectric effect. **Figure 3.18** (a) illustrates the experimental setup and process for XPS. In the aluminium anode, when electrons bombard the anode, it will generate the aluminium Kα X-ray. The X-ray is filtered by the monochromator and focused into a monochromatic beam, ensuring the specific energy when reaching the sample surface. The incident X-ray photons with energy of hv (v is the frequency) irradiate the sample and interact with the inner-shell electrons of the surface atoms. These photons provide enough energy to excite the inner-shell electrons, causing them to surpass the atomic binding energy (E_b) and escape from the atom with certain kinetic energy (E_k) and become what is known as photoelectrons. The emitted photoelectrons are collected and directed into a hemispherical analyzer, which separates the photoelectrons based

on their kinetic energy. The kinetic energy of the photoelectrons is related to their E_b in the material, which is characteristic of a specific element and its chemical states. The detector counts and measures the energy of these photoelectrons, creating a spectrum that shows the number of electrons versus their E_b. The E_b is the difference between final energy state E_f and the initial state E_i of the atom, given by:

$$E_b = E_f - E_i = h\nu - E_k \tag{11}$$

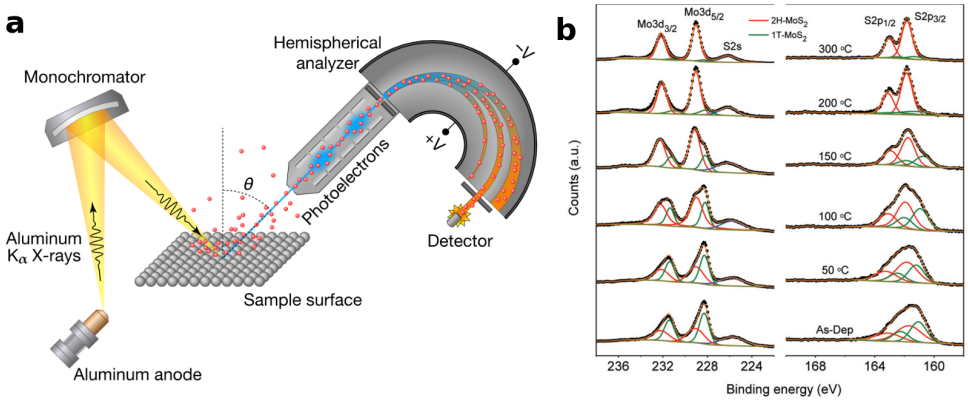


Figure 3.18: **The diagram of XPS process and typical XPS spectra of MoS_2.** (a) The diagram of experimental setup and process for XPS [255]. (b) XPS spectra of Mo 3d, S 2s and S 2p core level peak regions for MoS_2 annealed at various temperatures, with Shirley background subtraction [50].

Figure 3.18 (b) shows XPS spectra of Mo 3d, S 2s and S 2p core level peak regions for MoS_2 annealed at various temperatures, with Shirley background subtraction. In 2H-MoS_2, the Mo 3d spectra consist of peaks at around 229 and 232 eV that correspond to Mo^{4+} $3d_{5/2}$ and Mo^{4+} $3d_{3/2}$ components. The doublet peaks of S 2p are at 163 and 161.9 eV for S $2p_{1/2}$ and S $2p_{3/2}$, respectively. Additional peaks at higher energy regions can be found for lower annealing temperature samples as marked in green lines, which arise from the 1T-MoS_2. [50]

In this work, XPS measurements were conducted using an *Omicron EA 125 Energy Analyzer* (at CRANN, by Dr. Lee Gannon), equipped with a monochromated Al K-alpha source operating at 1486.7 eV. High-resolution core-level XPS scans were acquired in high magnification mode with a pass energy of 20 eV. The entrance and exit slits measured 6 mm and 3 mm, respectively, yielding an overall source and instrument resolution of 0.6 eV. The XPS spectra were calibrated to the adventitious carbon C 1s peak at 285 eV [118], and were analysed using *CasaXPS* software, with assistance from Dr. Lee Gannon and Prof. Cormac MacGuinness, employing a Shirley background subtraction for fitting.

Raman spectroscopy

Raman spectroscopy is a fast and non-destructive characterization method to detect material properties. It was first observed by an Indian physicist C. V. Raman [188] in 1928. Because the vibrational energy levels are specific to the molecular structure, the Raman spectrum is unique for each molecule, so it is also called 'fingerprint'.

In a typical Raman system, when a monochromatic laser is focused on the sample, the photon energy is transferred and absorbed by the molecule, leaving it in a higher energy state. This state is called a virtual state, as shown in **Fig. 3.19** (a). The classical theory for the origin of the Raman effect is shown in **Fig. 3.19** (b). [38] The oscillating electromagnetic field of the photon will drive the molecular electrons to oscillate. The electrons will be polarized and generate an induced dipole moment, leading to a built-in electric field. Additionally, the lattice vibration of the molecule, although it is much lower than the external electric field oscillation, will modulate the amplitude of the induced dipole moment oscillation from the molecular contracted state to the stretched state. (**Fig. 3.19** (b)).

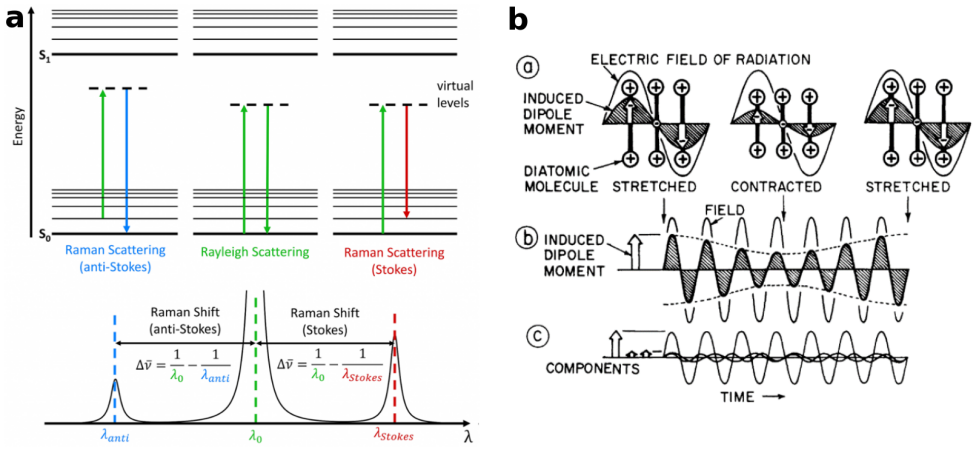


Figure 3.19: **Raman scattering process and the origin of Raman effect.** (a) Jablonski Diagram showing the Raman scattering process [98]. (b) Classical theory for the origin of the Raman effect. Diatomic molecule where "+" represents protons and "-" represents the centre of gravity of the electrons [38].

The virtual state with high energy is not stable, the photon is re-emitted almost immediately as light. The majority of the re-emitted photons are elastically scattered by the molecules without changing their energy, which remains the same wavelength as the incident photons. This dominant process is called Rayleigh scattering. Only a minority of photons (approximately 10^{-7} of incident photons) [212] are inelastically scattered by the sample, which contributes to the Raman scattering with energy shift from the incident photons. The scattered photons

will lose energy with increased wavelength or gain energy with decreased wavelength, which corresponds to the Stokes Raman scattering and anti-Stokes Raman scattering, respectively. (**Fig. 3.19**(a)) The possibility of Stokes and anti-Stokes scattering is quantum mechanically equal. However, most molecules keep in the ground vibrational level at room temperature. Thus, Stokes scattering is more likely to occur, resulting in a stronger intensity than the anti-Stokes. In the Raman system, a Rayleigh rejection filter only allows the Raman scattering signal to pass towards the confocal pinhole. The confocal pinhole ensures the signal comes from the target depth, and enables a depth independence measurement. The filtered signal will finally be injected into the spectrometer, dispersed by the grating, and the intensity of the light will be counted for different wavelengths.

The wavenumber is the frequency divided by the light speed, which is the reciprocal of wavelength with the unit of cm^{-1}, $\tilde{\nu} = \frac{\upsilon}{c} = \frac{1}{\lambda}$ [61]. The Raman shift in cm^{-1} describes the wavenumber shift between incident excitation light and scattered light, written as:

$$\Delta\nu = \frac{1}{\lambda_0} - \frac{1}{\lambda_1} \tag{12}$$

where λ_0 is the wavelength of incident laser and λ_1 is the Raman wavelength in nm. The Raman shift reflects the phonon modes of the crystal and thus can be used to analyse the crystal structure. The limit of detection (LOD) depends on the instrument (e.g., laser power and wavelength, spectrometer resolution, signal-to-noise ratio), the operation (e.g., integration time, focus) and the sample properties. The LOD can be calculated by $\frac{3.3 \times \sigma_{bg} - a}{b}$ [238], where σ_{bg} represents the standard deviation of the background, a and b represent the intercept and slop of the linear fits for each spectral resolution, respectively. The LOD is typically in the micromolar to millimolar range [210, 238].

Raman spectroscopy has been popularly used to study the quality and layer number of 2D material. **Fig. 3.20** (a) depicts the four typical Raman modes of bulk MoS_2 crystal. E^1_{2g} (at $\sim$ 383 cm^{-1}) and A_{1g} (at $\sim$ 408 cm^{-1}) are two first-order Raman modes of MoS_2, indicating the in-plane and out-of-plane vibration modes, respectively. Usually, the E^2_{2g} and E_{1g} modes are silent due to selection rules for our scattering geometry. [231] The thickness-dependent Raman spectra of MoS_2 are shown in **Fig. 3.20** (b). When the MoS_2 thickness decreases, E^1_{2g} peak exhibits a regular blue shift while A_{1g} shows an opposite red shift. For monolayer MoS_2, E^1_{2g} and A_{1g} peaks locate at the $\sim$ 384 cm^{-1} and $\sim$ 405 cm^{-1}. The peak frequency difference between E^1_{2g} and A_{1g} also shows a clear decreasing trend as a function of layer number (**Fig. 3.20** (c)). The frequency spacing is about 19 cm^{-1} for monolayer MoS_2 and increases to 25 cm^{-1} for bulk MoS_2 [125]. In addition, the

longitudinal acoustic (LA) mode refers to the longitudinal acoustic phonon mode where atoms move parallel to the direction of the phonon propagation which is enhanced in the resonant Raman scattering.

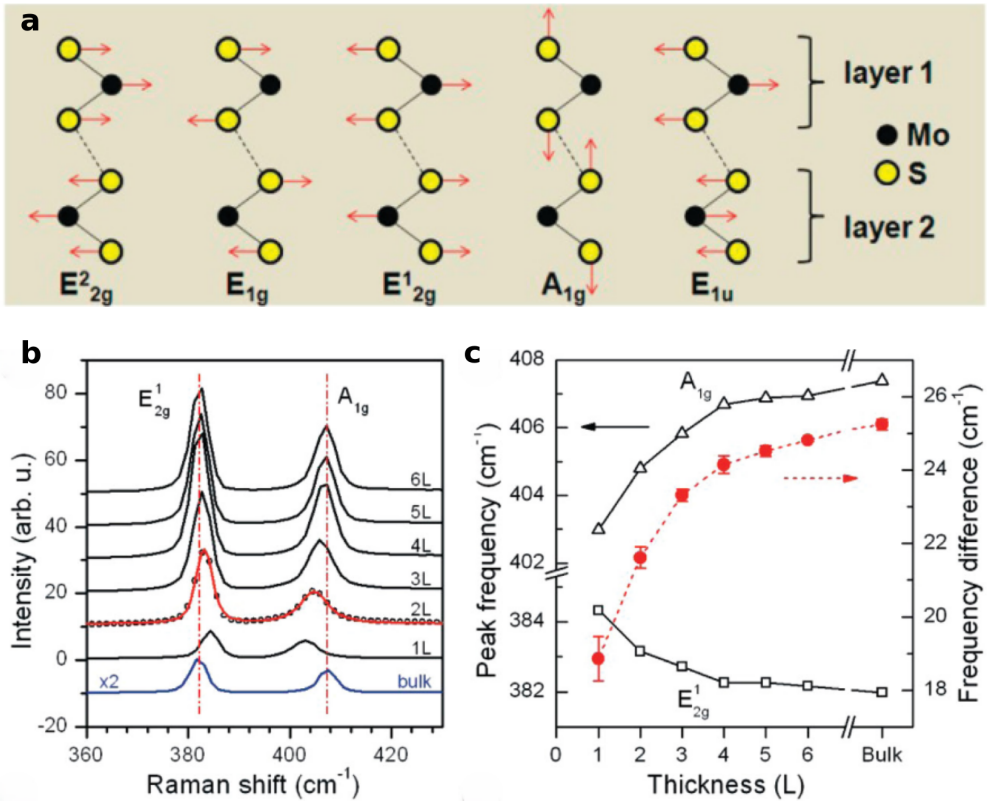


Figure 3.20: **Typical Raman active modes of MoS_2.** (a) Atomic displacements of the four Raman active modes and one IR-active mode (E_{1u}) in the unit cell of the bulk MoS_2 crystal as viewed along the [1000] direction. (b) Raman spectra of MoS_2 for different thicknesses. (c) Frequencies of the first-order Raman modes as a function of layer numbers. Adapted from [125].

The Raman spectra and mapping in this work were primarily collected by the Witec Alpha 300R system. The data were analysed with WITec Project 5.0 software and custom Python scripts. In some cases, Raman spectra were acquired using a Renishaw InVia Raman spectrometer in the Photonics Lab in CRANN, with the assistance of Dr. Jingjing Wang and Dr. Yunhong Shi. The measurements were typically performed using a 532 nm excitation laser with a power of 4.4 mW, employing a grating of 1800 lines/mm, a $\times 100$ microscope objective lens and 10 acquisitions per second. In certain experiments, a 633 nm laser was which will be specified along with the corresponding result discussion.

Photoluminescence spectroscopy (PL)

PL spectroscopy is a non-destructive and highly sensitive analytical technique that is widely used in materials science to explore material properties. When

atoms in a sample absorb photons of a certain energy, electrons transit from the valence band to the conduction band energy level, creating holes in the valence band. The electron-hole pair is termed an exciton. As the quasi-equilibrium state electrons relax and recombine with the hole, energy will be released in the form of a photon. The light emitting excited by external photons is called PL, as the schematic diagram shown in **Fig. 3.21** (a). Depending on the lifetime of the PL signal after removal of the incident light, it can be classified into fluorescence and phosphorescence, where the first case lasts less than 10 nanoseconds and the latter longer than 10 nanoseconds.

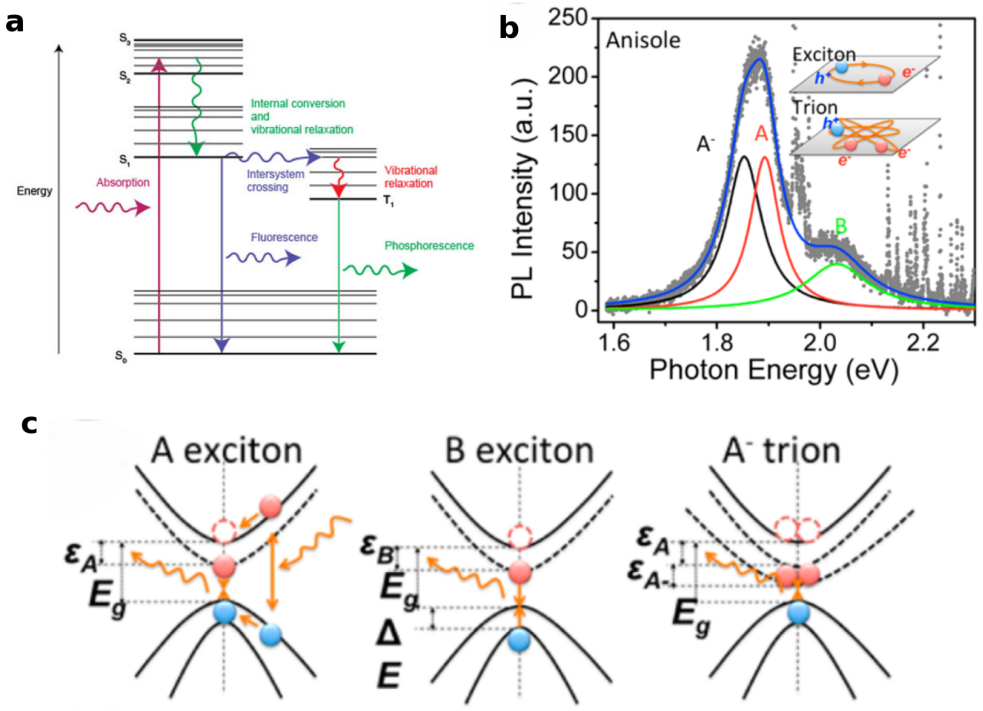


Figure 3.21: **The PL process and typical PL spectrum of monolayer MoS_2.** (a) The diagram of the PL process. (b) Typical PL spectrum of monolayer MoS_2. (c) Schematics of the exciton-related radiative transition at the K-point in the Brillouin zone. Figures are adapted from [150, 190].

However, it is essential to distinguish the optical bandgap from the electronic bandgap. Excitonic effects [189] play a crucial role in determining the optical bandgap of monolayer MoS_2. When an electron in the valence band absorbs energy, for example from a laser, and transitions to the conduction band, it leaves behind a positively charged hole. The electron and hole can bind together due to Coulomb attraction, forming a quasiparticle known as an exciton. This binding energy results in an optical bandgap that is slightly lower than the electronic bandgap because less energy is required to create an exciton compared to generating free electron-hole pairs [120].

The PL spectrum represents the emitted light intensity distribution over wavelengths, where the light wavelengths vary with material-specific characteristics. **Figure 3.21** (b) shows the typical PL spectrum of monolayer MoS_2. The bulk MoS_2 is an indirect bandgap semiconductor that exhibits a weak fluorescence effect. However, monolayer MoS_2 becomes a direct-gap semiconductor emitting an A exciton at approximately 1.85 eV. Additionally, B exciton at around 2 eV gives rise to a spin-orbit coupling of the energy band, which causes an energetic offset and a less-intense emission [216]. This phenomenon results from the splitting of the valence band by approximately 150 meV at the K-points in the Brillouin zone, caused by the interaction between the electron spin magnetic moment and its moving orbit's magnetic field [53]. Trions are charged excitons that two electrons are paired with one hole(**Fig. 3.21** (c)) or one electron is paired with two holes [110, 169].

The emission energy, intensity and full width at half maximum (FWHM) of the PL spectrum reflect the alterations in the band gap energy, quality of the crystal lattice, defects and other phenomena. In addition to MoS_2 thickness, the PL characteristics of MoS_2 are significantly influenced by lattice strain [158, 209], doping [169], and gate voltage [162].

The advantage of this technique is that it can be integrated with the Raman measurement system. It allows us to characterise the Raman and PL at the same time by simply changing the unit and range. The PL spectrum and mapping in this work were conducted via the WITec system with a laser wavelength of 532 nm.

X-ray diffraction (XRD)

XRD is a non-destructive technique to evaluate the crystalline structure, including the degree of crystallinity, the ratio of crystalline to amorphous phase, crystal size, the arrangement pattern of crystals and the distance between the planes of the crystal. In XRD system, the X-rays are generated by bombarding a metal target (typically copper) with high-energy electrons. When monochromic X-ray irradiates the crystalline sample, they are diffracted by the crystal planes. The electrons in the crystal vibrate in response to the periodically changed electric field. The diffracted X-rays interfere with each other, creating a pattern that can be detected and analyzed.

The condition for constructive interference that can be detected as a diffraction

peak follows Bragg's Law (**Fig. 3.22** (a)): eq. (13),

$$2d_{hkl} \sin\theta = n\lambda \tag{13}$$

where d_{hkl} is the distance between crystal planes, θ is the angle between the incident X-ray and the sample surface, n is the order of the diffraction and λ is the wavelength of the incident X-ray. It describes the relation between the diffraction peak and the crystal structure. Only when θ satisfies Bragg's Law, the diffraction peak can be detected as a diffraction pattern.

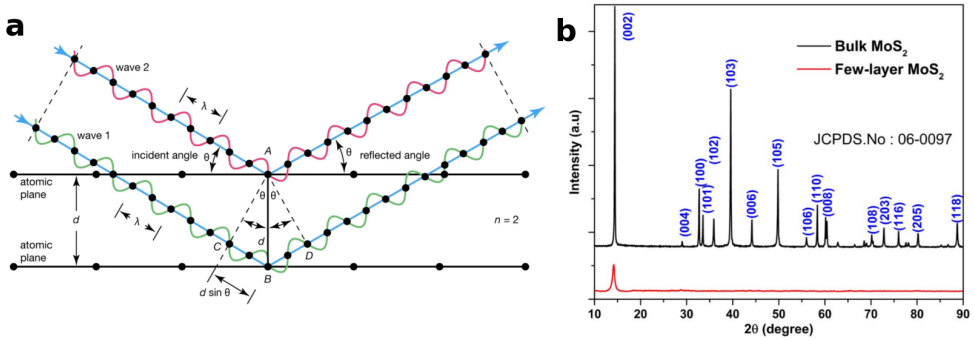


Figure 3.22: **Diagram of Bragg's Law and XRD spectra of MoS_2.** (a) Diagram of Bragg's Law for 2nd order (n=2) diffraction [18]. (b) XRD spectra of bulk and few-layer MoS_2 [198].

The typical XRD spectra of bulk and few-layer MoS_2 are shown in **Fig. 3.22** (b). The spectrum of bulk MoS_2 (black) indexed to rhombohedral MoS_2 (JCPDS No: 06-0097). For few-layer chMoS2, the strong peak at 14° indicates the material is highly oriented in [002] planes.

In this work, all the XRD measurements were performed using a *Bruker D8 Advance* diffractometer (at CRANN) equipped with a copper anode with an excitation wavelength of 1.5406 Å.

3.3.3 Thermal analysis

Thermo-gravimetric analysis (TGA)

TGA is a technique used in materials science and chemistry to analyze material thermal behaviour, by recording the mass changes under controlled atmosphere conditions. In TGA, a sample is heated to the setting temperature, typically in an inert atmosphere to prevent reactions with oxygen or other gases. During the heating process, the sample weight changes due to various processes such as decomposition, desorption of volatile components, oxidation, or reduction reactions. These weight changes are monitored by a highly sensitive balance with

high precision. The TGA plot gives the sample mass as a function of temperature or time, which provides information about the thermal stability, composition, purity, and kinetics of decomposition or reaction processes occurring within the sample.

In this thesis, TGA is used to characterise the thermal behaviour of promoter polymer, which will be discussed in chapter 4. The TGA thermal analysis was performed using a *Stanton Redcroft STA 1500* (Thorn Scientific, UK) calorimeter with platinum-rhodium crucibles and alumina as a reference. The experiments were carried out with a heating rate of 10 °C/min in N_2 atmosphere and conducted by Dr. Aran Rafferty (School of Chemistry, TCD).

3.3.4 Electrical measurement

Electrical measurement of two-terminal devices

In chapter 6, the MoS_2 memristor devices are fabricated to facilitate the analysis of electrical performance. The electrical measurement was conducted using a probe station combined with an optical microscope. The measurement system, configured with a two-probe setup, is schematically shown in **Fig. 3.23**. A Keysight B2912A source measurement unit is utilized to supply a voltage or current source and measure the output voltage and current spontaneously. The source meter is connected to two miBot probes (Imina Technologies) via coaxial cables. The miBot probes, equipped with 1 *mu*m sharp tips, facilitate precise contact with the micron-scale electrode pads on the device. One of the probes is connected to the bias output, while the other one is connected to the ground (GND).

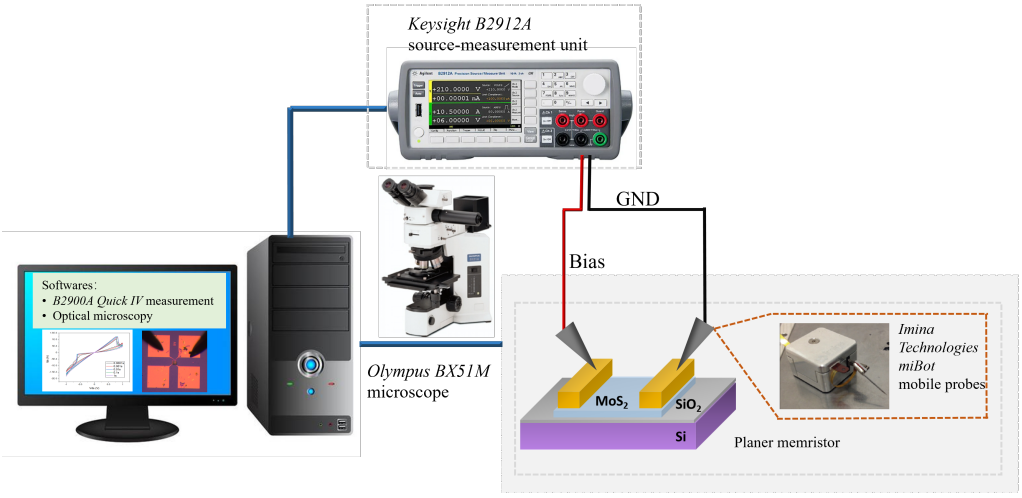


Figure 3.23: **Flow chart of two-probe configuration for performing electrical characterisation of MoS_2 memristor device.**

An Olympus BX51M optical microscope is used to monitor the position of the

miBot probes, ensuring proper contact with the device pads before initiating the electrical measurement. The source meter is controlled using the Agilent Quick IV measurement software, which allows the specification of the measurement parameters and the recording of measured data.

Measurement of charge concentration

In 2D materials, the carrier density can be calculated using the parallel-plate capacitor model:

$$n_{2D} = \frac{C_{ox} \cdot \Delta V_g}{e} \tag{14}$$

where gate oxide capacitance is $C_{ox} = \frac{\varepsilon_0 \varepsilon_{ox}}{d_{ox}}$, the permittivity of free space ε_0 is 8.85×10^{-12} Fm^{-1}, the ε_{ox} and d_{ox} are the permittivity and thickness of the oxide, the elementary charge $e = 1.6 \times 10^{-19}$ C, and the $\Delta V_g = V_g - V_{th}$ is the difference between gate voltage and the threshold voltage.

Measurement of barrier height

Several techniques are commonly used to determine the Schottky barrier height (SBH), e.g. current-voltage (IV) characteristics, capacitance-voltage (CV) measurements, the activation-energy method and the photoelectric method. Here, we will discuss the IV method which will be used in chapter 6.

In a Schottky contact, assuming that the current is predominantly governed by thermionic emission, the forward current can be described by the following equation:

$$I = A^* A T^2 \exp\left(-\frac{q\phi_B}{kT}\right)\left(\exp\left(\frac{qV}{kT}\right) - 1\right) \tag{15}$$

where I is the current, A^* is the Richardson constant (1.2×10^6 Am^{-2}K^{-2} [40]), A is the area, T is the temperature, V is the applied voltage, k is the Boltzmann constant (1.380649×10^{-23} JK^{-1})) and $q = 1.6 \times 10^{-19}$ C is the electronic charge.

If $V > 3kT/q$, the current expression can be simplified as:

$$I = I_s \left[\exp\left(\frac{qV}{nkT}\right)\right] \tag{16}$$

where $n = \frac{q}{kT}\frac{dV}{d(lnI)}$ is the ideality factor and I_s is the reverse saturation current given by:

$$I_s = A^* A T^2 \exp\left(-\frac{q\phi_B}{kT}\right) \tag{17}$$

In practical circuits, the voltage across the junction is different from the ap-

plied voltage V due to the voltage drop across the series resistance R. Thus, the modified current is:

$$I = I_s \left[\exp\left(\frac{q(V - IR)}{nkT} \right) \right] \tag{18}$$

By rearranging eq. (18), the voltage-current relation can be given by:

$$V = \frac{nkT}{q} \ln(I) + IR - \frac{nkT}{q} \ln(I_s) \tag{19}$$

By fitting the experimental IV curve by eq. (19). One can obtain the values for series resistance R, ideality factor n and reverse saturation current I_s. Then, the SBH ϕ_B can be calculated from the following equation, which is derived from eq. (17):

$$\phi_B = \frac{kT}{q} \left(\ln\left(\frac{A^* A T^2}{I_s} \right) \right) \tag{20}$$

The contact resistance at the barrier can be extracted from the differential voltage change with respect to the current $R_c = \frac{dV}{dI}$. The value of $\frac{dV}{dI}$ can be obtained from eq. (16), thus the contact resistance can be given by:

$$R_c = \frac{kT}{I_s q} \tag{21}$$

4 | Polymer-enhanced deposition of 2D MoS_2

"Everything is theoretically impossible, until it is done."

- Robert A. Heinlein

In this chapter, we discuss the development of a novel polymer promoter to realise controllable growth of two-dimensional (2D) MoS_2 on an amorphous SiO_2 substrate. We first briefly summarise the necessity of the work, emphasising the importance of large-scale contamination-free growth of 2D MoS_2. We then detail the preparation of the substrate and describe a typical promoter-enhanced chemical vapour deposition (CVD) process. The promoter effects on the MoS_2 growth are presented with a systematic comparison between homogeneous and heterogeneous nucleation at varying sulphur temperatures. We then explore the evolution of sulphur vacancies and their consequences on the morphology and properties of the flake. Finally, we propose a growth mechanism that accounts for the observations and serves for future growth optimisation.

4.1 Introduction

Two-dimensional transition metal dichalcogenides (TMDs) have emerged as promising candidates for 'More than Moore' technologies due to their atomic-level vertical dimension and reduced short-channel effects. The monolayer MoS_2, with its high theoretical charge carrier mobility ($\sim 400\ cm^2V^{-1}s^{-1}$), direct band gap ($\sim 1.9$ eV) and dangling bond-free surface, shows significant potential for next-generation electronic and optoelectronic devices, necessitating a scalable and controllable synthesis method for industrial applications.

CVD is the dominant approach to synthesising uniform 2D MoS_2 on a

large scale. The nucleation and lateral growth of MoS_2 flakes on a substrate are regulated by the thermodynamics and kinetics of the CVD system, while several chemical substances have been attempted to assist the growth of 2D films. For instance, alkali metal halides (e.g. NaCl [82, 211], KI [111]) and hydrates (e.g. NaOH [113]) can reduce the reaction temperature and weaken the interlayer adhesion, thereby enhancing the lateral growth of TMDs films. Similarly, wafer-scale 2D TMDs films are achieved when alkaline-earth metal chlorides (e.g. $CaCl_2$, $SrCl_2$ [140]) are introduced in the CVD process. However, the residual metal ions from those promoters are detrimental to the electrical properties of the CVD film [278].

Alternatively, organic promoters such as Perylene-3,4,9,10-tetracarboxylic acid tetrapotassium salt (PTAS) or 3,4,9,10-perylene-tetracarboxylicacid-dianhydride (PTCDA) [128, 129, 151] lead to millimetre size growth of 2D MoS_2, owing to the enhanced substrate adhesion of MoS_2 and heterogeneous nucleation sites. A thin film of polymer complex comprising anhydrous ammonium tetrathiomolybdate (ATM) and linearpoly (ethylenimine) (L-PEI) is observed to effectively improve the growth uniformity and control the thickness of MoS_2 films in the range of 2-30 nm [260]. However, precisely controlling the MoS_2 film thickness down to monolayer dimensions is still challenging, and the effects of promoter residues are not yet well documented. This chapter aims to develop a new growth promoter and enhance the growth control, achieving wafer-scale clean growth of 2D MoS_2 films.

4.2 Substrate preparation and typical CVD process

The polymer we used is a conventional photoresist known as S1813, which is of interest to us due to its potential patentability. S1813 consists of a cresol novolak resin and a photoactive compound (PAC), with electronic-grade propylene glycol monomethyl ether acetate (PGMEA) used as the solvent.

Prior to CVD process, a Si wafer coupon (1.5×1.5 cm^2) with a 285 nm SiO_2 layer is used as the substrate and is ultrasonically cleaned as described in section 3.1.1. To investigate the promoter effects within a single CVD run and avoid uncertainties arising from variations between different CVD runs, the substrate surface is divided into two regions, one decorated by the promoter while the other remains pristine (see **Fig. 4.1**). A 2-mm wide polydimethylsiloxane (PDMS) bar is attached to the middle of the substrate (as shown in **Fig. 4.1** (a)), acting as the boundary of the two regions and prevent the overflow of the polymer from one side to the other. S1813 is diluted by isopropyl alcohol (IPA) with a volume

ratio of 1:300 and is spun (by EMS spinner 4000) onto half of the sample at a speed of 5000 rpm for 45 seconds, followed by baking at 115 °C for 75 seconds in ambient. The PDMS bar is then removed after the spinning process. To avoid any uniformity that may have been due to the bar, the region we analysed is far from the bar region, as shown in **Fig. 4.2**.

The atomic force microscopy (AFM) topographic images in **Fig. 4.1** (b-c) reveal differences in the surface morphology between the two regions. The pristine region exhibits a uniform smooth surface with an root mean square (RMS) roughness of 0.87 nm, which is the typical morphology of a well-polished SiO_2 substrate. In contrast, particles, typically tens of nanometers high and hundreds of nanometers wide, are discerned on the promoter region (**Fig. 4.1** (c)). The promoter region hence exhibits a large RMS roughness of 1.34 nm. These results confirm the successful deposition of nanoscale particles, which act as promoters, on one side of the substrate surface.

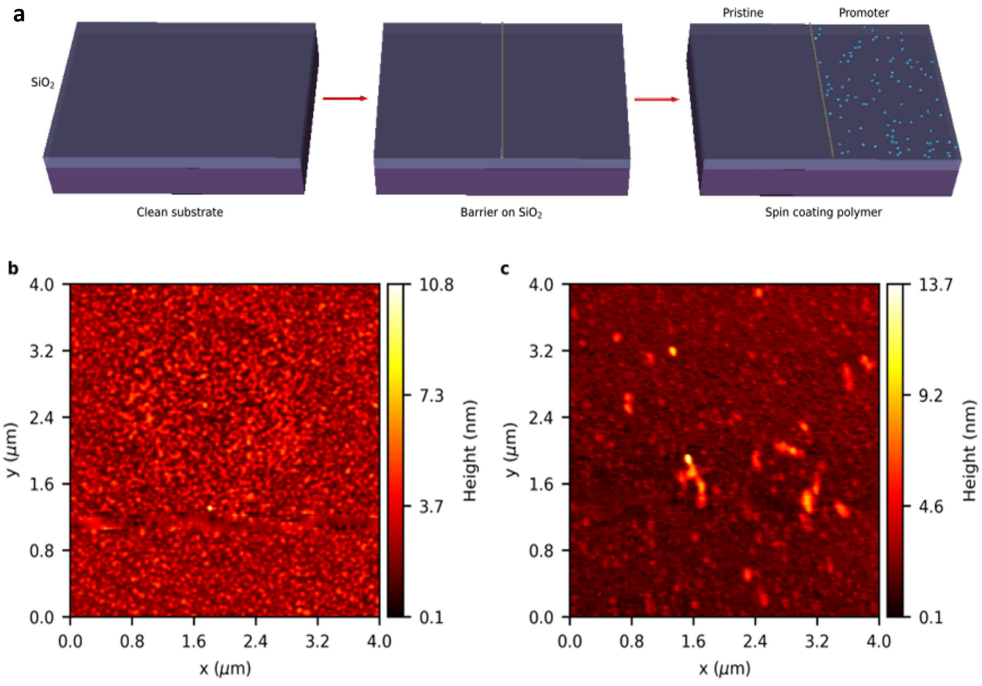


Figure 4.1: **Substrate preparation for polymer-enhanced growth.** (a) Process of substrate preparation. AFM height image for (b) the pristine region and (c) the promoter region. Half of the substrate surface has been decorated with nanosized promoter particles.

The CVD growth is conducted in a two-zone tube furnace (MIT, GSL-1100X). In a typical growth (see **Fig. 4.2** (a) top panel), a quartz crucible is loaded with 1 mg MoO_3 powder (Afla Aesar, 99.9%). The substrate is positioned 0.5 cm downstream from the MoO_3 powder and tilted at an angle of 120° relative to the tube

axis. Additionally, sulphur powder (120 mg, MaTecK, 99%) is placed in a separate crucible. Both crucibles are loaded into the furnace, with each crucible's temperature controlled independently. The heating controller for the sulphur source is energised when the substrate temperature reaches 765 $^{\circ}C$. During the growth process, the substrate/MoO_3 temperature is maintained at 835 $^{\circ}C$, and the sulphur temperature is kept at 250 $^{\circ}C$ for 5 minutes. Nitrogen gas (99.999%) is introduced as a protective carrier gas at a flow rate of 20 sccm throughout the reaction period.

4.3 Promoter effects on the MoS_2 growth

We note that the distance between the source and the deposition site can affect the growth behaviour. This is because the concentration and flow of reactants in the ambient vary with the distance. As such, for a set of growth parameters, we compare the growth behaviours at two equivalent locations sampled from the pristine and promoter regions, which undergo a similar reaction environment (e.g. reactant concentration and flow).

4.3.1 Enhanced growth on the promoter region

The most significant growth enhancement is observed by comparing two equivalent regions at the bottom of the substrate close to the crucible side walls. These regions, indicated by the dashed circles in the bottom panel of **Fig. 4.2** (a), are located 12 mm from the molybdenum source. The promoter region (right) exhibits a distinctly different color compared with the pristine region (left). A continuous dark olive green film is visible on the surface of the promoter region, while the contrast of the pristine surface is close to that of the bare Si substrate. The difference in optical contrast suggests that, at the macroscopic scale, the promoter region has significantly more 2D growth than the pristine region.

The optical micrographs of the pristine region (**Fig. 4.2** (b)) and the promoter region (**Fig. 4.2** (c)) corroborate the observations made through visual inspection. Sparse micrometre-sized particles are present in the pristine region with diminished 2D growth. In contrast, the promoter region features a uniform distribution of triangular MoS_2 flakes. Some triangular flakes merge, forming films up to approximately 33 μm in size. Optical micrographs with a field of view of 500 μm $\times$ 500 μm were further used for statistical analysis, and the analysis is conducted using Phython [275]. Only flakes larger than 2 μm are counted, taking into account the resolution of the optical microscopy. Approximately 534 small particles are identified in the pristine region, compared with about 224 μm-sized flakes

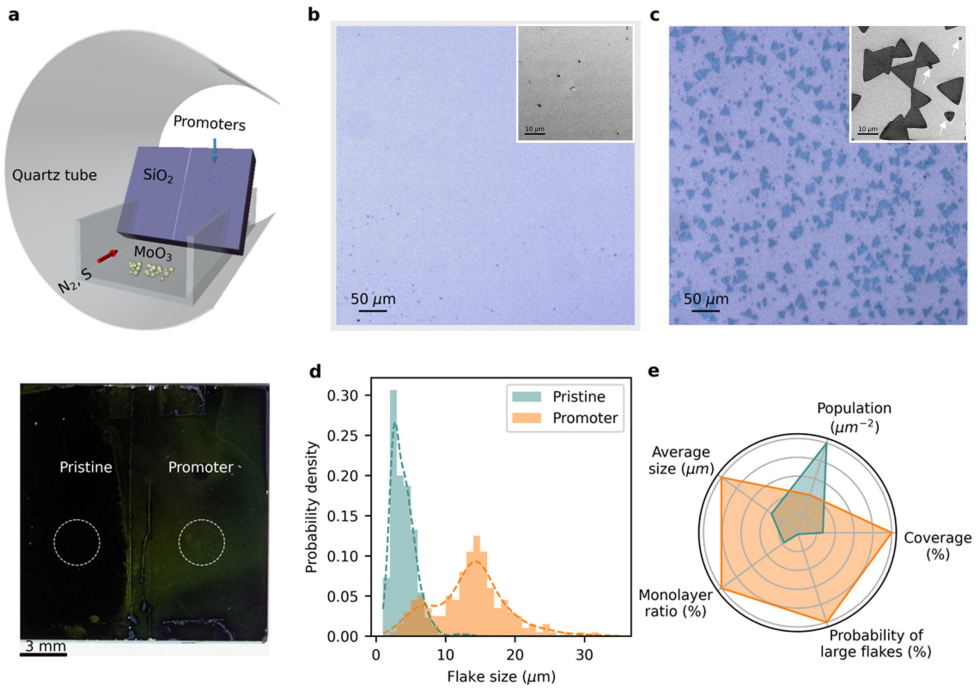


Figure 4.2: **A typical promoter-enhanced MoS_2 growth at a sulphur temperature of 250 °C.** (a) Top panel: an illustration of the key growth configuration. Bottom panel: An optical image of the wafer coupon post-growth. The white dashed circles highlight two equivalent regions—one from the pristine region and the other from the promoter region—under similar growth conditions, such as reactant concentration and flow. Optical micrographs for (b) the pristine substrate, which remains clean and (c) the promoter region covered by triangular MoS_2 flakes. (d) Statistical distribution of flake sizes comparing the growth in the pristine and promoter regions. (e) A radar chart comparing the average flake size, monolayer ratio, probability of large flake, coverage and population for the pristine substrate and promoter regions.

in the promoter region (**Fig.** 4.3 (a-b)). The histogram in **Fig.** 4.2 (d) illustrates that the flake size distribution in the pristine region follows a lognormal pattern with an average size of 3.9 μm (flake recognition see **Fig.** 4.3 (a)). The promoter area exhibits a bimodal Gaussian distribution. The first peak at 6.4 μm corresponds to the small flakes (as marked by white arrows in **Fig.** 4.2 (c) and shown in **Fig.** 4.3 (c)), which overlaps with the peak of the pristine region, indicating homogenous nucleation. The main peak at 14.4 μm represents the large triangular flakes (**Fig.** 4.3 (d)), which is more than 3 times larger than the pristine region, indicating the heterogenous nucleation induced by the nano promoters. **Figure** 4.2 (e) compares five key metrics of CVD growth, including the average size. The monolayer ratio, defined as the area ratio of monolayer MoS_2 to the total recognized area **Fig.** 4.3 (a-b), of the promoter region is 88.9%, approximately six times higher than that of the pristine region. The abundance percentage of large flakes ($\geq$10 μm) is 30.2% in the promoter region and 0.5% in the pristine region. The coverage, defined as the ratio of the area covered by flakes to the total substrate

area in the image, is significantly higher in the promoter region at 15.0%, more than three times that of the pristine region (4.0%). However, the population density, representing the number of flakes or particles per unit area, is lower in the promoter region (1.0×10^3 mm^{-2}) than in the pristine region (2.4×10^3 mm^{-2}). These quantitative statistical results confirm the enhanced growth of 2D MoS_2 in the promoter region.

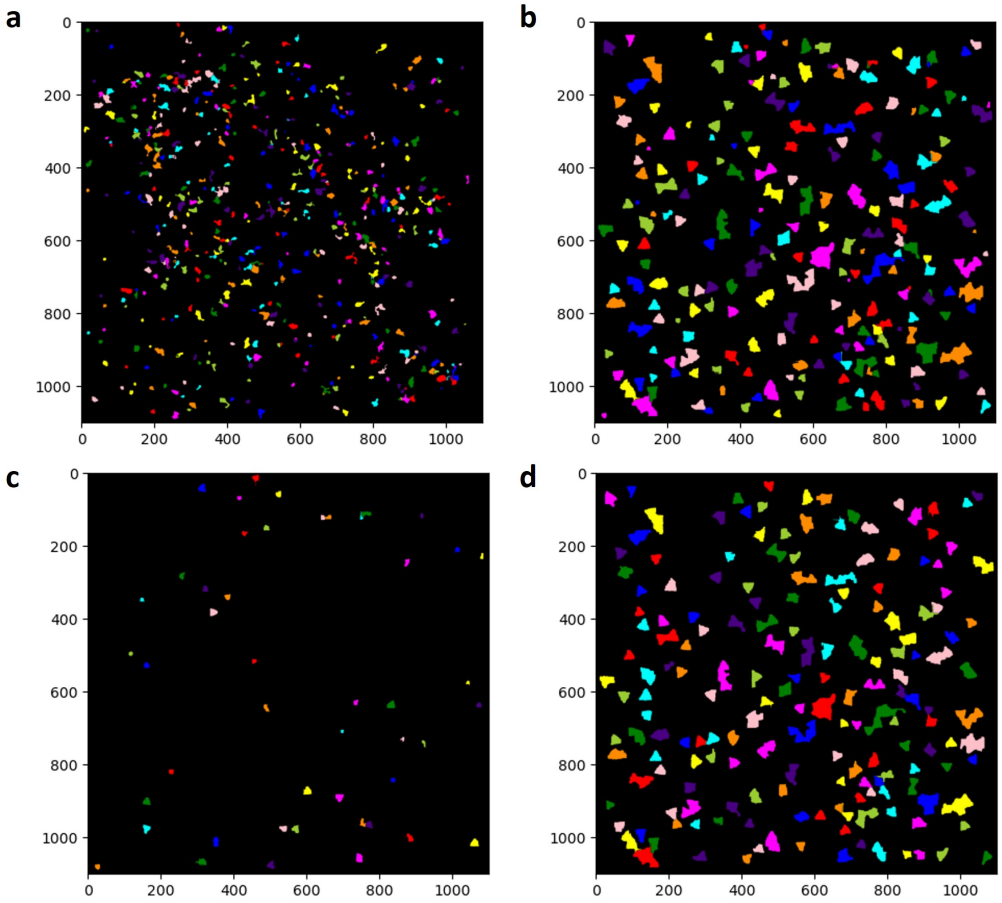


Figure 4.3: **Flake recognition using Python.** Flakes within the size range of 2-35 μm for the (a) pristine and (b) promoter regions. For the promoter region, flakes in the size range of 2-10 μm and 10-35 μm are shown in (c) and (d), respectively. The axis unit is pixels. Colours are used to highlight the identified flakes, with each flake marked by a distinct colour, although no specific meaning is assigned to the choice of colour.

4.3.2 Morphology of the 2D MoS_2 flakes

In this section, we systematically characterise the general morphology of individual MoS_2 flakes in the promoter region. The variation in flake thickness is initially identified using optical contrast (OC), as shown in the colour map in **Fig. 4.4** (a). The majority of the flakes appear monolayer (white), reflecting the uniformity of the sample in thickness. Some bilayer regions (light green) on triangular flakes suggest secondary growth, and a few dark green particles indicate additional nu-

cleation sites. This large-scale OC mapping reveals that approximately 95% of the flakes are monolayer, while around 5% are multilayer. Each flake exhibits an energetically favourable triangular shape, with slightly curved edges. The Scanning Electron Microscopy (SEM) image in **Fig. 4.4** (b) further reveals the secondary nucleation at the centre of a triangular flake, and it also reveals a grain boundary (GB) where two flakes with differing crystallographic orientations merge. AFM is employed to measure the MoS_2 thickness, as shown in **Fig. 4.4** (c). The line profile extracted from point A to point B, plotted in **Fig. 4.4** (d), demonstrates that the height difference between the MoS_2 film and the substrate is 0.68 nm, confirming the monolayer nature of the flake. The results demonstrate uniform monolayer growth of MoS_2 in the promoter region.

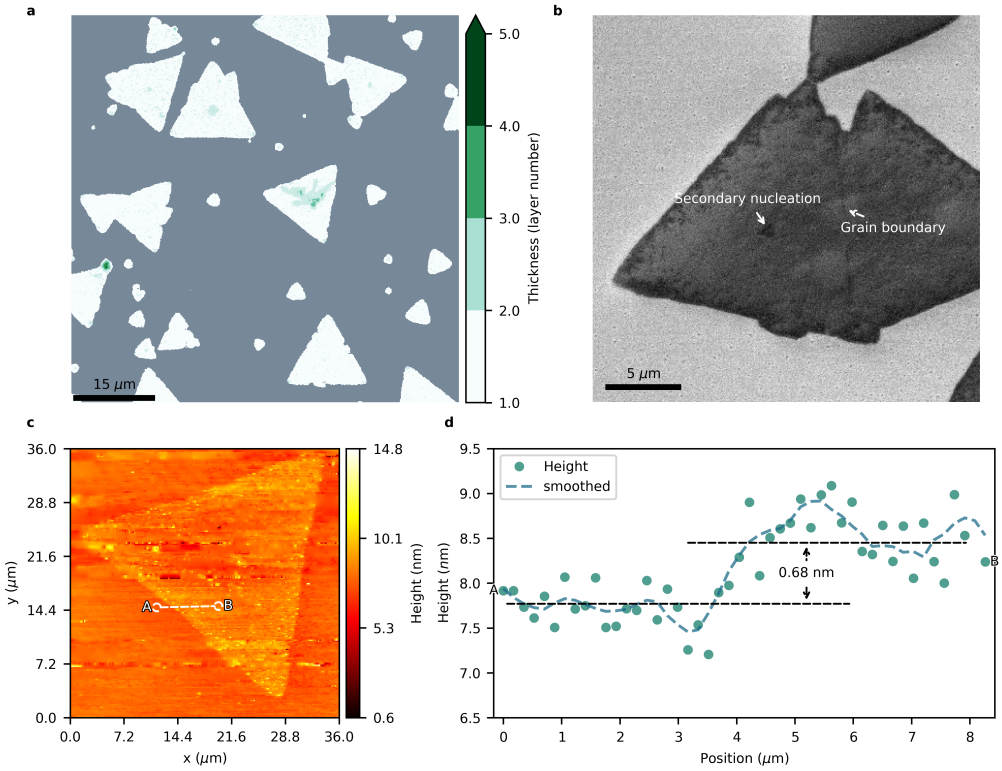


Figure 4.4: **Thickness analysis of MoS_2 in the promoter region with the sulphur source of 250 °C.** (a) The colour map of MoS_2 thickness is identified by optical contrast. (b) SEM image of two merged monolayer MoS_2 flakes. (c) AFM height image of a monolayer MoS_2 flake. (d) The line profile extracted from A to B marked in (c) shows the thickness of MoS_2 flake is 0.68 nm.

The MoS_2 flakes are further characterized by Raman spectroscopy and photoluminescence spectroscopy (PL). As shown in **Fig. 4.5** (a), the average Raman spectrum exhibits two significant peaks at 384.3 cm^{-1} and 405.1 cm^{-1} which correspond to the E^1_{2g} and A_{1g} modes of 2H MoS_2, respectively. The spacing, $\Delta\omega$, between the two Raman modes is 20.8 cm^{-1} whereas the peak intensity ratio of E^1_{2g} and A_{1g} is 0.72. These results again indicate the monolayer

nature of the MoS_2 flake [105, 137, 269]. A map of the $\Delta\omega$ is extracted and shown in **Fig. 4.5** (b). The majority (95%) of the flakes in the mapping region exhibit consistent values of $\Delta\omega \sim 20$ cm^{-1}, suggesting a high population of monolayer flakes. However, around 5% of areas show $\Delta\omega$ in the range of 22-24 cm^{-1}, which is attributed to multilayer MoS_2. The monolayer ratio is consistent with the OC result in **Fig. 4.4** (a). In the PL spectrum (**Fig. 4.5** (c)), a strong luminescence band appears at 1.845 eV and corresponds to the direct excitonic transition energy (A exciton) [157], indicating the direct band gap of the monolayer MoS_2 [161]. Moreover, the B exciton resonance is observed at 1.97 eV, which is due to the spin-orbital splitting of the valence band [161].

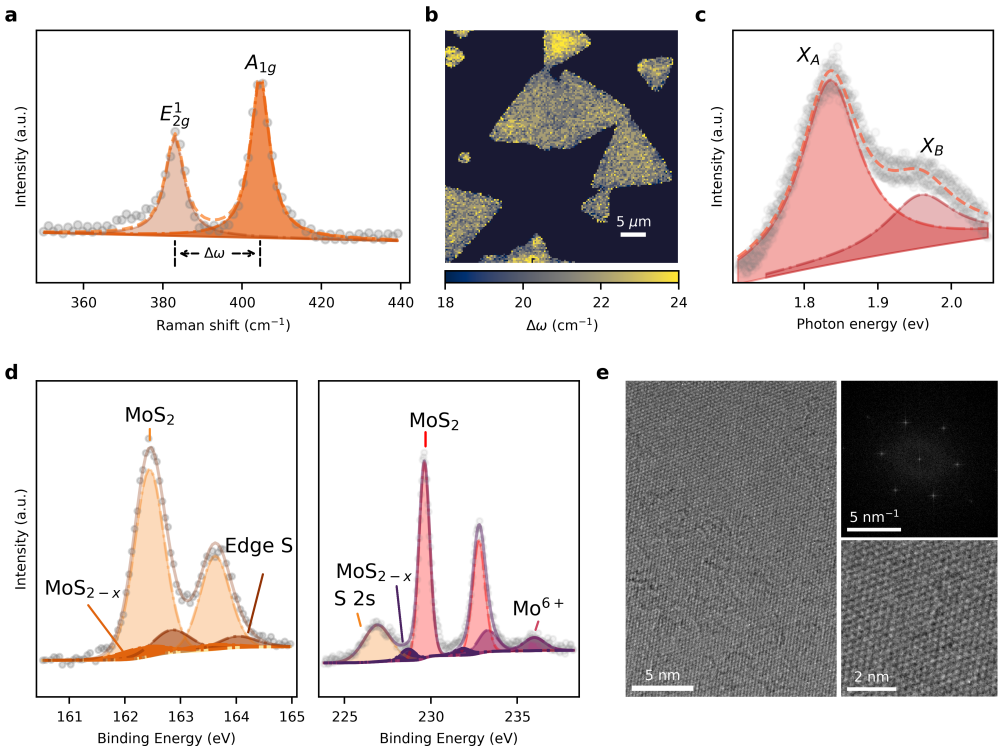


Figure 4.5: **Characterisation of the flakes on the promoter region.** (a) Average Raman spectrum shows A_{1g} and E^1_{2g} modes of 2H MoS_2 at 404.1 cm^{-1} and 384.5 cm^{-1} with a peak spacing of 19.6 cm^{-1}. (b) The mapping of the peak position difference shows a high population of monolayer flakes. (c) Averaged PL spectrum shows strong A exciton at 1.82 eV, indicating the direct band gap MoS_2 which corresponds to the behaviour of monolayer MoS_2. (d) Chemical states analyze by X-ray photoelectron spectroscopy (XPS): S 2p and Mo 3d core level XPS spectra. (e) High-resolution Transmission Electron Microscopy (HRTEM) shows the lattice planes of MoS_2. The top right panel is the Fourier transform of the HRTEM image, which implies a single crystalline hexagonal structure. The high-angle annular dark-field (HAADF)-Scanning Transmission Electron Microscopy (STEM) image in the bottom right panel confirms the disorder-free lattice and the 2H phase.

From the XPS survey spectra (**Fig. A.3**), peaks corresponding to Mo, S, C, O, and Si are observed, with no additional elements detected. **Figure 4.5** (d) shows the XPS of core level spectra S 2p and Mo 3d spectra of the films in the promoter

region. In the S 2*p* core-level spectrum, the doublets at 162.4 eV and 163.6 eV indicate the chemical states of S in 2H MoS_2 [107, 186]. The weak peaks at 164.1 eV and 162.9 eV can be attributed to the edge sulphur [7]. The doublet at 162.3 eV and 163.5 eV corresponds to the reduced chemical state of S, indicating a MoS_{2-x} phase. In the Mo 3*d* core level spectrum, the doublets at 229.6 eV and 232.8 eV indicate the chemical states of Mo in 2H MoS_2 [107, 186]. The relative weak peaks at 233.3 eV and 236.0 eV correspond to the Mo^{6+}, implying the presence of a small amount of MoO_3. The doublet at 228.70 eV and 231.84 eV corresponds to the MoS_{2-x} phase. The peak at 227.0 eV is attributed to the S 2s. The XPS results suggest that the film primarily consists of 2H MoS_2, with detectable sulphur vacancies and oxides species. The vacancy concentration was determined from stoichiometric calculations, based on the core-level spectra of Mo 3d and S 2p. The stoichiometry (atomic ratio) is calculated by:

$$\frac{\mathrm{Mo}}{\mathrm{S}} = \frac{\left(\frac{I_{\mathrm{Mo\ 3d}}}{\sigma_{\mathrm{Mo\ 3d}}}\right)}{\left(\frac{I_{\mathrm{S\ 2p}}}{\sigma_{\mathrm{S\ 2p}}}\right)} \tag{1}$$

where I denotes the integrated peak areas of Mo 3d and S 2p, and σ represents the sensitivity factors, taken as 2.47 for Mo 3d and 0.54 for S 2p [234]. The calculated stoichiometry is $MoS_{1.92}$ with a defect concentration of approximately 4%. In 2H-MoS_2, the sulfur–sulfur (S–S) distance is 3.162 Å, allowing the areal density of sulfur atoms in a monolayer to be estimated as $\sim 2.3 \times 10^{15}$ cm^{-2} [289]. An 4% sulfur deficiency yields a defect density of approximately $\sim 9.2 \times 10^{13}$ cm^{-2}, which is consistent with previously reported values for CVD-grown samples (typically 10^{13} cm^{-2} $\sim 10^{14}$ cm^{-2} [21, 67]).

The HRTEM image, see **Fig. 4.5** (e), shows the lattice of 2H MoS_2. The sixfold symmetry is evident in the Fourier transform of the image shown in the top right panel of **Fig. 4.5** (e). The 2D lattice shown in the bottom right panel confirms the high quality lattice structure and corroborates the 2H phase. The optical properties, chemical state and the lattice structure confirm that the flakes are monolayer 2H MoS_2.

4.3.3 Characterisation of the particles in pristine region

For completeness, we investigate the particles grown in the pristine region. As shown in **Fig. 4.6** (a) and (b), the XPS spectra of pristine region show a weak signal in the range of 224 – 239 eV (Mo 3*d* core level), and no peak is detected within the binding energy range of 162–164 eV (S 2*p* core level). This suggests the presence of a small amount of molybdenum compound but no detectable MoS_2.

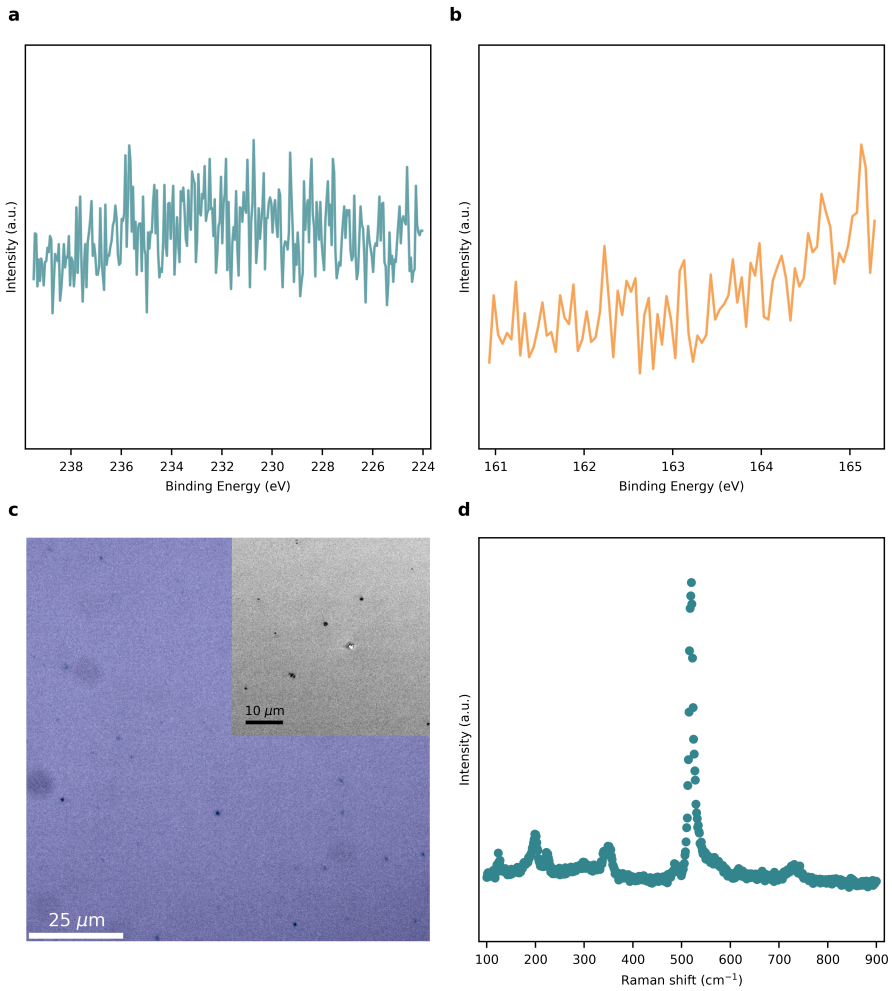


Figure 4.6: **Pristine region of the sample with sulphur temperature of 250 °C.** (a) XPS Mo 3*d* and (b) S 2*p* core-level spectra. (c) Optical image with SEM image inserts showing the particles. (d) The Raman spectrum of the particle shows molybdenum oxide peaks.

Moreover, **Fig. 4.6** (c) shows the morphology of the pristine particles with a size of less than 5 μm. The corresponding Raman spectrum in **Fig. 4.6** (d) reveals a strong peak at 520 cm^{-1}, which is a characteristic signature of the Si phonon mode corresponding to the crystalline Si substrate [132, 290]. Furthermore, the characteristic peaks at 203, 233, 363, 464, 496, 570, and 744 cm^{-1} [134], which align with the typical Raman vibrational frequencies of MoO_2 [101, 179, 213] are evident. The presence of these characteristic peaks suggests that the particles have crystallized in the MoO_2 phase. The formation of MoO_2 rather than MoS_2 suggests the ineffective sulphurisation reaction in the pristine region.

4.3.4 Cleanliness of the promoter-enhanced growth

To investigate the decomposition behaviour of the S1813 photoresist, thermogravimetric analysis (TGA) measurements were performed under a N_2 atmo-

sphere with a flow rate of 20 sccm (**Fig. A.4**). A rapid weight loss observed between 50 °C and 200 °C suggests the evaporation of solvents and volatile components. From 200 °C to 600 °C, a steep decline in weight indicates thermal degradation of the organic polymer matrix in the photoresist. Beyond 600 °C, a gradual weight loss continues, likely due to carbonisation or further decomposition of residual organics. At 835 °C, approximately 11% of the initial mass remains, indicating the non-volatile inorganic content or carbonaceous residue.

To verify if the non-volatile inorganic content or carbonaceous residue remains in our promoter-enhanced CVD method, the cleanliness of the growth is first checked by XPS. C 1*s* and O 1*s* core-level spectra are analysed and compared in **Fig. 4.7**. For both the pristine and promoter regions, in the O 1s core-level spectra shown in **Fig. 4.7** (a) and (d), the main peak at 533.2 eV represents the O-Si bond which arises from the substrate. The weak peaks at 532.2 eV and 531.0 eV correspond to O-C and O-Mo bonds [56]. In the C 1*s* core-level spectra (**Fig. 4.7** (b) and (e)), a prominent peak appears at approximately 285.0 eV for both the pristine and promoter regions, corresponding to C-C bonds. In addition, peaks at around 286.5 eV, 288.0 eV and 289.15 eV correspond to the C-O single bonds, C=O double bonds and O-C=O bonds, respectively. These peaks are typical for adventitious carbon [75, 148] which is usually found on the surface of most air-exposed samples. There is no evidence showing that C and O bond with Mo or S (for example, C-Mo bonds in C 1*s* at 284.2 eV [71, 148], C-S-C in S 2*p* at 163.5 eV and 164.8 eV [283]). The adventitious C signal is stronger in the promoter region than in the pristine region. A comparison of C 1*s* core-level spectra of the bare SiO_2 substrate and the bulk MoS_2 (**Fig. 4.7** (e) and (f)) shows consistently higher C intensity on MoS_2. This implies stronger C adsorption on the MoS_2 surface than the SiO_2, possibly due to the lower surface energy of MoS_2 than the SiO_2 [69, 145]. The results confirm the cleanliness of the nano promoter-enhanced growth.

Additionally, the Raman spectrum of carbon is dominated by the sp^2 bonding (e.g., graphite) and/or sp^3 bonding (e.g., diamond) [26, 233], which correspond to the G band, typical at ∼1575 cm^{-1}, and D band, typical at ∼1355 cm^{-1}, respectively [26, 76, 100, 147, 227]. Under visible excitation, Raman scattering is 50-230 times [195, 232] more sensitive to sp^2 sites due to the preferential excitation of π states [60]. As shown in the full-range Raman spectrum (**Fig. 4.7** (g)), no peak is observed within the range of 1100 to 2000 cm^{-1}, indicating that no carbon materials are present in the MoS_2 of the promoter region within the limit of detection (LOD) (see section 3.3.2). This indicates that the carbonaceous residue from the photoresist may be consumed during its reaction with MoO_3, thereby facilitating the reduction of MoO_3. Besides, a weak longitudinal acoustic (LA) peak

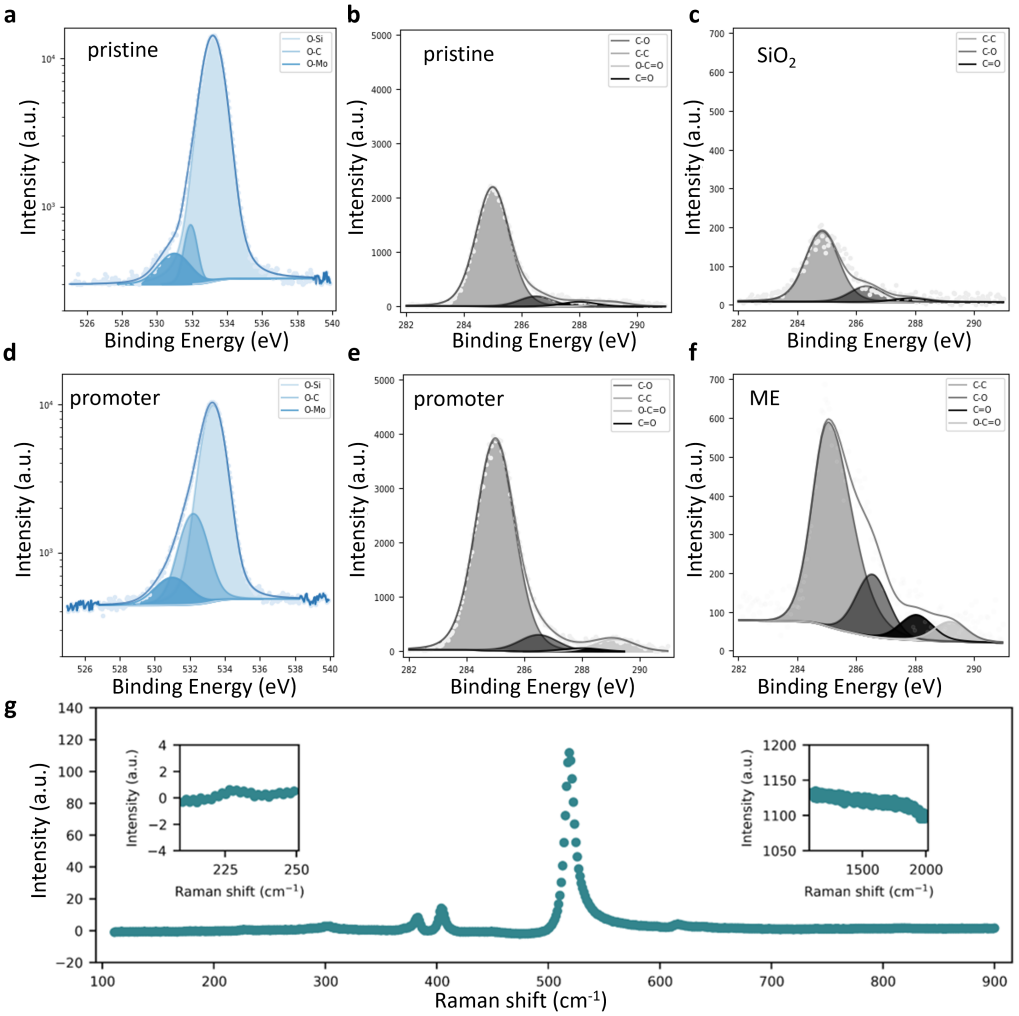


Figure 4.7: **Cleanliness of the promoter-enhanced growth.** (a, d) O 1*s* core-level spectra of the pristine and promoter regions, respectively. (b, e) The C 1*s* core-level spectra of the pristine and promoter regions, respectively. (c, f) The C 1*s* core-level spectra of the SiO_2 and mechanical exfoliation (ME) MoS_2, respectively. (g) Raman spectrum of the MoS_2 flake in the promoter region with the range of 1100-2000 cm^{-1}, no C peak is observed.

can be observed in the range of 210 to 250 cm^{-1}, characteristic of defect-induced Raman modes [165].

4.4 Effects of the sulphur-source temperature

To further investigate the effect of the nano promoter, we examine the evolution of the morphology and yield of MoS_2 as a function of the sulphur temperature. In this experiment, the temperature of Mo/substrate is maintained consistently at 835 $°C$ for all samples. Other parameters are kept the same as described in section 4.2.

4.4.1 Morphological changes in MoS_2

Figure 4.8 (a) and (b) display the optical images of the pristine and promoter regions at different sulphur temperatures, respectively. The insets are SEM images of the corresponding sample, providing detailed views of the morphology of individual flakes. In the pristine region (**Fig. 4.8** (a)), small particles (< 5 μm) are visible in all the samples regardless of the sulphur temperature. In contrast, the morphology of the CVD products (**Fig. 4.8** (b)) in the promoter region varies depending on the sulphur temperature. When the sulphur temperature is 180 °C, hexagonal MoS_2 flakes with rounded edges and a size of approximately 3 μm are observed, indicating insufficient sulphur concentration [22, 74]. As sulphur temperature increases to 200 °C, the MoS_2 flakes transition to a triangular shape with rounded edges, suggesting an increase in sulphur concentration though it remains inadequate. At the sulphur temperature of 220 °C, the triangular flakes grow larger and exhibit straighter edges. Further increasing sulphur temperature to 250 °C leads to uniformly distributed triangular MoS_2 flakes with increased flake size and well-defined straight edges. This indicates that the reactant concentration is sufficient for the 2D growth of stoichiometric MoS_2. When the sulphur temperature is 270 °C, the flakes show irregular shapes with sizes ranging from 0-30 μm, indicating the merging of multiple grains. The darker contrast at their centre suggests excessive growth of multilayer films, accompanied by the appearance of particles. Finally, at 300 °C, the MoS_2 appears as particles and submicron-sized triangular flakes. The presence of particles rather than the formation of films suggests that the nucleation rate exceeds the growth rate.

Further statistical analysis is conducted to compare growth in the pristine and promoter regions. The statistical data, derived from optical images shown in **Fig. 4.8** (a) and (b), are processed using Python. Considering the resolution limit of the optical images, we focus on CVD products with a size larger than 2 μm. The flake size distribution, presented in **Fig. 4.8** (c), compares the pristine and promoter regions at various sulphur temperatures. At a sulphur temperature of 180 °C, both regions exhibit similar size distributions with a narrow full width at half maximum (FWHM) and a mean size of approximately 3 μm. As the temperature increases from 200 °C to 250 °C, the pristine region maintains a narrow distribution, while the promoter region shows a broader distribution with a mean size shift, peaking at 13.5 μm at 250 °C. Beyond 250 °C, the mean size in the promoter region decreases, while the pristine region remains centred at ∼3 μm. By 300 °C, the two distributions overlap again, exhibiting similar FWHM and mean values. These results indicate that the promoter effect depends on sulphur temperature, dominating the growth when the sulphur temperature is within the range of 200

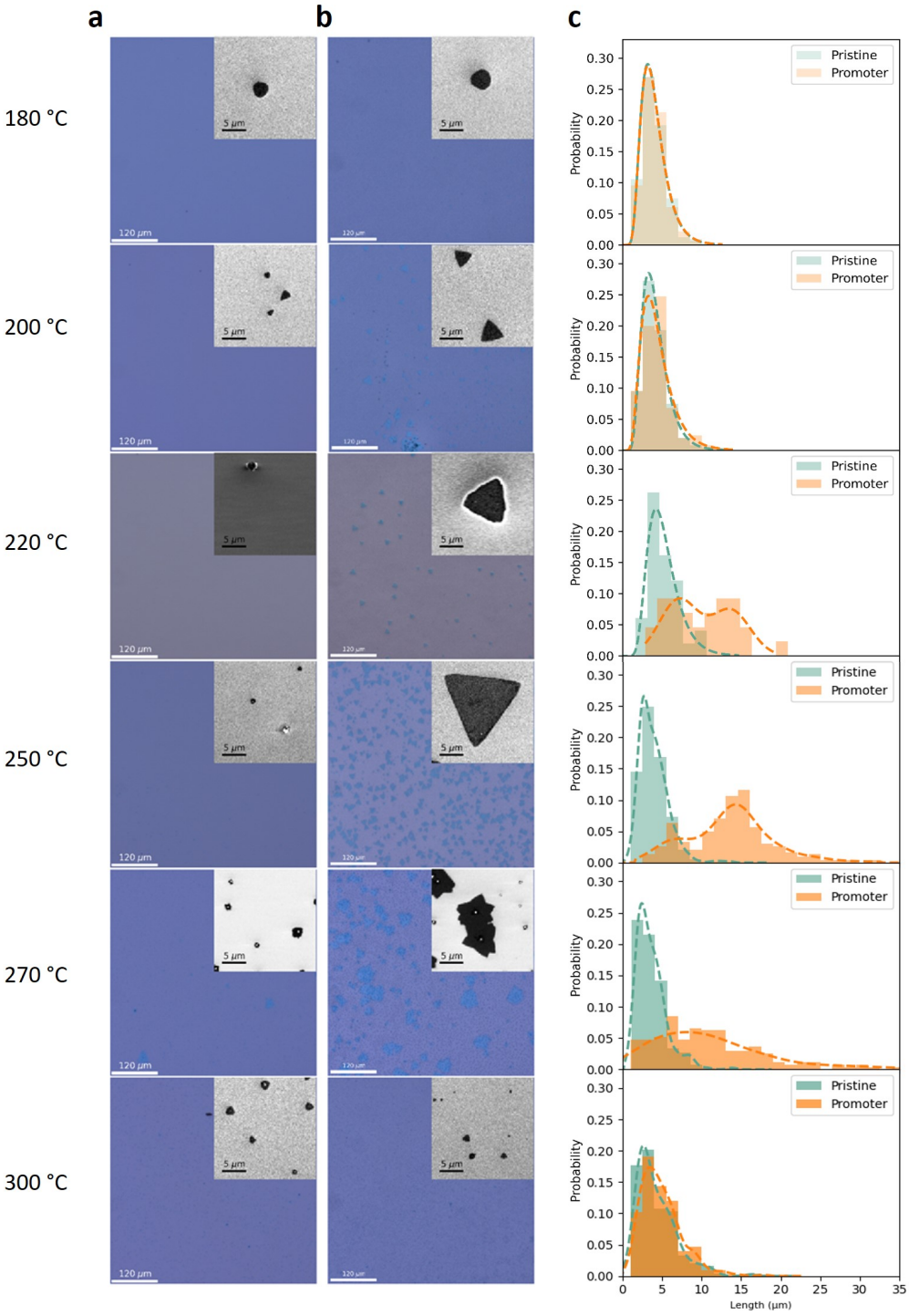


Figure 4.8: **Morphology and flake size distribution of samples at varied sulphur temperature.** Optical images and SEM images inserted for (a) the pristine region and (b) the promoter region. (c) Flake size distribution of samples at sulphur temperature of 180°C, 200°C, 220°C, 250°C, 270°C, 300°C, respectively. Scale bars in the optical images are 120 μm

°C to 270°C.

Figure 4.9 compares the five key growth metrics in the pristine and promoter

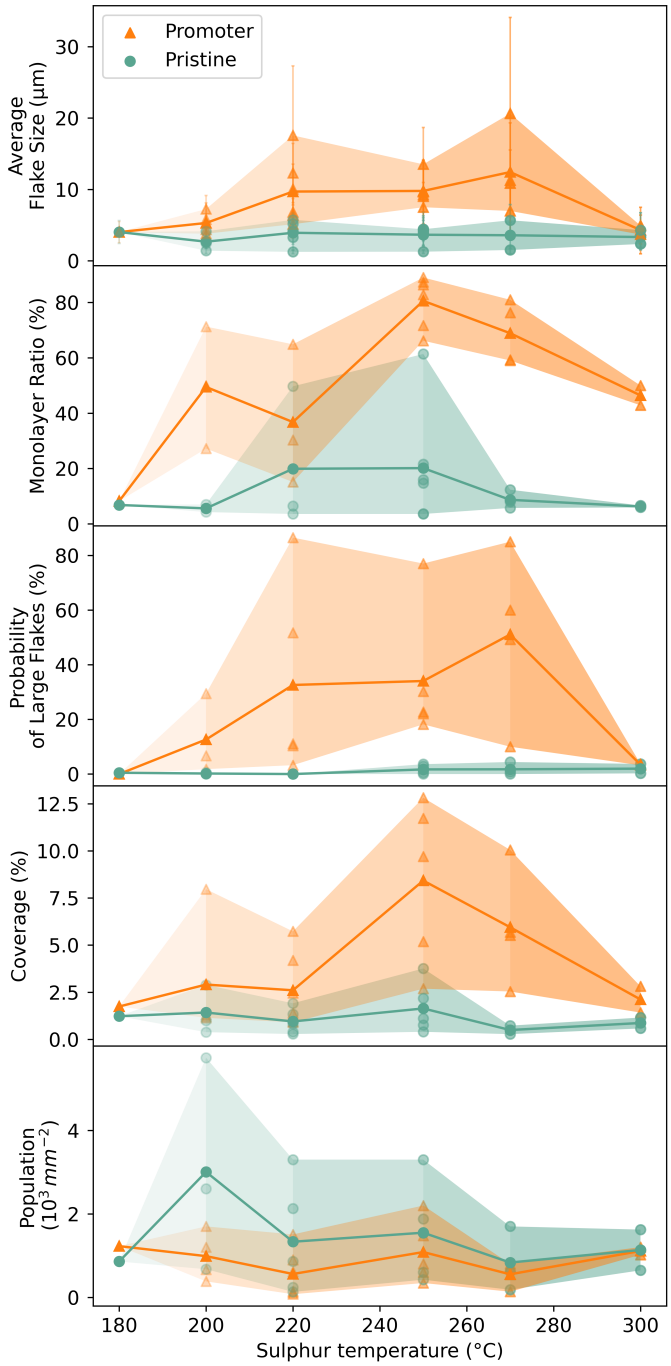


Figure 4.9: **Quantified statistical analysis of the samples after CVD at varied sulphur temperature.** It compares the (a) average flake size, (b) monolayer ratio, (c) probability of large flake, (d) coverage and (e) population in the promoter and pristine region, respectively. The orange triangle represents the promoter side, while the green circle corresponds to the pristine side. The data point at a given temperature represents multiple reproduced samples. The error bars in the top panel represent the standard deviation of multiple flakes.

regions. Multiple data points at a given temperature represent distinct samples grown under identical parameters, with error bars indicating the variation among flakes within each sample. The average flake size in the pristine region (**Fig. 4.9**

(a)) remains consistently within the range of 3–5 μm across all temperatures. In the promoter region, the average flake size is approximately 4 μm at 180 °C and increases with the sulphur temperature, reaching a peak of 9.8 μm at 250 °C and 11.2 μm at 270 °C. However, beyond 270 °C, the average flake size decreases, dropping to around 4 μm at 300 °C. The MoS_2 flakes in the promoter region are consistently larger than those in the pristine region, with the size difference peaking between the sulphur temperature of 250 °C and 270 °C.

The monolayer ratio (**Fig. 4.9** (b)), in the pristine region, remains around 5% between 180 °C and 200 °C, reaching a maximum of 20% at 220 °C and 250 °C, and decreases to 7% at 300 °C. In the promoter region, the monolayer ratio increases steadily with temperature, peaking at 82% at 250 °C, before declining to 48% at 300 °C. The promoter region exhibits a higher monolayer ratio at all sulphur temperatures, with the maximum difference between the two regions observed at 250 °C.

Using a definition of a large flake as being greater than 10 μm, the probability of large flakes (**Fig. 4.9** (c)), in the pristine side, remains steady at around 1.0% between 180 °C and 300 °C. On the promoter side, the probability is 0% at 180 °C,increases to 12.6% at 200 °C, rises significantly to a 35%-50% between 220 to 270 °C, and then decreases to 3.4% at 300 °C. These results show that the promoter region has a higher probability of large flakes, with the maximum occurring between 220 to 270 °C.

The promoter region exhibits significantly higher flake coverage (**Figure 4.9** (d)) compared to the pristine region within the sulphur temperature range of 200 °C - 270 °C, peaking at 250 °C (18%). In contrast, coverage in the pristine region remains relatively low between 0.5-2% across the temperature range of 180 °C - 300 °C. This highlights the enhancement of MoS_2 growth in the promoter region, particularly at 250 °C.

The population density (**Fig. 4.9** (e)), in the pristine side, increases from 0.8×10^3 to 3.1×10^3 mm^{-2} as the temperature rises from 180 °C to 200 °C. However, as the temperature continues to increase, the population density decreases to 1.3×10^3 mm^{-2} at 220 °C and remains around this value between 220 °C to 300 °C. In the promoter side, except at 180 °C, the population density is lower than that on the pristine side. At 180 °C, the population density in the promoter side is 2.5%, whereas between 200 °C and 300 °C, it ranges from 1.1% to 2.2%.

From the statistical results, the small average size and high population density indicate a high nucleation rate and a low film growth rate in the pristine region. It is evident that MoS_2 2D growth in the promoter region is significantly enhanced,

particularly when the sulphur temperature is between 220°C and 270°C, as indicated by increased flake sizes, monolayer ratio, probability of large flake and coverage.

4.4.2 Quality variation in MoS_2

To further evaluate the quality of the synthesized MoS_2 under different sulphur temperatures, we systematically conducted Raman and PL characterization of the promoter regions for the samples with the sulphur temperature ranging from 180 to 300 °C. The Raman spectra of the samples exhibit the characteristic A_{1g} and E^1_{2g} modes of MoS_2 at ∼383 cm^{-1} and ∼405 cm^{-1}, respectively. Additionally, weak peaks observed at ∼230 cm^{-1} corresponds to defects of MoS_2. These features confirm that the samples are MoS_{2-x}. The difference in peak positions between the Raman A_{1g} and E^1_{2g} modes, $\Delta\omega$, as shown in **Fig. 4.10** (a), is in the range of 19 cm^{-1} to 23 cm^{-1}. The $\Delta\omega$ is a function of film thickness, which increases with the film thickness (**Fig. 3.20** (c)). The change in the pseudo-color means the change in $\Delta\omega$ and hence the thickness. It is noted that for flakes larger than 5 μm, the $\Delta\omega$ distribution is non-uniform, with bright spots attributed to secondary nucleation events. For most of the film, as the temperature increases from 180 °C to 250 °C, the pseudo-colour of the flakes/particles transitions from bright yellow to grey, indicating a decrease in film thickness. The colour becomes brighter again at a temperature above 270 °C, suggesting increased film thickness.

Averaged Raman spectra obtained from the maps are depicted in **Fig. 4.10** (c), which are normalized against the Si peak at 520 cm^{-1} and fitted by Lorentzian functions. The normalisation removes intensity variations caused by fluctuations in laser power. No detectable Raman peaks are observed at 180 °C, which suggests a limited amount of deposition. For temperature between 200 °C and 250 °C, the E^1_{2g} at 383.8±0.7 cm^{-1}, while it redshifts to 381.9 cm^{-1} at 270 °C. The A_{1g} peak is at 406.4 cm^{-1} at 200 °C, which then features a redshift to ∼405.2 cm^{-1} at higher sulphur temperatures. The peak difference, $\Delta\omega$, varies accordingly. From 200 °C to 220 °C, the peak difference is around 22.1 cm^{-1}. At 250 °C, the peak difference is 20.8 cm^{-1} which is the minimum among all the samples, indicating the monolayer thickness. When the sulphur temperature exceeds 250 °C, $\Delta\omega$ increases, reaching 24.4 cm^{-1} at 300 °C. The increase in $\Delta\omega$ indicates an increase in MoS_2 thickness. Notably, the E^1_{2g} and A_{1g} peak positions of the sample grown at 250 °C are comparable to those of the ME sample, suggesting that the film quality is close to the ME sample.

The PL peak-position maps of the Xa are shown in **Fig. 4.10** (b). The colours on

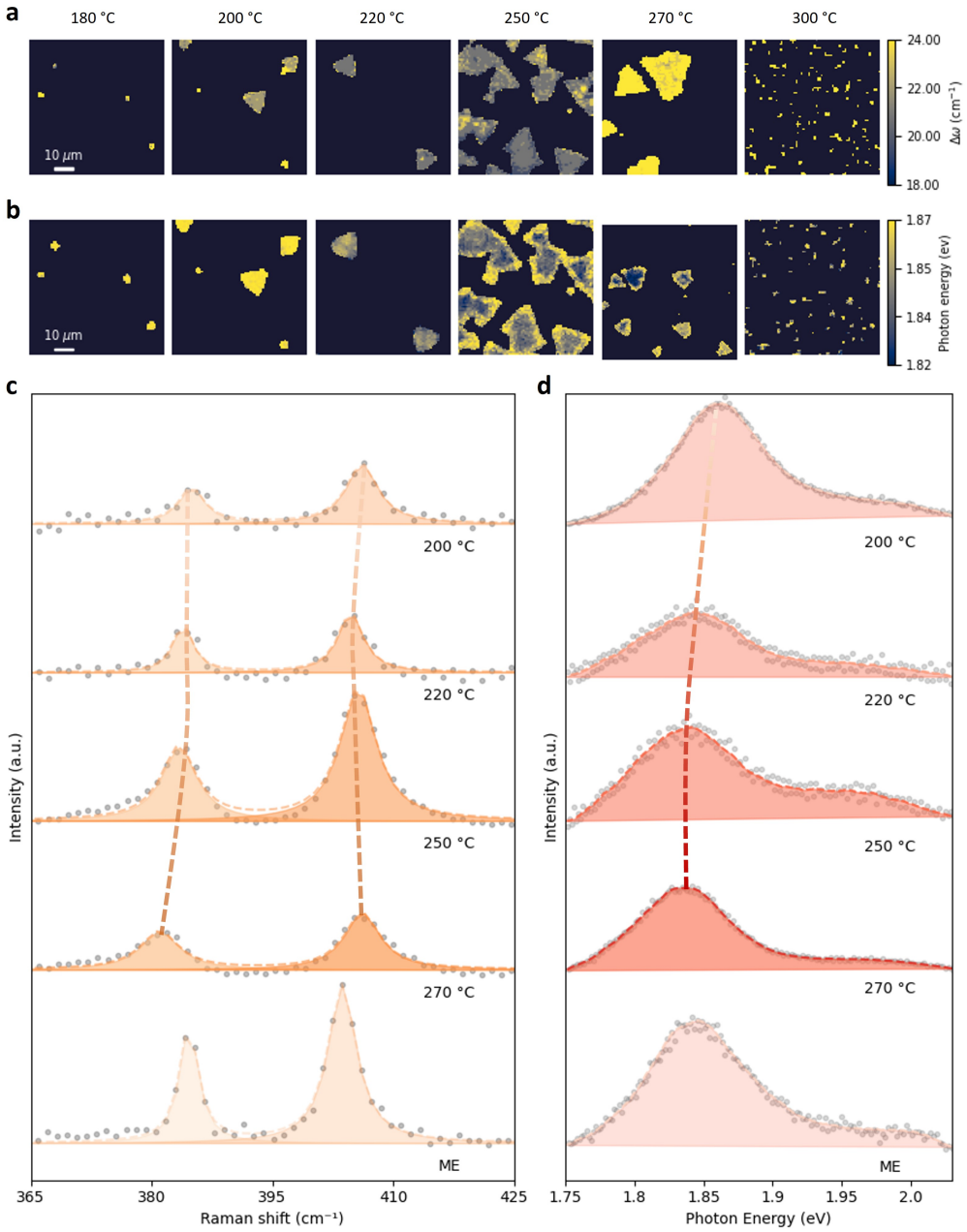


Figure 4.10: **MoS_2 quality at varied sulphur temperature.** (a) Raman mappings of the peak position difference between A_{1g} and E^1_{2g} modes, and (b) PL A exciton (Xa) position mapping at varying sulphur temperatures for the promoter regions. (c) Average Raman spectra of MoS_2 grown at varied sulphur temperature, compared to ME monolayer MoS_2. The spectra are normalized against the Si peak at 520 cm^{-1} and fitted by a Lorentzian function. (d) Average PL spectra of for CVD MoS_2 grown at varied sulphur temperatures and ME monolayer MoS_2.

the map represent the photon energy of the Xa, with brighter yellow indicating higher photon energy and darker shades representing lower photon energy. At 180 °C - 200 °C, the flakes appear bright yellow indicating high Xa exciton energy. With temperature increases, the colour of the flakes becomes darker. At 250 °C - 270 °C, the flakes show darker colour in the centre and bright colour at the edges,

which suggest higher Xa exciton energy at the edges than in the centre due to edge effects [63, 273]. At 300 °C, bright yellow particles are observed.

The average PL spectra in **Fig. 4.10** (d) reveal variations in the Xa exciton energy across different samples. No signal is observed at 180 °C and 300 °C, indicating weak light emission which may be due to the indirect bandgap. For MoS_2 synthesized at 200 °C, the Xa peak appears at 1.876 eV. As the temperature increases from 220 °C to 250 °C, the Xa peak redshifts to 1.851 eV and 1.845 eV (consistent with the ME sample), respectively. At 270 °C, the Xa peak shows a slight blueshift to approximately 1.846 eV. Compared to 250 °C, the blueshift of 0.031 eV observed at 200 °C suggests that excessive oxygen is incorporated into the film under a sulphur deficient condition, which also enhances the PL intensity [171]. The PL intensity is weak at 220 °C increases at 250 °C and decreases again at 270 °C. These results indicate that the highest film quality is achieved at 250 °C.

4.4.3 Sulphur vacancies in MoS_2

The CVD MoS_2 possesses native defects [289], e.g. sulphur vacancies, as observed from the full range Raman spectra in **Fig. 4.7** (g). The atomic defects significantly affect their electronic properties (e.g. carrier mobility, conductivity) and optical properties (e.g. optical bandgap). Thus, we further study the sulphur vacancies in MoS_2 at various sulphur temperatures.

In addition to the main Raman vibration modes of MoS_2 (E^1_{2g} and A_{1g}) shown in **Fig. 4.10** (c), the LA mode in the frequency region 210 - 250 cm^{-1} (**Fig. 4.11** (a)) appears exclusively for the defective structures. Given that sulphur vacancies are the predominant defects in MoS_2, this mode serves as a distinct signature of the sulphur vacancy [165]. The integrated intensity of the LA peaks are plotted in **Fig. 4.11** (h). The integrated intensity decreases as sulphur temperature increases from 200 - 250 °C and rises when the temperature exceeds 250 °C, indicating the lowest defect concentration in the sample at 250 °C. On the contrary, the sample at a temperature of 200 °C exhibits the highest LA intensity. The strong disorder-induced scattering reflects a higher defect density.

Additionally, XPS is employed to characterize the temperature dependence of sulphur vacancies. The Mo 3*d* and S 2*p* core-level spectra for samples at a sulphur temperature of 200 °C, 250 °C and 300 °C are illustrated in **Fig. 4.11** (b, d, f) and (c, e, g), respectively. At a sulphur temperature of 200°C, in the Mo 3*d* core-level spectra (**Fig. 4.11** (b)), multiple peaks indicate the co-existence of multiple chemical states of Mo. A doublet of 229.5 eV and 232.6 eV can be attributed to

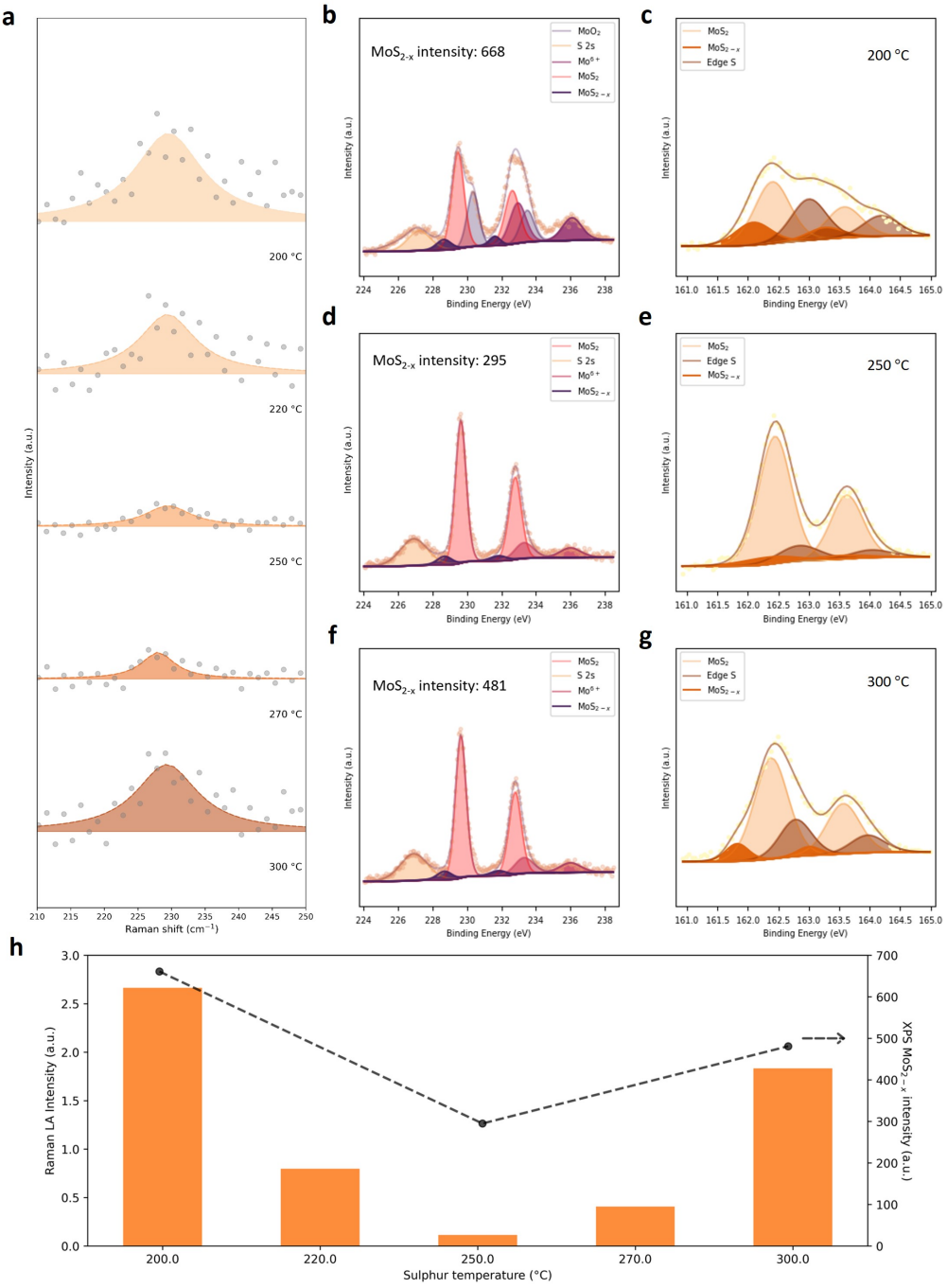


Figure 4.11: **Sulphur vacancy analysis by Raman spectroscopy and XPS.** (a) Raman spectra of the LA mode for samples at temperatures from 200 °C to 300 °C. The peaks are fitted using a Lorentzian function. (b, d, f) XPS Mo 3*d* and (c, e, g) S 2*p* core-level spectra for samples at sulphur temperature of 200 °C, 250 °C and 300 °C, respectively. (h) Raman LA peak intensity and XPS MoS_{2-x} phase intensity for samples at varied sulphur temperatures.

2H MoS_2 [9, 178]. The doublet at 230.1 eV and 233.5 eV is from MoO_2 [199]. Moreover, the other doublet of 229.1 eV and 232.2 eV is due to non-stoichiometric phase MoS_{2-x} [225, 289], and indicates the presence of sulphur vacancy (SV). In addition, Mo^{6+} peaks at 232.9 eV and 236.0 eV are also observed [33, 199].

The fitting of the S 2p core-level spectra in $2p$ core-level spectrum in **Fig. 4.11** (c) corroborate the observation - the doublet at 162.3 eV and 163.5 eV correspond to the 2H MoS_2 [9, 178] and the doublet at a lower energy of 162.1 eV and 163.3 eV can be assigned to the SV [225, 289]. Another doublet at 162.7 eV and 163.8 eV is attributed to edge S [7]. These results suggest that the 200°C sample consists of defective MoS_2 and oxygen. The prominent presence of edge S states implies that the flakes are small and the flake edge is dominantly terminated by sulphur atoms.

For the 250 °C sample, the Mo $3d$ doublet (**Fig. 4.11** (d)) at 229.6 eV and 232.8 eV shows a narrow FWHM indicating high purity 2H MoS_2. The fraction of the Mo^{6+} state at 233 eV and 236 eV has been much reduced. The minimal amount of MoS_{2-x} is observed at the binding energy of 22.87 eV and 231.8 eV. The S $2p$ core-level spectrum in **Fig. 4.11** (e) exhibits a clearly split doublet of S $2p_{3/2}$ and S $2p_{1/2}$ peaks at 162.4 eV and 163.6 eV, indicating the high purity of 2H MoS_2.

When the sulphur temperature is increased to 300 °C, in the Mo $3d$ core-level spectra in **Fig. 4.11** (f), the doublet at 229.6 eV and 232.8 eV corresponds to the 2H MoS_2. Small amounts of MoS_{2-x} and Mo^{6+} components can be observed. Compared to the sample synthesized at 250 °C, the concentration of MoS_{2-x} increases while the Mo^{6+} component remains at a comparable level. The S $2p$ spectrum in **Fig. 4.11** (g), compared with 250 °C, shows increased MoS_{2-x} and S-edge.

The integrated intensity of the MoS_{2-x} phase in Mo $3d$ spectra for samples at 200 °C, 250 °C and 300 °C is shown in **Fig. 4.11** (h). The 200 °C sample exhibits the highest MoS_{2-x} component while the 250 °C sample shows the lowest, which is consistent with the Raman analysis.

The sulphur vacancy in the 200 °C sample is further validated through Transmission Electron Microscopy (TEM) analysis. **Figure 4.12** (a) displays an HRTEM image of MoS_2 showing the lattice. The distinct diffraction spots in the selected-area diffraction (SAED) pattern (**Fig. 4.12** (b)) show six hexagon spots, indicating single-crystal nature. The high resolution aberration-corrected scanning transmission electron microscopy (ACSTEM) images (**Fig. 4.12** (c)) show the atomic arrangements within the MoS_2 lattice, where SV can be clearly observed. The intensity profile along the yellow box region is shown in **Fig. 4.12** (f). Single SV and double SV are identified by the reduced intensity.

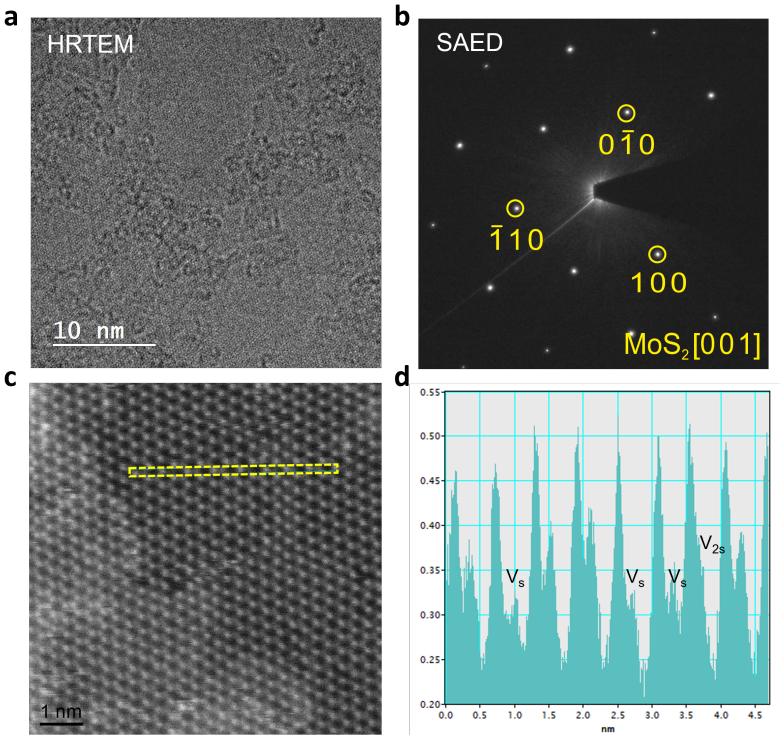


Figure 4.12: **Sulphur vacancy observation in the MoS_2 at sulphur temperature of 200 °C.** (a) HRTEM image shows the MoS_2 lattice planes. (b) SAED pattern of the 2H MoS_2. (c-e) ACSTEM images at varied magnification. (f) The line profile acquired along the line in (e). Images acquired by Dr. Xuyun Guo.

4.5 The mechanism of growth promotion

To explore and understand the significance of the promoter and sulphur in the growth process of MoS_2, the composition of the polymer and the thermal behaviour of the MoO_3 are thoroughly investigated, aiming to uncover the underlying mechanisms that drive the enhanced growth in the promoter region.

The TGA is conducted to compare the thermal behaviour of the MoO_3 with and without sulphur, as shown in **Fig. 4.13** (a). The Stage 1, ranging from room temperature to 330 °C, corresponds to sulphur sublimation, while Stage 2 spans from 330 °C to 740 °C, preceding the high rate Stage of MoO_3 sublimation. For MoO_3 without sulphur, there is no weight loss during Stage 1 and the weight loss in Stage 2 is 0.83%. In contrast, for the MoO_3 with sulphur, the initial sulphur to total mass ratio is 30.79%. The weight loss of Stage 1 is 28.79% indicating residual sulphur that may form $MoO_{2-x}S_x$. During Stage 2, the weight loss is 1.96%, giving the total weight loss of 30.75% after Stage 2, suggesting that sulphur remains in the compound.

The differential thermo-gravimetric (DTG), or first derivative of the weight with respect to time, curves plotted in **Fig. 4.13** (b) shows that the maximum

sublimation rate of MoO_3 is higher in the presence of sulphur (0.053 mg/s) compared to its absence (0.046 mg/s). Furthermore, MoO_3 with sulphur reaches its maximum sublimation rate earlier than without sulphur, indicating a faster acceleration of sublimation. This increased sublimation rate may result from the formation of intermediate product $MoO_{2-x}S_x$, which has weaker Mo-S bonds compared to Mo-O bonds [244], facilitating decomposition thus the sublimation. These findings suggest that the MoO_3 sublimation rate and gas phase concentration can be tuned by the sulphur concentration. In our experiment, the sulphur temperature plays a crucial role in regulating the sulphur evaporation rate. A higher sulphur temperature results in a greater sulphur concentration in the ambient, leading to an increased S-to-Mo ratio.

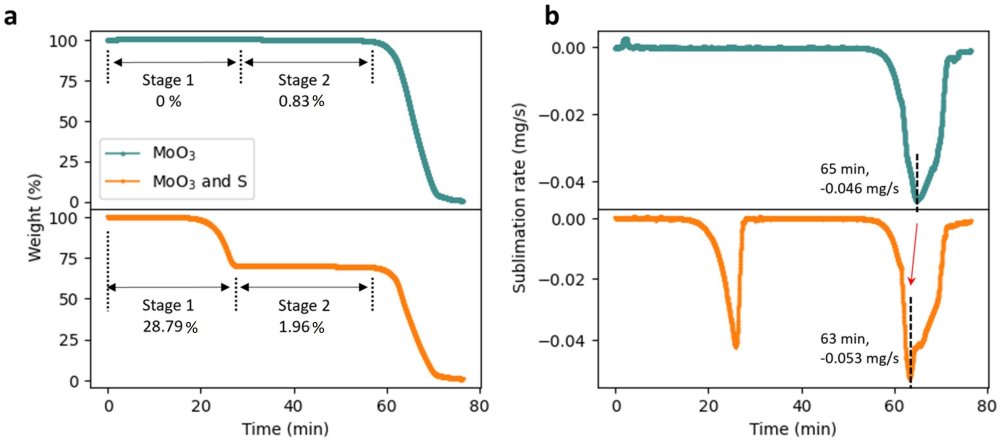


Figure 4.13: **Thermal behaviour of S and MoO_3.** (a) TGA and (b) DTG result of MoO_3 with and without S, which shows MoO_3 evaporation rate when the presence of S.

Energy-dispersive X-ray Spectroscopy (EDX) mapping of the Si wafer coupon reveals the chemical modifications of the substrate surface introduced by the polymer promoter. **Figure 4.14** (a) is an SEM image of the region where the left side is the polymer region and the right side is the pristine region. **Figure 4.14** (b) shows the S Kα element mapping. The promoter region exhibits a robust signal, significantly stronger than that of the pristine region, where the weak signal is attributed to the background. Subsequent EDX spectroscopy analysis, as depicted in **Fig. 4.14** (c) and (d), compares the element composition of the substrate with that of the promoter. The apparent S peak in **Fig. 4.14** (d) further confirms that the promoter particles contains detectable amount of sulphur.

The sulphur concentration is influenced not only by the temperature but also by the presence of nano promoters. Nano promoters locally increases the fractional sulphur concentration, promoting the reduction and sulphurisation of MoO_3, thereby facilitating MoS_2 nucleation. In contrast, in the pristine region, the insufficient reduction of MoO_3 results in the formation of MoOx instead of

MoS_2. Furthermore, the decomposition of nano promoters at high temperatures releases carbon, which further enhances the reduction of MoO_3 and inhibits the formation of MoOx.

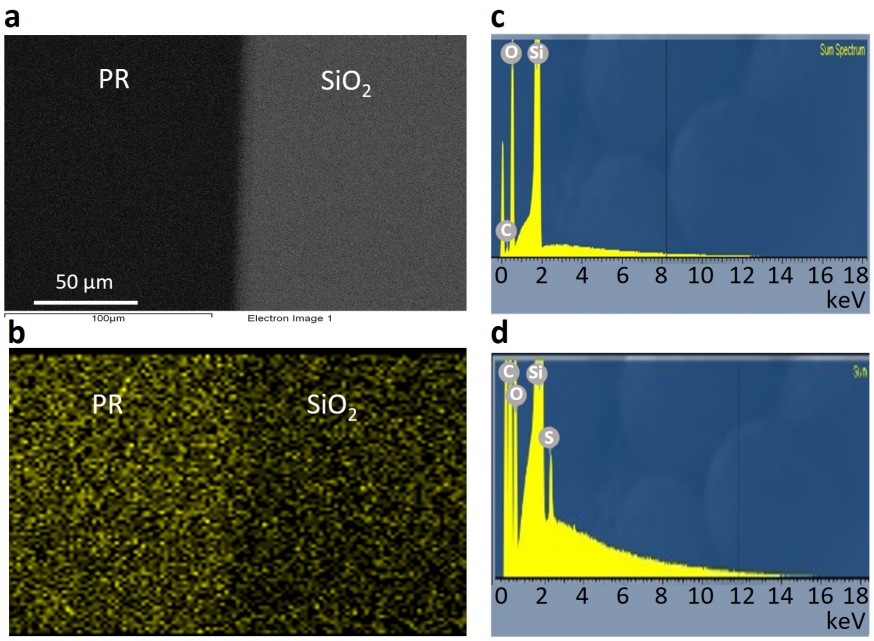


Figure 4.14: **Chemical composition analysis of the polymer promoter.** (a) SEM and (b) EDX mapping of the SiO_2 substrate and promoter. (c-d) EDX spectra compare the element component of the substrate and promoter, respectively.

Figure 4.15 presents a schematic illustrating the effects of the promoter at varying sulphur temperatures. At low temperature (e.g. 200 °C), the ambient sulphur concentration is insufficient. In the pristine region, MoS_2 nucleation is hindered due to the sulphur deficiency. In contrast, in the promoter region, sulphur supplied by the nano promoter enables MoS_2 nucleation. However, the overall low sulphur concentration remains inadequate to support extensive film growth. Consequently, the resulting flakes are small and exhibit either hexagonal geometry or small triangles with rounded edges, which are likely to contain significant sulphur vacancies.

As the temperature increases to 250 °C, the reactant concentration rises, ensuring a consistent and moderate supply of reactants. In the promoter region, this facilitates the 2D film growth with a triangular geometry and reduced defect density. Additionally, as previously discussed, the decomposition of the nano promoter at high temperatures provides carbon, which facilitates the reduction of MoO_3 and suppresses the deposition of MoOx on the substrate. This enhanced reduction of Mo combined with a sufficient supply of reactants, promotes preferential growth in the promoter region.

At higher temperatures (e.g. 300°C), there is abundant sulphur in the ambient, which also accelerates the consumption of MoO_3, leading to a peak concentration of both S and Mo reactant within a short timeframe. The supersaturated reactant concentration leads to a mass transport-limited CVD process [174], resulting in a high density of the particles across the entire substrate, regardless of promoter treatment. This indicates a highly homogeneous nucleation process in both pristine and promoter regions. Excess reactants spontaneously nucleate numerous MoS_2 particles throughout the substrate, without influence from any foreign surface (e.g. promoters). It's important to note that homogeneous nucleation doesn't exhibit any preferential attachment to the nano promoters on the substrate, instead, it results in a more dispersed distribution of MoS_2 particles. During the nucleation Stage, the rapid depletion of S and Mo reactants limits the availability of reactants for further film development.

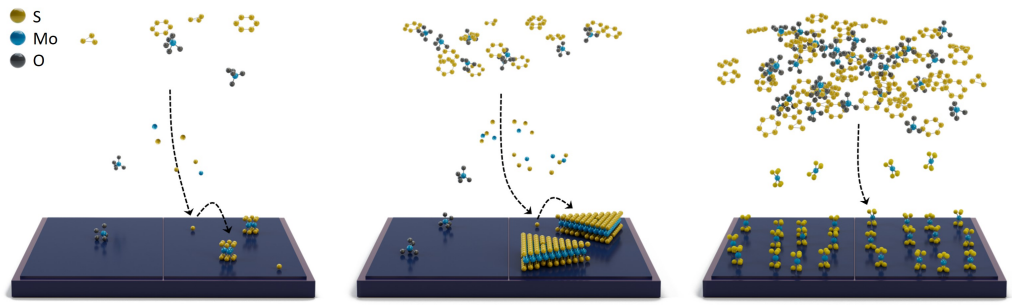


Figure 4.15: **A schematic illustration of the promoter effects:** at 200 °C (left), 250 °C (middle) and 300 °C (right), respectively.

To summarise, the heterogenous nucleation dominated MoS_2 growth occurs when the sulphur temperature is between 200 and 300 °C. This process is regulated by controllable nanoscale promoters in terms of position and density, leading to a more organized and well-structured growth compared to randomly homogeneous nucleation.

4.6 Conclusions

In summary, we have developed a novel strategy to access a clean and controllable growth of 2D materials on the amorphous SiO_2 substrate. The promoter effect has been investigated and confirmed by AFM, Raman, PL, SEM and XPS. It is demonstrated that the polymer-induced heterogeneous nucleation enhances the MoS_2 growth. Further study compares the homogeneous and heterogeneous nucleation at varied sulphur temperatures. Statistical analysis shows that the sulphur temperature of 250°C is optimum for the uniform growth of monolayer MoS_2 with a large flake size. The evolution of sulphur vacancy at varied sulphur

temperatures is studied by XPS, Raman and TEM measurement. It is found that SV concentration is high in the sample at low sulphur temperature due to insufficient S reactant concentration, while it is lowest for the sample at 250 °C. Our method achieves the clean and controllable growth of MoS_2, holding the potential for developing high-performance microelectronic devices with minimised device variability.

5 | Patterned growth of MoS_2

"To know what you know and what you do not know, that is true knowledge."

- Confucius

Direct patterned growth of MoS_2 on target substrates avoids contamination from transfer and etching [34, 206], simplifying fabrication and preserving intrinsic film properties. The previous chapter demonstrated that promoter-induced heterogeneous nucleation significantly enhances two-dimensional (2D) MoS_2 growth in the chemical vapour deposition (CVD) process. Building on this, we now leverage the patentability of photoresist S1813 by preparing the promoter patterns before the CVD process, aiming at achieving scalable and selective MoS_2 growth with tailored morphologies. This chapter first outlines the experimental methods and then the characterisation of the as-grown MoS_2 film. We then optimised growth conditions, including reactant concentration and the dimensions of the promoter arrays. This work demonstrates the feasibility of scalable selective MoS_2 growth on a SiO_2 substrate with precise thickness and geometry control, advancing its potential for device applications.

5.1 Substrate preparation and CVD process

Silicon wafers with a thin SiO_2 layer were used as the substrate. To define mesa arrays of the growth promoter on the SiO_2/Si wafer, laser direct writing (LDW) and optical lithography (OL) were employed for photoresist (PR) patterning. Prior to the patterning process, the wafers underwent ultrasonic cleaning in acetone, isopropyl alcohol (IPA), and deionized (DI) water for 5 minutes each, followed by nitrogen (N_2) drying for $\sim$ 5 seconds.

PR patterns were created on a 4-inch SiO_2/Si wafer (n-type, 300 nm thick thermal oxide) using LDW, with assistance from Dr. Chris Murray. The wafer was

spin-coated with S1813 photoresist at 7000 rpm, exposed to a 375 nm laser at 55.3 mW, and developed for 45 seconds in MF-319 developer. **Figure 5.1** (a) displays an image of the wafer after the LDW process. The LDW process patterned the wafer surface with 21 identical blocks. Each 15 $\times$ 15 mm^2 block consists of a 12 $\times$ 12 array of polymer mesas (**Fig. 5.1** (b)), arranged with a $\sim$ 0.7 mm spacing between individual mesas. As indicated by the white arrows, another array of four closely packed 5 $\times$ 5μm^2 PR mesas was written on the substrate to serve as alignment marks, referred to as such hereafter. The two arrays are interpenetrating, with their elements arranged in an alternating pattern. As shown in **Fig. 5.1** (c), each mesa has dimensions of 200 $\times$ 20 μm^2 and a height of 920 nm. The wafer is then diced into 21 individual substrates, each containing a complete array of polymer mesas.

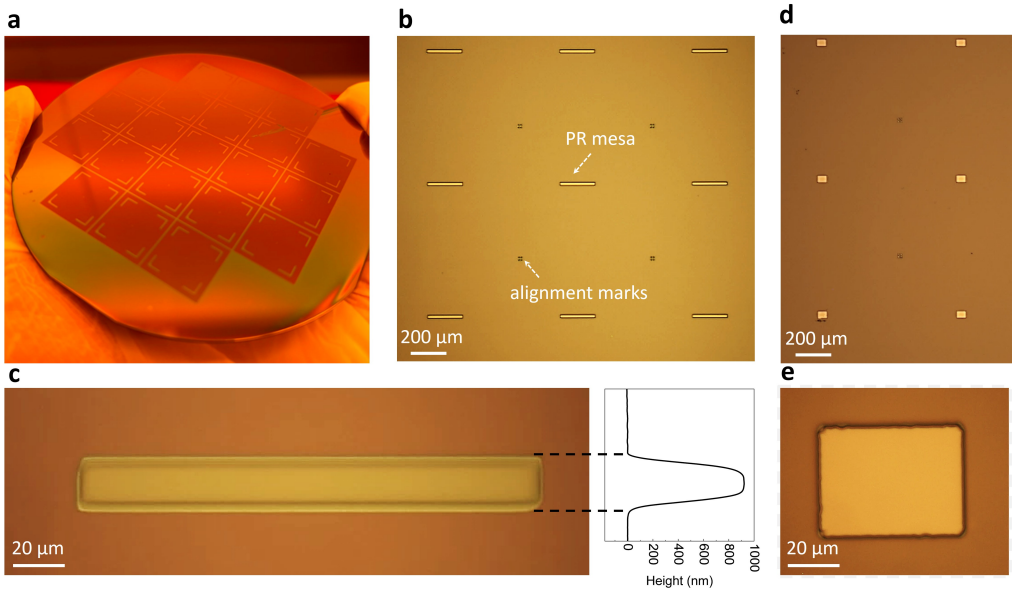


Figure 5.1: **Optical images of LDW PR patterns on SiO_2/Si.** (a) Patterns on a 4-inch SiO_2/Si wafer. (b) A substrate contains 9 mesas in 3 $\times$ 3 arrays created by LDW. (c) Optical image of one LDW mesa with a dimension of 200 $\times$ 20 μm^2 and a thickness of 920 nm. (d) 9 mesas in 3 $\times$ 3 arrays created by OL. (e) One OL mesa with a dimension of 50 $\times$ 40 μm^2.

We utilized OL as an alternative approach to effectively control the dimensions of the PR mesa arrays. The process begins with spin coating the PR onto a 15 $\times$ 15 mm^2 SiO_2/Si substrate (n-type, 285 nm thermal oxide) at 5000 rpm for 45 seconds, followed by ultraviolet (UV) exposure for 6.5 seconds and development in MF-319 for 45 seconds. This standard OL process yields PR patterns with a size of 50 $\times$ 40 μm^2 and a thickness of 1.3 μm (**Fig. 5.1** (d-e)). To achieve thinner PR patterns, flood exposure is applied. The PR thickness, ranging from 350 nm to 1.5 μm, can be controlled by adjusting the spin coating speed (1000 - 7000 revolutions

per minute (rpm)) and flood exposure duration (0 – 4 s).

The substrate with the as-patterned PR mesas is then subjected to CVD growth using the recipe outlined in chapter 3 section 3.1.1. A typical growth process is conducted at 835 °C under a N_2 flow of 20 sccm for 5 minutes at atmospheric pressure. As illustrated in **Fig. 5.2**, the substrate is tilted at an angle of 120° relative to the tube axis and positioned downstream from the MoO_3 powder in the crucible. The distance between the Mo source and the substrate is a critical factor influencing the reactant concentration, which varies based on the position of the PR mesas ($0 < y < 15$ mm) and the horizontal spacing between the MoO_3 powder and the bottom of the substrate (z). During a single growth run, z remains constant, while each mesa experiences a different growth environment due to variations in y. To systematically investigate the effect of reactant concentration on MoS_2 growth, z was adjusted across multiple growth runs (see section 5.3.2).

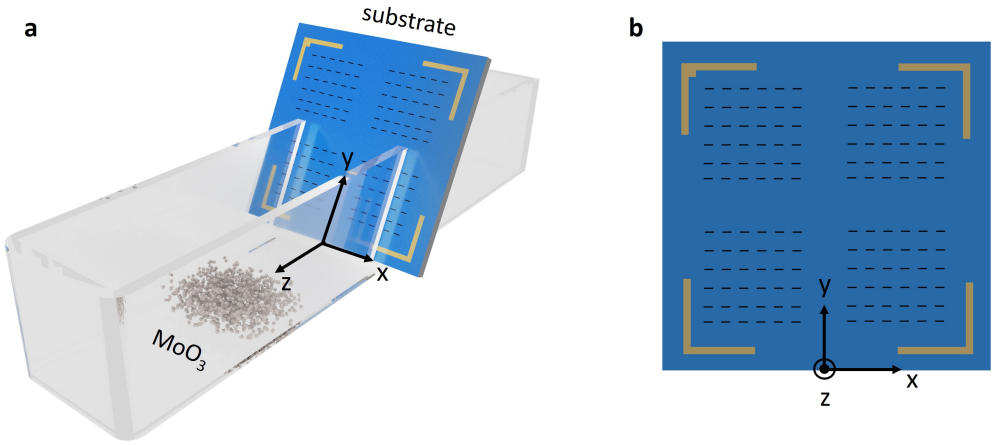


Figure 5.2: **Mesa positioning in the patterned growth.** A Cartesian coordinate system is used to define the position of a mesa within the array relative to the substrate and reactants.

It is worth noting that S1813 can be developed using various developers, including alkali hydroxide (e.g. NaOH, KOH), MF-319, etc. In this work, we select MF-319, which primarily consists of water and tetramethylammonium hydroxide $C_4H_{13}NO$, to maintain an alkaline environment while minimizing alkali ion contamination.

5.2 Patterned MoS_2 films using LDW mesas

5.2.1 General morphology

The optical micrograph in **Fig. 5.3** (a), acquired from the top-middle region of the substrate ($x \sim 2$ mm, $y \sim 12$ mm), reveals the characteristic morphology of the patterned growth following the CVD process. In the micrograph, the mesa regions appear black, surrounded by 30 μm-wide light-blue films that are distinctly visible against the substrate. A similar morphology is observed at the small alignment marks, where the CVD product forms light-blue films around the black mesa regions. Beyond the intentionally placed mesas, the substrate surface is covered with randomly distributed, micrometer-sized brown particles (see the inset of Figure 1.3(a)). These particles predominantly exhibit parallelogram or hexagonal shapes. Their irregular polygonal geometry suggests that they are crystallites belonging to a low-symmetry crystal system. Similar to the mesa regions, many of these polygonal particles are also encircled by light-blue films.

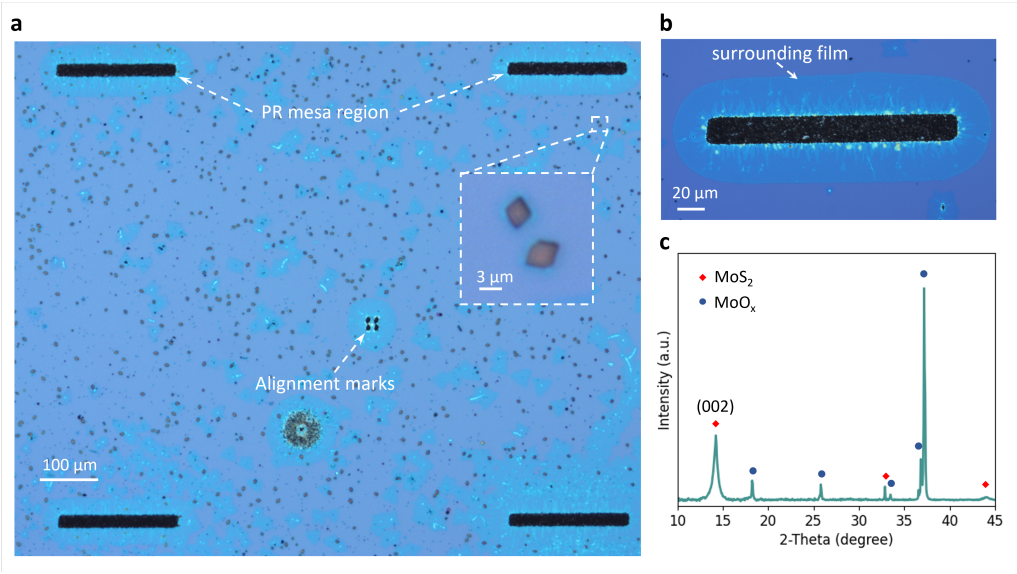


Figure 5.3: **Typical morphology of the CVD products synthesized using the LDW patterned mesa array.** (a) The mesa array after the growth reveals selective growth of thin films around individual mesas, while there are polygonal particles scattered on the substrate surface. (b) The surrounding film of a single mesa exhibits bright stripes. (c) X-ray diffraction (XRD) pattern of the as-growth sample suggests a mixture of MoO_x and MoS_2.

A magnified view of an individual mesa region is shown in **Fig. 5.3** (b). The light-blue film exhibits fine textures with streaks extending from the mesa towards its edges. The observed optical contrast suggests that the surrounding film and mesa may be composed of different materials and/or exhibit variations in thickness and surface roughness. Additionally, we note the detailed morphology

of the features (i.e. mesa, surrounding film, particles) varies across the substrate, which will be discussed in section 5.3)

The XRD pattern shown in **Fig. 5.3** (c) was obtained from a region approximately <1 mm in size. The observed peaks correspond to two primary phases: MoO_x and MoS_2. The MoS_2 phase exhibits a dominant peak at $2\theta = 14°$, corresponding to a lattice spacing of 0.62 nm, originating from the (002) plane of the 2H-MoS_2 phase (JCPDS No. 00-037-1492). The prominence of this peak indicates that the majority of the 2H-MoS_2 phase has its *c*-axis oriented perpendicular to the substrate surface. In contrast, the peaks associated with MoO_x likely correspond to multiple molybdenum oxides with varying stoichiometry, with MoO_2 (JCPDS No. 65-5787) being the predominant phase. Since the X-ray beam size is comparable to the spacing between the mesas, the diffraction pattern was most likely obtained from a region containing a single mesa. As a result, the dominant morphological features analyzed by XRD are the brown polygonal particles located between the mesas. The relatively high intensity of the MoO_x peaks suggests that these particles primarily consist of MoO_x, while the surrounding films are likely composed of *c*-oriented MoS_2.

Optical contrast (OC) analysis is employed to map the detailed topographical features of these CVD products. As shown in **Fig. 5.4** (a), the majority of the surrounding film (78%) is identified as monolayer MoS_2 (white), while the streaks appear to consist of a few layers (2–5 layers, green). However, the optical contrast of the mesa regions falls beyond the measurable range of OC analysis.

To further reveal the detailed topographical features of the CVD products, we conducted AFM measurements. **Figure 5.4** (b) presents a height image of the surrounding film near its outer edges. A line scan (**Fig. 5.4** (e)) across the substrate-film boundary confirms that the film thickness is approximately 0.68 nm, corresponding to a monolayer of MoS_2. Additionally, line scans across the streak boundaries, as shown in **Fig. 5.4** (e), reveal a sharp height increase of 0.68 nm. This indicates that the streaks consist of few-layer MoS_2, with an additional layer deposited on top of the base layer, rather than being embedded beneath it. These findings are consistent with the OC mapping results, suggesting that the surrounding film comprises two-dimensional MoS_2.

The height map of the mesa region, **Fig. 5.4** (c), and the corresponding line scan, **Fig. 5.4** (f) confirm that the CVD process reduced the mesa thickness by 35%, decreasing from 920 nm to approximately 600 nm at the mesa centre. A sharp height increase of $\sim$ 200 nm marks the boundary of the mesa region. Concurrently, the surface roughness within this region rises to approximately 100

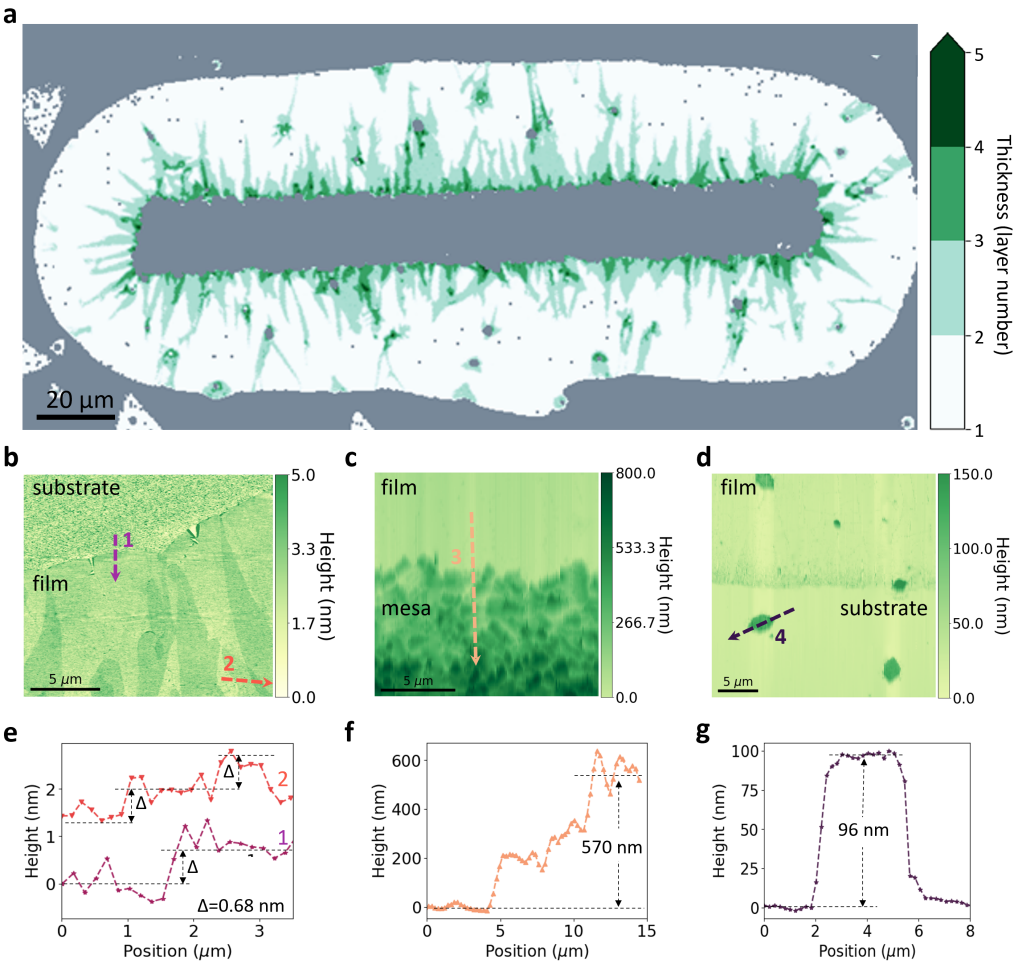


Figure 5.4: **Atomic force microscopy (AFM) characterisation of samples grown from LDW mesas.** (a)Thickness identification by MoS_2 OC screening, with the monolayer region shows in white. AFM height images of (b) the surrounding film region on the substrate, (c) the boundary between the surrounding film and mesa regions, and (d) hexagonal particles. (e-g) Line profiles extracted from the lines marked by dashed lines in (b-d).

nm, suggesting that, following the growth process, the mesa consists of densely packed particles several hundred nanometers in size. The significant reduction in mesa thickness indicates substantial mass loss and/or chemical transformation of the PR during the growth process. Additionally, the hexagonal particles exhibit an average thickness of approximately 120 nm and a surface roughness of 9 nm, as shown in **Fig. 5.4** (d) and **Fig. 5.4** (g). The essential topographical characteristics of the key CVD products are summarized in table 5.1.

Figure 5.5 (a) shows a Scanning Electron Microscopy (SEM) image of a region near the corner of a mesa, captured using the InLens detector on a Zeiss Supra SEM. The surrounding film appears darker than the SiO_2 substrate, indicating a lower secondary electron (SE) yield from the film. Additionally, the few-layered strips exhibit lower brightness compared to the monolayer regions. Given that the 2D film has a smooth surface with a roughness of 0.36 nm, topographical

	Substrate	Mesa region	Surrounding film	Particle
Height (nm)	0	600	0.68 – 3.3	120
Roughness (nm)	0.93	78	0.3	9
Geometry	-	granular thick film	2D	polygonal particle

Table 5.1: **Topological features of the CVD products using LDW mesas.** The meas is located at $(-1.1, 12.3, 10)$ mm, corresponding to **Fig. 5.4**.

contrast can be ruled out as the source of the observed brightness variations. Instead, these variations are attributed to thickness contrast: as the layer thickness increases, it attenuates substrate-generated SEs, resulting in thicker regions appear darker in the SE image. This interpretation is consistent with AFM and OC measurements. The SEM image also reveals finer structural details, as shown in **Fig. 5.5** (b)—a magnified view of the region marked by the white dashed box in **Fig. 5.5**(a). Grain-boundary-like features are evident within the monolayer film and are interspersed with nanometer-sized round particles. In contrast to the surrounding film, the mesa region and hexagonal particles have thicknesses significantly greater than the typical inelastic mean free path of SEs (a few nanometers), meaning their SE contrast is not primarily governed by thickness effects. The mesa region exhibits edge brightness, a characteristic feature of SE emission from nanoparticle surfaces. Furthermore, the brightness difference between the hexagonal particles and the SiO_2 substrate suggests variations in composition and work function.

We analysed the chemical composition of the CVD products using EDX integrated with the SEM. To map the distribution of molybdenum (Mo) and sulfur (S), we examined the Mo L_α (2.293 keV) and S K_α (2.307 keV) emission lines within the energy windows of Mo: [2.237, 2.350] keV and S: [2.251, 2.364] keV. However, due to their close proximity, the two peaks could not be resolved. As a result, we present a composite map of their combined signals in **Fig. 5.5** (c). The mesa region exhibits a significantly stronger signal than the particles, while the signal from the surrounding film is too weak to be distinguished from the substrate. This strong signal suggests that the mesa contains a higher concentration of Mo and/or S per analysed volume, likely due to its thickness or stoichiometry. In contrast, the oxygen signal primarily originates from the underlying SiO_2 substrate, with variations in intensity reflecting signal attenuation. The oxygen map of **Fig. 5.5** (c) shows that the particles exhibit an oxygen signal comparable to that of the surrounding film, despite being significantly thicker, indicating the presence of oxygen. Meanwhile, the mesa region shows a much weaker oxygen

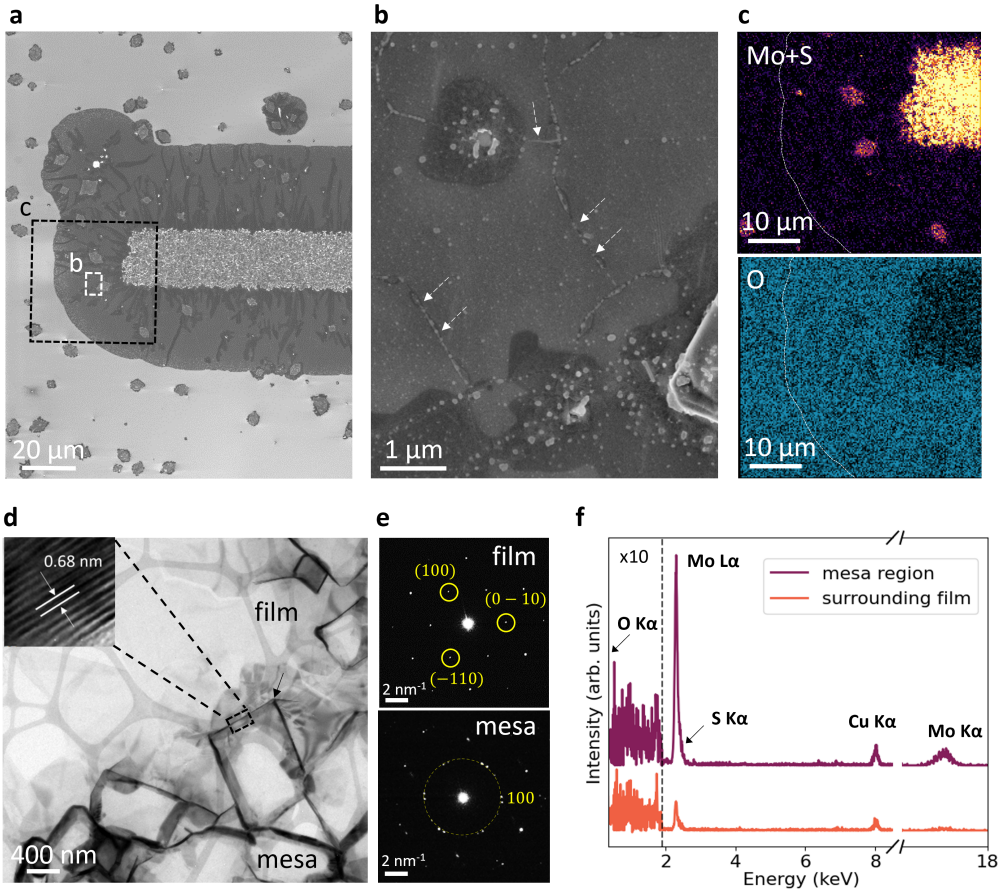


Figure 5.5: **Chemical analysis and microstructure of the patterned MoS_2.** (a) SEM image shows the surrounding film, mesa region and particles. The white dashed box is magnified in (b), showing the grain boundaries indicated by the white arrows. The Energy-dispersive X-ray Spectroscopy (EDX) mapping of the black dashed box is shown in (c), where the white lines mark the boundary of the surrounding film. (d) bright-field (BF) Transmission Electron Microscopy (TEM) image of the film and mesa region with its corresponding selected-area diffractions (SAEDs) in (e) and EDX spectra in (f).

signal, suggesting minimal, if any, oxygen content compared to SiO_2 substrate.

A portion of the surrounding film, along with the mesa region, was transferred onto a TEM grid. **Figure 5.5** (d) presents the BF image of the area near the film-mesa boundary. As expected, the film exhibits minimal contrast in the BF image due to its atomic thickness. Similarly, the grains in the mesa region appear translucent, suggesting that their thickness is less than a few hundred nanometers. The SAEDs from both the film and mesa region are shown in **Fig. 5.5** (e). The film displays a single-crystalline nature, with a set of diffraction spots aligned along the [001] zone axis of 2H-MoS_2. In contrast, the mesa region exhibits multiple sets of [001] zone patterns, each rotated slightly, indicating that the grains in this region retain the 2H symmetry while maintaining their c-axis alignment parallel to that of the surrounding film.

Notably, one of the grains is folded at its edge, as indicated by the black arrow in **Fig. 5.5** (d). The high-resolution lattice image of this folded region (inset of **Fig. 5.5** (d)) clearly reveals a lattice spacing of 0.68 nm, confirming that the mesa region also consists of 2H-MoS_2. Additionally, EDX spectra acquired from the same sample within the TEM confirm that the material is primarily composed of Mo and S, while the mesa region may contain trace amounts of oxygen. (The Cu signal originates from the TEM copper grids.)

5.2.2 Optical properties of patterned MoS_2

Raman spectroscopy and photoluminescence spectroscopy (PL) spectroscopy are essential techniques for characterising 2D materials. **Figure 5.6** (a) presents Raman mapping data, where the four panels, from top to bottom, correspond to the average Raman intensity (I_{all}) integrated over the spectral range of 100–1000 cm^{-1}, the average MoO_2 Raman intensity (I_{MoO_2}) over the range of 180–255 cm^{-1}, the E_{2g} peak shift relative to 385 cm^{-1}, and the A_{1g} peak shift relative to 403 cm^{-1}. The I_{all} map clearly delineates the morphological features discussed in previous sections, with the few-layered surrounding film exhibiting the highest intensity, while the mesa and particle regions show the lowest intensity, approaching the substrate level. This intensity distribution suggests that the Raman signal is predominantly contributed by MoS_2 (e.g. the surrounding film). We note that strong Raman intensity is observed around the hexagonal particles, indicating that they are enveloped by MoS_2 films.

In contrast, the I_{MoO_2} map highlights the spatial distribution of MoO_2, as MoS_2 does not exhibit Raman peaks in this spectral range, whereas MoO_2 features distinct vibrational modes at 190 cm^{-1} (A_g) and 210 cm^{-1} (B_g) [243]. Indeed, the Raman spectrum of the particle, as shown in **Figure 5.6** (b), confirms its composition as MoO_2, displaying all characteristic MoO_2 Raman peaks (marked by blue dots). The mapping results suggest that all the micrometer-sized hexagonal particles are composed of MoO_2. Additionally, the I_{MoO_2} map reveals the presence of small MoO_2 particles distributed throughout the surrounding film and the mesa region.

Figure 5.6 (b) compares the Raman spectra obtained from these regions, including the surrounding films (monolayer, bilayer, and few-layered regions), the mesa region, and the hexagonal particles. All spectra exhibit characteristic MoS_2 vibrational modes at approximately 385 cm^{-1} for E_{2g} and 403 cm^{-1} for A_{1g}, while the peak shift is evident in the spectra. The peak positions extracted from these spectra are summarized in Table 5.2. The E_{2g} peak exhibits a red shift across

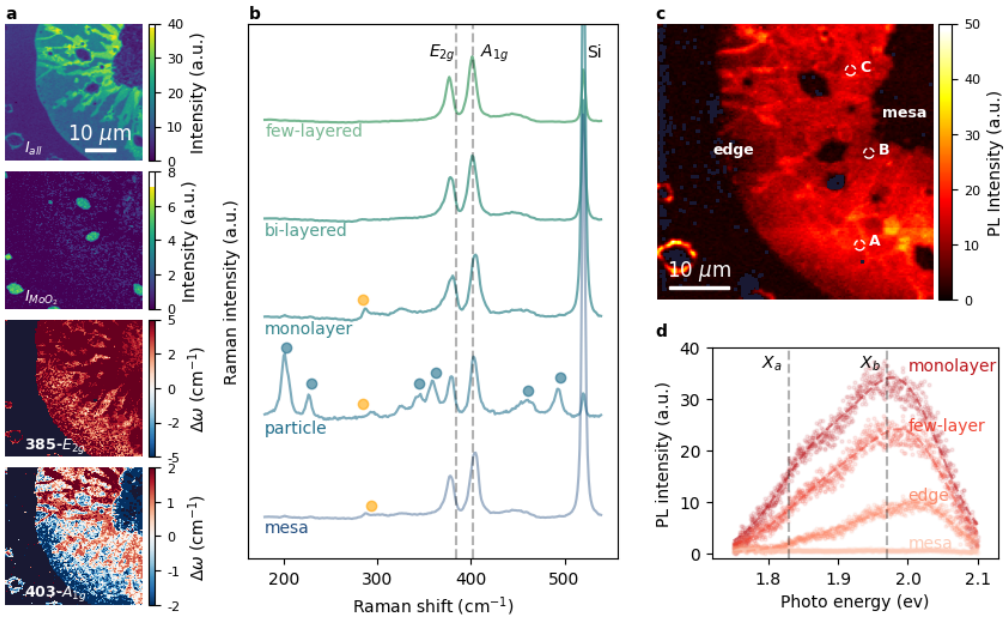


Figure 5.6: **Optical properties of the patterned MoS_2.** (a) Raman mapping of the sample, from top to bottom, the overall intensity mapping, the intensity in the range of 180-255 cm^{-1}, the peak shift of E_{2g} relative to 385 cm^{-1}, and the A_{1g} peak shift relative to 403 cm^{-1}. (b) Raman spectra of the surrounding film (monolayer, bilayer, few-layered regions), particles and mesa regions. (c) PL intensity mapping. (d) PL spectra of the regions marked in (c).

all regions, with the shift magnitude increasing with layer thickness, as shown in the third panel of **Fig. 5.6** (a). In contrast, the A_{1g} peak displays distinct behaviours depending on the region. A red shift is observed in the few-layered regions of the surrounding film, while in monolayer regions, the A_{1g} peak exhibits a blue shift. A red shift in Raman peaks generally indicates phonon mode softening, which can be attributed to structural defects, substrate interactions or tensile strain [226]. The blue shift of the A_{1g} peak in monolayer regions is associated with the reduction in interlayer van der Waals interactions, which weakens interlayer coupling and stiffens the out-of-plane vibrational mode. These Raman results suggest that the MoS_2 films contain a high density of structural defects. Furthermore, the peak at ∼290 cm^{-1} (marked with red dots) can be attributed to orthorhombic MoO_3 [243]. The presence of these oxides indicates an incomplete sulfurisation process.

Figure 5.6 (c) presents PL intensity mapping of excitonic emissions. Detectable PL signals are observed exclusively in the surrounding films, including regions adjacent to the hexagonal MoO_2 particles, confirming their few-layered nature. PL emission is generally enhanced in most of the monolayer regions and at grain boundaries. However, some few-layered regions also exhibit strong PL emission, although the underlying mechanism for this enhancement remains

unclear. In contrast, certain monolayer regions, labelled as "edge" in **Fig. 5.6** (c), exhibit significantly reduced PL intensity, suggesting a high density of non-radiative defects that quench luminescence [163].

	surrounding film			mesa	particles
	A	B	C		
E_{2g}	381.3	378.9	377.6	377.6	379.3
A_{1g}	404.5	401.9	401.9	404.5	402.7

Table 5.2: **MoS_2 Raman peaks detected from the LDW pattern.**

Figure 5.6 (e) presents the PL spectra corresponding to the regions marked in **Fig. 5.6** (c). All spectra exhibit a dominant X_b peak at approximately 1.9 eV, indicative of strong electron doping, which suppresses X_a emission. This observation suggests that the MoS_2 film is rich in sulfur vacancies, as these vacancies introduce shallow donor states that increase electron density and influence excitonic behaviour [130, 163].

The combined Raman and PL analyses confirm that the surrounding film consists of few-layered MoS_2 with a high concentration of sulfur vacancies. The substrate surface is decorated with MoO_2 particles, appearing as micrometer-sized irregular hexagonal structures and smaller nanoparticles. The mesa region is primarily composed of bulk MoS_2 with a minor degree of oxygen incorporation.

5.3 Morphology evolution of patterned MoS_2

We previously noted that the detailed morphology of the CVD products varies depending on the mesa's position. This variation arises from the non-uniform distribution of reactants across the substrate surface, as suggested by the configuration of the substrate and MoO_3 sources within the CVD system (see **Fig. 4.2** (a)). In this section, we investigate how morphological characteristics - including particle density, mesa height, and the width of the surrounding film — depend on mesa location. These insights will help elucidate the growth mechanism and inform strategies for optimising the patterned growth process.

5.3.1 Growth variation in a single CVD run

The optical images in **Fig. 5.7** (a) illustrate the morphological evolution across the substrate (see Appendix **Fig. A.5** for a complete set of optical images of the mesa array). Each image is labelled with its corresponding $[x, y]$ coordinates and

its distance, d, from the MoO_3 source [1]. The three mesas in the left column are positioned near the medial line of the substrate ($x \simeq 0$ mm), while those in the right column are adjacent to the crucible wall ($x = 4.6$ mm).

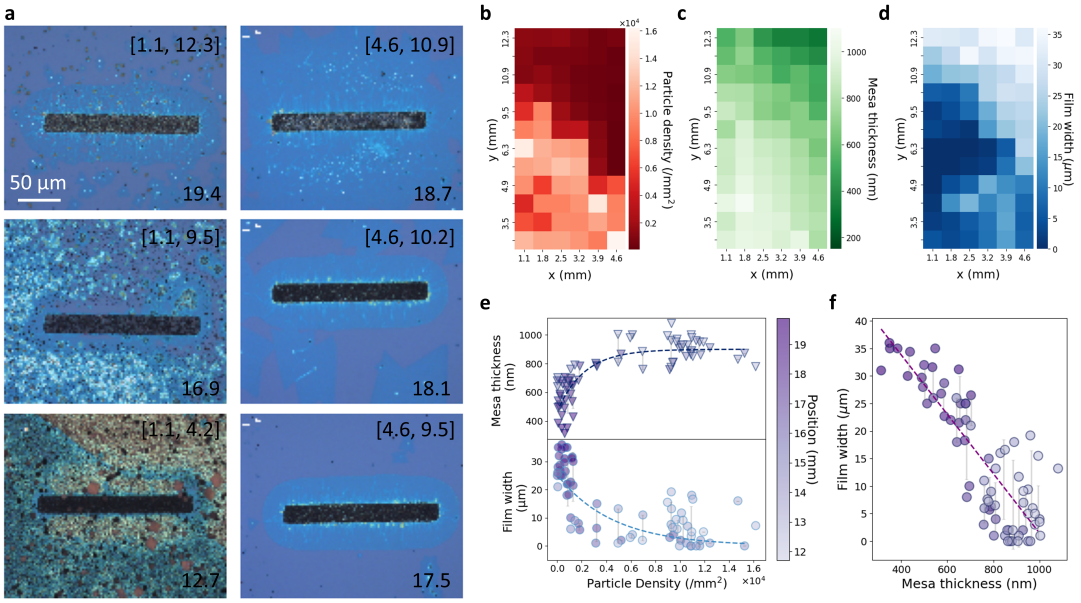


Figure 5.7: **Growth variation in a single CVD run with $z = 10$ mm.** (a) Optical images of typical the CVD-grown morphologies showing variations in particle density and surrounding film width. The coordinates $[x, y]$ of each mesa (in mm) are displayed in the top right corner of each image, while the distance from the MoO_3 source (in mm) is provided in the bottom right corner. The spatial distributions of particle density, mesa height and film width are mapped in (b), (c) and (d), respectively. (e) The mesa height (film width) and particle density show a positive (negative) correlation, while in (f) the film width and mesa height suggest an inverse linear relationship.

The region closest to the MoO_3 source ($d = 12.7$ mm) exhibits a high density of large black and brown polygonal particles. As the mesa–MoO_3 distance increases, both the density and size of these particles progressively decrease, as shown in **Fig. 5.7** (b), which maps the particle density distribution across the right half of the substrate with respect to the medial line. Meanwhile, the map in **Fig. 5.7** (c) demonstrates a reduction in mesa height with increasing distance from the MoO_3 source, whereas **Fig. 5.7** (d) reveals a corresponding increase in the width of the surrounding 2D film.

The relationships among particle density, mesa thickness and film width are

[1] In the CVD growth process, the substrate is inclined at an angle of 60° relative to the tube axis, with the centre of its bottom edge positioned at $z = 10$ mm from the MoO_3 source (see figure***). Consequently, the distance between a mesa at $[x, y]$ and the MoO_3 source is given by

$$d = \sqrt{x^2 + y^2 + z^2 + 2zy\cos\theta}.$$

The uncertainty in d can be up to 1 mm.

further analysed in **Fig. 5.7** (e), where the color of the data points represents the mesa–MoO_3 distance (see color bar). The data indicate that lower particle density correlates with thinner mesa regions and broader 2D films. Notably, **Fig. 5.7** (f) suggests an inverse linear relationship between film width and mesa thickness, implying that the formation of the surrounding 2D film may be driven by material consumption from the mesa region.

Furthermore, a significant density of MoO_x particles, ranging from 2×10^3 to 1.6×10^4 mm^{-2}, is observed across the substrate. This suggests that MoO_x remains in excess relative to sulfur in the local growth environment adjacent to the substrate.

5.3.2 Reduction of MoO_x in the growth environment

As discussed in the previous section, the CVD environment contains an excessive concentration of MoO_x, leading to the uncontrollable deposition of MoO_x particles. This section explores an approach to mitigating this issue by reducing MoO_x concentration during growth. To achieve this, the CVD process was conducted with double the sulfur partial pressure, increasing sulfur consumption from 36 mg in the previous growth to 72 mg. Simultaneously, the substrate was positioned further from the MoO_3 source, increasing the distance from 10 mm to 12 mm. All other growth parameters remained unchanged to the extent permitted by the system.

The results, shown in **Fig. 5.8** (a), indicate that these modifications led to a twofold reduction in particle density. Additionally, the average mesa height decreased by approximately 50%, as shown in **Fig. 5.8** (b). However, the width of the surrounding film remained largely unchanged. In certain regions of the substrate, a continuous thin MoS_2 film formed between mesas, as indicated by the white-coloured regions enclosed by red borders in **Fig. 5.8** (c). Since these continuous films prevent an accurate evaluation of controlled pattern growth on individual mesas, they were excluded from the subsequent analysis.

Figure 5.8 (d) (top panel) illustrates that reducing Mo concentration while increasing sulfur availability does not alter the correlation between mesa thickness and particle density, as also observed in **Fig. 5.7** (d). This result suggests that mass loss in the mesa region remains strongly dependent on Mo availability. A higher Mo concentration in the ambient results in lower mass loss and, consequently, thicker mesas after CVD growth. In contrast, the bottom panel of **Fig. 5.8** (d) shows that the surrounding film width exhibits a maximum as the particle density (i.e., MoO_x concentration) decreases. The colour of the scatter points in

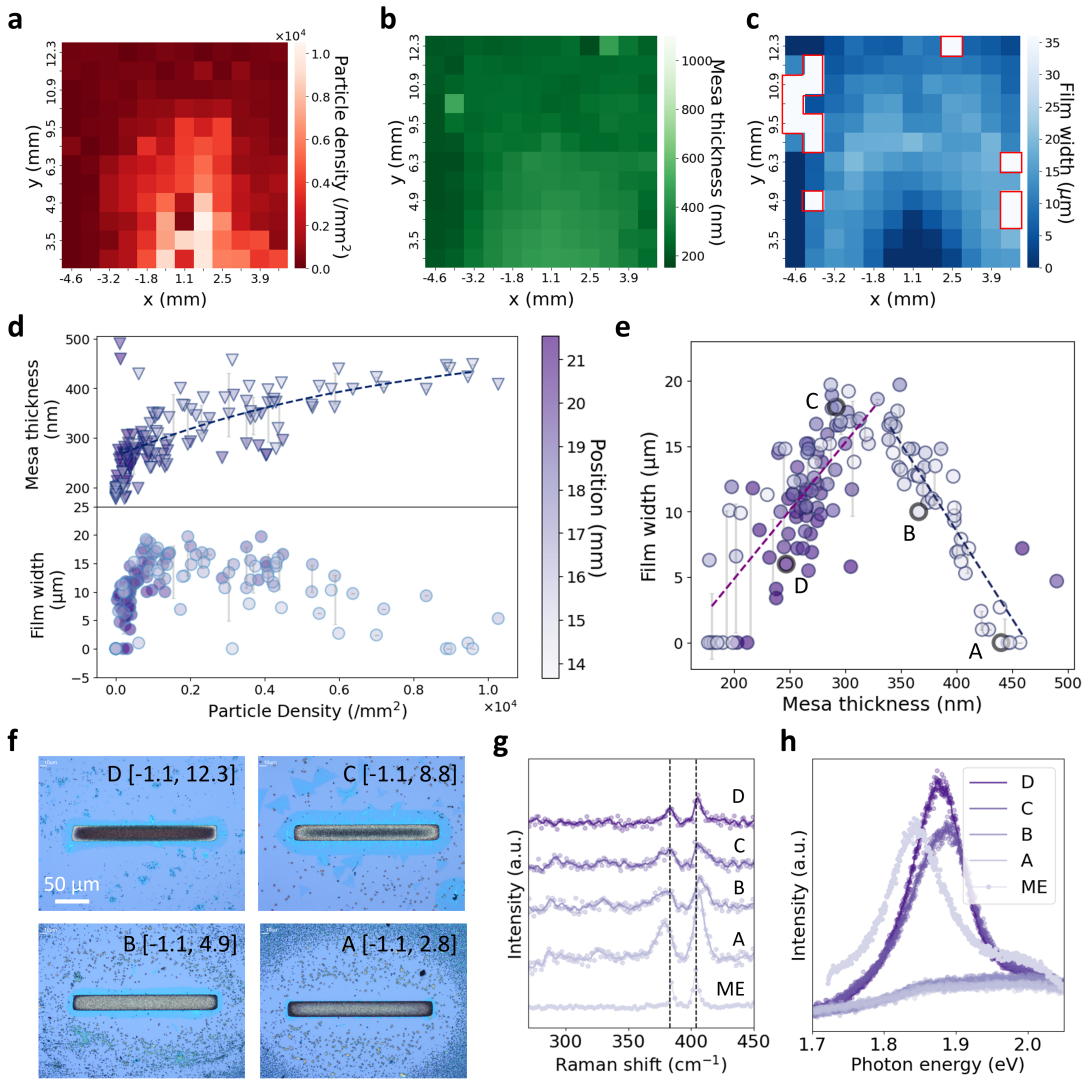


Figure 5.8: **Patterned growth in a reduced MoO_x environment, $z = 12$ mm with increased sulfur supply.** The spatial distributions of particle density, mesa height and film width are mapped in (a), (b) and (c), respectively. (d) A positive correlation is observed between mesa height and particle density, while the film width exhibits a maximum, indicating a transition in growth behaviour. (e) The film width and mesa height exhibit a maximum, suggesting an optimal Mo concentration for film formation. (f) Optical micrographs of the mesa regions marked in (e), along with their corresponding Raman (g) and PL (h) spectra, reveal variations in material properties with changing MoO_x concentration.

Fig. 5.8 (d) and (e) represents the distance of the mesa from the MoO_3 source, with regions of lower particle density located farther from the source (indicated by darker colours).

The relationship between film width and mesa height follows a distinct trend. When the mesa height is less than $\sim$ 320 nm, the film width increases monotonically. However, when the mesa height exceeds $\sim$ 320 nm, the film width exhibits an inverse linear dependence, with a slope nearly twice that observed in

the previous Mo-rich growth conditions, as shown in **Fig. 5.7** (f). This transition in growth behaviour marks a shift in the limiting factor of film formation. Notably, the mesas with the broadest surrounding film are located in a belt at the middle of the substrate, corresponding to the light blue-coloured region in **Fig. 5.8** (c). This observation suggests the existence of an optimal Mo concentration for 2D film growth.

To further investigate the effects of tuning MoO_x concentration, four mesa regions—A, B, C, and D in **Fig. 5.8** (e)—were analysed at increasing distances from the MoO_x source. Optical micrographs in **Fig. 5.8** (f) reveal clear variations in particle density and surrounding film morphology, as previously described. In particular, the particle density is significantly lower near the mesa, suggesting a localised reduction in the Mo concentration.

Raman spectra of the surrounding films from these regions, along with that of mechanical exfoliation (ME) monolayer MoS_2, are shown in **Fig. 5.8** (g). All spectra exhibit the characteristic E_{2g} and A_{1g} modes of 2H-MoS_2, confirming the composition of the film. However, the E_{2g} peak is redshifted compared to ME MoS_2, with the shift diminishing as the mesa-to-MoO_3 distance increases. The spectrum from Region D, which is the farthest from the MoO_3 source, closely matches that of ME MoS_2. Since the E_{2g} redshift is associated with sulfur vacancies, this trend suggests a decreasing defect concentration in films grown at greater distances from the MoO_3 source, indicating a more sulfur-rich growth environment. This conclusion is further supported by the PL spectra in **Fig. 5.8** (h), where films farther from the MoO_3 source, such as Region D, exhibit stronger PL intensity. Additionally, the exciton peak exhibits less blue shift, implying lower strain and doping levels.

These findings indicate that increasing sulfur partial pressure and adjusting substrate positioning effectively modulate the MoO_x concentration, thereby influencing particle deposition, mesa morphology and film quality. The observed maximum in the film width suggests a shift in the limiting parameters governing film formation, which is directly related to the Mo concentration in the growth environment.

5.4 Growth mechanism of MoS_2 patterns

In this section, we investigate the growth mechanism of patterned MoS_2, focusing on the key factors that govern growth controllability and the quality of the final CVD products. We begin by summarizing the essential experimental find-

ings, followed by a detailed discussion of the fundamental physical and chemical processes involved in the CVD growth.

5.4.1 Morphological variations with distance from the MoO_3 source

Figure 5.9 demonstrates the correlation between critical morphological features of patterned growth and the distance of the deposition site from the MoO_3 source. Specifically, the figure evaluates the MoO_2 particle density, post-growth mesa thickness, and the width of surrounding 2D films. The blue scatter points represent data from the CVD growth scenario with an excess of MoO_x (referred to as Mo-rich growth, discussed in section section 5.3.1), while orange scatter points correspond to conditions with enhanced sulfur concentration (referred to as S-rich growth, discussed in section section 5.3.2).

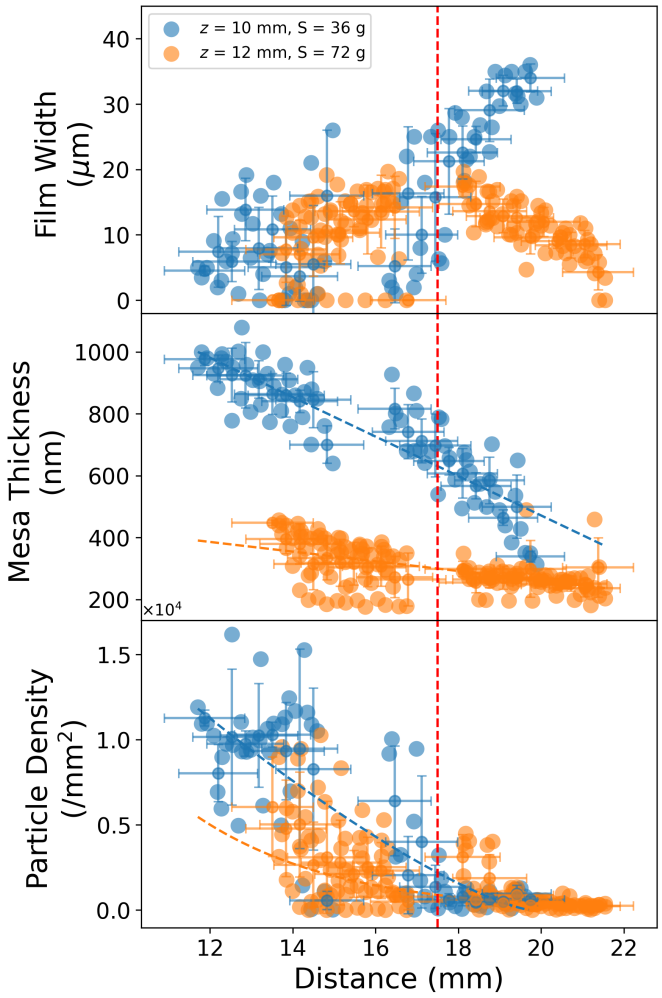


Figure 5.9: **Critical morphological features of patterned growth.** Correlation between critical morphological features of patterned growth and the distance of the deposition site from the MoO_3 source.

The bottom panel of **Fig. 5.9** illustrates a clear reduction in MoO_2 particle density with increasing distance from the MoO_3 source under both growth conditions. This trend arises due to the decrease in MoO_x concentration as the distance from the source increases. The concentration gradient is described by the advection-diffusion equation, whose steady-state solution indicates a monotonic decline in MoO_x concentration with distance. The nucleation rate (J) of MoO_3 particles follows a power-law relationship with the reactant concentration ($J \sim C^n$), enabling inference of local MoO_x concentrations based on observed particle density. Notably, the Mo-rich growth scenario exhibits a substantially higher particle density compared to the S-rich growth at similar distances. This finding underscores that, beyond distance, sulfur concentration significantly influences the availability of MoO_x. The elevated sulfur levels in the S-rich growth likely diminish the available MoO_x through the formation of MoS_2 in the vapour phase.

The concentration of MoO_x directly influences the mesa thickness. The middle panel of **Fig. 5.9** demonstrates an inverse relationship between mesa thickness and the distance from the MoO_3 source for both growth conditions. Notably, the slope of this correlation is approximately four times greater in the Mo-rich growth scenario, resulting in mesa thicknesses roughly twice those observed under S-rich conditions. Previous systematic characterization has confirmed that the post-growth mesas primarily consist of MoS_2 with a minor presence of MoO_x. Considering that sub-millimeter-scale MoS_2 growth exclusively occurs within mesa regions, direct vapor-phase sulfur adsorption onto bare substrates is insufficient to sustain the growth; otherwise, similar MoS_2 mesas would form randomly at other locations. Therefore, the sulfur necessary for MoS_2 mesa formation must originate from the mesa itself. This sulfur could potentially be supplied either from sulfur stored within PR mesas or from a substantially higher sulfur adsorption affinity on mesa surfaces compared with the silicon substrate.

The primary component of the PR (S1813) is novolac resin, a phenol-formaldehyde polymer rich in hydroxyl (-OH) and aromatic functional groups. At temperatures exceeding 200 °C, elemental sulfur undergoes ring-opening polymerization, enabling it to react readily with organic compounds. Specifically, sulfur can crosslink novolac resin through radical polymerization or vulcanization-like reactions, resulting in sulfur incorporation up to approximately 30 wt%. In the CVD process, pre-heating polymer mesas in sulfur vapor prior to MoO_x evaporation establishes sulfur reservoirs within these mesas via S incorporation into the photoresist. Conversely, the possibility of enhanced sulfur adsorption at the mesa surface as the sulfur source for MoS_2 mesa formation can be excluded. Such surface adsorption would lead to uniform mesa thickness

regardless of deposition location and significantly thicker mesas under S-rich growth conditions—both outcomes contradict experimental observations. Therefore, the sulfur required for MoS_2 mesa formation must originate from sulfur previously incorporated within the S1813 polymer, suggesting a uniform level of sulfur storage in these mesas before MoO_x evaporation during the CVD process.

At temperatures above 725 °C, MoO_x evaporation generates sufficient vapour-phase MoO_x, triggering reactions between MoO_x and sulfur stored within the mesas to form MoS_2. This process effectively fixes sulfur within the mesa regions. Simultaneously, sulfur diffuses outward from the mesa, leaving behind a carbon-rich residue that subsequently reduces MoO_x to volatile byproducts, thus decreasing the mesa height. Consequently, the final mesa height is determined by the balance between MoS_2 formation (within the mesa region) and sulfur diffusion (away from the mesa region). Higher rates of MoS_2 formation result in a larger volume of mesa material converting into MoS_2, yielding thicker mesas following the CVD process. Since the reaction rate is directly proportional to the local Mo concentration, the Mo-rich growth scenario leads to thicker mesas. Additionally, the pronounced slope observed for the Mo-rich growth condition in the middle panel of **Fig. 5.9** can be attributed to its significant gradient in MoO_x concentration, as indicated in the bottom panel of the same figure.

Sulfur diffusing from the mesa region into the surrounding area interacts with Mo atoms that have adsorbed on the substrate surface and diffused to the same surrounding area, leading to the formation of 2D MoS_2 films. When there is adequate Mo availability, a greater diffusion of sulfur from the mesas results in wider surrounding 2D films, as demonstrated by the Mo-rich growth scenario shown in the top panel of **Fig. 5.9**. In this scenario, film width increases with greater distance from the MoO_3 source. Here, the increased distance corresponds to lower local Mo concentrations, enabling more sulfur atoms to diffuse outward due to slower fixation rates within the mesa regions. Conversely, under S-rich growth conditions, once a critical distance (indicated by the red dashed vertical line in **Fig. 5.9**) is surpassed, further increases in sulfur diffusion cause the surrounding 2D films to narrow. This narrowing occurs due to limited Mo availability, where reduced Mo concentrations restrict the growth of MoS_2 films despite the abundance of sulfur.

5.4.2 Growth mechanism of patterned MoS_2

The growth process is depicted in **Fig. 5.10**. Patterned growth begins with sulfur uptake in the PR mesa at approximately 725 °C. Initially, a stable sulfur concen-

tration is established within the growth environment prior to the evaporation of the MoO_3 source. As temperature increases further, MoO_3 vapour forms and adsorbs onto the substrate surface as MoO_x species. The progressive accumulation of adsorbed MoO_x eventually leads to supersaturation, triggering spontaneous nucleation and the random formation of MoO_2 particles due to thermodynamic fluctuations.

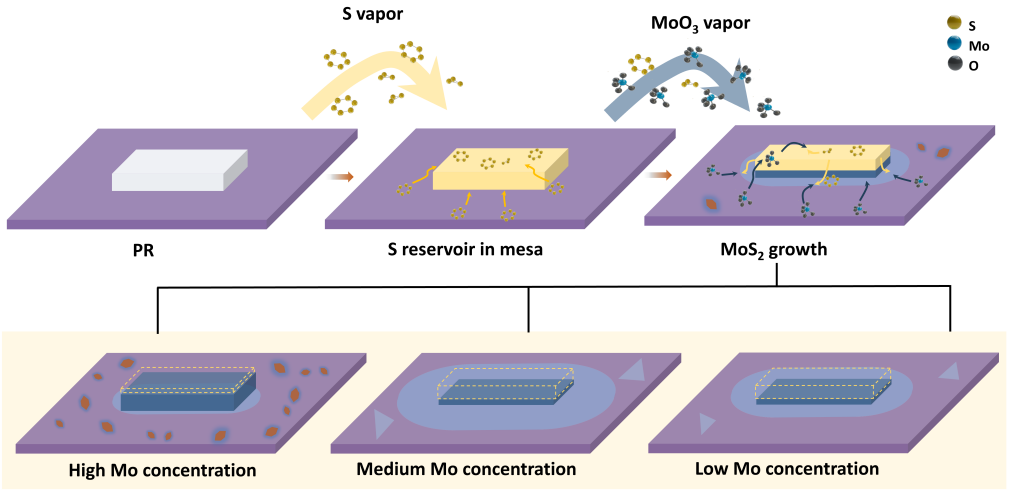


Figure 5.10: **Growth mechanism of patterned MoS_2.** The width of the surrounding film is regulated by the growth kinetics and the amount of sulfur stored in the mesa.

Adsorbed MoO_x species diffuse toward the mesa region, where they react with sulfur according to the following chemical reaction:

$$MoO_x + \left(2 + \frac{x}{2}\right) S \rightarrow MoS_2 + \left(\frac{x}{2}\right) SO_2$$

This reaction converts the mesa into nonvolatile MoS_2, simultaneously reducing the local MoO_x concentration. As a result, a concentration gradient develops between the mesa and its surroundings, driving a continuous inward diffusion of MoO_x towards the mesa. This maintains the MoO_x gradient and sustains ongoing MoS_2 formation within the mesa, effectively immobilizing sulfur at these sites.

Simultaneously, sulfur atoms diffuse outward from the mesa into surrounding regions, driven by a chemical potential gradient. MoS_2 crystallites formed at the base of the mesa serve as energetically favorable nucleation sites for the subsequent growth of 2D MoS_2 films. The rate of 2D MoS_2 film growth primarily depends on local MoS_2 concentration and is governed by reaction kinetics, which can be limited by either sulfur or MoO_x availability. Importantly, nucleation of additional MoS_2 grains—even at edges or corners of existing films—requires sufficient local MoS_2 supersaturation.

As the sulfur concentration decreases with increasing distance from the mesa, 2D film growth eventually halts when sulfur availability falls below the thermodynamic threshold required for MoS_2 formation. At high MoO_x concentrations, sulfur fixation within the mesa is highly efficient, restricting outward sulfur diffusion, limiting local sulfur level and thereby 2D film expansion. In contrast, reducing MoO_x concentration promotes outward sulfur diffusion, facilitating larger-area 2D film formation.

Over time, continued outward sulfur diffusion gradually flattens the sulfur concentration profile, and even the local sulfur concentration may initially exceed the thermodynamic threshold. Thus, the boundary defining the minimum sulfur concentration necessary for MoS_2 formation progressively expands outward. To achieve large-area MoS_2 films, the speed of film growth must equal or exceed the rate of outward expansion of this sulfur boundary. At high MoO_x concentrations, film growth rate surpasses the outward movement of the sulfur threshold boundary, limiting the film size primarily to the amount of sulfur diffused from the mesa. Conversely, at low MoO_x concentrations, the growth rate becomes limited by the MoO_x supply, slowing the expansion of the growth front. Ultimately, the film ceases to grow wherever local sulfur concentrations fall below the thermodynamic minimum, regardless of the initial sulfur quantity diffused from the mesa.

5.4.3 Evidence supporting the growth mechanism

The growth mechanism proposed in the previous subsection has several implications. In this section, we discuss these implications and present additional experimental evidence supporting the proposed mechanism.

Figure 5.11 illustrates the crystallographic relationship between the MoS_2 grains within the mesa and those in the surrounding films. The Scanning Transmission Electron Microscopy (STEM) image shown in the left panel was captured near the mesa border. The brighter region at the top of the image corresponds to the mesa, whereas the surrounding 2D film exhibits significantly lower brightness. Both regions are clearly distinguishable from the underlying carbon support film of the TEM grids. The contrast observed in the STEM image primarily results from mass thickness variations, with brighter regions indicating thicker areas. Additionally, a distinct micro-crack is visible in the image, marked by two sets of arrows highlighting its boundaries, which divides the surrounding film into left and right sections.

Diffraction patterns were collected from four labelled regions (A, B, C and

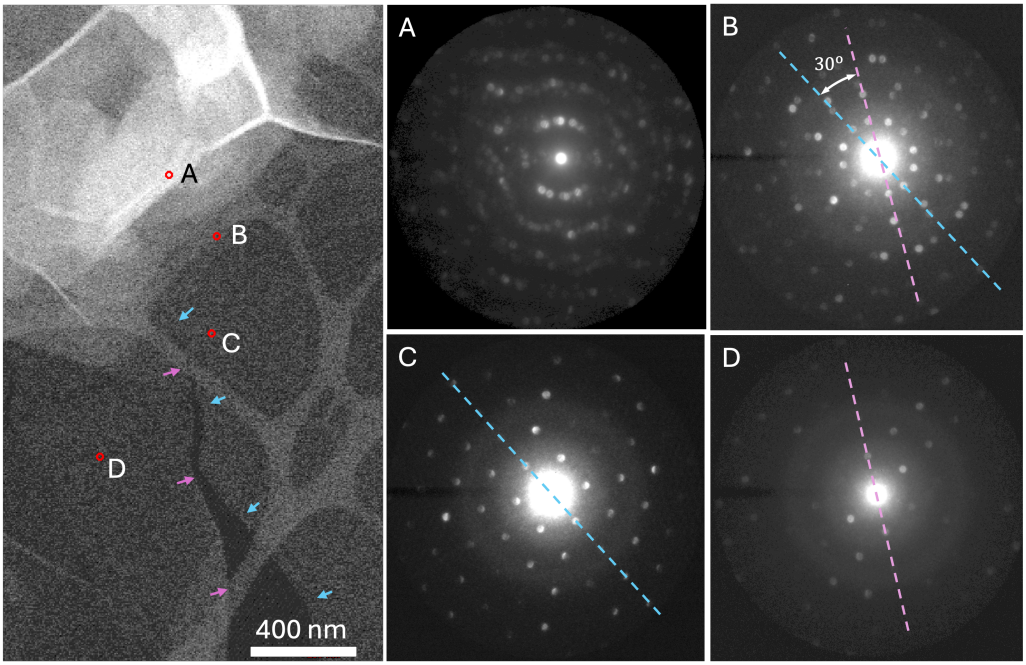


Figure 5.11: **Initiation of 2D film growth.** Nanodiffraction patterns obtained from MoS_2 particles within the mesa region and grains in the surrounding film reveal aligned crystallographic orientations, indicating in-plane epitaxial growth. Region A is at the edge of the mesa.

D). The diffraction pattern from location A, representing a thicker portion of the mesa, demonstrates polycrystallinity characterized by a common 001 zone axis. This suggests multiple 2H MoS_2 nanocrystallites stacked along the *c*-axis without basal-plane alignment. The boundaries between these nanocrystallites are discernible in the STEM image as borders separating regions with varying brightness.

At the mesa-film interface (location B), two distinct sets of diffraction patterns were identified, signifying the overlap of two MoS_2 crystallites from the mesa. Their *a*-axes exhibit a clear 30° rotational twist. The STEM image supports this finding, clearly showing two grains: one extending downward and connecting with the left section of the surrounding film; the other shorter grain terminating at the micro-crack boundary and connecting exclusively to the right section of the film.

Notably, the diffraction patterns obtained separately from the two sections of the surrounding film (locations C and D) display a similar 30° rotational twist, aligning closely with the pattern from location B. The combination of patterns from C and D effectively replicates the pattern obtained at B. This compelling alignment strongly suggests that the 2D film growth originates directly from the mesa grains, reinforcing the validity of the proposed growth mechanism.

The proposed mechanism indicates that the interdiffusion of sulfur and MoO_x plays a crucial role in determining the growth kinetics of the 2D MoS_2 film. Beyond influencing the width of the surrounding film, this mechanism has two significant additional implications: (1) the overall shape and (2) the grain structures of the surrounding 2D film.

Figure 5.12 (a) and **Fig. 5.12** (b) illustrate and compare the geometrical profiles of the surrounding films grown under Mo-rich and S-rich conditions, respectively. Under Mo-rich conditions (**Fig. 5.12** (a)), the surrounding film exhibits a uniform growth rate, resulting in consistent and symmetrical film width around the mesa. In contrast, the film grown under S-rich conditions (**Fig. 5.12** (b)) with low Mo concentration demonstrates an irregular profile, indicative of variable growth rates at different positions around the mesa. The mechanism suggests a uniform sulfur concentration at a given distance from the mesa, which corresponds with the consistent outer boundary of the surrounding film observed under Mo-rich conditions. Thus, when molybdenum is abundant, the growth rate of the 2D film is primarily constrained by local sulfur availability and hence the sulfur distribution. Conversely, under S-rich (Mo-limiting) conditions, local molybdenum concentrations fluctuate considerably due to the stochastic nature of adsorption and diffusion processes, causing variable growth rates and irregular film profiles.

The grain structures observed experimentally further support this growth kinetics model. As demonstrated in **Fig. 5.12** (c), Mo-rich conditions produce distinctive grain structures adjacent to the mesa boundary. Near the mesa, grains exhibit significant elongation perpendicular to the mesa edge, resulting in grains with high aspect ratios. This elongation is particularly evident from secondary growth patterns (black stripes in the figure) along grain boundaries of the initial layer. However, the aspect ratio progressively decreases as grains approach the film's outer boundary. The mechanism attributes this elongated grain structure near the mesa to limited lateral growth and negligible secondary nucleation. The secondary nucleation on bare substrates is negligible due to depletion of MoO_x concentrations resulting from mesa growth (**Fig. 5.12** (e), dashed lines). As such, nucleation predominantly occurs on mesa crystallites near the mesa boundary. After initial lateral merging, subsequent growth mainly proceeds outward, perpendicular to the mesa edge, forming elongated grains. As the growth front progresses outward, increased MoOx concentrations enable more frequent nucleation events, producing smaller, non-elongated grains. Eventually, the 2D film growth terminates when sulfur concentrations fall below the thermodynamic threshold necessary for further growth (indicated by the red circle in the top

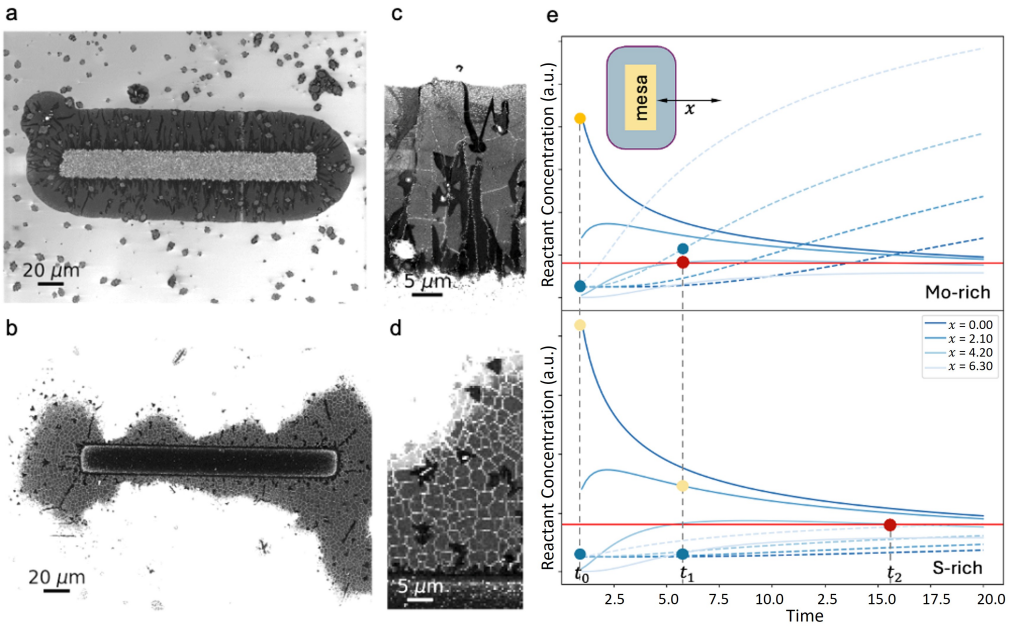


Figure 5.12: **Growth kinetics of 2D Films: geometry and grain structure** The Mo-rich growth leads to uniform and symmetrical surrounding film in (a), while the S-rich growth results in irregular film profiles in (b). (c) The Mo-rich growth exhibits a unique grain structure with varying aspect ratio, compared with small and non-elongated grains from S-rich growth in (d). (e) The growth kinetics depends on the time/location variations of sulfur and MoO_x concentrations, which is regulated by the diffusion process.

panel of **Fig. 5.12** (e)). In **Fig. 5.12** (e), the solid and dashed curves represent the dimensionless concentrations of sulphur and molybdenum at varying distances x (measured from the mesa edge) over time t. These profiles are calculated using the one-dimensional diffusion equation (detailed calculation see appendix A.7).

Under S-rich conditions, fluctuations in local molybdenum concentration result in irregular nucleation patterns, yielding smaller grains without notable elongation. Additionally, the generally lower overall molybdenum concentration under S-rich conditions significantly reduces growth rates. For example, **Figure 5.12** (e) demonstrates that at a given time t_1, Mo-rich growth extends considerably further ($x = 4.2$) compared with S-rich growth, which only reaches $x = 2.1$. Ultimately, the surrounding film's width is governed by the average growth rate, directly influenced by the average molybdenum supply over time. At each position x, sulfur concentration eventually declines below the required growth threshold. Thus, the maximum achievable film width corresponds to the farthest distance the growth front can reach before sulfur availability becomes insufficient. The lower panel of **Fig. 5.12** (e) illustrates this clearly: by time t_2, the film has expanded to $x = 4.2$, beyond which sulfur is inadequate to sustain additional growth.

5.5 Optimisation of the patterned growth

Understanding the underlying growth mechanisms allows us to further optimise the patterned growth of MoS_2. For example, **Figure 5.13** (a) illustrates the successful growth of a MoS_2 array on a SiO_2/Si substrate using OL PR mesas, achieved by increasing the substrate-source distance to 15 cm. Detailed growth parameters for all samples discussed in this chapter are summarised in table 5.3, and a comprehensive set of optical micrographs for all mesa samples is included in appendix A.6.

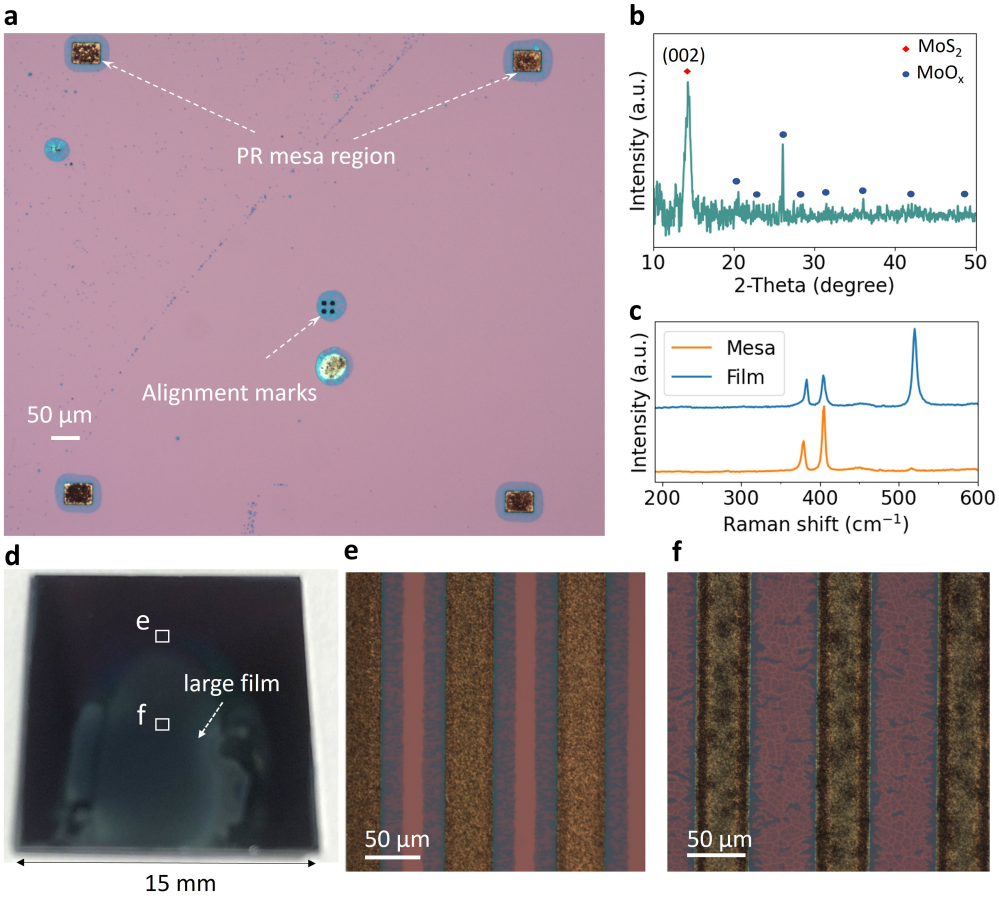


Figure 5.13: **Optimisation of Patterned Growth of MoS_2.** (a) Optical micrograph illustrating patterned MoS_2 grown from an optimized OL PR method with increased substrate-source distance, significantly reducing unwanted particle deposition. (b) XRD analysis of the as-grown MoS_2, confirming the dominance of the 2H MoS_2 phase with minor oxide presence. (c) Raman spectra comparing the mesa structures and the surrounding films, clearly exhibiting characteristic 2H MoS_2 peaks without detectable oxide impurities. (d) Optical micrograph of the full substrate, with white boxes indicating the locations where figures (e) and (f) were taken. (e, f) Demonstration of mm-scale growth of 2D MoS_2 films derived from a line-space mesa array, underscoring the scalability of the optimized process.

For the mesas presented in **Fig. 5.13** (a), the surrounding MoS_2 film has a

consistent width of approximately 30 μm, and significantly, the formation of unwanted MoO_2 particles is substantially suppressed. The XRD spectrum in **Fig. 5.13** (b) displays a prominent peak at 14°, corresponding to the (002) plane diffraction of 2H MoS_2. While minor oxide-related peaks remain, their intensities are notably weaker compared with those observed in Mo-rich samples (see **Fig. 5.3** (c)). Moreover, Raman spectroscopy from the mesa and surrounding regions, as shown in **Fig. 5.13** (c), clearly identifies the characteristic E_{2g} and A_{1g} Raman modes of 2H MoS_2, with oxide peaks entirely absent in the measured mesa area. These results strongly indicate that reducing MoO_x concentration within the growth environment—achievable by increasing the substrate-source distance—can effectively minimize MoO_2 impurity formation. Exploring further reductions in impurity formation presents a promising avenue for future research.

A central objective of this research is achieving wafer-scale and precisely controlled growth of 2D MoS_2. This goal has been effectively realised through the use of a line-space pattern, demonstrated in **Fig. 5.13** (d) and (e). The PR mesas were fabricated by standard optical lithography on a SiO_2/Si substrate, measuring up to 1.5 cm in length, with widths of 50 μm and pitches of 100 μm. After the CVD process (detailed growth parameters available in table 5.3), 2D MoS_2 films extend seamlessly from the mesas onto adjacent bare substrate areas, as illustrated in **Fig. 5.13** (d). The width of these films varies with respect to their location relative to the MoO_3 source. In some regions, films originating from adjacent mesas merge into continuous films, completely covering the substrate between mesas. The coverage of these continuous films can reach millimetre-scale dimensions, as illustrated by the approximately 0.25 mm field-of-view in **Fig. 5.13** (e). Nonetheless, variability in film morphology at different deposition sites remains apparent, reflecting limitations in reactant transport control within our current CVD configuration. Despite this challenge, the method holds significant potential for achieving wafer-scale, highly uniform, and impurity-free growth. Furthermore, this growth strategy offers considerable versatility in controlling the growth patterns, sizes, and locations, representing valuable directions for optimisation in future studies.

Sample	Figure	PR	sub-MoO_3 distance (cm)	S used (g)	MoO_3 used (g)
Mo-rich	**Fig. 5.7**	LDW	10	36	1
S-rich	**Fig. 5.8**	LDW	12	72	0.9
Clean	**Fig. 5.13** (a)	OL	15	-	-
Scalable	**Fig. 5.13** (d, e)	OL	15	90	-

Table 5.3: **Detailed CVD Parameters for Patterned Growth.** All growth processes employed the following standardized conditions: carrier gas N_2 was continuously introduced during the entire growth cycle at a flow rate of 20 sccm; substrate temperature was ramped from room temperature to 105 °C and kept for 1 hour before reaching the growth temperature 825°C over a duration of 52 minutes and subsequently held constant for 5 minutes; the sulfur precursor was positioned upstream, 21.5 cm from the substrate.

5.6 Conclusion

We have demonstrated a scalable and highly controllable polymer-assisted CVD method for the selective growth of 2D MoS_2 films, advancing beyond conventional synthesis techniques. By strategically incorporating polymer mesas patterned via LDW and OL, we achieved precise spatial control over nucleation and growth processes, enabling the selective deposition of MoS_2 films with customizable morphologies.

Spatial analyses across the substrate revealed a clear correlation among MoO_x particle density, mesa thickness, and surrounding film dimensions, highlighting the critical influence of reactant concentrations, particularly MoO_x and sulfur, on MoS_2 growth outcomes. These findings elucidate the diffusion-controlled growth mechanisms responsible for patterned MoS_2 formation. Notably, the polymer mesas served dual functions as localized nucleation centers and sulfur reservoirs, substantially influencing growth kinetics and the resulting morphology of the MoS_2 layers.

Comprehensive characterizations employing Raman spectroscopy, photoluminescence spectroscopy, atomic force microscopy, scanning electron microscopy, and transmission electron microscopy confirmed that the selectively grown films exhibit physical properties suitable for electronic and optoelectronic device applications. Although elevated sulfur vacancy concentrations were observed under specific growth conditions, adjusting reactant ratios effectively reduced defect densities and enhanced optical properties.

Importantly, this method was successfully scaled to achieve centimeter-scale patterned growth, demonstrating significant potential for industrial adoption. By

carefully controlling the initial polymer thickness and pattern geometry, we consistently produced monolayer MoS_2 films with lateral dimensions exceeding 5 mm.

In conclusion, this work establishes polymer-assisted CVD as a robust method for the large-scale, patterned synthesis of MoS_2, providing unprecedented control over film morphology and dimensions through a single-step process. This approach not only deepens our fundamental understanding of patterned growth dynamics but also presents practical pathways for integrating scalable 2D materials into next-generation electronic and optoelectronic devices.

6 | Resistive switching in MoS_2 based planar memristors

"Every brilliant experiment, like every great work of art, starts with an act of imagination."

- Jonah Lehrer

This chapter explores planar MoS_2-based memristor devices fabricated using the patterned MoS_2 outlined in chapter 5. The device fabrication process is first described, followed by a systematic electrical characterization, including electroforming as well as quasi-dynamic and dynamic device responses. The mechanism underlying the resistive switching is also investigated. The switching arises from electric-field-induced defect migration, which modulates the Schottky barrier at the electrode-channel interface, thereby controlling the resistance state. Finally, we illustrate the artificial synaptic characteristics of these devices, highlighting their promising potential for neuromorphic computing applications.

6.1 Device fabrication

To investigate memristor behaviour and avoid contamination during the transfer and etching processes, we first prepare MoS_2 arrays using the patterned growth method as discussed in the previous chapter. The MoS_2 thin films used in this chapter are synthesized through the patterned growth method on a 15×15 mm^2 SiO_2/Si substrate (n-type 100 Si with 285 nm thermal oxide). The photoresist (PR) mesas, each measuring 50 μm $\times$ 40 μm, are fabricated using optical lithography (OL). The S1813 photoresist first undergoes a spin coating stage at 6000 rpm for 45 seconds, followed by ultraviolet (UV) exposure for 6.5 seconds and development in MF-319 for 45 seconds. The PR mesas are further thinned through a 2-second flood UV exposure to achieve a final PR mesa thickness of 520 nm. The patterned substrate is then subjected to the chemical vapour deposition (CVD) process at

825 °C for 5 minutes, with a N_2 gas flow of 20 sccm. The distance between the MoO_3 source and substrate, see **Fig. 5.2**, is $z = 2$ mm.

The as-grown patterned MoS_2 mesas are used to fabricate memristor devices. The process begins by spin-coating the substrate with S1813 photoresist (Shipley) at 5000 rpm. The coated samples are then exposed using an OAI mask aligner for 8 s with a dose of 66 mJ·cm^{-2}. Following UV exposure, the sample undergoes development in Microposit MF-319 developer (Shipley) for 45 s, rinsing with deionized (DI) water, and a subsequent hard bake at 90 °C for 90 s. During development, the UV exposed photoresist dissolves in the developer, exposing the underlying MoS_2 films. Metallization is then performed via electron beam (e-beam) evaporation, depositing layers of 1 nm Ti followed by 35 nm Au. Finally, lift-off process is carried out by immersing the sample in 1165 remover at 80 °C for 20 minutes, accompanied by 10 seconds of ultrasonic agitation.

Figure 6.1 (a) shows an Scanning Electron Microscopy (SEM) image of a planer MoS_2 memristor device featuring four top electrodes. Each electrode is 4 μm wide and connects to a 250 μm $\times$ 250 μm contact pad (not shown in the figure) for electrical measurements. As illustrated schematically in **Fig. 6.1** (b), the lateral spacing between adjacent electrodes are 12 μm, 8 μm and 4 μm, defining the left channel (Ch_L), middle channel (Ch_M) and right channel (Ch_R), respectively. During electrical measurements, DC voltage is applied across these top electrodes. Owing to the presence of the thick SiO_2 dielectric layer, electric current predominantly flows laterally from one electrode through the MoS_2 film to the adjacent electrode.

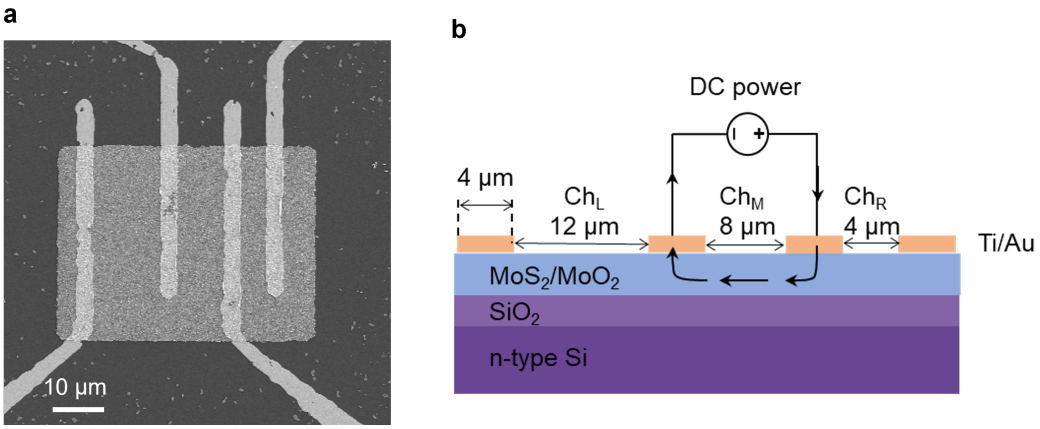


Figure 6.1: **MoS_2 based planar memristor device.** (a) SEM image of the MoS_2 planar memristors. (b) Schematic cross-sectional view of the device, illustrating its structure and electrical connection example.

6.2 Electroforming and quasi-static response

We first study the *I-V* characteristics of the middle channel through two-terminal measurement under ambient conditions using an Imina probe station connected to a Keysight B2912A source measure unit, as illustrated in **Fig. 6.1** (b). During testing, a voltage bias is applied to the right electrode of the middle channel while the left electrode of the same channel is grounded. Unless otherwise specified, the voltage sweep is performed using incremental steps of 8 mV at a sweep rate of 400 mV/s.

Electroforming: **Figure 6.2** (a) shows the resulting *I-V* curves of the device. Initially, a voltage sweep loop is applied from -1 V to 1 V and then returns to -1 V. The resulting *I-V* curve (light blue) exhibits non-Ohmic behaviour, while no noticeable hysteresis loop is observed, suggesting the absence of resistive switching at this stage.

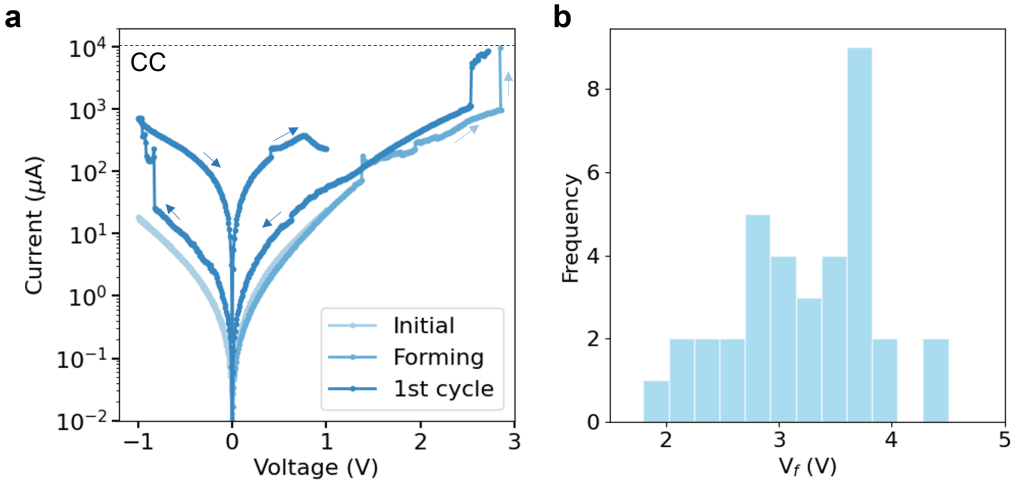


Figure 6.2: **Electroforming of the memristor device.** (a) Semilog *I-V* curves of the initial state, electroforming and the first cycle after forming. (b) Forming voltage distribution over 36 memristor devices.

We then increase the voltage range, performing a sweep from 0 V to 3 V with a compliance current (CC) of 10 mA, which limits the maximum level of the current. As shown by the mild blue curve in **Fig. 6.2** (a), the current rises steadily with voltage until it experiences an abrupt surge at approximately 2.8 V, surpassing the set CC. This sudden increase in current, triggered by the elevated voltage, marks the electroforming process, and the corresponding threshold voltage is referred to as the forming voltage (V_f). After the electroforming, the voltage sweep is reversed from 2.8 V to -1 V and subsequently increased to 1 V to complete the cycle. The *I-V* characteristic during the first cycle after electroforming is shown

by the dark blue curve, with blue arrows indicating the direction of the voltage sweep. In the first cycle, a distinct pinched[1] hysteresis loop emerges, highlighted by abrupt current increases around -1 V and decreases near 1 V.

The device demonstrates bistable behaviour, exhibiting a high resistance state (HRS) and a low resistance state (LRS), controlled by the applied voltage bias. The HRS and LRS states are commonly referred to as OFF and ON states, respectively. To switch or 'SET' the device from HRS to LRS, a bias of -1 V is applied, turning on the device. Conversely, applying a bias of 1 V 'RESETs' the device, switching it from LRS back to HRS and turning it off. The opposite voltage polarities required for the 'SET' and 'RESET' processes confirm the bipolar nature of the memristor device. The ON/OFF ratio, defined as the current ratio between the LRS and HRS, is approximately 50 at -1 V. The ON-state current increases significantly - by a factor of $\sim$70 - compared with its initial pre-forming state.

The histogram shown in **Fig. 6.2** (b) illustrates the distribution of the forming voltage V_f measured across 36 devices. The data indicates noticeable device-to-device variability, with an average forming voltage of 3.3 ± 0.7 V. Various factors may influence the forming voltage, including material properties (e.g. thickness, chemical composition) and environmental conditions (e.g. temperature). As discussed in the preceding chapter, the patterned mesas exhibit varying properties at different locations, potentially contributing to the observed variability in V_f. Nevertheless, further investigation is required to establish a definitive correlation between specific mesa properties and variations in forming voltage.

Quasi-static response: **Figure 6.3** (a) compares the I-V characteristic of the device at varying sweep rate, with voltage sweeps conducted from -1 V to 1 V and then returning to -1 V. The sweep rate r expressed in mV/s relates to the frequency f of the applied voltage as $f = r/(4 \times V)$ Hz. It is observed that as the frequency decreases, the ON-state current increases while the OFF-state current decreases, leading to a larger hysterisis window and an increased ON/OFF ratio - a characteristic behaviour commonly observed in memristor devices.

Figure 6.3 (b) shows the semi-logarithmic I-V characteristics of the device measured at various voltage amplitudes, maintaining a consistent sweep direction (negative-positive-negative). The results show that the device exhibits no switching behaviour when the amplitude is below 0.6 V. However, clear resistive switching emerges when the amplitude exceeds 0.8 V, with the ON/OFF ratio in-

[1] A "pinched hysteresis loop" is a characteristic shape in the current-voltage (I-V) response of a memristor, appearing as a loop that narrows or "pinches" near the origin (where voltage and current are both zero).

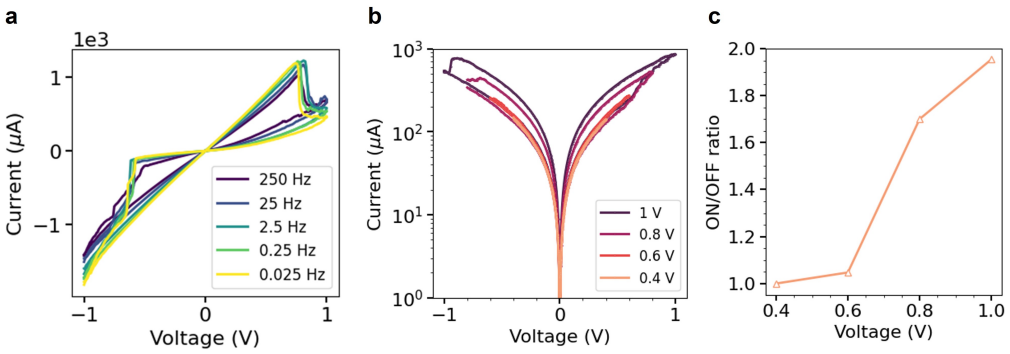


Figure 6.3: **Device quasi-static properties.** (a) *I-V* characteristic of the frequency dependence. (b) *I-V* characteristics under varying operating voltage. (c) The dependence of ON/OFF ratio on the amplitude of the operating voltage.

creasing accordingly **Fig. 6.3** (c). Since a voltage amplitude of 0.4 V does not alter the resistance state of the memristor, this voltage level will be used for reading the resistance state of the device in subsequent analyses.

To evaluate the cycle-to-cycle variability of the device, voltage sweeps from -1 V to 1 V are performed over 25 consecutive cycles, as shown in **Fig. 6.4** (a). The consistent patterns of the hysteresis loops demonstrate stable switching behaviour throughout these cycles, although a gradual decrease in the ON-state current is observed as the number of cycles increases. **Figure 6.4** (b) shows the distribution of SET voltage (V_{set}) and RESET voltage (V_{reset}) across these 25 cycles. The average V_{set} and V_{reset} are -0.60 and 0.93 V, respectively, with minor variations of 0.02 V and 0.01 V, respectively. The low operation voltage indicates the device's low power consumption, calculated to be ∼0.5 mW. **Figure 6.4** (c) depicts the resistance of the device over these cycles, measured at -0.05 V. The OFF-state resistance remains stable throughout the cycles, while the ON-state resistance increases gradually with the number of cycles. Consequently, the ON/OFF ratio (**Fig. 6.4** (d)) decreases from 5.3 in the first cycle to 2.6 by the 25_{th} cycle, indicating progressive device degradation.

The device undergoes further testing with additional voltage sweeps (from -1 V to 1 V and back to -1 V). The ON/OFF ratio decreases with increasing cycle number, eventually reducing to approximately 1 by the 40_{th} cycle. **Figure 6.5** (a) compares the *I-V* characteristics for the first cycle and after fatigue. The disappearance of the hysteresis loop indicates fatigue in the switching behaviour. Raman spectra in **Fig. 6.5** (b), normalized by A_{1g} peak, compare the initial material state with that after 100 cycles. Both spectra show prominent MoS_2 E^1_{2g} and A_{1g} modes at 383.2 cm^{-1} and 409.2 cm^{-1}, confirming the presence of the 2H-MoS_2 phase. The peak positions and intensity ratio ($I_{A_{1g}}/I_{E^1_{2g}}$) remain unchanged. In

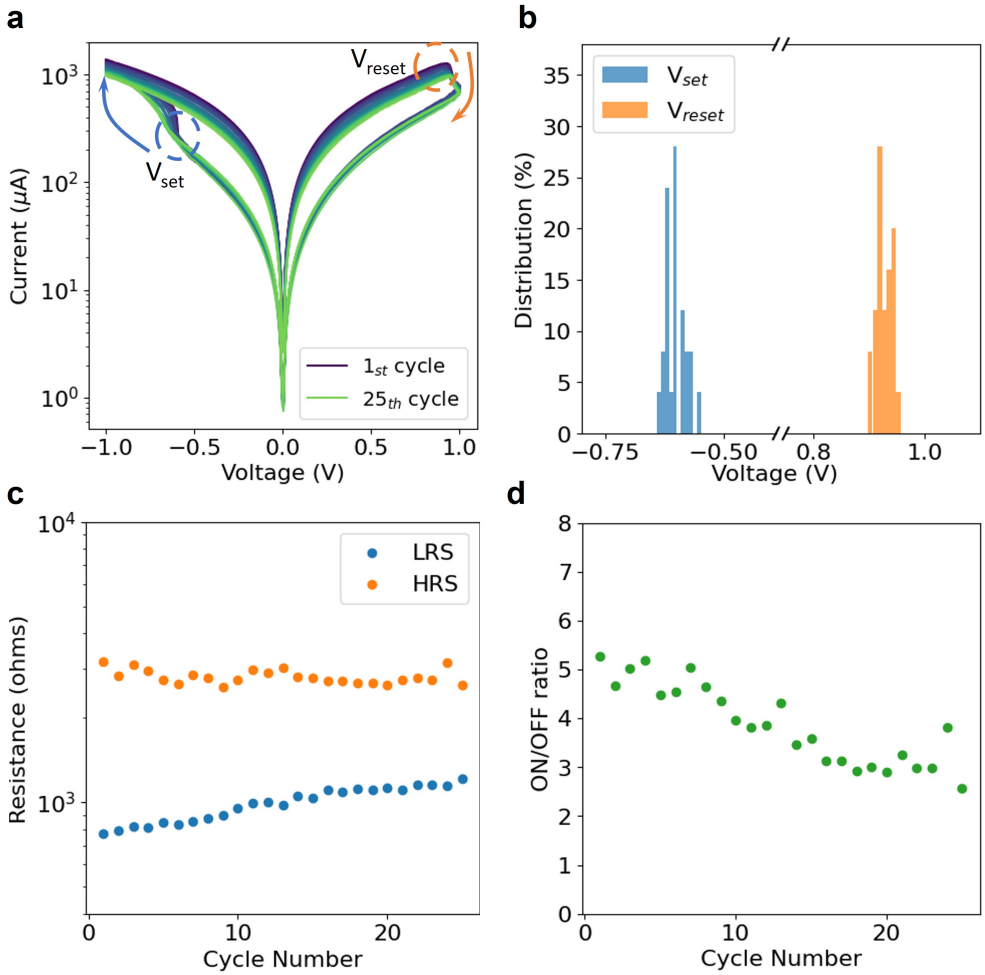


Figure 6.4: **Device cycling performance.** (a) Semi-logarithmic *I-V* characteristics of the device for 25 consecutive cycles of voltage sweeps. (b) The distribution of set voltage and reset voltage across the cycles. (c) Resistance evolution over the cycles. (d) ON/OFF ratio across the cycles.

addition, weaker MoO_2 peaks at 204.6 cm^{-1}, 230.1 cm^{-1}, 285.9 cm^{-1}, 346.6 cm^{-1}, 351.8 cm^{-1}, 364.9 cm^{-1}, 454.6 cm^{-1} and 497.0 cm^{-1} are observed. The peaks at 204.6 cm^{-1} 204.6 cm^{-1} and 364.9 cm^{-1} (highlighted in the right panel of **Fig. 6.5** (b)) show clear attenuation after 100 switching cycles. This observation suggests a reduction in the MoO_2 component after prolonged cycling.

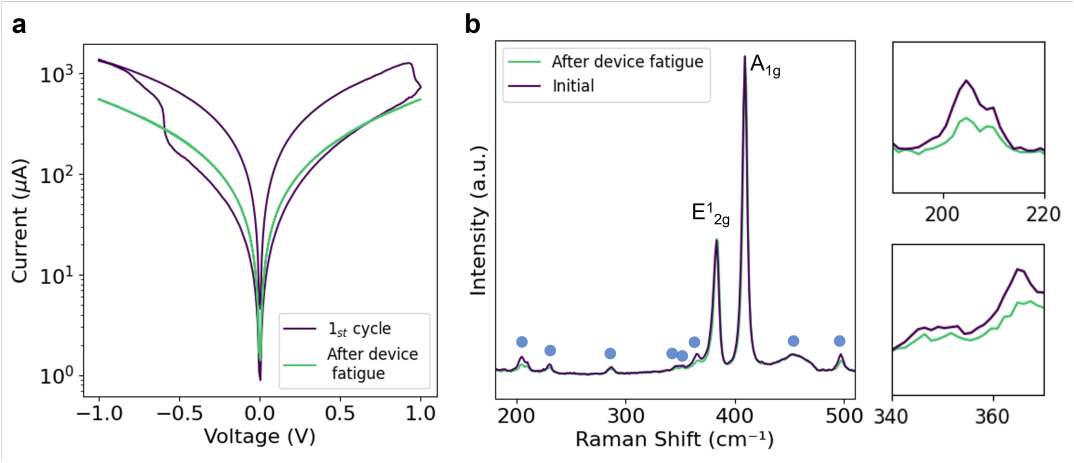


Figure 6.5: **Device fatigue.** (a) Semi-logarithmic *I-V* characteristics for the first cycle and after device fatigue. (b) Raman spectrum of the initial state and after device fatigue. The two subplots in the right panel show the peak between 190-220 cm^{-1} and 340-370 cm^{-1}.

6.3 Dynamic response and conduction mechanism

Minimum pulse width: We further study the dynamic response of the device. **Figure 6.6** (a) illustrates the programming pulse sequence employed for SET/RESET operations, interleaved with read pulses after each switching event. Each cycle comprises one RESET pulse, one SET pulse, and two read pulses. The SET and RESET pulses maintain a constant amplitude of -1 V and 1 V, while the read pulses have an amplitude of 2 mV and a duration of 1 ms. The RESET and SET pulses have equal widths within each cycle; however, the pulse width increases incrementally across cycles, increasing from 1 ms to 15 ms in 1 ms steps. For each pulse width, three identical cycles are performed consecutively within the pulse train. The average resistance and standard deviation calculated from these cycles are plotted in **Fig. 6.6** (b) and (c).

After 45 cycles — comprising 15 distinct pulse widths (ranging from 1 ms to 15 ms), each repeated three times — the resistances measured after the RESET pulse are shown in **Fig. 6.6** (b). The error bars indicate the standard deviation calculated from the three measurements performed for each pulse width. The resistance after RESET (i.e. RESET resistance) increases progressively from approximately 5 kΩ to around 8 kΩ as the pulse width increases from 1 ms to 12 ms. Beyond 12 ms, the RESET resistance stabilises at $\sim$ 8 kΩ, indicating that the device has reached the OFF state (i.e. HRS). In contrast, SET operations, even at the shortest pulse width of 1 ms, consistently switch the device fully into its ON state (see **Fig. 6.6** (c)). Thus, the device consistently begins in the same ON state prior to each RESET operation. These results establish 12 ms as the minimum required pulse width for achieving a stable and consistent binary RESET operation, while

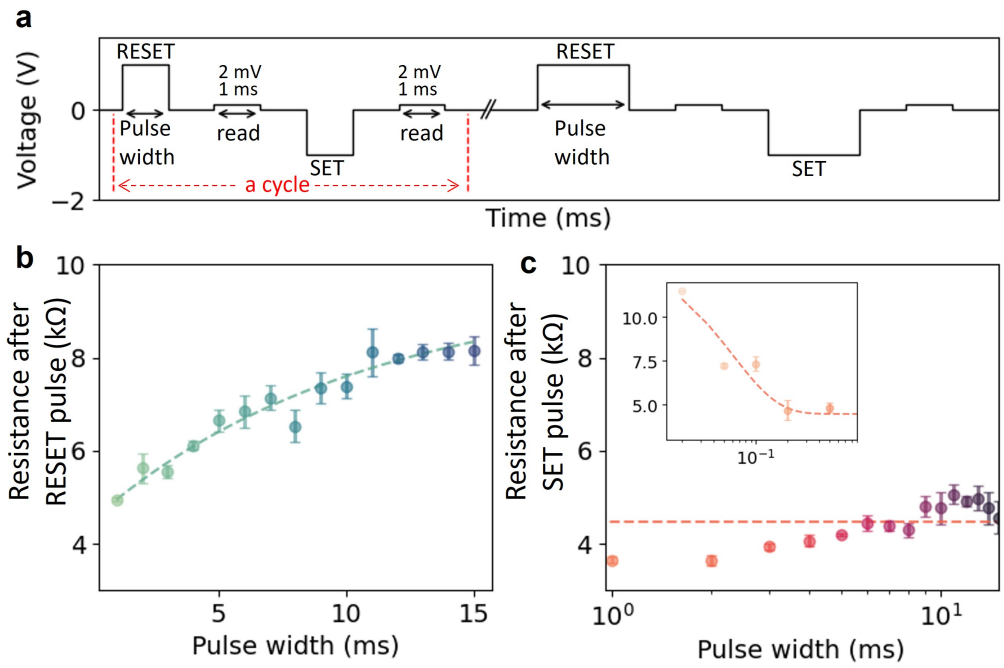


Figure 6.6: **The effect of pulse width on memristor resistance.** (a) Programming pulse sequence for SET/RESET cycling with read pulses after each operation pulse. (b) The resistance after the reset pulse (1 V) at varied pulse widths. (c) The resistance after the set pulse (-1 V) at varied pulse widths.

shorter RESET pulses producing intermediate resistance states may enable multi-level switching functionality.

To determine the minimum pulse width required for achieving a stable SET operation, shorter SET pulses were applied sequentially at widths of 0.02 ms, 0.05 ms, 0.1 ms, 0.2 ms and 0.5 ms, each preceded by a RESET pulse of 10 ms to ensure consistent initial conditions. **Figure 6.6** (c) presents the resistance measurements following these SET pulses. The results that a significant decrease in resistance from 11.5 kΩ to 4.5 kΩ as the pulse width increased from 0.02 ms to 0.2 ms. Beyond 0.2 ms, the SET resistance stabilises around 4.5 kΩ, suggesting the device reliably reaches the ON state (LRS). Data presented in **Figure 6.6** (b) and insert of (c) were fitted using the exponential equation $R = R_r + R_0 e^{-\frac{t}{\tau}}$. Analysis of the fitting revealed that the RESET time constant ($\tau = 10.6$ ms) is approximately 180 times greater than the SET time constant ($\tau = 0.06$ ms), highlighting a significantly faster SET response compared with RESET.

Conduction mechanism: To investigate the conduction mechanisms in these resistance states, *I-V* measurements were conducted for device states prepared using varying pulse widths. The pulse train utilised in this study is illustrated in **Fig. 6.7** (a), where the red arrow indicates an individual cycle comprising a

RESET pulse, a SET pulse and two subsequent reading processes (I-V measurements). Within each cycle, RESET and SET pulses have identical amplitudes of 1 V but opposite polarities. Following each switching pulse, a forward voltage sweep ranging from 0 V to 0.4 V, incremented in steps of 3.2 mV, was applied to record the corresponding I-V characteristics. After each measurement cycle, the device was returned to the LRS, ensuring a consistent initial state for subsequent cycles. Measurements were systematically conducted over multiple cycles with pulse widths applied in the following sequence: 10 ms, 5 ms, 2 ms, 1 ms, 0.8 ms, 0.6 ms, 0.5 ms, 0.4 ms, 0.3 ms, 0.2 ms, 0.1 ms, 0.08 ms, 0.06 ms, 0.04 ms, 0.03 ms and 0.02 ms.

Figure 6.7 (b) compares the measured I-V curves recorded after RESET pulses of varying pulse widths. As anticipated, the overall current level decreases with increasing pulse width. To analyse the conduction mechanisms involved, five models - Ohmic conduction, Fowler-Nordheim (FN) tunnelling, Schottky emission, Poole-Frankel (PF) emission and space charge limited conduction (SCLC) - were evaluated. Among those mechanisms, the FN tunnelling and Schottky emission are contact limited conduction, while the others are bulk limited. The recorded I-V curves were fitted according to the theoretical behaviours predicted by these models, as presented in A.9. Among these conduction mechanisms, the Schottky emission model, characterised by $ln(I) \propto \sqrt{V}$, demonstrated the highest R^2 values, indicating the best fit. The inset of **Fig. 6.7** (b) illustrates the Schottky model fitting of the I-V characteristics measured after a 10 ms RESET pulse, yielding an R^2 value of 0.9985. It is worth mentioning that, for the shortest pulse width of 0.02 ms, the R^2 values for Ohmic conduction and Schottky emission model are comparable (A.9 (d)), suggesting that the RESET process was incomplete at this pulse duration.

Figure 6.7 (c) presents the I-V characteristics obtained after applying SET pulses of varying pulse widths. The overall current level increases as the pulse width increases. Fitting of these I-V datasets (see A.10) predominantly indicates Ohmic conduction behaviour. However, at the shortest pulse width of 0.02 ms, the R^2 values for Ohmic conduction and Schottky emission become comparable. The inset of **Fig. 6.7** (c) presents the Ohmic fitting for a 10 ms pulse which shows a R^2 of 0.9975. These findings suggest that conduction in the HRS is primarily governed by Schottky emission, whereas Ohmic conduction increasingly dominates in the LRS as the SET pulse width increases.

The thermionic emission model facilitates the extraction of the Schottky barrier height (SBH) (eq. (19)), presented in the upper panels of **Fig. 6.8** (a) and

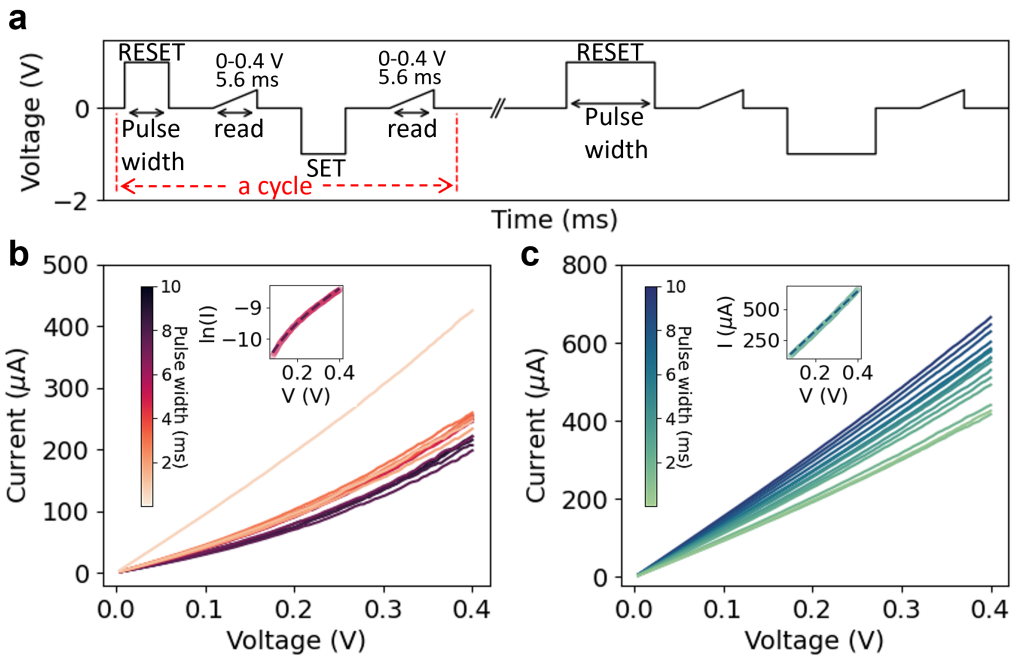


Figure 6.7: **Conduction mechanisms.** (a) Programming pulse sequence for SET/RESET cycles with *I-V* measurements after each switching pulse. (b) and (c) are *I-V* characteristics after switching operation at varying pulse widths for RESET and SET processes, respectively.

Fig. 6.8 (b) for the RESET and SET processes, respectively. In the RESET process, the SBH increases from $\sim$ 0.32 eV to $\sim$ 0.35 eV as the pulse width increases from 0.02 ms to 1 ms. It stabilises around 0.35 eV for pulse widths exceeding 1 ms. Conversely, during the SET process, the SBH decreases from $\sim$ 0.32 eV to $\sim$ 0.30 eV as the pulse width increases from 0.02 ms to 5 ms, and subsequently remains stable at $\sim$ 0.30 eV for pulse widths greater than 5 ms. These variations in SBH suggest that the switching behaviour of the device is significantly influenced by changes occuring at the electrode-MoS_2 interface.

It is well-established that the SBH can be modulated by adjusting the dopant concentration at the semiconductor surface [220], and consequently, the dopant concentration N_d can be derived from the SBH eq. (4). The values of N_d obtained after the RESET and SET processes are plotted against the pulse width in the lower panels of **Fig. 6.8** (a) and **Fig. 6.8** (b), respectively. During the RESET process, the dopant concentration decreases with increasing pulse width, whereas during the SET process, it increases. This observation suggests that dopants migrate away from the interface during the RESET process and toward the interface during the SET process. Within the device channel materials (MoS_2 with minor oxides), oxygen impurities and sulfur vacancies act as mobile n-type dopants under an applied electric field.

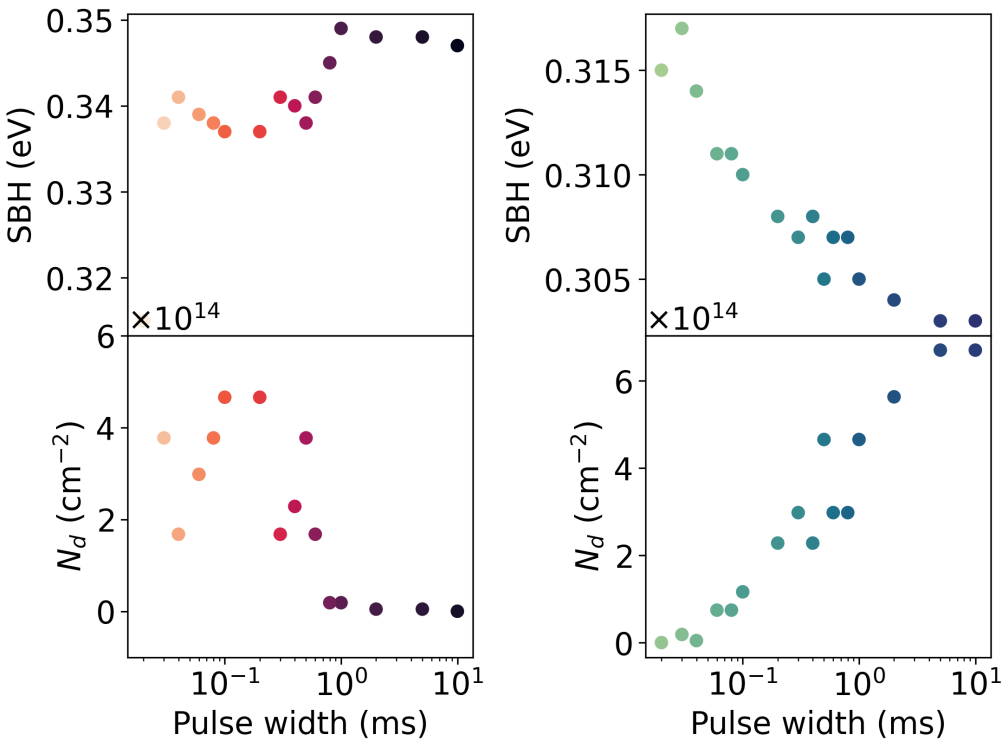


Figure 6.8: **Schottky barrier height and dopant concentration.** (a) SBH extracted after RESET pulses at varying pulse widths and calculated dopant concentration N_d. (b) SBH extracted after SET pulses at varying pulse widths and N_d.

6.4 Switching mechanism

The previous section focused on two-terminal *I-V* measurements of a single channel, indicating that the resistance state is primarily governed by the SBH at the metal-semiconductor interface. To further verify this model, three-channel devices were utilized (see **Fig. 6.1**), as modulation of the SBH in one channel is expected to influence the conduction properties of adjacent channels. An optical image of a representative three-channel device is shown in **Fig. 6.9**. For clarity, electrodes are labelled E_4, E_3, E_2, and E_1 from left to right, with the corresponding channels designated as Ch_L, Ch_M, and Ch_R, respectively.

During these measurements, the middle channel (Ch_M) serves as the active channel, undergoing electroforming, RESET and SET operations. Concurrently, the resistances of the adjacent channels (Ch_L and Ch_R) are also recorded alongside that of Ch_M. The voltage polarity is consistently maintained, with the left electrode of a channel always grounded when the channel is measured. For example, when operating the Ch_M, the bias voltage is applied to E_2 while E_3 is grounded. To ensure that the operations of Ch_M do not inadvertently influence Ch_L and Ch_R, electrodes E_3 and E_4 are held at the same potential, as are electrodes

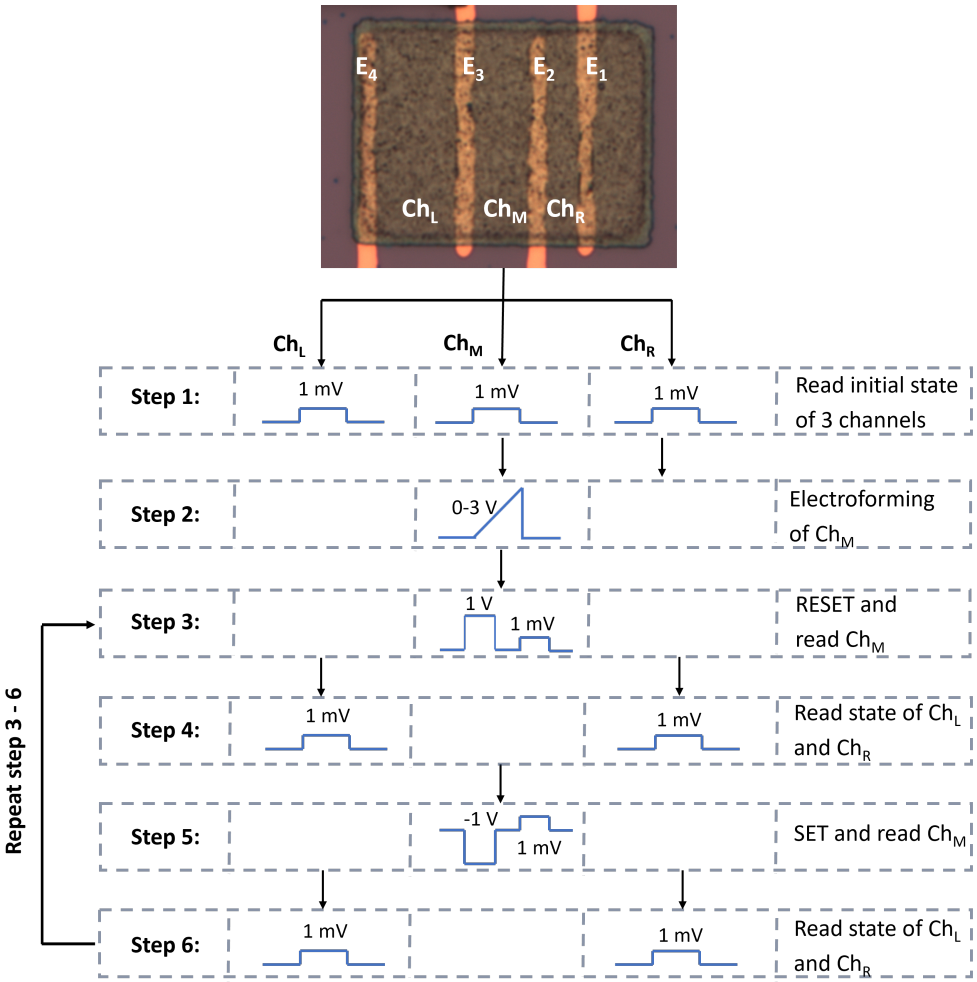


Figure 6.9: **The flow chart of the measurement steps for 3-channel measurement.** The specific device under investigation is located at coordinates $(x, y) = [-1.1, 10.8]$. The electrodes and channels are labelled E_4, E_3, E_2, E_1, and Ch_L, Ch_M and Ch_R, respectively, from the left to right. The blue curves sketch the profile of the applied voltage.

E_1 and E_2. This configuration effectively prevents unintended voltage bias across Ch_L and Ch_R while operating on Ch_M.

The measurement procedure for the 3-channel device is illustrated in **Fig. 6.9**. The process involves the following sequential steps:

Step 1: Initial resistances of channels Ch_L, Ch_M, and Ch_R are measured individually using 500 reading pulses per channel, each pulse having an amplitude of 1 mV and a duration of 1 ms.

Step 2: Electroforming of Ch_M is conducted via a voltage sweep from 0 to 3 V.

Step 3: A RESET operation is conducted on Ch_M by applying a 1 V voltage pulse, followed by 10 reading pulses to confirm its resistance state.

Step 4: The resistances of channels Ch_L and Ch_R are subsequently monitored us-

ing another set of 500 reading pulses.

Step 5: A SET operation is performed on Ch_M to achieve LRS using a pulse amplitude of -1 V, again followed by 10 reading pulses to verify the state.

Step 6: Finally, resistances of channels Ch_L and Ch_R are re-evaluated with an additional set of 500 reading pulses.

To ensure the reproducibility of the observed electrical behavior, Steps 3 to 6 are repeated once more.

Initially, as shown in **Fig. 6.10** for pulse number 0-500, the resistances measured for channels Ch_L, Ch_M and Ch_R are approximately 5.0 MΩ, 4.5 MΩ and 5.9 MΩ, respectively. Variations among these values may likely arise from differences in channel lengths and minor changes in channel width introduced during device fabrication.

For pulse numbers between 500 and 1000, resistance measurements reflect the states of the channels after the electroforming and RESET operation on Ch_M. Compared with their initial states, Ch_M and Ch_L exhibit significant resistance decreases by nearly three orders of magnitude, reaching approximately 5.8 kΩ and 6.5 kΩ, respectively. Conversely, Ch_R experiences a slight resistance increase, reaching 7.4 MΩ.

Following the SET operation on Ch_M, as shown by pulse numbers 1000-1500, Ch_M resistance further decreases to 3.4 kΩ. Ch_L exhibits similar behaviour, with its resistance lowering to $\sim$ 3.6 kΩ, whereas Ch_R maintains a high resistance of $\sim$ 7.4 MΩ.

To verify reproducibility, Steps 3 through 6 were repeated, as illustrated by pulse numbers 1500-2500 in **Fig. 6.10**. The resistance behaviours observed during both RESET and SET operations in this repeated cycle closely replicate the results from pulse numbers 500-1500, confirming consistent device performance.

These results confirm that the resistive switching of the three channels is both reversible and reproducible. Importantly, when the state of Ch_M is changed, Ch_L correspondingly updates its state, while Ch_R remains unaffected and retains its initial resistance. This behaviour suggests that the SBH at electrode E_3 is modulated during the operations on Ch_M. Conversely, the lack of significant resistance variation in Ch_R suggests minimal modulation of SBH at the electrode E_2.

These findings support the proposed switching model and confirm that the resistance in the two-terminal device (single channel) is predominantly influenced by the modulation of the SBH at one electrode-channel interface. The symmetry

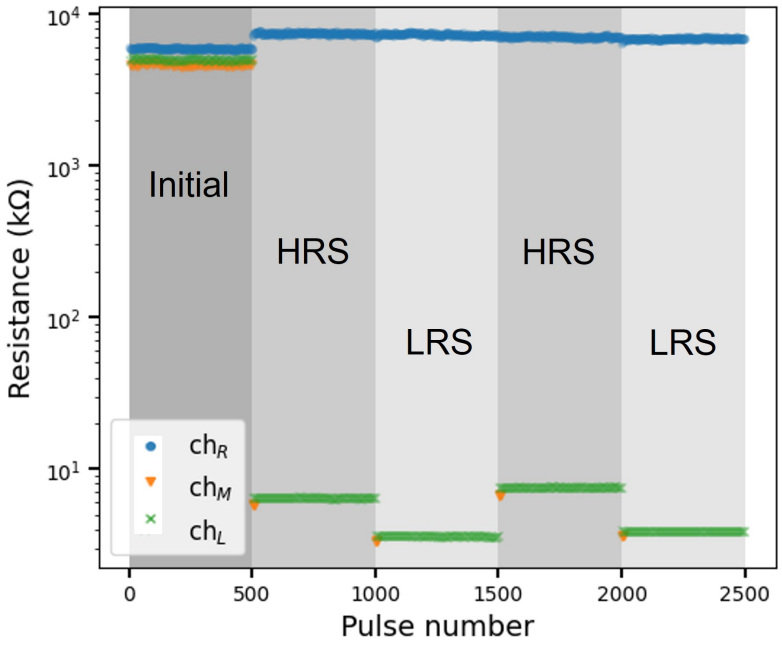


Figure 6.10: **Resistance of three channels at different operation states of Ch_M.** Resistance of three channels at different operation states of Ch_M: initial state, HRS and LRS.

between the two electrodes is disrupted during the electroforming process, and subsequent switching operations (RESET and SET) modulate the SBH through defect migration, thus enabling reversible resistance switching.

Compositional analysis during switching: From detailed characterisation in chapter 5 and Raman characterisation in **Fig. 6.4**, it is clear that the channel material of the device mainly consists of MoS_2 with minor amount of MoO_2. Quantitative elemental analysis is crucial to elucidating the underlying switching mechanism in the memristor device. Thus, Energy-dispersive X-ray Spectroscopy (EDX) was used to evaluate the ratio of MoS_2 to MoO_2.

Figure 6.11 (a) and (b) display the EDX elemental mappings of Mo+S and O, respectively, which were collected at an electron beam energy of 10 keV. The mappings reveal a uniform distribution of Mo+S and O across the mesa surface. However, in the electrode regions, the intensity of both Mo+S and O signals is significantly reduced due to attenuation by the overlying Ti/Au layers.

The EDX spectrum in **Fig. 6.11** (c), obtained at an electron beam energy of 10 keV, features a strong asymmetric peak at near 2.3 keV corresponding to the Mo Lα, with an evident tail around 2.4 keV, indicating the presence of S Kα. The Si peak observed at 1.7 keV originates from the substrate, whereas the O peak at $\sim$ 0.5 keV may include contributions from the substrate and the mesa film. Despite the clear detection of Mo, S and O signals in the channel, determining the

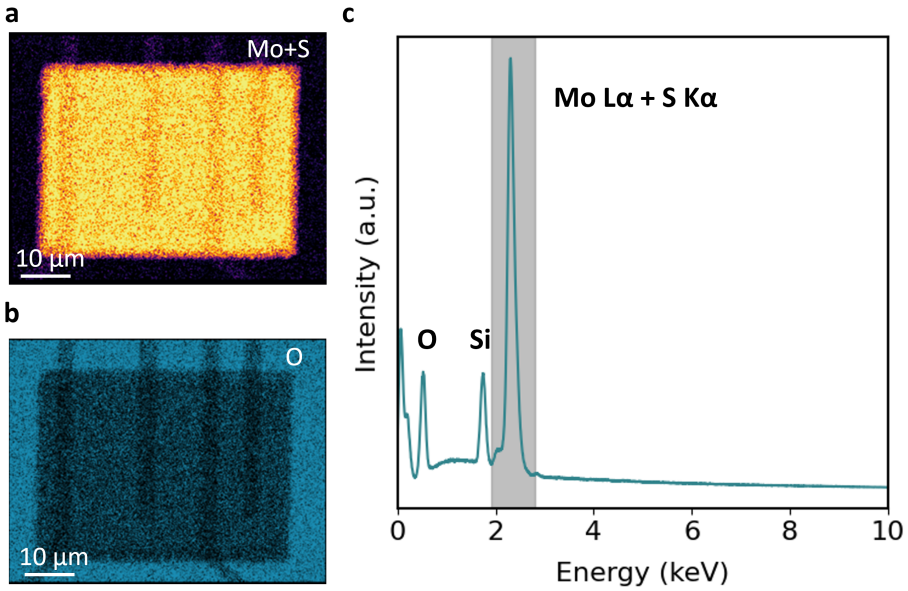


Figure 6.11: **EDX of MoS_2/MoO_2 at an electron beam energy of 10 keV.** (a-b) EDX mapping of a MoS_2/MoO_2 memristor device on SiO_2/Si substrate. (c) EDX spectrum of MoS_2/MoO_2 collected with an electron beam energy of 10 keV.

precise elemental ratio among them remains challenging for main two reasons: (1) the spectral overlapping between S kα and Mo Lα peaks, and (2) the presence of O originating from the SiO_2/Si substrate.

To circumvent the spectral overlapping between Mo $L\alpha$ and S $K\alpha$ peaks, we can use the Mo $K\alpha$ peak which is attainable using an electron beam with sufficient energy. In addition, Monte Carlo simulation can be conducted (using Casino software) to assess the evolution of the intensity ratio, $\frac{MoK\alpha}{MoL\alpha+SK\alpha}$, at varying S/Mo ratios in the material. **Fig. 6.12** (a) illustrates the model used in the simulation. The model consists of a 100 nm MoS_2/MoO_2 on 285 nm SiO_2/Si. The applied electron energy is 30 keV, which is the same as the experimental result in **Fig. 6.12** (d). **Figure 6.12** (b) shows the simulated electron-sample interaction volume when electrons are injected from the MoS_2/MoO_2 film, while colours represent the electron intensity. The simulation shows that the penetration depth is about 6.5 µm. Since the oxygen signal may originate from both the channel and the substrate SiO_2, the S/O ratio in the film cannot be reliably determined. However, the Mo/O ratio can be inferred from the measured Mo/S ratio.

The simulation clearly shows that the intensity of Mo $L\alpha$, Mo $K\alpha$, and S $K\alpha$ varies with different S/Mo ratios. The intensity ratio, $MoK\alpha/(MoL\alpha + SK\alpha)$, at different S/Mo atomic ratio is calculated and plot in **Fig. 6.12** (c). The graph shows that the intensity ratio decreases with the increase of the S/Mo atomic ratio. The intensity ratio is around 0.062 for MoS_2 while it is around 0.089 for MoS_2/MoO_2 with a ratio of 1:1. **Figure 6.12** (d) shows the EDX spectrum in the

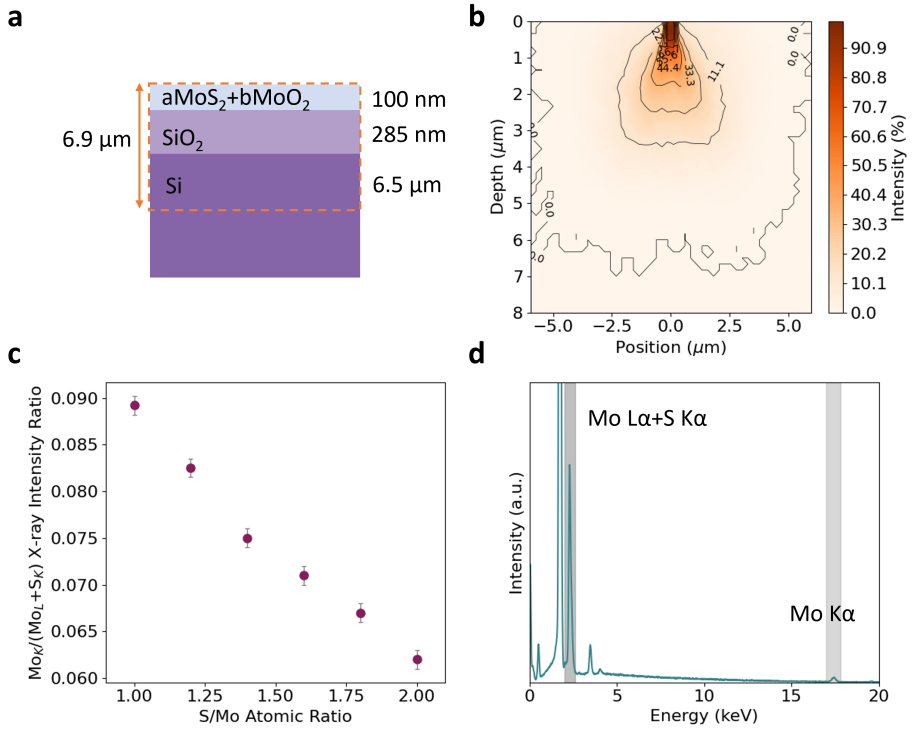


Figure 6.12: **Simulation and experimental EDX of MoS_2/MoO_2 at an electron beam energy of 30 keV.** (a) The sample structure model highlights the depth of electrons go through. (b) Monte Carlo simulation result for electron interaction volume on 100 nm MoS_2/MoO_2 film. (c) Monte Carlo simulation for X-ray intensity ratio of Mo $K\alpha$/(Mo $L\alpha$ + S $K\alpha$) versus the S/Mo atomic ratio. (d) Experimental data of EDX spectra for the as-grown MoS_2/MoO_2 film.

range of 0-20 keV, which is collected from the as-grown film using an electron beam energy of 30 keV. The peak at 2.3 keV corresponds to the overlapping peak of $MoL\alpha$ and $SK\alpha$, while the peak at 17.4 keV is the Mo $K\alpha$. The integrated intensity ratio is calculated to be 0.067. Compare with the simulation result in **Fig. 6.12** (c), the S to Mo ratio is around 1.8, which indicates the MoS_2 and MoO_2 ratio in the film is 9:1. Although oxygen can substitute chalcogen atoms (X) in MX_2 (transition metal dichalcogenides (TMDs)) without altering its crystal structure, with x reaching as high as 1.48 in MO_xX_{2-x} [256]. However, the X-ray diffraction (XRD) result in **Fig. 5.3** (c) revealed additional peaks other than MoS_2 phase. This suggests the presence of other phases. Therefore, our material is a mixed phase consisting of MoS_2 and MoO_2, with a ratio of 9:1. These results support the presence of a minor amount of oxygen in the channel materials, which may act as dopants to modulate the SBH.

Although this approach demonstrates the potential for detecting variations in S and/or O concentrations at the interface during switching, reliably conducting such experiments remains extremely challenging. Future studies could explore in-situ electron microscopy methods to investigate defect concentrations, provid-

ing deeper insights into the underlying switching mechanisms.

6.5 Neuromorphic Applications

We also investigate the memristor SET and RESET processes by accumulated pulse measurements. Initially, as shown in **Fig. 6.13** (a), three consecutive pulses, each with an amplitude of 1.5 V and a duration of 200 ms, are applied to RESET the device. During the first pulse, the resistance gradually increases to 700 ohms and the current decreases to 2 mA. In the second pulse, the resistance slightly increases in the first 0.1 s and then remains stable. At the third pulse, both the current and resistance remain, indicating the stable HRS. Subsequently, three consecutive pulses are applied to SET the device, each with an amplitude of -1.5 V and a duration of 200 ms. From the first pulse, the amplitude of the current immediately increases to 4 mA, and the resistance reduces to 400 ohms, indicating a rapid transition from the HRS to the LRS. The current and resistance remain stable during the second and third pulses. No gradual changes are observed during the SET process but the RESET process, revealing that the SET process occurs faster than the RESET process.

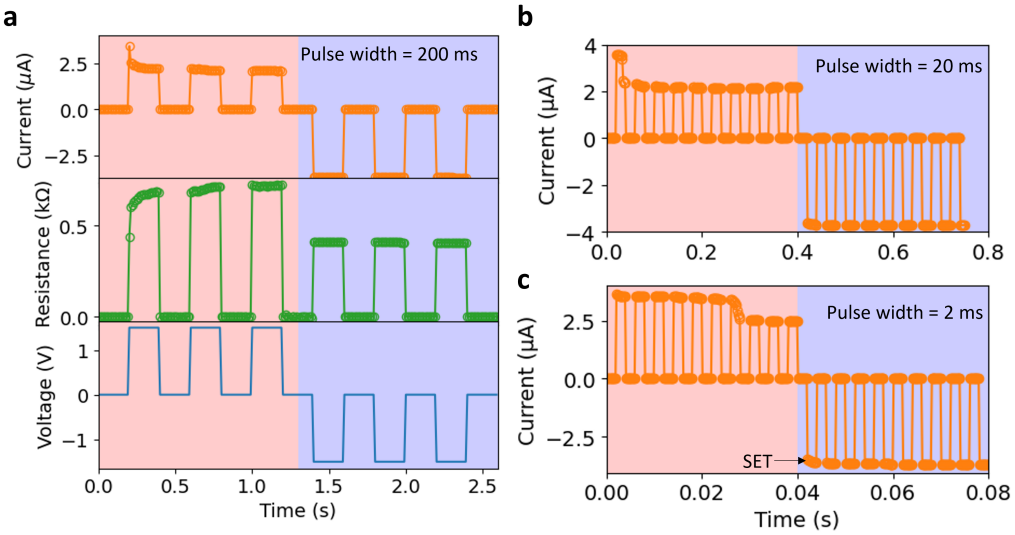


Figure 6.13: **Observation of biosynaptic behaviour.** Accumulated pulse measurement with a pulse amplitude of 1.5 V and pulse width of (a) 200 ms, (b) 20 ms and (c) 2 ms.

To observe the rapid change of the SET process, further measurements are conducted with the same pulse amplitude but reduced pulse width and increased pulse numbers (10 pulses for SET and RESET, respectively). When the pulse duration is 20 ms, as shown in **Fig. 6.13** (b), the RESET process takes around 10 ms while the SET process is still not identical. When the pulse duration is reduced to 2 ms (**Fig. 6.13** (c)), it takes approximately 30 ms for the device to RESET from

LRS to HRS. For the SET process, a steeper increase in current is observed during the first pulse, a 2 ms SET duration, being one-fifteenth the duration of the RESET process. Gradual changes in conductance under continuous negative or positive voltage stimulation (with constant pulse width), analogous to biosynaptic behaviour exhibiting progressively varying synaptic weights, mimicking the long-term potentiation (LTP) AND long-term depression (LTD). The results also suggest that pulses with shorter durations require a greater number of repetitions to change the synaptic weights.

Synapse behavior is further investigated by applying a step function voltage to the MoS_2/MoO_2 memristor device. When 250 negative pulses with a height of -8 mV and a width of 20 ms are applied (**Figure 6.14** (a)) the conductance of the device increases steadily. The increased conductance of the memristor in response to the positive pulses mimics the LTP process in biological synapses. Subsequently, when 250 positive pulses with a height of 8 mV and a width of 20 ms are applied, the conductance of the memristor decreased gradually (**Fig. 6.14** (b)). The memristor conductance decreased with the negative pulses, mimicking the LTD in biological synapses. The result clearly illustrates the dynamic synaptic behaviour of the memristor, which is crucial for applications in neuromorphic computing.

The MoS_2/MoO_2 memristor devices as artificial electronic synapses are verified and compared using image classification tasks as a function of a training epoch with the assistance of Dr. Navaj. B. Mullani. Furthermore, the linearity of the LTP and LTD curves, which is the most essential factor for determining the accuracy of artificial neural networks (ANN) computations based on neuromorphic devices, is regulated by pulses during synaptic measurements. The potential for image recognition is implemented by an ANN for classifying the Modified National Institute of Standards and Technology (MNIST) [45] and Fashion MNIST [253] datasets. These datasets consist of 50,000 training and 10,000 test images (28×28 pixels) across 10 categories. Our architecture comprises a three-layer perceptrons with 768, 200, and 10 neurons, where input images are flattened before processing through the network. **Figure 6.14** (c) presents an illustration of the ANN approach adopted for the Fashion-MNIST and MNIST pattern recognition.

To implement synaptic weights, we adopted a differential scheme using two devices to accommodate negative weights, where the effective weight was calculated as $\omega = G^+ + G^- - 0.1$. We normalized the LTP and LTD conductance values between 0.0 and 1.0 to align with typical ANN weight ranges. Previous

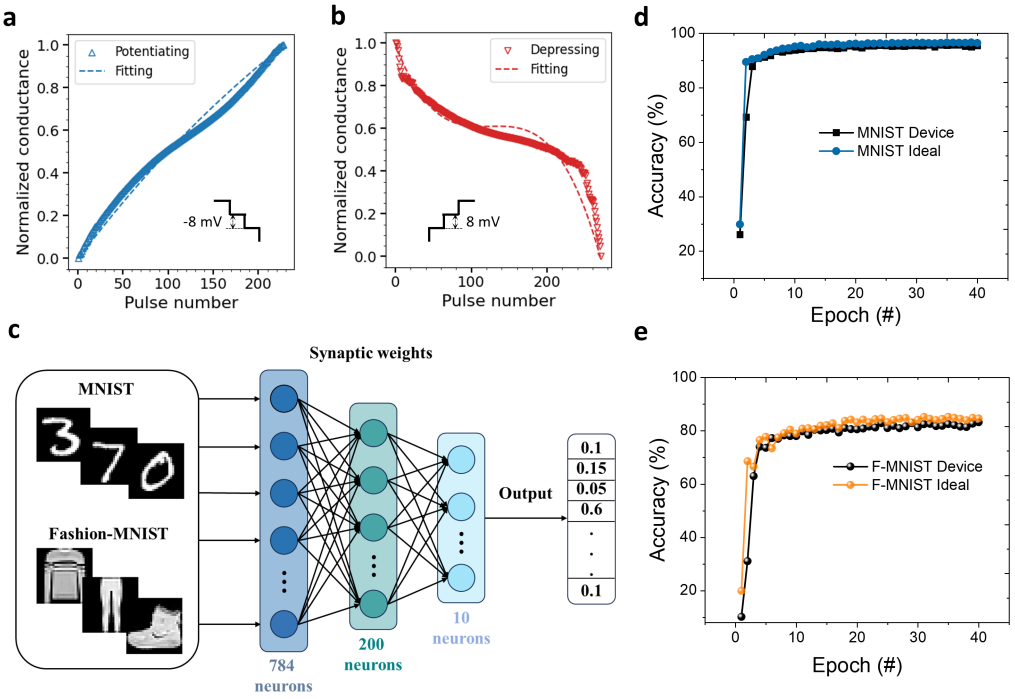


Figure 6.14: **ANN pattern recognition of MNIST and Fashion-MNIST.** Potentiation and depression synapse behavior of a MoS_2/MoO_2 memristor. Measured under 250 continuous positive pulse voltage (8 mV, 20 ms) and 250 negative pulse voltage (-8 mV, 20 ms). (a) Normalized conductance curves from 0 to 0.1 V. (c) Schematic of a neural network for Fashion-MNIST pattern recognition stimulation (784 neurons - 200 neurons - 10 neurons). Pattern recognition stimulation accuracy curves for (c) MNIST and (d) Fashion-MNIST. (e) ANN was used to simulate digits and fashion images from the MNIST and Fashion-MNIST datasets. Data in **Fig. 6.14** (d) and (e) are collected and processed by Dr. Navaj. B. Mullani.

works [31, 116, 261] commonly model their LTP (G^+) and LTD (G^-) curves for synaptic weights using:

$$G^+ = G^+_{\text{min}} + \frac{G^+_{\text{max}} - G^+_{\text{min}}}{1 - e^{-v^+ \cdot P_{\text{max}}}} \cdot \left(1 - e^{-v^+ \cdot P}\right) + \sigma \tag{1}$$

$$G^- = G^-_{\text{min}} + \frac{G^-_{\text{max}} - G^-_{\text{min}}}{1 - e^{-v^- \cdot P_{\text{max}}}} \cdot \left(1 - e^{v^- \cdot (P - P_{\text{max}})}\right) + \sigma \tag{2}$$

where G^+ and G^- represent normalized conductances, v^+ and v^- are nonlinearity coefficients, P_{max} denotes maximum pulse number, and σ represents device variation noise sampled from a normal distribution to account for device variability. While our LTP curve follows the expected exponential behavior like eq. (1), our LTD curve exhibits different characteristics from eq. (2). Here, we approximated the LTD curve using a cubic polynomial: $-x^3 + 0.25x^2 + 1.25$ (see **Fig. 6.14** (b)).

To further optimize device performance and training efficiency, we imple-

mented several key strategies. First, we prioritized power efficiency by applying single pulses for conductance updates while maintaining unidirectional conductance changes for both LTP and LTD. Additionally, we incorporated a reset mechanism to maintain training stability when conductances reached their extremes. The fitted curves showed nonlinearity coefficients of $v^+ = 0.004$, where zero represents ideal linear behavior. The accuracy curves for the two datasets are shown in **Fig. 6.14** (d) and (e). The simulated digits and images are depicted in **Fig. 6.14** (c). Based on experimental results on the MNIST and Fashion MNIST datasets demonstrated that despite hardware constraints, our device achieved comparable performance to the ideal case: 95.55% versus 96.48% (ideal) for MNIST, and 83.23% versus 84.67% (ideal) for Fashion MNIST, with both scenarios following similar training trajectories.

6.6 Conclusions

We have successfully demonstrated the memristive devices based on the patterned-grown MoS_2/MoO_2 films. The electroforming process is required to enable the device switching. The memristor can operate with a low voltage, ± 1 V, which is promising for energy-efficient applications. The *I-V* curves and SBH change observed are evident that the device conduction is dominated by Schottky emission. The accumulation of the vacancies at the electrode-MoS_2 contact acts as dopants that tune the Schottky barrier height and R_c. Mento Carlo simulation is used to qualitatively analyze chemical composition of the material, where the as-grown film is found to be MoS_2/MoS_2 with a ratio of 9:1. We further demonstrated the potential of the device as an artificial synapse by mimicking the LTP and LTD processes, highlighting its promise for neuromorphic applications.

7 | Conclusions and Outlook

"Never lose a holy curiosity."

- Albert Einstein

7.1 Conclusions

In this thesis, with the aim of achieving large-scale, controllable growth of few-layer MoS_2 and its application in electronic devices, systematic research has been conducted on MoS_2 synthesis, material properties, and its electronic characterisation. The key contributions of this work are summarized as follows:

We first developed a novel contamination-free growth promoter, photoresist S1813, enabling the clean and controlled growth of two-dimensional (2D) MoS_2 with desirable grain structures. A notable promoter-induced enhancement is observed at a sulfur temperature of 250 °C, increasing monolayer coverage by over three times and boosting the density of large-area flakes ($\geq$ 10 μm) by 60-fold. Varying sulfur temperature provided insight into nucleation behaviour, revealing a transition from homogeneous to heterogeneous nucleation. Furthermore, sulfur temperature was found to strongly influence sulfur vacancy density, with implications for tuning material properties.

Leveraging the patternability of photoresist, we established a scalable polymer-assisted chemical vapour deposition (CVD) method for the selective growth of MoS_2. By strategically incorporating polymer mesas patterned via laser direct writing (LDW) and optical lithography (OL), we achieved precise spatial control over nucleation site and film morphology. Systematic analyses across the substrate at varied positions revealed a clear correlation among MoO_x particle density, mesa thickness, and surrounding film dimensions, highlighting the critical influence of reactant concentrations, particularly MoO_x and sulfur, on MoS_2 growth outcomes. These findings elucidate the diffusion-controlled

growth mechanisms responsible for patterned MoS_2 formation. This approach was scaled up to achieve centimeter-scale patterned MoS_2 films with lateral dimensions exceeding 5 mm, underscoring its industrial adoption.

The growth strategy was further validated through the fabrication of planar memristors based on the MoS_2 films. These devices exhibit an on/off ratio of $\sim$50 and a low operation voltage, $<$1 V, which is promising for power-efficient applications. Under applied bias, the memristor is driven by defect migration and Schottky barrier modulation at the MoS_2-metal interface. The ability to control the growth of MoS_2 enabled precise tuning of the memristor resistance states and switching dynamics, highlighting the potential of MoS_2-based memristors for future electronic applications. The as-grown film composition was found to be MoS_2/MoO_2 with an atomic ratio of 9:1, as confirmed via Monte Carlo simulation of Energy-dispersive X-ray Spectroscopy (EDX) data. The memristors also demonstrated neuromorphic capabilities by mimicking long-term potentiation (LTP) and long-term depression (LTD), suggesting their potential for low-power, data-centric neuromorphic systems.

7.2 Outlook

Overall, this thesis has provided significant insights into the controlled synthesis of 2D MoS_2 and its application in electronic devices, laying the groundwork for future research in 2D materials and their applications. The research presented in this thesis opens several avenues for future exploration:

1. Material synthesis: The uniformity of film growth can be further optimised by refining the reactant concentration during the CVD process. This approach helps control and reduce defect density (e.g., sulfur vacancy concentration), thereby enhancing the material's optical properties.

2. Doping and functionalization: The controlled growth method allows for the exploration of selective doping and functionalization of MoS_2 films. For example, stable p-type doping could be achieved by modify the polymer chemicals, which is essential to enable the fabrication of complementary metal-oxide semiconductor (CMOS) devices. Additionally, patterned functional blocks with structure could be developed for specific applications.

3. Advanced device architectures: It is essential to study the electrical properties of the large-scale monolayer MoS_2. Future research could focus on integrating the synthesized 2D MoS_2 films into more complex device architectures, such as heterostructures or hybrid systems. This could enable the

development of multifunctional devices with enhanced performance, such as improved transistors, photodetectors, and energy storage devices.

4. Neuromorphic applications: The demonstrated potential of MoS_2 memristors as artificial synapses motivates further investigation into their neuromorphic capabilities. Future studies could explore the integration of these devices into larger neural networks and assess their performance in more complex neuromorphic tasks.

5. Scalability and commercialization: To move towards commercialization, future work should address the scalability of the synthesis process and the reproducibility of device performance. Collaboration with industry partners could help translate the findings of this thesis into real-world applications, particularly in the fields of flexible electronics, wearable technology, and neuromorphic computing.

6. Expansion to other transition metal dichalcogenides (TMDs): The growth strategy developed for MoS_2 can be extended to other TMDs, such as WS_2, ReS_2. By applying similar techniques, it may be possible to achieve large-area, high-quality growth of these materials, expanding their potential applications in electronics, optoelectronics, and sensing.

References

[1] Samuel Aldana, Jakub Jadwiszczak, and Hongzhou Zhang. "On the switching mechanism and optimisation of ion irradiation enabled 2D MoS_2 memristors". In: *Nanoscale* 15.13 (2023), pp. 6408–6416 (cit. on pp. 29, 32).

[2] Adrien Allain et al. "Electrical contacts to two-dimensional semiconductors". In: *Nature Materials* 14.12 (2015), pp. 1195–1205 (cit. on pp. 12–14).

[3] Michael Amato and Vladimir Rumennik. "Comparison of lateral and vertical DMOS specific on-resistance". In: *1985 International Electron Devices Meeting*. IEEE. 1985, pp. 736–739 (cit. on p. 21).

[4] Tsuneya Ando, Alan B Fowler, and Frank Stern. "Electronic properties of two-dimensional systems". In: *Reviews of Modern Physics* 54.2 (1982), p. 437 (cit. on p. 8).

[5] M Arita et al. "Resistance switching properties of molybdenum oxide films". In: *Thin Solid Films* 520.14 (2012), pp. 4762–4767 (cit. on p. 35).

[6] C Ataca et al. "A comparative study of lattice dynamics of three-and two-dimensional MoS_2". In: *The Journal of Physical Chemistry C* 115.33 (2011), pp. 16354–16361 (cit. on p. 6).

[7] Claudia Backes et al. "Edge and confinement effects allow in situ measurement of size and thickness of liquid-exfoliated nanosheets". In: *Nature Communications* 5.1 (2014), p. 4576 (cit. on pp. 85, 97).

[8] Claudia Backes et al. "Guidelines for exfoliation, characterization and processing of layered materials produced by liquid exfoliation". In: *Chemistry of Materials* 29.1 (2017), pp. 243–255 (cit. on p. 16).

[9] MA Baker et al. "XPS investigation of preferential sputtering of S from MoS_2 and determination of MoSx stoichiometry from Mo and S peak positions". In: *Applied Surface Science* 150.1-4 (1999), pp. 255–262 (cit. on pp. 96, 97).

[10] Pantelis Bampoulis et al. “Defect dominated charge transport and fermi level pinning in MoS_2/metal contacts”. In: *ACS Applied Materials & Interfaces* 9.22 (2017), pp. 19278–19286 (cit. on p. 13).

[11] CA Bates and KWH Stevens. “Localised electron states in semiconductors”. In: *Reports on Progress in Physics* 49.7 (1986), p. 783 (cit. on p. 12).

[12] MM Benameur et al. “Visibility of dichalcogenide nanolayers”. In: *Nanotechnology* 22.12 (2011), p. 125706 (cit. on pp. 52, 53).

[13] Alexander A Bessonov et al. “Layered memristive and memcapacitive switches for printable electronics”. In: *Nature Materials* 14.2 (2015), pp. 199–204 (cit. on pp. 16, 17, 28, 34, 35, 37).

[14] Shubhadeep Bhattacharjee et al. “Emulating synaptic response in n-and p-channel MoS_2 transistors by utilizing charge trapping dynamics”. In: *Scientific Reports* 10.1 (2020), p. 12178 (cit. on p. 31).

[15] Ya-Qing Bie et al. “Site-Specific Transfer-Printing of Individual Graphene Microscale Patterns to Arbitrary Surfaces”. In: *Advanced Materials* 23.34 (2011), pp. 3938–3943 (cit. on p. 43).

[16] Th Böker et al. “Band structure of MoS_2, $MoSe_2$, and α-$MoTe_2$: Angle-resolved photoelectron spectroscopy and ab initio calculations”. In: *Physical Review B* 64.23 (2001), p. 235305 (cit. on p. 7).

[17] John B Boland et al. “Liquid phase exfoliation of GeS nanosheets in ambient conditions for lithium ion battery applications”. In: *2D Materials* 7.3 (2020), p. 035015 (cit. on p. 16).

[18] Britannica. *Bragg law*. https://www.britannica.com/science/Bragg-law (cit. on p. 72).

[19] Lola Brown et al. “Twinning and twisting of tri-and bilayer graphene”. In: *Nano Letters* 12.3 (2012), pp. 1609–1615 (cit. on p. 61).

[20] Bruker. *Automated deconvolution and quantification of peak overlaps in MoS_2*. https://www.bruker.com/it/products-and-solutions/elemental-analyzers/eds-wds-ebsd-SEM-Micro-XRF/quantax-flatquad/automated-deconvolution-and-quantification-of-peak-overlaps-MoS2.html (cit. on p. 63).

[21] Fabio Bussolotti et al. “Impact of S-vacancies on the charge injection barrier at the electrical contact with the MoS2 monolayer”. In: *ACS nano* 15.2 (2021), pp. 2686–2697 (cit. on p. 85).

[22] Dan Cao et al. “Role of chemical potential in flake shape and edge properties of monolayer MoS_2”. In: *The Journal of Physical Chemistry C* 119.8 (2015), pp. 4294–4301 (cit. on p. 89).

[23] Andres Castellanos-Gomez et al. “Isolation and characterization of few-layer black phosphorus”. In: *2D Materials* 1.2 (2014), p. 025001 (cit. on p. 16).

[24] Xiang Chen et al. “Lithography-free plasma-induced patterned growth of MoS_2 and its heterojunction with graphene”. In: *Nanoscale* 8.33 (2016), pp. 15181–15188 (cit. on p. 21).

[25] Yang Chen et al. “Mobility enhancement of strained MoS_2 transistor on flat substrate”. In: *ACS Nano* 17.15 (2023), pp. 14954–14962 (cit. on p. 8).

[26] ZY Chen et al. “Observation of sp^3 bonding in tetrahedral amorphous carbon using visible Raman spectroscopy”. In: *Journal of Applied Physics* 88.5 (2000), pp. 2305–2308 (cit. on p. 87).

[27] Long Cheng and Yuanyue Liu. “What limits the intrinsic mobility of electrons and holes in two dimensional metal dichalcogenides?” In: *Journal of the American Chemical Society* 140.51 (2018), pp. 17895–17900 (cit. on p. 8).

[28] Peifu Cheng, Kai Sun, and Yun Hang Hu. “Memristive behavior and ideal memristor of 1T phase MoS_2 nanosheets”. In: *Nano Letters* 16.1 (2016), pp. 572–576 (cit. on pp. 18, 30, 37).

[29] Manish Chhowalla, Debdeep Jena, and Hua Zhang. “Two-dimensional semiconductors for transistors”. In: *Nature Reviews Materials* 1.11 (2016), pp. 1–15 (cit. on p. 14).

[30] Manish Chhowalla et al. “The chemistry of two-dimensional layered transition metal dichalcogenide nanosheets”. In: *Nature Chemistry* 5.4 (2013), pp. 263–275 (cit. on p. 28).

[31] Hoyeon Cho et al. “Double-floating-gate van der Waals transistor for high-precision synaptic operations”. In: *ACS Nano* 17.8 (2023), pp. 7384–7393 (cit. on p. 149).

[32] Kyungjune Cho et al. “Electrical and optical characterization of MoS_2 with sulfur vacancy passivation by treatment with alkanethiol molecules”. In: *ACS Nano* 9.8 (2015), pp. 8044–8053 (cit. on p. 9).

[33] J-G Choi and LT Thompson. “XPS study of as-prepared and reduced molybdenum oxides”. In: *Applied Surface Science* 93.2 (1996), pp. 143–149 (cit. on p. 96).

[34] Nitin Choudhary et al. “Centimeter scale patterned growth of vertically stacked few layer only 2D MoS_2/WS_2 van der Waals heterostructure”. In: *Scientific Reports* 6.1 (2016), p. 25456 (cit. on pp. 21, 103).

[35] Leon Chua. “Memristor-the missing circuit element”. In: *IEEE Transactions on Circuit Theory* 18.5 (1971), pp. 507–519 (cit. on p. 24).

[36] Leon O Chua and Sung Mo Kang. “Memristive devices and systems”. In: *Proceedings of the IEEE* 64.2 (1976), pp. 209–223 (cit. on p. 25).

[37] Jonathan N Coleman et al. “Two-dimensional nanosheets produced by liquid exfoliation of layered materials”. In: *Science* 331.6017 (2011), pp. 568–571 (cit. on p. 16).

[38] Norman Colthup. *Introduction to infrared and Raman spectroscopy*. Elsevier, 2012 (cit. on p. 67).

[39] Áine Coogan and Yurii K Gun’ko. “Solution-based “bottom-up” synthesis of group VI transition metal dichalcogenides and their applications”. In: *Materials Advances* 2.1 (2021), pp. 146–164 (cit. on p. 17).

[40] CR Crowell. “The Richardson constant for thermionic emission in Schottky barrier diodes”. In: *Solid-State Electronics* 8.4 (1965), pp. 395–399 (cit. on p. 74).

[41] Huanyao Cun et al. “Wafer-scale MOCVD growth of monolayer MoS_2 on sapphire and SiO_2”. In: *Nano Research* 12 (2019), pp. 2646–2652 (cit. on p. 18).

[42] Saptarshi Das et al. “High performance multilayer MoS_2 transistors with scandium contacts”. In: *Nano Letters* 13.1 (2013), pp. 100–105 (cit. on p. 15).

[43] Isha M Datye et al. “Strain-enhanced mobility of monolayer MoS_2”. In: *Nano Letters* 22.20 (2022), pp. 8052–8059 (cit. on p. 8).

[44] J. Debdeep and K. Aniruddha. “Enhancement of carrier mobility in semiconductor nanostructures by dielectric engineering”. In: *Physical Review Letters* 98 (2007), p. 136805 (cit. on p. 9).

[45] Li Deng. “The mnist database of handwritten digit images for machine learning research [best of the web]”. In: *IEEE Signal Processing Magazine* 29.6 (2012), pp. 141–142 (cit. on p. 148).

[46] Durjoy Dev et al. “2D MoS_2-based threshold switching memristor for artificial neuron”. In: *IEEE Electron Device Letters* 41.6 (2020), pp. 936–939 (cit. on pp. 30, 37).

[47] Horacio Coy Diaz et al. "Molecular beam epitaxy of the van der Waals heterostructure $MoTe_2$ on MoS_2: phase, thermal, and chemical stability". In: *2D Materials* 2.4 (2015), p. 044010 (cit. on p. 17).

[48] WM Ranjith Divigalpitiya, S Roy Morrison, and RF Frindt. "Thin oriented films of molybdenum disulphide". In: *Thin Solid Films* 186.1 (1990), pp. 177–192 (cit. on p. 17).

[49] Renhao Dong, Tao Zhang, and Xinliang Feng. "Interface-assisted synthesis of 2D materials: trend and challenges". In: *Chemical Reviews* 118.13 (2018), pp. 6189–6235 (cit. on p. 17).

[50] Goki Eda et al. "Photoluminescence from chemically exfoliated MoS_2". In: *Nano Letters* 11.12 (2011), pp. 5111–5116 (cit. on pp. 5, 7, 66).

[51] *Electron energy loss spectroscopy (EELS) for chemical and compositional analysis*. https://www.gatan.com/techniques/eels (cit. on p. 65).

[52] Chris D English et al. "Improved contacts to MoS_2 transistors by ultra-high vacuum metal deposition". In: *Nano Letters* 16.6 (2016), pp. 3824–3830 (cit. on p. 15).

[53] Xiaofeng Fan, David J Singh, and Weitao Zheng. "Valence band splitting on multilayer MoS_2: mixing of spin–orbit coupling and interlayer coupling". In: *The Journal of Physical Chemistry Letters* 7.12 (2016), pp. 2175–2181 (cit. on p. 71).

[54] Xuge Fan et al. "Rapid and large-area visualization of grain boundaries in MoS_2 on SiO_2 using vapor hydrofluoric acid". In: *ACS Applied Materials & Interfaces* 12.30 (2020), pp. 34049–34057 (cit. on p. 19).

[55] Y Feldman et al. "High-rate, gas-phase growth of MoS_2 nested inorganic fullerenes and nanotubes". In: *Science* 267.5195 (1995), pp. 222–225 (cit. on p. 42).

[56] Nan Feng et al. "A polymer-direct-intercalation strategy for MoS_2/carbon-derived heteroaerogels with ultrahigh pseudocapacitance". In: *Nature Communications* 10.1 (2019), p. 1372 (cit. on p. 87).

[57] Li-ping Feng et al. "Tuning the electronic properties of Ti-MoS_2 contacts through introducing vacancies in monolayer MoS_2". In: *Physical Chemistry Chemical Physics* 17.10 (2015), pp. 6700–6704 (cit. on pp. 13, 15).

[58] Qingliang Feng et al. "Growth of $MoS_{2(1-x)}Se_{2x}$ (x= 0.41-1.00) monolayer alloys with controlled morphology by physical vapor deposition". In: *ACS Nano* 9.7 (2015), pp. 7450–7455 (cit. on p. 17).

[59] Xuewei Feng et al. "A fully printed flexible MoS_2 memristive artificial synapse with femtojoule switching energy". In: *Advanced Electronic Materials* 5.12 (2019), p. 1900740 (cit. on p. 30).

[60] Andrea C Ferrari and John Robertson. "Interpretation of Raman spectra of disordered and amorphous carbon". In: *Physical Review B* 61.20 (2000), p. 14095 (cit. on p. 87).

[61] John R Ferraro. *Introductory raman spectroscopy*. Elsevier, 2003 (cit. on p. 68).

[62] Daniel S Fox et al. "Nanopatterning and electrical tuning of MoS_2 layers with a subnanometer helium ion beam". In: *Nano Letters* 15.8 (2015), pp. 5307–5313 (cit. on pp. 9, 10).

[63] Wei Fu et al. "Toward edge engineering of two-dimensional layered transition-metal dichalcogenides by chemical vapor deposition". In: *ACS Nano* 17.17 (2023), pp. 16348–16368 (cit. on p. 95).

[64] Cian Gabbett et al. "Understanding how junction resistances impact the conduction mechanism in nano-networks". In: *Nature Communications* 15.1 (2024), p. 4517 (cit. on p. 17).

[65] Sai Manoj Gali et al. "Electronic and transport properties in defective MoS_2: impact of sulfur vacancies". In: *The Journal of Physical Chemistry C* 124.28 (2020), pp. 15076–15084 (cit. on p. 9).

[66] Enlai Gao et al. "Mechanical exfoliation of two-dimensional materials". In: *Journal of the Mechanics and Physics of Solids* 115 (2018), pp. 248–262 (cit. on p. 16).

[67] Angel T Garcia-Esparza et al. "Local structure of sulfur vacancies on the basal plane of monolayer MoS2". In: *ACS nano* 16.4 (2022), pp. 6725–6733 (cit. on p. 85).

[68] Riley Gatensby et al. "Controlled synthesis of transition metal dichalcogenide thin films for electronic applications". In: *Applied Surface Science* 297 (2014), pp. 139–146 (cit. on pp. 18, 22).

[69] Anand PS Gaur et al. "Surface energy engineering for tunable wettability through controlled synthesis of MoS_2". In: *Nano Letters* 14.8 (2014), pp. 4314–4321 (cit. on p. 87).

[70] Ruijing Ge et al. "A library of atomically thin 2D materials featuring the conductive-point resistive switching phenomenon". In: *Advanced Materials* 33.7 (2021), p. 2007792 (cit. on pp. 18, 30).

[71] Dechao Geng et al. “Controlled growth of ultrathin Mo_2C superconducting crystals on liquid Cu surface”. In: *2D Materials* 4.1 (2016), p. 011012 (cit. on p. 87).

[72] Subhamoy Ghatak, Atindra Nath Pal, and Arindam Ghosh. “Nature of electronic states in atomically thin MoS_2 field-effect transistors”. In: *ACS Nano* 5.10 (2011), pp. 7707–7712 (cit. on p. 9).

[73] Joseph I Goldstein et al. *Scanning electron microscopy and X-ray microanalysis*. springer, 2017 (cit. on p. 59).

[74] Ananth Govind Rajan et al. “Generalized mechanistic model for the chemical vapor deposition of 2D transition metal dichalcogenide monolayers”. In: *ACS Nano* 10.4 (2016), pp. 4330–4344 (cit. on p. 89).

[75] Lauren H Grey, Heng-Yong Nie, and Mark C Biesinger. “Defining the nature of adventitious carbon and improving its merit as a charge correction reference for XPS”. In: *Applied Surface Science* 653 (2024), p. 159319 (cit. on p. 87).

[76] MH Grimsditch and AK Ramdas. “Brillouin scattering in diamond”. In: *Physical Review B* 11.8 (1975), p. 3139 (cit. on p. 87).

[77] Xingzhong Guo et al. “The novel and facile preparation of multilayer MoS_2 crystals by a chelation-assisted sol-gel method and their electrochemical performance”. In: *RSC advances* 7.15 (2017), pp. 9009–9014 (cit. on p. 17).

[78] Yunfan Guo et al. “Additive manufacturing of patterned 2D semiconductor through recyclable masked growth”. In: *Proceedings of the National Academy of Sciences* 116.9 (2019), pp. 3437–3442 (cit. on p. 22).

[79] Deepika Gupta, Vishnu Chauhan, and Rajesh Kumar. “Sputter deposition of 2D MoS_2 thin films-a critical review from a surface and structural perspective”. In: *Inorganic Chemistry Communications* 144 (2022), p. 109848 (cit. on p. 18).

[80] Varshita Gupta et al. “Resistive random access memory: a review of device challenges”. In: *IETE Technical Review* 37.4 (2020), pp. 377–390 (cit. on p. 26).

[81] SW Han et al. “Band-gap transition induced by interlayer van der Waals interaction in MoS_2”. In: *Physical Review B* 84.4 (2011), p. 045409 (cit. on p. 7).

[82] Wei Han et al. "Salt-assisted chemical vapor deposition of two-dimensional materials". In: *Science China Chemistry* 62 (2019), pp. 1300–1311 (cit. on pp. 19, 78).

[83] Yongli He et al. "Electric-double-layer transistors for synaptic devices and neuromorphic systems". In: *Journal of Materials Chemistry C* 6.20 (2018), pp. 5336–5352 (cit. on p. 27).

[84] Heinz K. Henisch. *Semiconductor contacts: An approach to ideas and models*. Oxford science publications, 1984 (cit. on p. 10).

[85] Yenny Hernandez et al. "High-yield production of graphene by liquid-phase exfoliation of graphite". In: *Nature Nanotechnology* 3.9 (2008), pp. 563–568 (cit. on p. 16).

[86] DW Hess et al. "Chemical vapor deposition: principles and applications". In: *Chemical Vapour Deposition: Principles and Applications* (1993) (cit. on p. 40).

[87] TW Hickmott. "Low-frequency negative resistance in thin anodic oxide films". In: *Journal of Applied Physics* 33.9 (1962), pp. 2669–2682 (cit. on p. 24).

[88] Jinhua Hong et al. "Exploring atomic defects in molybdenum disulphide monolayers". In: *Nature Communications* 6.1 (2015), p. 6293 (cit. on p. 9).

[89] Li Huang and Yang Gan. "A review on SEM imaging of graphene layers". In: *Micron* (2024), p. 103716 (cit. on p. 59).

[90] Pinshane Y Huang, Jannik C Meyer, and David A Muller. "From atoms to grains: Transmission electron microscopy of graphene". In: *MRS Bulletin* 37.12 (2012), pp. 1214–1221 (cit. on p. 61).

[91] Pinshane Y Huang et al. "Grains and grain boundaries in single-layer graphene atomic patchwork quilts". In: *Nature* 469.7330 (2011), pp. 389–392 (cit. on p. 61).

[92] Yuan Huang et al. "Universal mechanical exfoliation of large-area 2D crystals". In: *Nature Communications* 11.1 (2020), pp. 1–9 (cit. on p. 16).

[93] Woong Huh, Donghun Lee, and Chul-Ho Lee. "Memristors based on 2D materials as an artificial synapse for neuromorphic electronics". In: *Advanced Materials* 32.51 (2020), p. 2002092 (cit. on pp. 27, 28).

[94] Woong Huh et al. "2D Materials: synaptic barristor based on phase-engineered 2D heterostructures". In: *Advanced Materials* 30.35 (2018), p. 1870266 (cit. on p. 28).

[95] Woong Huh et al. "Synaptic barristor based on phase-engineered 2D heterostructures". In: *Advanced Materials* 30.35 (2018), p. 1801447 (cit. on p. 28).

[96] Jiali Huo et al. "Quasi-volatile MoS_2 barristor memory for 1T compact neuron by correlative charges trapping and Schottky barrier modulation". In: *ACS Applied Materials & Interfaces* 14.51 (2022), pp. 57440–57448 (cit. on pp. 16, 34).

[97] Saban M Hus et al. "Observation of single-defect memristor in an MoS_2 atomic sheet". In: *Nature Nanotechnology* 16.1 (2021), pp. 58–62 (cit. on pp. 18, 30).

[98] Edinburgh Instruments. *What is Raman Spectroscopy?* http://www.edinst.com/blog/what-is-raman-spectroscopy/ (cit. on p. 67).

[99] Oxford instruments. *Inductively coupled plasma etching (ICP RIE)*. https://plasma.oxinst.com/technology/icp-etching (cit. on p. 48).

[100] Kengo Ishimaru et al. "Characterization of sp^2-and sp^3-bonded carbon in wood charcoal". In: *Journal of Wood Science* 53 (2007), pp. 442–448 (cit. on p. 87).

[101] Vijaya Jadkar et al. "Synthesis of orthorhombic-molybdenum trioxide (α-MoO_3) thin films by hot wire-CVD and investigations of its humidity sensing properties". In: *Journal of Materials Science: Materials in Electronics* 28 (2017), pp. 15790–15796 (cit. on p. 86).

[102] Jakub Jadwiszczak et al. "MoS_2 memtransistors fabricated by localized helium ion beam irradiation". In: *ACS Nano* 13.12 (2019), pp. 14262–14273 (cit. on pp. 31, 32, 37).

[103] Deep Jariwala et al. "Emerging device applications for semiconducting two-dimensional transition metal dichalcogenides". In: *ACS Nano* 8.2 (2014), pp. 1102–1120 (cit. on p. 5).

[104] Debdeep Jena, Kaustav Banerjee, and Grace Huili Xing. "Intimate contacts". In: *Nature materials* 13.12 (2014), pp. 1076–1078 (cit. on p. 14).

[105] Jaeho Jeon et al. "Layer-controlled CVD growth of large-area two-dimensional MoS_2 films". In: *Nanoscale* 7.5 (2015), pp. 1688–1695 (cit. on p. 84).

[106] He Jiang et al. "Two-dimensional Czochralski growth of single-crystal MoS_2". In: *Nature Materials* (2025), pp. 1–9 (cit. on p. 19).

[107] Kristen Kaasbjerg, Kristian S Thygesen, and Karsten W Jacobsen. "Phonon-limited mobility in n-type single-layer MoS_2 from first principles". In: *Physical Review B* 85.11 (2012), p. 115317 (cit. on pp. 8, 85).

[108] Gerald Kada, Ferry Kienberger, and Peter Hinterdorfer. "Atomic force microscopy in bionanotechnology". In: *Nano Today* 3.1-2 (2008), pp. 12–19 (cit. on p. 55).

[109] Kibum Kang et al. "High-mobility three-atom-thick semiconducting films with wafer-scale homogeneity". In: *Nature* 520.7549 (2015), pp. 656–660 (cit. on p. 19).

[110] Reelika Kaupmees, Hannu-Pekka Komsa, and Jüri Krustok. "Photoluminescence study of B-trions in MoS_2 monolayers with high density of defects". In: *Physica Status Solidi (b)* 256.3 (2019), p. 1800384 (cit. on p. 71).

[111] HoKwon Kim et al. "Suppressing nucleation in metal-organic chemical vapor deposition of MoS_2 monolayers by alkali metal halides". In: *Nano Letters* 17.8 (2017), pp. 5056–5063 (cit. on pp. 19, 78).

[112] Hong-Sik Kim et al. "Vertical growth of MoS_2 layers by sputtering method for efficient photoelectric application". In: *Sensors and Actuators A: Physical* 269 (2018), pp. 355–362 (cit. on p. 18).

[113] Hyun Kim et al. "Role of alkali metal promoter in enhancing lateral growth of monolayer transition metal dichalcogenides". In: *Nanotechnology* 28.36 (2017), 36LT01 (cit. on pp. 17, 19, 78).

[114] Ki Kang Kim, Hyun Seok Lee, and Young Hee Lee. "Synthesis of hexagonal boron nitride heterostructures for 2D van der Waals electronics". In: *Chemical Society Reviews* 47.16 (2018), pp. 6342–6369 (cit. on p. 41).

[115] Ki Seok Kim et al. "Non-epitaxial single-crystal 2D material growth by geometric confinement". In: *Nature* 614.7946 (2023), pp. 88–94 (cit. on pp. 22, 23).

[116] Minjae Kim et al. "Filamentary and interface-type memristors based on tantalum oxide for energy-efficient neuromorphic hardware". In: *ACS Applied Materials & Interfaces* 14.39 (2022), pp. 44561–44571 (cit. on p. 149).

[117] Seongjae Kim et al. "Vertically integrated electronics: new opportunities from emerging materials and devices". In: *Nano-Micro Letters* 14.1 (2022), p. 201 (cit. on p. 28).

[118] Dongjin Ko et al. "Few-layered MoS_2 vertically aligned on 3D interconnected porous carbon nanosheets for hydrogen evolution". In: *Applied Catalysis B: Environmental* 248 (2019), pp. 357–365 (cit. on p. 66).

[119] Unni Krishnan et al. "A synoptic review of MoS_2: Synthesis to applications". In: *Superlattices and Microstructures* 128 (2019), pp. 274–297 (cit. on p. 5).

[120] Ashok Kumar and PK Ahluwalia. "A first principle comparative study of electronic and optical properties of 1H-MoS_2 and 2H-MoS_2". In: *Materials Chemistry and Physics* 135.2-3 (2012), pp. 755–761 (cit. on p. 70).

[121] Duygu Kuzum, Shimeng Yu, and HS Philip Wong. "Synaptic electronics: materials, devices and applications". In: *Nanotechnology* 24.38 (2013), p. 382001 (cit. on p. 27).

[122] Junyoung Kwon et al. "200-mm-wafer-scale integration of polycrystalline molybdenum disulfide transistors". In: *Nature Electronics* (2024), pp. 1–9 (cit. on p. 21).

[123] Ki Chang Kwon et al. "Memristive devices based on two-dimensional transition metal chalcogenides for neuromorphic computing". In: *Nano-Micro Letters* 14.1 (2022), p. 58 (cit. on pp. 28, 30, 34).

[124] Mario Lanza et al. "Recommended methods to study resistive switching devices". In: *Advanced Electronic Materials* 5.1 (2019), p. 1800143 (cit. on p. 26).

[125] Changgu Lee et al. "Anomalous lattice vibrations of single-and few-layer MoS_2". In: *ACS Nano* 4.5 (2010), pp. 2695–2700 (cit. on pp. 68, 69).

[126] Do Hee Lee et al. "Metal–organic chemical vapor deposition of 2D van der Waals materials—The challenges and the extensive future opportunities". In: *Apl Materials* 8.3 (2020) (cit. on p. 18).

[127] Eunho Lee et al. "Realizing electronic synapses by defect engineering in polycrystalline two-dimensional MoS_2 for neuromorphic computing". In: *ACS Applied Materials & Interfaces* 15.12 (2023), pp. 15839–15847 (cit. on pp. 27, 28).

[128] Yi-Hsien Lee et al. "Synthesis and transfer of single-layer transition metal disulfides on diverse surfaces". In: *Nano Letters* 13.4 (2013), pp. 1852–1857 (cit. on pp. 20, 78).

[129] Yi-Hsien Lee et al. "Synthesis of large-area MoS_2 atomic layers with chemical vapor deposition". In: *Advanced Materials* 24.17 (2012), pp. 2320–2325 (cit. on pp. 17, 20, 41, 78).

[130] Jong-Young Lee et al. "Evolution of defect formation during atomically precise desulfurization of monolayer MoS_2". In: *Communications Materials* 2.1 (2021), p. 80 (cit. on p. 113).

[131] Kangho Lee et al. “High-performance sensors based on molybdenum disulfide thin films”. In: *Advanced Materials (Deerfield Beach, Fla.)* 25.46 (2013), pp. 6699–6702 (cit. on p. 18).

[132] Bibo Li, Dapeng Yu, and Shu-Lin Zhang. “Raman spectral study of silicon nanowires”. In: *Physical Review B* 59.3 (1999), p. 1645 (cit. on p. 86).

[133] Da Li et al. “MoS_2 memristors exhibiting variable switching characteristics toward biorealistic synaptic emulation”. In: *ACS Nano* 12.9 (2018), pp. 9240–9252 (cit. on pp. 34, 36, 37).

[134] Dawei Li et al. “Large-area 2D/3D MoS_2-MoO_2 heterostructures with thermally stable exciton and intriguing electrical transport behaviors”. In: *Advanced Electronic Materials* 3.7 (2017), p. 1600335 (cit. on p. 86).

[135] Guanmeng Li et al. “Direct growth of continuous and uniform MoS_2 film on SiO_2/Si substrate catalyzed by sodium sulfate”. In: *The Journal of Physical Chemistry Letters* 11.4 (2020), pp. 1570–1577 (cit. on p. 20).

[136] Hai Li et al. “Preparation and applications of mechanically exfoliated single-layer and multilayer MoS_2 and WSe_2 nanosheets”. In: *Accounts of Chemical Research* 47.4 (2014), pp. 1067–1075 (cit. on p. 16).

[137] Hong Li et al. “From bulk to monolayer MoS_2: evolution of Raman scattering”. In: *Advanced Functional Materials* 22.7 (2012), pp. 1385–1390 (cit. on p. 84).

[138] Junzhu Li et al. “Wafer-scale single-crystal monolayer graphene grown on sapphire substrate”. In: *Nature Materials* 21.7 (2022), pp. 740–747 (cit. on p. 41).

[139] Shisheng Li et al. “Wafer-scale and deterministic patterned growth of monolayer MoS_2 via vapor-liquid-solid method”. In: *Nanoscale* 11.34 (2019), pp. 16122–16129 (cit. on p. 22).

[140] Shouheng Li et al. “Growth mechanism and atomic structure of group-IIA compound-promoted CVD-synthesized monolayer transition metal dichalcogenides”. In: *Nanoscale* 13.30 (2021), pp. 13030–13041 (cit. on pp. 20, 78).

[141] Taotao Li et al. “Epitaxial growth of wafer-scale molybdenum disulfide semiconductor single crystals on sapphire”. In: *Nature Nanotechnology* 16.11 (2021), pp. 1201–1207 (cit. on p. 19).

[142] Tianshu Li and Giulia Galli. “Electronic properties of MoS_2 nanoparticles”. In: *The Journal of Physical Chemistry C* 111.44 (2007), pp. 16192–16196 (cit. on p. 7).

[143] Weisheng Li et al. “Approaching the quantum limit in two-dimensional semiconductor contacts”. In: *Nature* 613.7943 (2023), pp. 274–279 (cit. on p. 15).

[144] Weiwei Li et al. “Large-scale ultra-robust MoS_2 patterns directly synthesized on polymer substrate for flexible sensing electronics”. In: *Advanced Materials* 35.8 (2023), p. 2207447 (cit. on p. 23).

[145] Yuan Li et al. “Site-specific positioning and patterning of MoS_2 monolayers: The role of Au seeding”. In: *ACS Nano* 12.9 (2018), pp. 8970–8976 (cit. on pp. 22, 23, 87).

[146] Yuhao Li et al. “Rapid identification of two-dimensional materials via machine learning assisted optic microscopy”. In: *Journal of Materiomics* 5.3 (2019), pp. 413–421 (cit. on p. 52).

[147] Zheling Li et al. “Raman spectroscopy of carbon materials and their composites: Graphene, nanotubes and fibres”. In: *Progress in Materials Science* 135 (2023), p. 101089 (cit. on p. 87).

[148] Tao Liang et al. “Intrinsically substitutional carbon doping in CVD-grown monolayer MoS_2 and the band structure modulation”. In: *ACS Applied Electronic Materials* 2.4 (2020), pp. 1055–1064 (cit. on p. 87).

[149] Ee Wah Lim and Razali Ismail. “Conduction mechanism of valence change resistive switching memory: a survey”. In: *Electronics* 4.3 (2015), pp. 586–613 (cit. on p. 28).

[150] Yuxuan Lin et al. “Dielectric screening of excitons and trions in single-layer MoS_2”. In: *Nano Letters* 14.10 (2014), pp. 5569–5576 (cit. on p. 70).

[151] Xi Ling et al. “Role of the seeding promoter in MoS_2 growth by chemical vapor deposition”. In: *Nano Letters* 14.2 (2014), pp. 464–472 (cit. on pp. 20, 41, 78).

[152] Eike Linn et al. “Complementary resistive switches for passive nanocrossbar memories”. In: *Nature Materials* 9.5 (2010), pp. 403–406 (cit. on p. 27).

[153] D Liu et al. “Sulfur vacancies in monolayer MoS_2 and its electrical contacts”. In: *Applied Physics Letters* 103.18 (2013), p. 183113 (cit. on p. 15).

[154] HF Liu, Swee Liang Wong, and DZ Chi. “CVD growth of MoS_2-based two-dimensional materials”. In: *Chemical Vapor Deposition* 21.10-11-12 (2015), pp. 241–259 (cit. on p. 42).

[155] Juqing Liu et al. “Preparation of MoS_2-polyvinylpyrrolidone nanocomposites for flexible nonvolatile rewritable memory devices with reduced graphene oxide electrodes”. In: *Small* 8.22 (2012), pp. 3517–3522 (cit. on pp. 17, 34).

[156] Keng-Ku Liu et al. “Growth of large-area and highly crystalline MoS_2 thin layers on insulating substrates”. In: *Nano Letters* 12.3 (2012), pp. 1538–1544 (cit. on pp. 22, 41).

[157] Yuan Liu et al. “Promises and prospects of two-dimensional transistors”. In: *Nature* 591.7848 (2021), pp. 43–53 (cit. on pp. 8, 84).

[158] Zheng Liu et al. “Strain and structure heterogeneity in MoS_2 atomic layers grown by chemical vapour deposition”. In: *Nature Communications* 5.1 (2014), pp. 1–9 (cit. on p. 71).

[159] Michal Macha et al. “Wafer-scale MoS_2 with water-vapor assisted showerhead MOCVD”. In: *Nanoscale Advances* 4.20 (2022), pp. 4391–4401 (cit. on p. 18).

[160] Masoud Mahjouri-Samani et al. “Patterned arrays of lateral heterojunctions within monolayer two-dimensional semiconductors”. In: *Nature Communications* 6.1 (2015), p. 7749 (cit. on p. 17).

[161] Kin Fai Mak et al. “Atomically thin MoS_2: a new direct-gap semiconductor”. In: *Physical Review Letters* 105.13 (2010), p. 136805 (cit. on pp. 7, 84).

[162] Kin Fai Mak et al. “Tightly bound trions in monolayer MoS_2”. In: *Nature Materials* 12.3 (2013), pp. 207–211 (cit. on p. 71).

[163] Kathleen M McCreary et al. “A-and B-exciton photoluminescence intensity ratio as a measure of sample quality for transition metal dichalcogenide monolayers”. In: *Apl Materials* 6.11 (2018) (cit. on p. 113).

[164] Stephen McDonnell et al. “Defect-dominated doping and contact resistance in MoS_2”. In: *ACS Nano* 8.3 (2014), pp. 2880–2888 (cit. on pp. 12, 15).

[165] Sandro Mignuzzi et al. “Effect of disorder on Raman scattering of single-layer MoS_2”. In: *Physical Review B* 91.19 (2015), p. 195411 (cit. on pp. 88, 95).

[166] Jill A Miwa et al. “Van der Waals epitaxy of two-dimensional MoS_2–graphene heterostructures in ultrahigh vacuum”. In: *ACS Nano* 9.6 (2015), pp. 6502–6510 (cit. on p. 17).

[167] Peter Moens et al. “Reliability assessment of integrated power transistors: lateral DMOS versus vertical DMOS”. In: *Microelectronics Reliability* 48.8-9 (2008), pp. 1300–1305 (cit. on p. 21).

[168] Sandeep Kumar Mondal et al. “Inkjet-printed, high-performance MoS_2 transistors and unipolar logic electronics”. In: *ACS Applied Materials & Interfaces* (2024) (cit. on p. 23).

[169] Shinichiro Mouri, Yuhei Miyauchi, and Kazunari Matsuda. “Tunable photoluminescence of monolayer MoS_2 via chemical doping”. In: *Nano Letters* 13.12 (2013), pp. 5944–5948 (cit. on p. 71).

[170] Sina Najmaei et al. “Vapour phase growth and grain boundary structure of molybdenum disulphide atomic layers”. In: *Nature Materials* 12.8 (2013), pp. 754–759 (cit. on p. 19).

[171] Haiyan Nan et al. “Strong photoluminescence enhancement of MoS_2 through defect engineering and oxygen bonding”. In: *ACS Nano* 8.6 (2014), pp. 5738–5745 (cit. on p. 95).

[172] Kostya S Novoselov et al. “Electric field effect in atomically thin carbon films”. In: *Science* 306.5696 (2004), pp. 666–669 (cit. on p. 1).

[173] Kostya S Novoselov et al. “Two-dimensional atomic crystals”. In: *Proceedings of the National Academy of Sciences* 102.30 (2005), pp. 10451–10453 (cit. on p. 16).

[174] Milton Ohring. *Materials science of thin films: depositon and structure*. Elsevier, 2001 (cit. on pp. 18, 39, 40, 101).

[175] Mitsuhiro Okada et al. “Direct chemical vapor deposition growth of WS_2 atomic layers on hexagonal boron nitride”. In: *ACS Nano* 8.8 (2014), pp. 8273–8277 (cit. on p. 41).

[176] Merve Öper et al. “Controlled CVD growth of ultrathin Mo_2C (MXene) flakes”. In: *Journal of Applied Physics* 131.2 (2022) (cit. on p. 41).

[177] Seoungwoong Park et al. “Layer-selective synthesis of MoS_2 and WS_2 structures under ambient conditions for customized electronics”. In: *ACS Nano* 14.7 (2020), pp. 8485–8494 (cit. on p. 22).

[178] Woanseo Park et al. “Photoelectron spectroscopic imaging and device applications of large-area patternable single-layer MoS_2 synthesized by chemical vapor deposition”. In: *ACS Nano* 8.5 (2014), pp. 4961–4968 (cit. on pp. 22, 96, 97).

[179] S Kumar Singh Patel et al. “Synthesis of α-MoO_3 nanofibers for enhanced field-emission properties”. In: *Adv. Mater. Lett.* 9.8 (2018), pp. 585–589 (cit. on p. 86).

[180] Keith R Paton et al. “Scalable production of large quantities of defect-free few-layer graphene by shear exfoliation in liquids”. In: *Nature Materials* 13.6 (2014), pp. 624–630 (cit. on p. 16).

[181] Carroll F Powell et al. “Vapor deposition”. In: *Journal of the electrochemical society* 113.10 (1966), p. 266C (cit. on p. 39).

[182] The Materials Project. *2H MoS_2*. https://next-gen.materialsproject.org/materials/mp-2815 (cit. on p. 6).

[183] Yancong Qiao et al. “Fabricating molybdenum disulfide memristors”. In: *ACS Applied Electronic Materials* 2.2 (2019), pp. 346–370 (cit. on p. 30).

[184] Hao Qiu et al. “Hopping transport through defect-induced localized states in molybdenum disulphide”. In: *Nature Communications* 4.1 (2013), p. 2642 (cit. on p. 9).

[185] Branimir Radisavljevic and Andras Kis. “Mobility engineering and a metal–insulator transition in monolayer MoS_2”. In: *Nature Materials* 12.9 (2013), pp. 815–820 (cit. on pp. 8, 10).

[186] Branimir Radisavljevic et al. “Single-layer MoS_2 transistors”. In: *Nature Nanotechnology* 6.3 (2011), pp. 147–150 (cit. on pp. 9, 85).

[187] Amritesh Rai et al. “Progress in contact, doping and mobility engineering of MoS_2: an atomically thin 2D semiconductor”. In: *Crystals* 8.8 (2018), p. 316 (cit. on pp. 8, 14).

[188] Chandrasekhara Venkata Raman and Kariamanikkam Srinivasa Krishnan. “A new type of secondary radiation”. In: *Nature* 121.3048 (1928), pp. 501–502 (cit. on p. 67).

[189] Ashwin Ramasubramaniam. “Large excitonic effects in monolayers of molybdenum and tungsten dichalcogenides”. In: *Physical Review B—Condensed Matter and Materials Physics* 86.11 (2012), p. 115409 (cit. on p. 70).

[190] Ranishaw. *Photoluminescence spectroscopy and fluorescence explained*. https://www.renishaw.com/fr/photoluminescence-spectroscopy-and-fluorescence-explained--25809 (cit. on p. 70).

[191] C Hanumanth Rao et al. “A review on printed electronics with digital 3D printing: fabrication techniques, materials, challenges and future opportunities”. In: *Journal of Electronic Materials* 51.6 (2022), pp. 2747–2765 (cit. on p. 23).

[192] Juan B Roldán et al. “Variability in resistive memories”. In: *Advanced Intelligent Systems* 5.6 (2023), p. 2200338 (cit. on p. 29).

[193] Shrawan Roy et al. “Atomic observation of filling vacancies in monolayer transition metal sulfides by chemically sourced sulfur atoms”. In: *Nano Letters* 18.7 (2018), pp. 4523–4530 (cit. on p. 9).

[194] Puranjay Saha et al. “Solution-processed robust multifunctional memristor of 2D layered material thin film”. In: *ACS Nano* 18.1 (2023), pp. 1137–1148 (cit. on pp. 17, 34).

[195] Stephanie R Sails et al. “Monitoring the quality of diamond films using Raman spectra excited at 514.5 nm and 633 nm”. In: *Diamond and Related Materials* 5.6-8 (1996), pp. 589–591 (cit. on p. 87).

[196] Vinod K Sangwan et al. “Gate-tunable memristive phenomena mediated by grain boundaries in single-layer MoS_2”. In: *Nature Nanotechnology* 10.5 (2015), pp. 403–406 (cit. on pp. 18, 28, 31, 37).

[197] Vinod K Sangwan et al. “Multi-terminal memtransistors from polycrystalline monolayer molybdenum disulfide”. In: *Nature* 554.7693 (2018), pp. 500–504 (cit. on pp. 13, 15, 18, 28, 35–37).

[198] S Sathiyan et al. “Evolution of the polarizing effect of MoS_2”. In: *IEEE Photonics Journal* 7.6 (2015), pp. 1–10 (cit. on p. 72).

[199] David O Scanlon et al. “Theoretical and experimental study of the electronic structures of MoO_3 and MoO_2”. In: *The Journal of Physical Chemistry C* 114.10 (2010), pp. 4636–4645 (cit. on p. 96).

[200] Thomas F Schranghamer, Aaryan Oberoi, and Saptarshi Das. “Graphene memristive synapses for high precision neuromorphic computing”. In: *Nature Communications* 11.1 (2020), p. 5474 (cit. on p. 28).

[201] Dieter K Schroder. *Semiconductor material and device characterization*. John Wiley & Sons, 2015 (cit. on p. 11).

[202] Philippe Sciau and Marie Godet. “Spectroscopy and diffraction using the electron microscope”. In: *Spectroscopy, Diffraction and Tomography in Art and Heritage Science*. Elsevier, 2021, pp. 71–102 (cit. on p. 65).

[203] Ana Senkić et al. “Effects of CVD growth parameters on global and local optical properties of MoS_2 monolayers”. In: *Materials Chemistry and Physics* 296 (2023), p. 127185 (cit. on p. 42).

[204] Luca Seravalli and Matteo Bosi. “A review on chemical vapour deposition of two-dimensional MoS_2 flakes”. In: *Materials* 14.24 (2021), p. 7590 (cit. on p. 42).

[205] Martha I Serna et al. "Large-area deposition of MoS_2 by pulsed laser deposition with in situ thickness control". In: *Acs Nano* 10.6 (2016), pp. 6054–6061 (cit. on p. 17).

[206] Akhil Sharma et al. "Large area, patterned growth of 2D MoS_2 and lateral MoS_2-WS_2 heterostructures for nano-and opto-electronic applications". In: *Nanotechnology* 31.25 (2020), p. 255603 (cit. on pp. 21, 22, 103).

[207] Tao Shen et al. "High mobility monolayer MoS_2 transistors and its charge transport behaviour under E-beam irradiation". In: *Journal of Materials Science* 55 (2020), pp. 14315–14325 (cit. on p. 19).

[208] Yaqing Shen et al. "Variability and yield in h-BN-based memristive circuits: the role of each type of defect". In: *Advanced Materials* 33.41 (2021), p. 2103656 (cit. on p. 29).

[209] Bong Gyu Shin et al. "Indirect bandgap puddles in monolayer MoS_2 by substrate-induced local strain". In: *Advanced Materials* 28.42 (2016), pp. 9378–9384 (cit. on p. 71).

[210] Alankar Shrivastava, Vipin B Gupta, et al. "Methods for the determination of limit of detection and limit of quantitation of the analytical methods". In: *Chron. Young Sci* 2.1 (2011), pp. 21–25 (cit. on p. 68).

[211] Aditya Singh et al. "NaCl-assisted substrate dependent 2D planar nucleated growth of MoS_2". In: *Applied Surface Science* 538 (2021), p. 148201 (cit. on pp. 19, 78).

[212] Ewen Smith and Geoffrey Dent. *Modern Raman spectroscopy: a practical approach*. John Wiley & Sons, 2019 (cit. on p. 67).

[213] Giulio Solferino and Alan J Anderson. "Thermal reduction of molybdite and hematite in water and hydrogen peroxide-bearing solutions: Insights on redox conditions in hydrothermal diamond anvil cell (HDAC) experiments". In: *Chemical Geology* 322 (2012), pp. 215–222 (cit. on p. 86).

[214] Intek Song et al. "Patternable large-scale molybdenium disulfide atomic layers grown by gold-assisted chemical vapor deposition". In: *Angewandte Chemie* 126.5 (2014), pp. 1290–1293 (cit. on p. 22).

[215] Viacheslav Sorkin et al. "The effects of point defect type, location, and density on the Schottky barrier height of Au/MoS_2 heterojunction: a first-principles study". In: *Scientific Reports* 12.1 (2022), p. 18001 (cit. on p. 12).

[216] Andrea Splendiani et al. "Emerging photoluminescence in monolayer MoS_2". In: *Nano Letters* 10.4 (2010), pp. 1271–1275 (cit. on pp. 7, 8, 71).

[217] Dmitri B Strukov et al. "The missing memristor found". In: *Nature* 453.7191 (2008), pp. 80–83 (cit. on pp. 24, 34).

[218] Jie Su et al. "Defect induced gap states in monolayer MoS_2 control the Schottky barriers of Pt-mMoS_2 interfaces". In: *Applied Physics Letters* 110.16 (2017) (cit. on p. 34).

[219] Dezheng Sun et al. "Chemical vapor deposition growth of a periodic array of single-layer MoS_2 islands via lithographic patterning of an SiO_2/Si substrate". In: *2D Materials* 2.4 (2015), p. 045014 (cit. on p. 22).

[220] Simon M Sze, Yiming Li, and Kwok K Ng. *Physics of semiconductor devices*. John Wiley & Sons, 2021 (cit. on pp. 8, 140).

[221] Baoshan Tang et al. "Wafer-scale solution-processed 2D material analog resistive memory array for memory-based computing". In: *Nature Communications* 13.1 (2022), p. 3037 (cit. on p. 17).

[222] Kai Tang et al. "Electronic and photoelectronic memristors based on 2D materials". In: *Advanced Electronic Materials* 8.4 (2022), p. 2101099 (cit. on p. 31).

[223] Alexey Tarasov et al. "Highly uniform trilayer molybdenum disulfide for wafer-scale device fabrication". In: *Advanced Functional Materials* 24.40 (2014), pp. 6389–6400 (cit. on p. 18).

[224] Ruiyuan Tian et al. "Liquid exfoliated SnP_3 nanosheets for very high areal capacity lithium-ion batteries". In: *Advanced Energy Materials* 11.4 (2021), p. 2002364 (cit. on p. 16).

[225] Rupika Tomar et al. "Probing sulfur vacancies in CVD-grown monolayer MoS_2 on SiO_2/Si in the temperature range 750-900 °C". In: *Journal of Electronic Materials* 52.8 (2023), pp. 5513–5520 (cit. on pp. 96, 97).

[226] Manoj Tripathi et al. "Structural defects modulate electronic and nanomechanical properties of 2D materials". In: *ACS Nano* 15.2 (2021), pp. 2520–2531 (cit. on p. 112).

[227] F Tuinstra and Jack L Koenig. "Raman spectrum of graphite". In: *The Journal of Chemical Physics* 53.3 (1970), pp. 1126–1130 (cit. on p. 87).

[228] Illinois State University. *Field emission scanning electron microscope*. https://about.illinoisstate.edu/fesem/capability/ (cit. on p. 58).

[229] Arend M Van Der Zande et al. "Grains and grain boundaries in highly crystalline monolayer molybdenum disulphide". In: *Nature Materials* 12.6 (2013), pp. 554–561 (cit. on pp. 61, 62).

[230] Vincent Vandalon et al. “Atomic layer deposition of Al-doped MoS_2: synthesizing a p-type 2D semiconductor with tunable carrier density”. In: *ACS Applied Nano Materials* 3.10 (2020), pp. 10200–10208 (cit. on p. 18).

[231] J. L. Verble and T. J. Wieting. “Lattice mode degeneracy in MoS_2 and other layer compounds”. In: *Physical Rreview Letters* 25.6-10 (1970), p. 362 (cit. on p. 68).

[232] N Wada, PJ Gaczi, and SA Solin. ““Diamond-like” 3-fold coordinated amorphous carbon”. In: *Journal of Non-Crystalline Solids* 35 (1980), pp. 543–548 (cit. on p. 87).

[233] N Wada and SA Solin. “Raman efficiency measurements of graphite”. In: *Physica B+ C* 105.1-3 (1981), pp. 353–356 (cit. on p. 87).

[234] Carlos D Wagner et al. “Empirical atomic sensitivity factors for quantitative analysis by electron spectroscopy for chemical analysis”. In: *Surface and interface analysis* 3.5 (1981), pp. 211–225 (cit. on p. 85).

[235] Miao Wang et al. “Robust memristors based on layered two-dimensional materials”. In: *Nature Electronics* 1.2 (2018), pp. 130–136 (cit. on pp. 16, 33).

[236] Qing Hua Wang et al. “Electronics and optoelectronics of two-dimensional transition metal dichalcogenides”. In: *Nature Nanotechnology* 7.11 (2012), pp. 699–712 (cit. on pp. 1, 7–9).

[237] Qinqin Wang et al. “Wafer-scale highly oriented monolayer MoS_2 with large domain sizes”. In: *Nano Letters* 20.10 (2020), pp. 7193–7199 (cit. on pp. 19, 21).

[238] Xianli Wang et al. “Low resolution Raman: The impact of spectral resolution on limit of detection and imaging speed in hyperspectral imaging”. In: *Analyst* 145.20 (2020), pp. 6607–6616 (cit. on p. 68).

[239] Xiaotian Wang et al. “Location-specific growth and transfer of arrayed MoS_2 monolayers with controllable size”. In: *2D Materials* 4.2 (2017), p. 025093 (cit. on p. 22).

[240] Xinsheng Wang et al. “Controlled synthesis of highly crystalline MoS_2 flakes by chemical vapor deposition”. In: *Journal of the American Chemical Society* 135.14 (2013), pp. 5304–5307 (cit. on p. 22).

[241] Yudan Wang et al. “High on/off ratio black phosphorus based memristor with ultra-thin phosphorus oxide layer”. In: *Applied Physics Letters* 115.19 (2019) (cit. on p. 28).

[242] Zhendong Wang et al. "Metal induced growth of transition metal dichalcogenides at controlled locations". In: *Scientific Reports* 6.1 (2016), p. 38394 (cit. on p. 22).

[243] Nasrullah Wazir et al. "Comparative studies on two-dimensional (2D) rectangular and hexagonal molybdenum dioxide nanosheets with different thickness". In: *Nanoscale Research Letters* 15 (2020), pp. 1–9 (cit. on pp. 111, 112).

[244] Surface Science Western. *X-ray Photoelectron Spectroscopy (XPS) Reference Pages*. https://www.xpsfitting.com/2009/10/molybdenum.html (cit. on p. 99).

[245] *What is transmission electron microscopy?* URL: https://www.nanoscience.com/techniques/transmission-electron-microscopy/ (visited on 2024) (cit. on p. 60).

[246] Wiki. *Electron interaction with matter*. https://commons.wikimedia.org/wiki/File:Electron_Interaction_with_Matter.svg (cit. on p. 58).

[247] Wikipedia. *Ammonium tetrathiomolybdate*. https://en.wikipedia.org/wiki/Ammonium_tetrathiomolybdate (cit. on p. 21).

[248] Wikipedia. *Synapse*. https://en.wikipedia.org/wiki/Synapse (cit. on p. 27).

[249] John M Woods et al. "One-step synthesis of MoS_2/WS_2 layered heterostructures and catalytic activity of defective transition metal dichalcogenide films". In: *ACS Nano* 10.2 (2016), pp. 2004–2009 (cit. on pp. 18, 22, 23).

[250] Di Wu et al. "Effect of substrate symmetry on the dendrite morphology of MoS_2 film synthesized by CVD". In: *Scientific Reports* 7.1 (2017), p. 15166 (cit. on p. 19).

[251] Qinke Wu et al. "Space-confined one-step growth of 2D MoO_2/MoS_2 vertical heterostructures for superior hydrogen evolution in alkaline electrolytes". In: *Small* 18.32 (2022), p. 2201051 (cit. on p. 42).

[252] Yin Xia et al. "12-inch growth of uniform MoS_2 monolayer for integrated circuit manufacture". In: *Nature Materials* 22.11 (2023), pp. 1324–1331 (cit. on pp. 19, 21).

[253] Han Xiao, Kashif Rasul, and Roland Vollgraf. "Fashion-mnist: a novel image dataset for benchmarking machine learning algorithms". In: *ArXiv preprint arXiv:1708.07747* (2017) (cit. on p. 148).

[254] Miao Xie et al. "Homogeneous Intercalation Chemistry and Ultralow Strain of 1T"' MoS_2 for Stable Potassium Storage". In: *Advanced Functional Materials* 33.49 (2023), p. 2306550 (cit. on p. 17).

[255] *XPS and UPS Background*. https://grimmgroup.net/research/xps/background/ (cit. on p. 66).

[256] Wenshuo Xu et al. "Ultrathin transition metal oxychalcogenide catalysts for oxygen evolution in acidic media". In: *Nature Synthesis* (2025), pp. 1–9 (cit. on p. 146).

[257] Guodong Xue et al. "Modularized batch production of 12-inch transition metal dichalcogenides by local element supply". In: *Science Bulletin* 68.14 (2023), pp. 1514–1521 (cit. on p. 19).

[258] Xiaobing Yan et al. "Robust $Ag/ZrO_2/WS_2/Pt$ memristor for neuromorphic computing". In: *ACS Applied Materials & Interfaces* 11.51 (2019), pp. 48029–48038 (cit. on p. 28).

[259] Xiaobing Yan et al. "Vacancy-induced synaptic behavior in 2D WS_2 nanosheet–based memristor for low-power neuromorphic computing". In: *Small* 15.24 (2019), p. 1901423 (cit. on p. 28).

[260] Heeseung Yang et al. "Highly scalable synthesis of MoS_2 thin films with precise thickness control via polymer-assisted deposition". In: *Chemistry of Materials* 29.14 (2017), pp. 5772–5776 (cit. on pp. 20, 78).

[261] Jihoon Yang et al. "Wafer-scale memristor array based on aligned grain boundaries of 2D molybdenum ditelluride for application to artificial synapses". In: *Advanced Functional Materials* 34.15 (2024), p. 2309455 (cit. on p. 149).

[262] Jing Yang et al. "Tuning the conductivity type in monolayer WS_2 and MoS_2 by sulfur vacancies". In: *Physica Status Solidi (RRL)-Rapid Research Letters* 14.9 (2020), p. 2000248 (cit. on p. 13).

[263] Lingming Yang et al. "Chloride molecular doping technique on 2D materials: WS_2 and MoS_2". In: *Nano Letters* 14.11 (2014), pp. 6275–6280 (cit. on p. 15).

[264] Xiu-Tian Yan Yongdong Xu. *Chemical vapour deposition: an integrated engineering design for advanced materials*. Springer, 2010 (cit. on pp. 40–42).

[265] Justin R Young et al. "Uniform large-area growth of nanotemplated high-quality monolayer MoS_2". In: *Applied Physics Letters* 110.26 (2017) (cit. on pp. 18, 22).

[266] Hua Yu et al. "Eight In. wafer-Scale epitaxial monolayer MoS_2". In: *Advanced Materials* 36.30 (2024), p. 2402855 (cit. on p. 19).

[267] Hua Yu et al. "Wafer-scale growth and transfer of highly-oriented monolayer MoS_2 continuous films". In: *ACS Nano* 11.12 (2017), pp. 12001–12007 (cit. on pp. 19, 61).

[268] Shimeng Yu. "Neuro-inspired computing with emerging nonvolatile memorys". In: *Proceedings of the IEEE* 106.2 (2018), pp. 260–285 (cit. on p. 27).

[269] Yifei Yu et al. "Controlled scalable synthesis of uniform, high-quality monolayer and few-layer MoS_2 films". In: *Scientific Reports* 3.1 (2013), p. 1866 (cit. on p. 84).

[270] Zhihao Yu et al. "Towards intrinsic charge transport in monolayer molybdenum disulfide by defect and interface engineering". In: *Nature Communications* 5.1 (2014), p. 5290 (cit. on pp. 8, 9).

[271] Yongjie Zhan et al. "Large area vapor phase growth and characterization of MoS_2 atomic layers on SiO_2 substrate". In: *ArXiv preprint arXiv:1111.5072* (2011) (cit. on p. 18).

[272] Yongjie Zhan et al. "Large-area vapor-phase growth and characterization of MoS_2 atomic layers on a SiO_2 substrate". In: *Small* 8.7 (2012), pp. 966–971 (cit. on p. 41).

[273] Chendong Zhang et al. "Direct imaging of band profile in single layer MoS_2 on graphite: quasiparticle energy gap, metallic edge states, and edge band bending". In: *Nano Letters* 14.5 (2014), pp. 2443–2447 (cit. on p. 95).

[274] Enze Zhang et al. "Tunable charge-trap memory based on few-layer MoS_2". In: *ACS Nano* 9.1 (2015), pp. 612–619 (cit. on p. 31).

[275] Hongzhou Zhang. *Python code for statistical analysis*. https://github.com/Lulin-66/MS-Data-analysis. 2024 (cit. on p. 80).

[276] Jing Zhang et al. "Scalable growth of high-quality polycrystalline MoS_2 monolayers on SiO_2 with tunable grain sizes". In: *ACS Nano* 8.6 (2014), pp. 6024–6030 (cit. on p. 19).

[277] John XJ Zhang and Kazunori Hoshino. "Fundamentals of nano/microfabrication and scale effect". In: *Molecular Sensors and Nanodevices* (2019), pp. 43–111 (cit. on p. 50).

[278] Kehao Zhang et al. "Considerations for utilizing sodium chloride in epitaxial molybdenum disulfide". In: *ACS Applied Materials & Interfaces* 10.47 (2018), pp. 40831–40837 (cit. on pp. 20, 78).

[279] Lei Zhang et al. “Memristive devices based on emerging two-dimensional materials beyond graphene”. In: *Nanoscale* 11.26 (2019), pp. 12413–12435 (cit. on pp. 28, 31).

[280] Peng Zhang et al. “Structural phase transition effect on resistive switching behavior of MoS_2-polyvinylpyrrolidone nanocomposites films for flexible memory devices”. In: *Small* 12.15 (2016), pp. 2077–2084 (cit. on pp. 18, 30, 37).

[281] Yu Zhang et al. “Controlled growth of high-quality monolayer WS_2 layers on sapphire and imaging its grain boundary”. In: *ACS Nano* 7.10 (2013), pp. 8963–8971 (cit. on p. 42).

[282] Baolin Zhao et al. “2D van der Waals heterojunction of organic and inorganic monolayers for high responsivity phototransistors”. In: *Advanced Functional Materials* 31.42 (2021), p. 2105444 (cit. on p. 19).

[283] Qianjun Zhi et al. “Dithiine-linked metalphthalocyanine framework with undulated layers for highly efficient and stable H_2O_2 electroproduction”. In: *Nature Communications* 15.1 (2024), p. 678 (cit. on p. 87).

[284] Hangbo Zhou et al. “Design-dependent wwitching mechanisms of Schottky-barrier-modulated memristors based on 2D semiconductor”. In: *Advanced Electronic Materials* 9.6 (2023), p. 2201252 (cit. on p. 34).

[285] Wu Zhou et al. “Intrinsic structural defects in monolayer molybdenum disulfide”. In: *Nano Letters* 13.6 (2013), pp. 2615–2622 (cit. on pp. 9, 19).

[286] Yangbo Zhou et al. “Quantitative secondary electron imaging for work function extraction at atomic level and layer identification of graphene”. In: *Scientific Reports* 6.1 (2016), p. 21045 (cit. on p. 59).

[287] Wenjuan Zhu et al. “Electronic transport and device prospects of monolayer molybdenum disulphide grown by chemical vapour deposition”. In: *Nature Communications* 5.1 (2014), p. 3087 (cit. on p. 9).

[288] Xiaojian Zhu et al. “Ionic modulation and ionic coupling effects in MoS_2 devices for neuromorphic computing”. In: *Nature Materials* 18.2 (2019), pp. 141–148 (cit. on p. 28).

[289] Yiru Zhu et al. “Room-temperature photoluminescence mediated by sulfur vacancies in 2D molybdenum disulfide”. In: *ACS Nano* 17.14 (2023), pp. 13545–13553 (cit. on pp. 85, 95–97).

[290] Jian Zi et al. “Raman shifts in Si nanocrystals”. In: *Applied Physics Letters* 69.2 (1996), pp. 200–202 (cit. on p. 86).

[291] Xiaolong Zou, Yuanyue Liu, and Boris I Yakobson. “Predicting dislocations and grain boundaries in two-dimensional metal-disulfides from the first principles”. In: *Nano Letters* 13.1 (2013), pp. 253–258 (cit. on p. 19).

Appendices

A.1. Optical contrast analyze of MoS_2

To analyse the layer of MoS_2, the optical images of MoS_2 were opened by the Image J software (version 1.53c, National Institutes of Health, USA) and then split channels by using the command from "Image→Color→Split Channels" in the menu. As the R channel has a stronger contrast than the G and B channels, we extract the grayscale image from the R channel. In the grayscale image, we dragged the left button of the mouse to draw a line across the atomically thin MoS_2 sheet and then pressed "Ctrl+K" to obtain the line profile of intensity difference. In the plot of the line profile, we clicked "List" to show the intensity values of the MoS_2 sheet and SiO_2 substrate.

A.2. Grain boundary visibility

Scanning Electron Microscopy (SEM) images are utilized for the grain structure analysis. The SEM image quality highly relies on the operating conditions, for example, the correct detector, accelerating voltage and aperture. Therefore, to analyze the grain structure of as-grown MoS_2 and maximise the visibility of the grain boundary, we first optimise the detector and accelerating voltage at a fixed aperture (30 μm).

Figure A.1 shows the SEM images of MoS_2 thin film taken under InLens mode and secondary electron (SE)2 mode, respectively, under the accelerating voltage of 3 kV with a working distance of 4.8 mm. For the InLens mode SEM image (**Fig. A.1** (a)), monolayer MoS_2 appears brighter. This is because the thinner film has a higher escape probability of SE1 to escape from the surface and reach the detector. The thin film also results in less electron scattering, enhancing the signal and therefore brightness. In contrast, the bilayer MoS_2 appears darker because the increased thickness leads to more electron scattering and absorption of electrons within the sample. This reduces the number of detectable SE1, thus decreasing the brightness. In addition, the grain boundaries are easily distinguishable by their brighter contrast. This high generation of SE1 is due to its special electron structure. These surface and near-surface features are readily detected by the InLens detector.

In contrast, in the SE2 image shown in **Fig. A.1** (b), monolayer MoS_2 appears darker because the thinner film has a lower density of SE2 generated from a deeper region of the sample. (detailed discussion see chapter 3, section 3.3.1) Under this mode, bilayer MoS_2 appears brighter because the increased thickness generates more SE2 from deeper layers, contributing to a relatively higher signal in the SE2 detector. Moreover, the contrast between the grain boundary and the MoS_2 film diminishes, making the grain boundary less distinct or even invisible in SE2 mode.

As discussed, InLens mode provides better visibility of thin film grain structure. Therefore, we will use it for the following analysis. To further enhance the MoS_2 grain boundary visibility, we will examine the SEM images of MoS_2 at varying accelerating voltages. (**Fig. A.2**(a-f)) shows SEM images taken under accelerating voltages of 2, 3, 5, 7, 10, and 15 kV, respectively. Distinct variations in contrast and grain boundary visibility can be observed. At lower accelerating voltages (2-5 kV), the electron interaction is confined to the near-surface region, enhancing the sensitivity to surface features. When the accelerating voltage is in the range of 3 kV to 5 kV, grain boundaries exhibit high contrast and clear

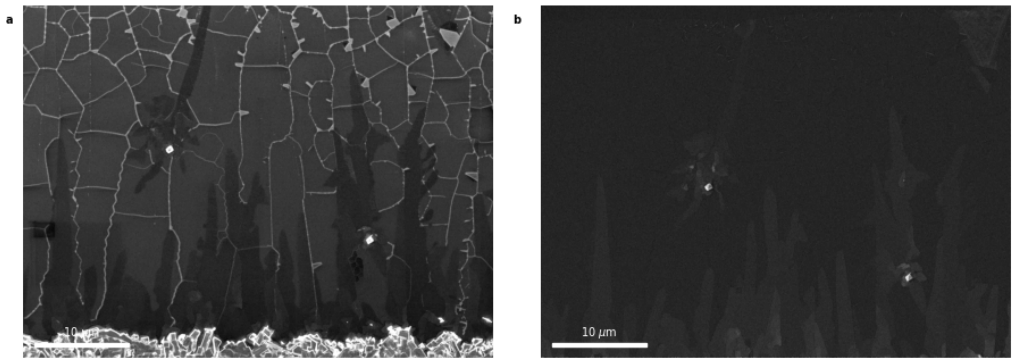


Figure A.1: MoS_2 grain boundary visibility in SEM images at varying modes: (a) InLens mode and (b) SE2 mode.

visibility due to the pronounced differences in SE emission compared to single crystal regions. As the accelerating voltage increases to 7 kV or higher, the interaction volume expands into the sample, and this reduces the SE1 signal intensity. When the voltage reaches 15 kV or higher, the interaction volume increases further, causing more electron scattering and a greater contribution from subsurface regions. This results in decreased contrast of grain boundaries as the differences in SE emission are averaged out over a larger volume.

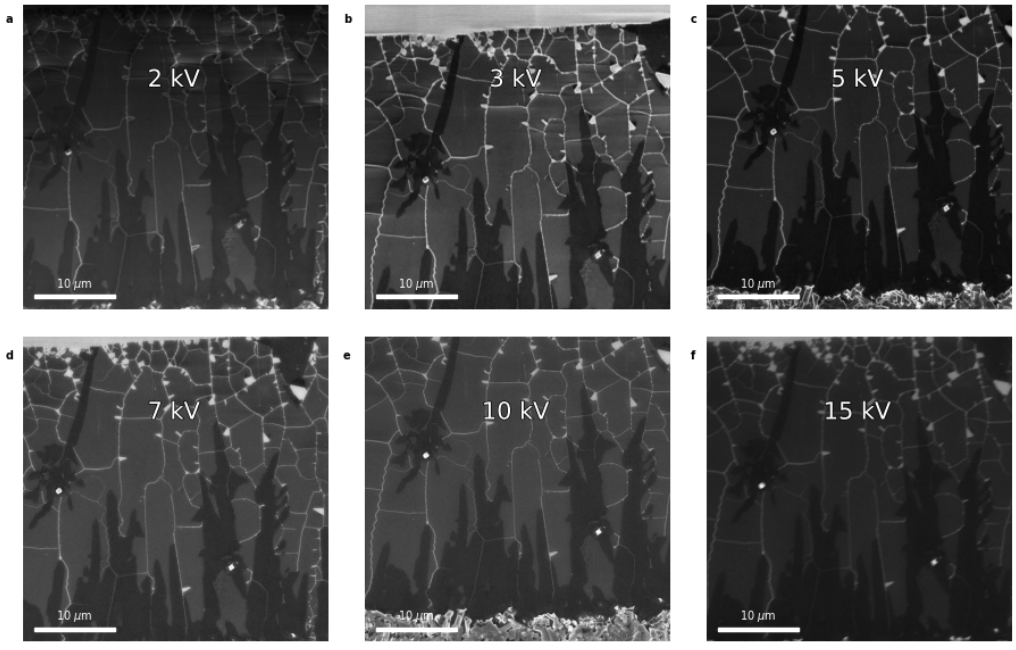


Figure A.2: MoS_2 grain boundary visibility in SEM images. Images are taken under InLens mode with accelerating voltages of (a-f) 2 kV, 3 kV, 5 kV, 7 kV, 10 kV and 15 kV, respectively.

A.3. Survey spectra of X-ray photoelectron spectroscopy (XPS)

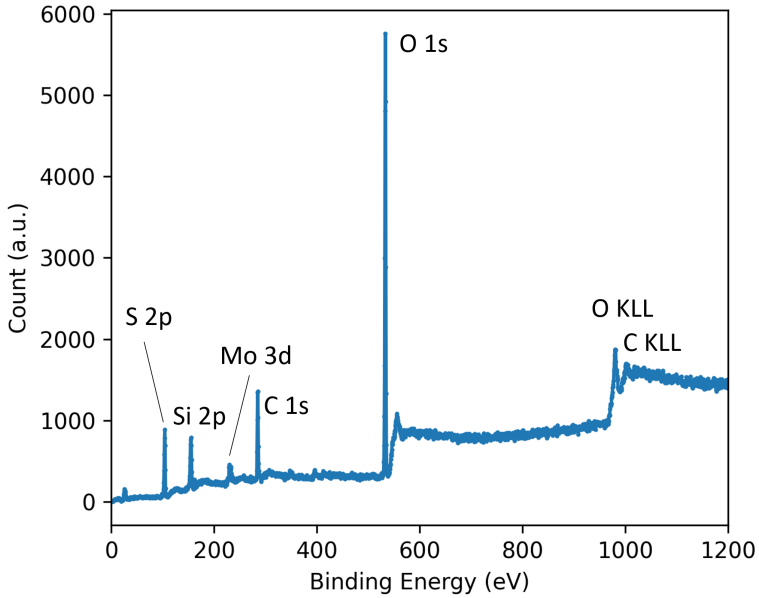


Figure A.3: XPS survey spectra of MoS_2 grown at suphur temperature of 250 °C.

A.4. Thermal stability of photoresist S1813

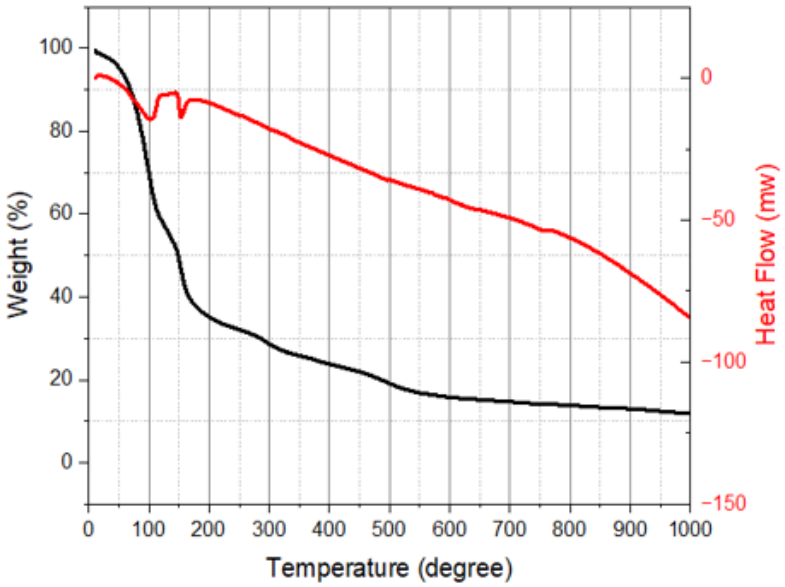


Figure A.4: Thermal stability of photoresist S1813.

A.5. XRD main peaks of Mo_xS_y and Mo_xO_y

Phase	2-Theta	d (Å)	hkl	Intensity
2H MoS_2	14.378	6.16	002	100
	39.538	2.28	103	58
	49.787	1.83	105	29
	32.676	2.73	100	22
Mo_3S_4 (PDF 00-027-0319)	13.696	6.49	101	100
	46.737	1.942	223	95
	34.008	2.634	122	90
	41.704	2.164	131	60
$Mo_{15}S_{19}$ (mp-31257)	11.921	7.424	10-10	100
	14.358	6.169	10-12	40
	45.629	1.988	4-2-25	33
	32.586	2.748	3-1-23	17
Mo_2S_3 (mp-1627)	16.041	5.525	10-1	100
	42.735	2.116	11-3	67
	40.109	2.248	112	46
	35.056	2.560	012	32

Table A.1: X-ray diffraction (XRD) main peaks of Mo_xS_y.

Phase	2-Theta	hkl	Intensity
MoO_2	26.033	-111	100
	37.025	-211	70
	37.392	-202	35
	36.774/36.852	200/111	30
MoO_3	27.334	021	100
	23.328	110	82
	25.704	040	61
	33.731	111	35
Mo_4O_{11}	22.206	211	100
	23.707	311	95
	25.576	601	85
$Mo_{17}O_{47}$	33.497	441	100
	22.502	001	80
	24.523	440	80
Mo_9O_{25}	22.720	911	100
	24.611	001	50
	25.938	1111	25
Mo_5O_{14}	22.566	001	100
	24.771	540	60
	31.337	810	30
Mo_8O_{23}	21.928	400	100
	26.033	012	90
	25.651	-403	70
Mo_9O_{26}	25.879	-204	100
	22.038	010	90
	22.783	401	70
Mo_2O_7 (mp-1180296)	27.44	11-1	100
	12.174	100	75
	18.354	002	75
MoO_4	15.203	011	100
	26.635	101	30
	26.154	110	28

Table A.2: XRD main peaks of Mo_xO_y.

A.6. Overview of patterned growth samples

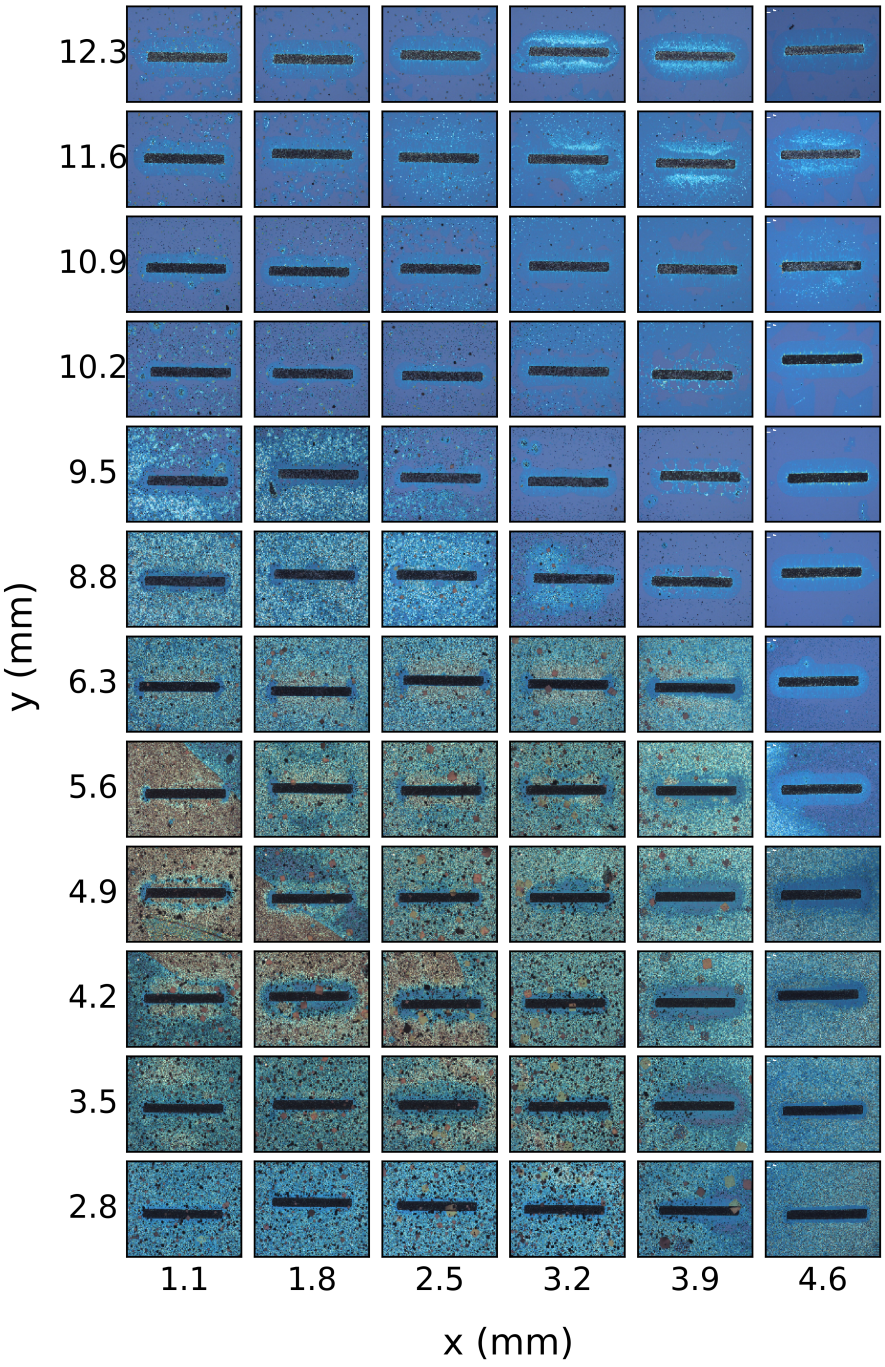


Figure A.5: MoS_2 patterned growth after chemical vapour deposition (CVD) under a sulphur-deficient condition at z = 10 mm.

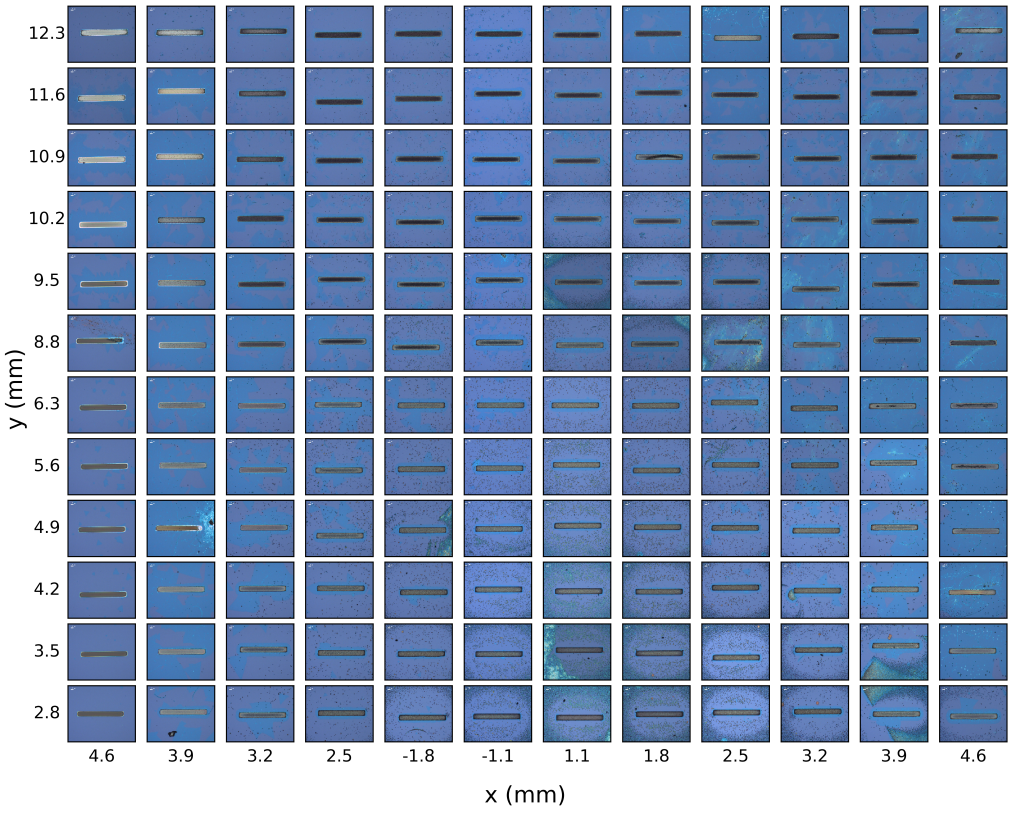


Figure A.6: MoS_2 patterned growth after CVD under a sulphur-moderate condition at z = 12 mm.

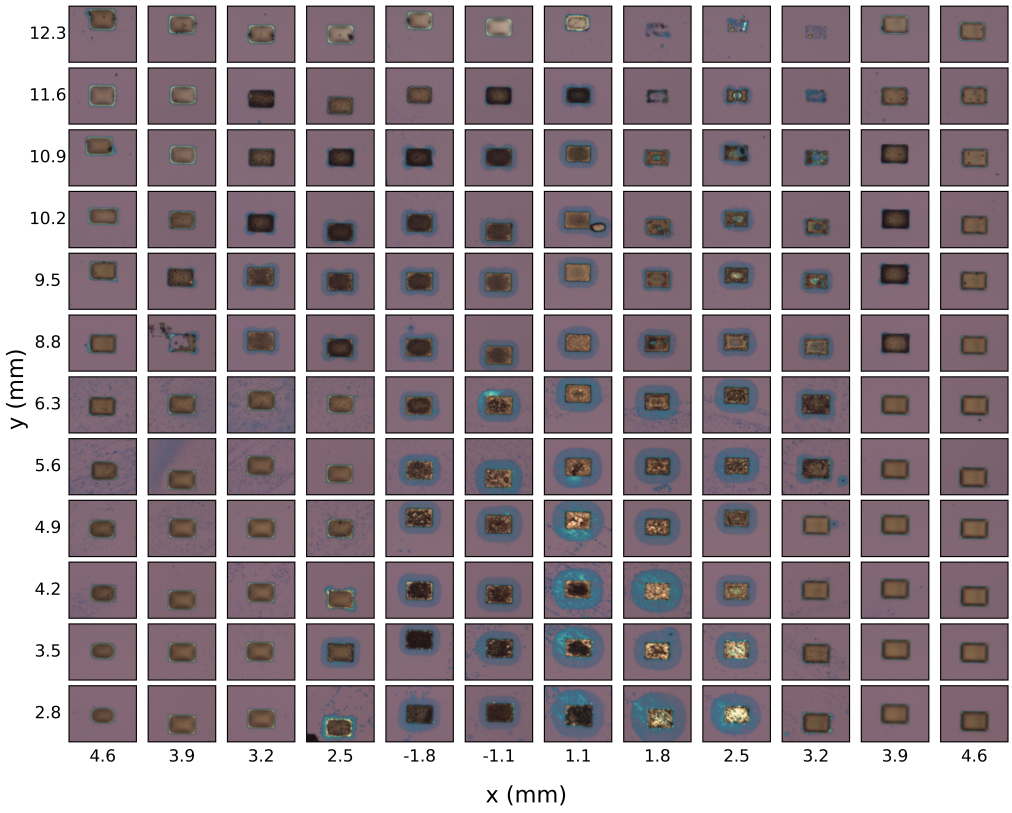


Figure A.7: MoS_2 patterned growth after CVD under a sulphur-rich condition at z = 15 mm.

A.7. Diffusion process of sulphur and molybdenum

The 1D diffusion equation is given by Fick's second law:

$$\frac{\partial u}{\partial t} = D\frac{\partial^2 u}{\partial x^2} \tag{1}$$

where $u(x,t)$ is the concentration at position x and time t, D is the diffusion coefficient (units: m^2/s).

In our approximate calculation, the S is treated as a delta function source at the centre of the mesa at t=0, which gives the classic analytical solution:

$$u(x,t) = \frac{u_0}{\sqrt{4\pi Dt}}\, e^{-\frac{x^2}{4Dt}} \tag{2}$$

where u_0 is the initial concentration.

Mo sources is treated as a continuous fixed source at sufficiently large distance from the mesa, which gives the solution of error function.

$$u(x,t) = u_0 \,\mathrm{erfc}\left(\frac{x}{4\sqrt{Dt}}\right) \tag{3}$$

We further simplify the diffusion coefficients of S and Mo are approximately equal to 1. The t spans in the range of [0, 20] and x in the range of [0, 6.3].

A.8. Transfer length method (TLM) measurement

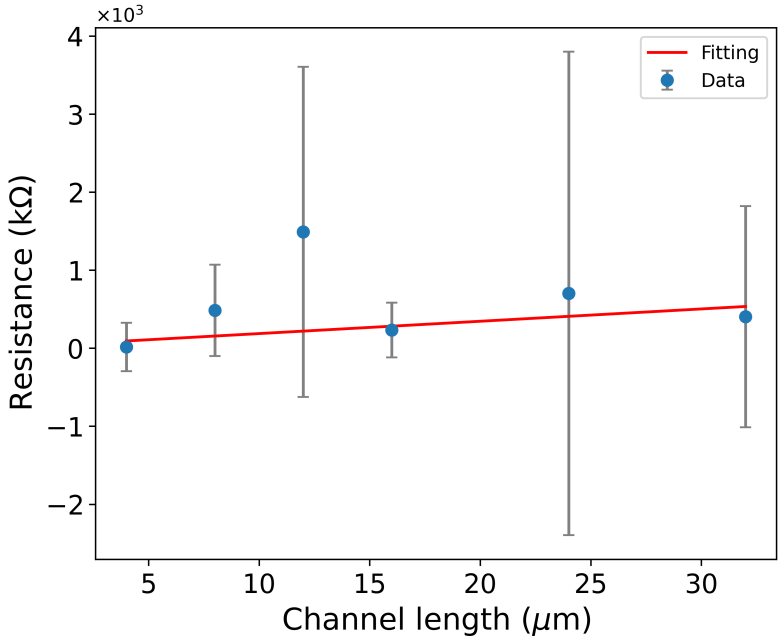


Figure A.8: **TLM measurements in the initial state of the devices.** Error bars indicate the standard deviation from five samples. The contact resistance, obtained from linear fitting, is calculated to be 14.7 kΩ.

A.9. *I-V* fittings

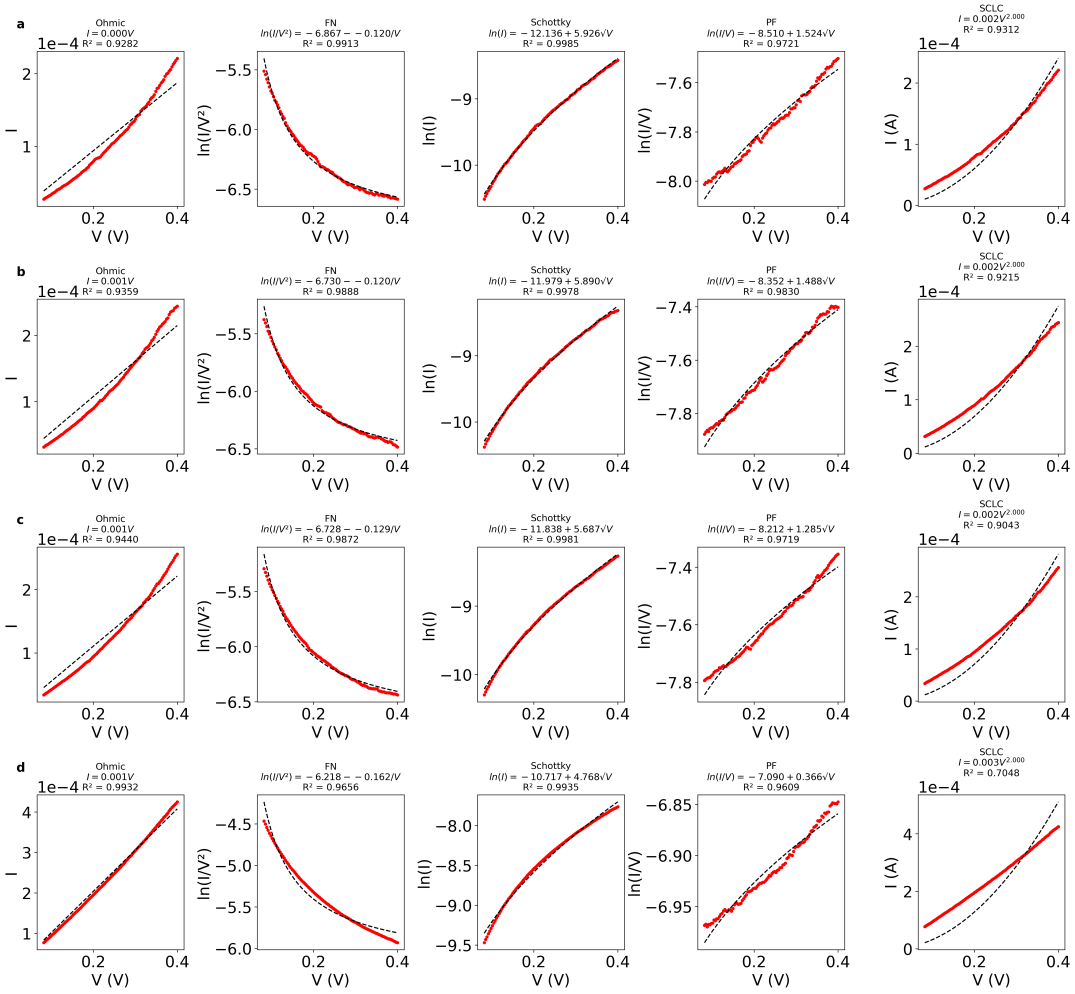


Figure A.9: **Five conduction mechanism fitting for RESET with varied pulse width.** Ohimc conduction, Fowler-Nordheim (FN) tunneling, Schottky emission, Poole-Frankel (PF) emission and Space charge limited conduction (SCLC) fitting for RESET process with pulse width of (a) 10 ms, (b) 0.6 ms, (c) 0.1 ms and (d) 0.02 ms, respectively.

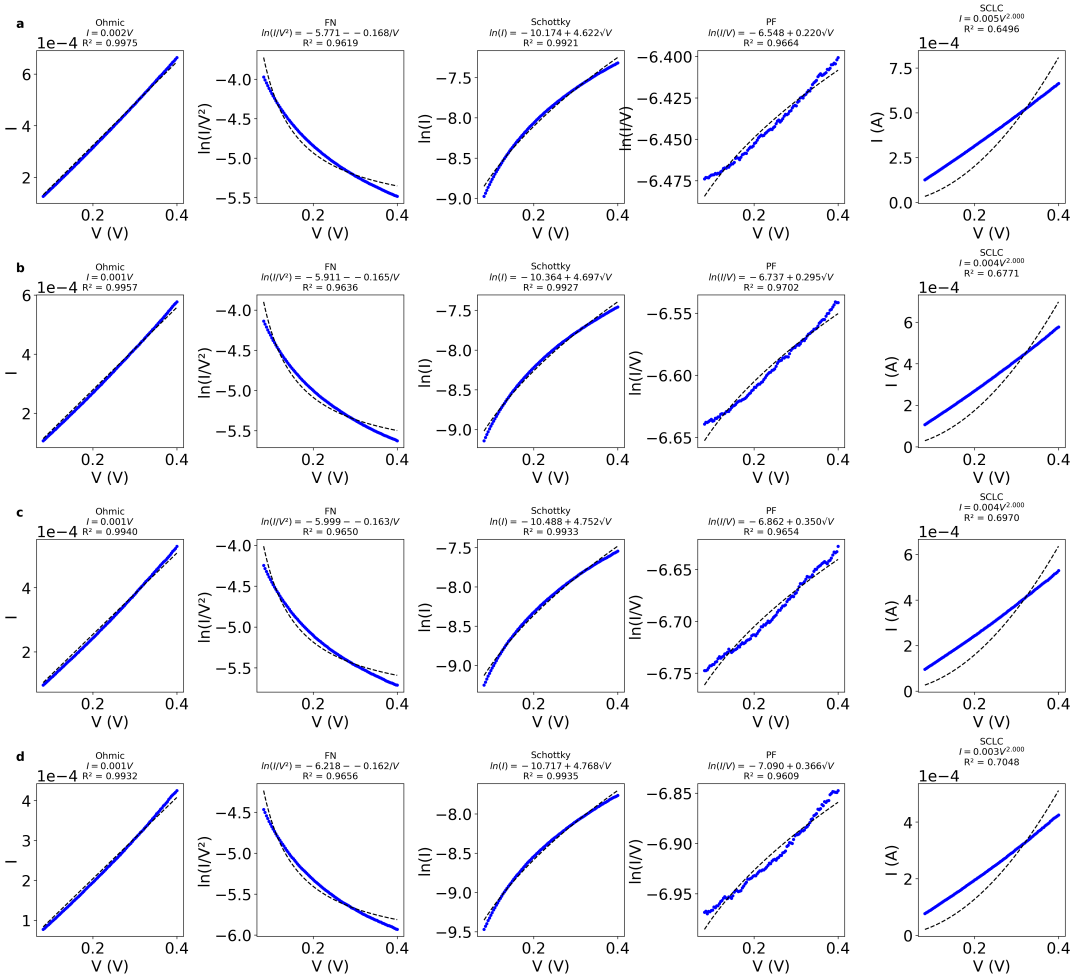


Figure A.10: **Five conduction mechanism fitting for SET with varied pulse width.** Ohmic conduction, FN, Schottky emission, PF and SCLC fitting for SET process with pulse width of (a) 10 ms, (b) 0.6 ms, (c) 0.1 ms and (d) 0.02 ms, respectively.